

CONTENTS

Valerii Stavytskyi, Oleksandr Bashta, Pavlo Nosko, Yurii Tsybrii <i>Determination of Hydrodynamic Power Losses in A Gearing</i>	1
Krzysztof Sokół, Piotr Ptak <i>Experimental Evaluation of Circuit Board Components under Extreme Conditions</i>	8
Hongli Cao <i>Design of a Fuzzy Fractional Order Adaptive Impedance Controller with Integer Order Approximation for Stable Robotic Contact Force Tracking in Uncertain Environment</i>	16
Paweł Bałon, Edward Rejman, Bartłomiej Kielbaso, Robert Smusz <i>Using HSM Technology in Machining of Thin-Walled Aircraft Structures.....</i>	27
Ildar Sharifullin, Andrey Nosko, Eugene Safronov <i>Mathematical Model of the Pallet Motion on a Magnetic Brake Roller of a Gravity Flow Rack</i>	34
Roman A. Usenkov, Igor A. Popov, Yuri F. Gortyshov, Svetlana Y. Kokhanova, Ravil A. Latypov <i>Thermodynamic Calculation of a Rotary Engine With External Heat Supply Based on The Ideal Rallis Cycle</i>	40
Zoulikha Bouhamatou, Foudil Abedssem <i>Fuzzy Synergetic Control for Dynamic Car-Like Mobile Robot.....</i>	48
Mohamed Belhorma, Aboubakar S. Bouchikhi <i>Multi-Objective Optimisation of the Electric Wheelchair Ride Comfort and Road Holding Based on Jourdain's Principle Model and Genetic Algorithm</i>	58
Meriem Toumi, Mohamed Bouzit, Fayçal Bouzit, Abderrahim Mokhefi <i>MHD Forced Convection using Ferrofluid over a Backward Facing Step Containing a Finned Cylinder</i>	70
Vladimir Morkun, Vitalii Tron, Vadym Zymohliad <i>Modelling of Iron Ore Processing in Technological Units Based on The Hybrid Approach</i>	82
<i>Abstracts.....</i>	V

ABSTRACTS

Valerii Stavitskyi, Oleksandr Bashta, Pavlo Nosko, Yurii Tsybrii

Determination of Hydrodynamic Power Losses in A Gearing

Despite the relatively numerous experimental studies, there are few published works on the topic of development of mathematical models that describe the hydrodynamic processes in gears. There is no generic analytical model that integrates all types of losses. The purpose of this work is to develop a modern generalised methodology for calculating the hydrodynamic power losses of high-speed gears. For each gear, partially or fully immersed into an oil bath, the power spent to overcome the hydromechanical resistance can be represented as the sum of the following: the Coriolis force moment arising from the radial movement of the oil in the tooth spaces of the rotating gear, the viscous friction forces moment on the periphery of the gear addendums in the oil bath and the viscous friction forces moment at the face of the gear in the oil bath. The hydrodynamic power losses due to the Coriolis force action, viscosity friction losses at the periphery of the gear and the viscosity friction at the face of the gear (both turbulent and laminar modes) were observed separately. From the mathematical simulation of the rotation processes when the gear is immersed into the oil bath, an analytical dependence was obtained. It allows predicting the influence of the geometrical parameters of the gearing on the hydrodynamic power losses. Analysis of the calculation results of the power losses due to the action of hydraulic resistance forces and results from experimental studies is provided for several gears with different hydromechanical parameters. The proposed method of calculating power loss due to hydromechanical resistance of the oil bath to the rotation of the gear gave results that were close to the experimental data. Acceptable coincidence of theoretical and experimental results allows recommending the received analytical dependencies for practical calculations of high-speed gears.

Krzysztof Sokół, Piotr Ptak

Experimental Evaluation of Circuit Board Components under Extreme Conditions

Designing products operating in harsh conditions is a challenging task. Years of experience, developed standards and good practices are crucial in achieving the intended result. The article shows a methodology for designing electronic systems based on the worst-case analysis (WCA) and comparing its outcomes with the experimental verification of an actual circuit through large-scale tests. The analysed diode-based semiconductor circuit is part of a temperature measuring system of industrial application. The objective of the design and analysis process is to achieve a reliable solution, which has all the required functionalities under actual, extreme operating conditions. The preliminary circuit design is developed using ideal components. The truth table, which represents customer requirements, is created to check the correct operation of the system. Simulation software, such as LTSpice, are used as the main tools to verify the correct functioning based on ideal or close-to-real component models. Next, based on the results of computer simulations, the WCA is conducted, considering all extreme (worst) operating environment parameters, such as, among others, ambient temperature or ageing. WCA results were verified through an experimental, large-scale measurement of the real system, with defined forward voltage as a function of the current flowing through the semiconductor at various ambient temperatures.

Hongli Cao

Design of a Fuzzy Fractional Order Adaptive Impedance Controller with Integer Order Approximation for Stable Robotic Contact Force Tracking in Uncertain Environment

Current research in robot compliance control is unable to take both transient contact force overshoots and steady-state force tracking problems into account. To address this problem, we propose a fuzzy fractional order (FO) adaptive impedance controller to avoid the force overshoots in the contact stage while keeping force error in the dynamic tracking stage, where traditional control algorithms are not competent. A percentage gain is adopted to map FO parameters to integer order (IO) parameters by their natural properties, and a fuzzy logical controller is introduced to improve the system stability. The simulation results indicate that the proposed controller can be made more stable than and superior to the general impedance controller, and the force tracking results also have been compared with the previous control methods

Paweł Bałon, Edward Rejman, Bartłomiej Kielbasa, Robert Smusz
Using HSM Technology in Machining of Thin-Walled Aircraft Structures

Subtracting manufacturing technologies have entered that realm of production possibilities which, even a few years ago, could not be directly adapted to direct production conditions. The current machines, i.e. heavy, rigid cutting machines using high spindle speed and high feed speed, allow for manufacturing very thin and relatively long parts for use in the automotive or aerospace industry. In addition, the introduction and implementation of new 70XX aluminium alloys with high strength parameters, as well as monolithic diamond cutting tools for special machining, have had a significant impact on the introduction of high-speed machining (HSM) technologies. The main advantage of the applied manufacturing method is obtaining a very good smoothness and surface roughness, reaching even $S_z = 6-10 \mu m$ and $S_a < 3 \mu m$, and about four times faster and more efficient machining compared to conventional machining (for the beam part). Moreover, fixed and repeatable milling process of the HSM method, reduction of operational control, easy assembly of components and increase in the finishing efficiency compared to other methods of plastic processing (forming) are other benefits. The authors present a method using HSM for the manufacturing of aircraft parts, such as the chassis beam at the front of a commuter aircraft. The chassis beam assembly is made of two parts, front and rear, which – through a bolted connection – form a complete element replacing the previous part made using traditional technology, i.e., cavity machining, bending and plastic forming. The implementation of HSM technology eliminates many operations related to the construction of components, assembling the components (riveting) and additional controls during construction and assembly.

Ildar Sharifullin, Andrey Nosko, Eugene Safronov
Mathematical Model of the Pallet Motion on a Magnetic Brake Roller of a Gravity Flow Rack

The brake roller is one of the elements for the safe operation of gravity flow pallet racks. The brake roller of the magnetic (eddy current) type magnetic brake roller (MBR) is the most promising brake type. The working principle of the MBR is based on electromagnetic induction laws, according to which the braking of a conductor moving in the magnetic field is caused by the interaction of the conductor's eddy currents with the external magnetic field. In the paper, a mathematical model of the pallet motion on an MBR was developed. The equation of motion of the pallet on the MBR was derived. The calculation results were compared with the results of experimental studies of the pallet motion velocity on the MBR. For pallet speed under "drag peak" speed, the error of the mathematical model is $< 7.7\%$, and the error starts increasing once over the "drag peak" speed. Additional investigation of the coefficient of magnetic viscosity for speeds greater than the "drag peak" speed is required.

Roman A. Usenkov, Igor A. Popov, Yuri F. Gortyshov, Svetlana Y. Kokhanova, Ravil A. Latypov
Thermodynamic Calculation of a Rotary Engine With External Heat Supply Based on The Ideal Rallis Cycle

The design and kinematic scheme of the operation of a rotary external combustion engine with offset shafts have been developed. Expressions are obtained that make it possible to calculate the values of the increasing and decreasing functions of the working volume of the hot and cold cavities with a change in the angle of rotation of the rotor. An expression is obtained for calculating the compression ratio in the cold cavity of a rotary heat engine with an external heat supply. An expression has been determined that makes it possible to calculate the total torque of a rotary external combustion engine. A comparative analysis of the torque values of a rotary heat engine with an external heat supply and a Wankel engine is carried out. An assessment of the efficiency of an external combustion engine with offset shafts is carried out. Based on the thermodynamic calculations using ideal Erickson and Rallis cycles for a rotary external combustion engine, the processes occurring inside the hot and cold cavities of a heat engine are described. The thermodynamic condition parameters at the characteristic points of the cycle are determined and expressions are obtained that determine the thermal efficiency of the ideal Erickson and Rallis cycles in relation to the considered external combustion engine. A method for calculating the ideal cycle for an external combustion engine with offset shafts is presented.

Zoulikha Bouhamatou, Foudil Abedssemmed
Fuzzy Synergetic Control for Dynamic Car-Like Mobile Robot

This paper aims to present the dynamic control of a Car-like Mobile Robot (CLMR) using Synergetic Control (SC). The SC control is used to make the linear velocity and steering velocity converge to references. Lyapunov synthesis is adopted to assure controlled system stability. To find the optimised parameters of the SC, the grey wolf optimiser (GWO) algorithm is used. These parameters depend on the best-selected fitness function. Four fitness functions are selected for this purpose, which is based on the integral of the error square (ISE), the integral of the square of the time-weighted error (ITSE), the integral of the error absolute (IAE) and the integral of the absolute of the time-weighted error (TIAE) criterion. To go further in the investigation, fuzzy logic type 2 is used to get at each iteration the appropriate controller parameters that give the best performances and robustness. Simulations results are conducted to show the feasibility and efficiency of the proposed control methods.

Mohamed Belhorma, Aboubakar S. Bouchikhi

Multi-Objective Optimisation of the Electric Wheelchair Ride Comfort and Road Holding Based on Jourdain's Principle Model and Genetic Algorithm

The paper addresses the multi-body modelling of an electric wheelchair using Jourdain's principle. First, a description of the adopted approach was presented. Next, the mathematical equations were developed to obtain the dynamic behaviour of the concerned system. The numerical computation was performed with MATLAB (matrix laboratory: a high performance language of technical computing) and validated by MBD (Multi-Body Dynamics) for Ansys, a professional multi-body dynamics simulation software powered by RecurDyn. Afterwards, the model was treated as an objective function included in genetic algorithm. The goal was to improve the ride quality and the road holding as well as the suspension workspace. The multi-objective optimisation aimed to reduce the Root-Mean-Square (RMS) of the seat's vertical acceleration, the wheels load and the workspace modulus by varying the bodies' masses, the spring-damper coefficients and the characteristics of the tires. Acceptable solutions were captured on the Pareto fronts, in contrast to the relatively considerable processing time involved in the use of a random road profile generated by the power spectral density (PSD). During the process, the compatibility and the efficiency of Jourdain's equations were inspected.

Meriem Toumi, Mohamed Bouzit, Fayçal Bouzit, Abderrahim Mokhefi

MHD Forced Convection using Ferrofluid over a Backward Facing Step Containing a Finned Cylinder

In this paper, a numerical study of forced convection on a backward facing step containing a single-finned fixed cylinder has been performed, using a ferrofluid and external magnetic field with different inclinations. The partial differential equations, which determine the conservation equations for mass, momentum and energy, were solved using the finite element scheme based on Galerkin's method. The analysis of heat transfer characteristics by forced convection was made by taking different values of the Reynolds number (Re between 10 and 100), Hartmann number (Ha between 0 and 100), nanoparticles concentration (φ between 0 and 0.1) and magnetic field inclination (γ between 0° and 90°); also, several fin positions α [0° – 180°] were taken in the counter clockwise direction by a step of 5. After analysing the results, we concluded that Hartmann number, nanoparticles concentration, Reynolds number and magnetic field angles have an influence on the heat transfer rate. However, the fin position on the cylinder has a big impact on the Nusselt number and therefore on heat transfer quality. The best position of the fin is at ($\alpha = 150^\circ$), which gives the best Nusselt number and therefore the best heat transfer, but the fin position at ($\alpha = 0^\circ$) remains an unfavourable case that gives the lowest Nusselt values.

Vladimir Morkun, Vitalii Tron, Vadym Zymohliad

Modelling of Iron Ore Processing in Technological Units Based on The Hybrid Approach

The process line of concentrating iron ore materials is considered as a sequence of connected concentration units, some of which partially return ore materials to the previous unit. The output product of the final concentration unit in the process line is the end product of the whole line. Characteristics of ore, such as distribution of ore particles by size and distribution of iron content by size classes, are considered. Processing of iron ore materials by process units (a cycle, a scheme) is characterised by a separation characteristic – namely the function of extracting elementary fractions depending on physical properties of ore particles. The results of fraction analysis of ore samples in different points of the process line provide an experimental definition of separation characteristics and numerical values of the Rosin–Rammmler equation factors. To identify dependencies that cannot be analytically described, the hybrid approach accompanied by the Takagi–Sugeno fuzzy models, in accompaniment with triangular membership functions determining fuzzy sets in preconditions, are used. To identify fuzzy sets in rule preconditions, triangular membership functions are used. Introduction of a-priori data on iron ore concentration as constraints for model parameters is a promising trend of further research, since it enables increased accuracy of identification despite limited availability of experimental data.

DETERMINATION OF HYDRODYNAMIC POWER LOSSES IN A GEARING

Valerii STAVYTSKYI*, Oleksandr BASHTA**, Pavlo NOSKO**, Yurii TSYBRII***

*Educational and Scientific Institute of Transport and Building, Volodymyr Dahl East Ukrainian National University, Tsentralnyi ave., 59-a, 93400, Severodonetsk, Ukraine

**Department of Applied Mechanics and Materials Engineering, Aerospace Faculty, National Aviation University, Lubomyr Husar ave., 1, 03058, Kyiv, Ukraine

***Faculty of Mechanical Engineering, Bialystok University of Technology, Wiejska st., 45C, Bialystok, 15-351, Poland

friction.pairs@ukr.net, nosko_p@ukr.net, oleksandr.bashta@npp.nau.edu.ua, tsybrii@ukr.net

received 4 July 2021, revised 17 September 2021, accepted 25 September 2021

Abstract: Despite the relatively numerous experimental studies, there are few published works on the topic of development of mathematical models that describe the hydrodynamic processes in gears. There is no generic analytical model that integrates all types of losses. The purpose of this work is to develop a modern generalised methodology for calculating the hydrodynamic power losses of high-speed gears. For each gear, partially or fully immersed into an oil bath, the power spent to overcome the hydromechanical resistance can be represented as the sum of the following: the Coriolis force moment arising from the radial movement of the oil in the tooth spaces of the rotating gear, the viscous friction forces moment on the periphery of the gear addendums in the oil bath and the viscous friction forces moment at the face of the gear in the oil bath. The hydrodynamic power losses due to the Coriolis force action, viscosity friction losses at the periphery of the gear and the viscosity friction at the face of the gear (both turbulent and laminar modes) were observed separately. From the mathematical simulation of the rotation processes when the gear is immersed into the oil bath, an analytical dependence was obtained. It allows predicting the influence of the geometrical parameters of the gearing on the hydrodynamic power losses. Analysis of the calculation results of the power losses due to the action of hydraulic resistance forces and results from experimental studies is provided for several gears with different hydromechanical parameters. The proposed method of calculating power loss due to hydromechanical resistance of the oil bath to the rotation of the gear gave results that were close to the experimental data. Acceptable coincidence of theoretical and experimental results allows recommending the received analytical dependencies for practical calculations of high-speed gears.

Keywords: hydrodynamic power losses, gearing, tooth spaces, high-speed gears, Coriolis force, mathematical model

1. INTRODUCTION

The current state of research on gear trains can be said to be evolving in several directions. One of them is development of the geometry of new gearings based on the classic geometric and kinematic theories of gearing developed by, for instance, Bolotovskiy, 1974 [6] and Litvin, 1968 [27]–[29] and expanded by, for instance, Shishov, 2001 [37], Karpov, 2017 [24], Tkach, 2018 [43, 44] and Franulovic et al., 2017 [18]. Besides, Hlebanja, 2012 [20] proposed an alternative S-gear tooth geometry, which improves the contact circumstances by lowering the contact pressure, which consequently enables the thickening of the oil film, diminishes the amount of sliding and thus lowers friction. Kapelevich, 2000 [23] presented a method of research and design of gears with asymmetric teeth that enables increases in the load capacity and reduction of the weight, size and vibration level. Litvin 2002 [30] investigated and compared two versions of face-gear drives based on the application of a spur pinion of two versions of geometry and conjugated face gear. The following advantages were obtained with the new version of geometry: (i) longitudinal orientation of bearing contact, which enables avoidance of the edge contact; and (ii) reduction of contact stresses.

The other direction is the study of the stressed state of gear teeth to develop the most reliable analysis of the strength (Resh-

etov, 1989 [35]; loselevich, 1988 [22], Litvin, 2002 [30]), for instance. Senthil Kumar, et al., 2008 [25] presented the optimisation of the asymmetric spur gear drive, which was carried out by using an iterative procedure on the calculated maximum fillet stresses through finite element method (FEM) for different rack cutter offsets, and finally, the optimum values of rack cutter offsets are suggested for the given centre distance and the speed ratio of the asymmetric gear drive.

One more direction of gear train research is improvement of the existing synthesis techniques of gear drives by designing gearings on the basis of optimisation models (Chen et al., 2016 [12], Zhuravlev, 2001 [45], Chen et al., 2019 [11], Fong et al., 2002 [17] and Gao et al., 2002 [21]) and B-spline curves, interpolating a number of discrete points on involute profiles. In this case, tooth surfaces are modelled by sweeping the B-spline profiles along user-defined trajectories (Barone, 2001 [4]). Besides, a mathematical model of the helical spur gear under condition of gear non-undercutting, as well as the software to generate the complete geometry of a gear, including the involute tooth surfaces, the modified root fillets and the modified tip fillets, has been developed by Chen and Tsay [10], using experimental studies of the teeth tense state in order to refine the existing calculation methods.

Amania et al., 2017 [3] performed an independent investigation of tip pointing and undercutting conditions. A non-dimensional

methodology was introduced, and the order of the multi-parametric problem was reduced. This model took into account all applicable geometric and kinematical conditions and constraints to qualify each point in the design space (hence each combination of geometrical gear design parameters) in terms of manufacturability and geometrical compatibility.

Increase in transmitted capacities and speeds causes considerable energy dissipation and, as a consequence, an increase in the temperature in a gearing. This impairs the mechanical characteristics of gear drive parts and reduces their service life. As a generalised criterion of the effectiveness of high-speed gear drive, the efficiency of a gearing can be considered, taking into account the conditions and modes of operation, materials and manufacturing process, transmitted load and peripheral speed.

Power losses can be conditionally divided (Niemann, 2003 [32]) into those that depend on the transmitted load (mechanical friction in a gearing and bearings) and those that are independent of the load (aero-hydrodynamic resistance, periodic compression and expansion between teeth) (Changenet, 2006 [9], 2007 [7], 2008 [8], Seetharaman et al., 2009 [36], Zhouet al., 2014 [46], Polly et al., 2017 [34]). An exhaustive study of different kinds of power loss distributions was conducted by Heingartner (2005) [19] and Lechner and Naunheimer [26].

In the study of hydrodynamic resistance while immersing gears into an oil bath, most authors have developed empirical equations to determine the dimensionless moment coefficient of hydrodynamic resistance (Mann, 1961 [31]) and considered a rotor, disc or gear immersed into the oil bath. In addition, Ahsan (2016) [1] investigated this phenomenon of hydrodynamic power dissipation in elastic systems (discs) oscillating in viscous fluids, which may provide a viable means for reducing energy losses.

Based on the results of experiments, Daily et al., (1960) [14] proposed the consideration of four modes of flow around a disc that is completely immersed into a liquid.

The phenomena occurring in the area between the teeth were considered by Akin et al. (1975) [1]. They proposed a vector model for estimating the depth of oil filling in rotating gear spaces and Concli (2012) expanded this idea [13].

Dawson, 1984 [15] proposed and, in 1988 [16], modified an approximate formula for determining power losses, obtained from the results of an experimental study of losses separately at the ends of a spur gear and at its periphery.

Pechersky et al. (1987) [33] developed a numerical model for locking a certain volume of oil–air mixture between gear and pinion teeth addendum and dedendum in engagement. It was determined that the speed of the oil–air mixture in gears with a larger module is greater.

The results of the Changenet experiment (2008) [8] showed that with the reduction in side clearance between a rotating gear and a fixed wall, the power losses are decreased due to hydrodynamic resistance. It was also found that the relative reduction in power losses caused by the presence of the side clearance does not depend on the speed of gear rotation and its geometrical parameters.

2. PROBLEM STATEMENT

Despite the relatively numerous experimental studies, there are only few published works on the development of mathematical models that describe the hydrodynamic processes in gears. There

is no generic analytical model that integrates all types of losses.

The purpose of this work is to develop a modern generalised methodology for calculating hydrodynamic power losses of high-speed gears.

In order to determine the integral characteristics of energy dissipation due to aero-hydrodynamic resistance in analytical form, a simplified mathematical model based on the following assumptions is proposed.

- aerodynamic drag in a gear tooth space is determined by the Coriolis force caused by the radial flow rate of the oil–air mixture during its rotation together with the toothed gear;
- additional sources of energy dissipation include the viscous friction of the oil–air mixture on the working surfaces and heads of teeth, the face surfaces of the gear and inhibition of the flow of the mixture in the clearance between a gear and gearbox;
- the radial speed of the oil–air mixture in the gear tooth spaces and the speed of rotation of a gear are constant;
- transient modes of relative flow of oil–air mixture (either laminar or turbulent mode) are absent;
- losses caused by bearings and sealings are relatively small and can be neglected.

2.1. Mathematical simulation of power losses when immersing a gear in an oil bath

Depending on the operating conditions, different methods of oil supply to parts and gear drive units are used. They are mainly lubrication by immersion into oil bath, spraying from the main oil bath and circulating-type oil supply.

In the general case, when lubricating the gear by immersion into the oil bath, the gears are affected by actions such as the force of aerodynamic resistance and the force of hydrodynamic resistance.

At a relative immersion depth $h_i = \frac{h_i}{r_{ai}} \leq 0$, the lubricating oil does not come into contact with the gear (circulating oil supply).

The immersion depth $h_i \geq 2$ corresponds to the case of complete immersion of the gear into the oil bath.

At a depth of $h_i = 2$, the angle $\varphi_i = \pi$ and the lubricating surface at the ends of the gear is $A_{wash} = 2 \cdot \pi \cdot r_{ai} \cdot b_i$. When $h_i \leq 0$, similar to the case of $h_i = 2$, we can consider that the wheel is completely immersed, but in air. The force of hydrodynamic resistance is converted into the force of aerodynamic resistance.

The ratio of the aerodynamic and hydrodynamic resistance forces is determined by the oil level in the oil bath.

Power losses due to the action of the Coriolis force are caused by the presence of radial velocity of the oil–air mixture in the spaces of rotating gear. They were validated on the basis of the results of mathematical modelling of processes in the spaces of a rapidly rotating gear [42] and also by the experiment of Akin and Moss [2], among others.

For each gear, partially or fully immersed into the oil bath, the power spent to overcome the hydromechanical resistance can be represented as the sum of the following components:

$$M_a = M_k + M_v + M_f \quad (1)$$

where M_k is the moment of the Coriolis force arising due to the radial movement of the oil in the tooth spaces of the rotating gear

in newton-metres; M_v is the moment of viscous friction forces on the periphery of the gear addendums in the oil bath, in newton-metres; M_f is the moment of viscous friction forces at the gear face end in the oil bath, in newton-metres.

3. THE PROBLEM SOLUTION

3.1. Determination of hydrodynamic power losses due to Coriolis force action

The Coriolis force F_k that acts on the working surface of one of the gear teeth is determined by the formula

$$F_k = m_{bm} \cdot a_k \quad (2)$$

where $m_{bm} = \frac{m_{bmax} + m_{bmin}}{2}$ is the average mass of the oil in the gear tooth spaces, in kilograms; m_{bmax} is the mass of the oil in the tooth spaces at the time of its exit from the oil bath, in kilograms; m_{bmin} is the mass of the oil in the tooth spaces at the time of beginning of the gear immersion into the oil bath, in kilograms; a_k is the Coriolis acceleration that occurs due to the movement of the oil-air mixture in the tooth spaces in the radial direction of a rotating gear, in metres per square second.

The Coriolis acceleration is determined by the formula

$$a_k = 2 \cdot \omega_i^2 \cdot r_i \cdot \sin\alpha \cdot \cos\beta \quad (3)$$

where β is the angle of the tooth line inclination, in radians; α_i is the operating pressure angle at any point of the involute of radius r_i ; ω_i is the angular velocity; r_i is the radius to any point on the tooth profile curve.

The average mass of the oil in a tooth space located in the oil bath can be determined by the following formula:

$$m_{bm} = \frac{Q_3 \cdot \Delta t}{2} \quad (4)$$

where Q_3 is the mass consumption of the oil when filling the tooth spaces through the backlash area of the tooth immersed into the oil bath, in kilograms per second; Δt is the time period when a tooth space is in the oil bath, in seconds.

$$\Delta t = \frac{\overline{AC}}{\omega_i} = \frac{2 \cdot \phi_i \cdot r_i}{\omega_i} = \frac{2 \cdot r_i \cdot \arccos(1-h_i)}{\omega_i} \quad (5)$$

\overline{AC} is the arc length determined by the immersion depth of the gear in the oil bath; h_i is the tooth height at any point of the tooth; ϕ_i is the angle of gear rotation in the process of meshing.

Mass consumption of the oil while filling the tooth spaces in the case of its immersion into the oil bath Q_3 depends on the end cross-sectional area of the tooth space, the actual speed of its filling with oil and the density of the oil:

$$Q_3 = A_a \cdot \rho_m \cdot V_3 \quad (6)$$

where ρ_m is the density of the lubricant at a specified temperature of the oil bath, in kilograms per cubic metre; $A_a = \sum_{i=1}^2 S_{bn} \cdot y_i$ is the cross-sectional area of the tooth spaces in the axial direction, in cubic metres; y_i is the backlash coefficient obtained by the experiment; S_{bn} is the tooth cross-sectional area, in square metres; V_3 is the actual velocity of the filling of the tooth spaces by the axial flow of oil when the gear is immersed into the oil bath, in metres per second.

Then,

$$m_{bm} = \frac{A_a \cdot \rho_m \cdot V_3 \cdot r_i \cdot \arccos(1-h_i)}{\omega_i} \quad (7)$$

The magnitude of the velocity of filling of the tooth spaces in the axial direction is determined by Bernoulli's law:

$$\rho_m \cdot \frac{V_3^2}{2} = p_b - p_j - p_g + p_h + \rho_m \cdot \frac{k_0^2 \cdot V_3^2}{2}, \quad (8)$$

where p_b is the oil pressure in the tooth spaces due to the action of the friction forces, in megapascals; p_j is the oil pressure in the tooth spaces due to centrifugal forces, in megapascals; p_g is the oil pressure in the tooth spaces due to the action of gravity, in megapascals; p_h is the hydrostatic pressure in the tooth spaces, in megapascals; $V_t = \omega \cdot r \cdot \sin\alpha \cdot \cos\beta$ is the velocity of the oil flow, which is displaced by the tooth profile from the tooth spaces in the radial direction, in metres per second; k_0 is the velocity coefficient, which depends on the shape of the oil flow from the tooth spaces of the gear.

Equation (8) describes the processes occurring in the tooth spaces that are immersed into the oil bath: the oil is ejected from the tooth spaces by gravitational and centrifugal forces and held in the tooth spaces by viscous and hydrostatic forces. But some of the oil is emitted in the radial direction at velocity V_1 , and arrives axially at velocity V_3 .

If the relative addendum circle radius of the gear is $R_a = r_a \cdot r_i$ and the relative dedendum circle radius $R_b = r_f \cdot r_i$, we get the relative pressure of the oil centrifugal forces of inertia:

$$p_j = \frac{p_j}{\rho_m \cdot \omega_i^2 \cdot r_i^2} = \frac{1}{2} \cdot (R_a^2 - R_b^2), \quad (9)$$

where r_a is the tip fillet radius; r_f is the root fillet radius.

The area of the wetted surface is determined as

$$A_{wash} = b \cdot r_i^2 \cdot (\tan^2\alpha_a - \tan^2\alpha_f) \cdot \cos\alpha. \quad (10)$$

Taking into account that the Reynolds number is $Re = \frac{\omega_i \cdot r_i^2}{\nu_m}$, the relative oil pressure in the tooth spaces due to viscous friction forces is calculated as

$$p_b = \frac{p_b}{\rho_m \cdot \omega_i^2 \cdot r_i^2} = \frac{V_t^{1.5} \cdot (\tan^2\alpha_a - \tan^2\alpha_f) \cdot \cos\alpha}{\phi_i^{1.5} \cdot A_i \cdot \sqrt{3 \cdot Re}} \quad (11)$$

where

$$\begin{aligned} \phi_i &= \left(\frac{V_t}{\omega_i}\right)^{1.5} \cdot \frac{(\tan^2\alpha_a - \tan^2\alpha_f) \cdot \cos\alpha}{R_a \cdot \sqrt{3}} = \\ &= \left(\frac{\sin\alpha \cdot \cos\beta}{\omega_i}\right)^{1.5} \times \frac{(\tan^2\alpha_a - \tan^2\alpha_f) \cdot \cos\alpha}{R_a \cdot \sqrt{3}}. \end{aligned}$$

The relative pressure of the gravitational forces is

$$p_g = \frac{(R_a - R_b) \cdot r_i \cdot g \cdot \rho_m}{\rho_m \cdot \omega_i^2 \cdot r_i^2} = \frac{(R_a - R_b)}{F_r} \quad (12)$$

where $F_r = \frac{\omega_i^2 \cdot r_i}{g}$ is Froude's number; g is the acceleration due to gravity.

The relative hydrostatic pressure of the oil in the tooth spaces at the pitch circle is determined in the following way:

$$p_h = \frac{r_i \cdot h_i \cdot g \cdot \rho_m}{\rho_m \cdot \omega_i^2 \cdot r_i^2} = \frac{h_i}{F_r} \quad (13)$$

Substituting Eqs (9) and (11–13) into Eq. (8), we obtain the Bernoulli equation in the dimensionless form:

$$V_3^2 = (R_a^2 - R_b^2) + \frac{2}{F_r} (h_i - R_a - R_b) + \frac{2\Phi_i}{\sqrt{Re}} + (k_o \cdot \sin\alpha \cdot \cos\beta)^2$$

The dimensionless filling velocity of the tooth spaces immersed into the oil bath is

$$\frac{V_3}{\omega_i r_i} = V_3 = k_s \times \sqrt{(R_a^2 - R_b^2) + \frac{2}{F_r} (h_i - R_a - R_b) + \frac{2\Phi_i}{\sqrt{Re}} + (k_o \cdot \sin\alpha \cdot \cos\beta)^2} \quad (14)$$

where k_s is the speed coefficient of the end face section of the gear tooth spaces ($k_s = 0.85$ for absolutely sharp edges of teeth, $k_s = 0.9$ in the case of additional processing of edges of teeth).

Then, we obtain

$$Q_3 = \frac{(\pi - 4 \cdot x \cdot \tan\alpha)}{z} \cdot \frac{r_i^3 \cdot (R_a^2 - R_b^2)}{2} \times \sum_{i=1}^2 y_i \cdot \rho_m \cdot \omega_i \cdot V_3 \cdot \cos\beta \quad (15)$$

and

$$m_{bm} = \frac{\rho_m \cdot r_i^3 \cdot (\pi - 4 \cdot x \cdot \tan\alpha) \cdot (R_a^2 - R_b^2)}{2 \cdot z} \times \frac{\sum_{i=1}^2 y_i \cdot V_3 \cdot \arccos(1 - h_i) \cdot \cos\beta}{2 \cdot z} = \frac{\rho_m \cdot r_i^3 \cdot m_{bm}}{2 \cdot z} \quad (16)$$

where $y_i = \frac{4 \cdot R_b \cdot \delta_i}{(R_a^2 - R_b^2)}$ is the coefficient of backlash area, which is considered as the ratio of the radial clearance area of one tooth to the area of the tooth spaces.

The Coriolis force is

$$F_k = \rho_m \cdot r_i^4 \cdot \frac{m_{bm}}{z_i} \cdot \omega_i^2 \cdot \sin\alpha \cdot \cos\beta \quad (17)$$

The Coriolis force moment in the case where the gear is immersed into the oil bath (torque of the resistance of gear) is:

$$M_k = \frac{\arccos(1 - h_i) \cdot z_i}{\pi} \cdot F_k \cdot r_i; \quad M_k = \frac{\rho_m \cdot \omega_i^2 \cdot r_i^5}{\pi} \cdot (\pi - 4 \cdot x \cdot \tan\alpha) \cdot (R_a^2 - R_b^2) \times \sum_{i=1}^2 y_i \cdot V_3 \cdot \arccos^2(1 - h_i) \cdot \sin\alpha \cdot \cos^2\beta \quad (18)$$

For a zero-toothed gear, expression (18) is partially simplified as

$$M_k = \rho_m \cdot \omega_i^2 \cdot r_i^5 \cdot (R_a^2 - R_b^2) \times \sum_{i=1}^2 y_i \cdot V_3 \cdot \arccos^2(1 - h_i) \cdot \sin\alpha \cdot \cos^2\beta \quad (19)$$

When the zero-toothed gear is immersed into the oil bath, the dimensionless moment of the Coriolis force is

$$C_k = 2 \cdot (R_a^2 - R_b^2) \cdot \frac{(\pi - 4 \cdot x \cdot \tan\alpha)}{\pi} \times \sum_{i=1}^2 y_i \cdot V_3 \cdot \arccos^2(1 - h_i) \cdot \sin\alpha \cdot \cos^2\beta \quad (20)$$

3.2. Determination of losses due to viscosity friction at the periphery of the toothed gear

A gearing, partially or fully immersed into the oil bath, is subject to the forces of hydrodynamic friction, both on the periphery of the gear and on the lateral surfaces of gears.

The boundary conditions for oil circulation along the periphery of the gear are $V_{out} = \omega_i \cdot r_{ai}$ when $r = r_{ai}$; and $V_{out} = 0$

when $r \rightarrow \infty$; where ω_i is the angular velocity of the gear and $r \in (r_{ai}, \infty)$. Solving Eq. (19) with the given boundary conditions, we obtain the flow velocity at the periphery of the gear as

$$V_{out} = \frac{\omega_i \cdot r_{ai}^2}{r} \quad (21)$$

Then, at a given dynamic viscosity, the radial, axial and tangential components of the stress on the toothed gear periphery due to the gear rotation are determined as follows:

$$\tau_{out} = 2 \cdot \mu_m \cdot \frac{\partial V_{out}^r}{\partial r} = 0; \quad (22)$$

$$\tau_{out} = 2 \cdot \mu_m \cdot \left(\frac{1}{r} \frac{\partial V_{out}^r}{\partial r} + \frac{V_{out}^r}{r} \right) = 0; \quad (23)$$

$$\tau_{out} = \mu_m \cdot r \cdot \frac{\partial}{\partial r} \left(\frac{V_{out}^r}{r} \right) + \frac{1}{r} \cdot \frac{\partial V_{out}^r}{\partial r} = - \frac{2 \cdot \mu_m \cdot \omega_i \cdot r_{ai}^2}{r^2} \quad (24)$$

It can be seen from Eqs (22–24) that only the tangential component of the stress at the gear periphery is not equal to zero. It follows from Eq. (24) that on the periphery of the toothed gear $r = r_{ai}$, the tangential stress is equal to $\tau_{out} = 2 \cdot \mu_m \cdot \omega_i$ and the resistance force is equal to

$$F_{out} = A_{wash} \cdot \tau_{out} = 2 \cdot A_{wash} \cdot \mu_m \cdot \omega_i, \quad (25)$$

where $A_{wash} = 2 \cdot \phi_i \cdot r_{ai} \cdot b_i$ is the wetted surface area, in square metres.

The ultimate torque of the hydrodynamic resistance on the periphery of a single gear is determined as follows:

$$M_{out} = F_{out} \cdot r_{ai} = 4 \cdot \mu_m \cdot b_i \cdot r_{ai}^2 \cdot \omega_i \cdot \phi_i; \quad (26)$$

$$M_{out} = \frac{4 \cdot \mu_m \cdot R_a^2 \cdot b_i \cdot r_{ai}^5 \cdot \omega_i^2 \cdot \phi_i \cdot \rho_m}{\rho_m \cdot \omega_i^2 \cdot r_i^2} = \frac{4 \cdot R_a^2 \cdot \rho_m \cdot b_i \cdot r_{ai}^5 \cdot \omega_i^2 \cdot \phi_i^2}{Re}$$

Substituting the angle $\phi_i = \arccos(1 - h_i)$, the dimensionless torque of toothed gear rotation resistance due to viscosity friction at the tooth periphery equals

$$C_{out} = \frac{M_{out}}{\rho_m \cdot r_i^5 \cdot \omega_i^2} = \frac{8 \cdot R_a^2 \cdot b_i \cdot \arccos(1 - h_i)}{Re} \quad (27)$$

3.3. Determination of viscosity friction at the face end of the toothed gear

The dimensional torque of hydraulic resistance due to viscous friction of oil under laminar flow conditions is

$$C_M^{lam} = \frac{\sqrt{v_m}}{\sqrt{3 \cdot l_* \cdot \omega_i \cdot r_i^2}} = \frac{1}{\sqrt{3 \cdot l_* \cdot Re}} = \frac{1}{\sqrt{6 \cdot A_i \cdot \sqrt{h_i(2 - h_i)} \cdot Re}} \quad (28)$$

where $l_* = 2r_{ai} \sqrt{h_i(2 - h_i)} = 2A_i r_i \times \sqrt{h_i(2 - h_i)}$ is the characteristic linear size, in metres.

The hydraulic resistance force due to friction of the oil at the face surface of the gear under laminar flow conditions is found as

$$F_T^{lam} = \rho_m \cdot A_i^2 \cdot \omega_i^2 \cdot r_i^4 \times \frac{[\arccos(1 - h_i) - \sqrt{h_i(2 - h_i)}] \cdot (1 - h_i)}{\sqrt{6 \cdot A_i \cdot \sqrt{h_i(2 - h_i)} \cdot Re}} \quad (29)$$

The torque of the hydraulic resistance due to the friction of the

oil at the face surface of the toothed gear under laminar flow conditions is defined as $M_T^{lam} = F_T^{lam} \cdot r_i$;

$$M_T^{lam} = \rho_m \cdot A_i^2 \cdot \omega_i^2 \cdot r_i^5 \times \frac{[\arccos(1-h_i) - \sqrt{h_i \cdot (2-h_i)} \cdot (1-h_i)]}{\sqrt{6 \cdot A_i \cdot \sqrt{h_i \cdot (2-h_i)} \cdot Re}} \quad (30)$$

The dimensionless torque of hydraulic resistance due to oil friction at the face surface of the toothed gear under laminar flow conditions is

$$C_T^{lam} = \frac{M_T^{lam}}{0.5 \cdot \rho_m \cdot \omega_i^2 \cdot r_i^5} = \frac{2 \cdot A_i^2 \cdot [\arccos(1-h_i) - \sqrt{h_i \cdot (2-h_i)} \cdot (1-h_i)]}{\sqrt{6 \cdot A_i \cdot \sqrt{h_i \cdot (2-h_i)} \cdot Re}} \quad (31)$$

For turbulent flow mode,

$$C_M^{turb} = 0.0276 \cdot \left(\frac{v_m}{l \cdot \omega_i \cdot r_i} \right)^{\frac{1}{7}} = \frac{0.0276}{\sqrt[7]{2 \cdot A_i \cdot \sqrt{h_i \cdot (2-h_i)} \cdot Re}} \quad (32)$$

The hydraulic resistance due to friction of the oil at the face surface of the gear under turbulent flow conditions is determined similar to Eq. (29):

$$F_T^{turb} = 0.5 \cdot \rho_m \cdot \omega_i^2 \cdot r_i^2 \cdot 2 \cdot A_{wash} \cdot C_M^{turb} \quad (33)$$

Substituting Eqs (10) and (32) into Eq. (33), the moment of friction viscosity forces in turbulent motion is

$$M_T^{turb} = F_T^{turb} \cdot r_i = \rho_m \cdot A_i^2 \cdot \omega_i^2 \cdot r_i^5 \times \frac{0.0276 \cdot [\arccos(1-h_i) - \sqrt{h_i \cdot (2-h_i)} \cdot (1-h_i)]}{\sqrt[7]{2 \cdot A_i \cdot \sqrt{h_i \cdot (2-h_i)} \cdot Re}} \quad (34)$$

The dimensionless torque of hydraulic resistance due to oil friction at the face surface of the toothed gear under turbulent flow conditions is

$$C_T^{turb} = \frac{M_T^{turb}}{0.5 \cdot \rho_m \cdot \omega_i^2 \cdot r_i^5} = A_i^2 \cdot \frac{0.0276 \cdot [\arccos(1-h_i) - \sqrt{h_i \cdot (2-h_i)} \cdot (1-h_i)]}{\sqrt[7]{2 \cdot A_i \cdot \sqrt{h_i \cdot (2-h_i)} \cdot Re}} \quad (35)$$

The total torque of the hydromechanical resistance of the gear immersed into the oil bath is determined as follows:

$$M = 0.5 \cdot \rho_m \cdot \omega_i^2 \cdot r_i^5 \cdot (C_k + C_T + C_{out}) \quad (36)$$

Power loss due to the hydrodynamic resistance to rotating gear immersed into the oil bath is

$$P = 0.5 \cdot \rho_m \cdot \omega_i^3 \cdot r_i^5 \cdot (C_k + C_T + C_{out}) \quad (37)$$

Based on the obtained formulas, the mathematical modelling in the symbolic module MathCAD 12 was carried out (Stavitskiy, 2011, 2012 [38], [39], [40], [41], [42]), with variable parameters such as the kinematic viscosity v_m and density of the lubricant at a specified temperature of the oil bath ρ_m :

$$\log[\log(v_m + 0.6)] = A \cdot \log T + B,$$

where T is the oil temperature in kelvins, and A and B are constant coefficients.

Figure 1 represents the analysis of the calculation results of the power losses due to the action of hydraulic resistance forces

(37) and the experimental studies by Blok, 1962 [5], in which the research was carried out with several gears, the hydromechanical parameters of which were varied in the following ranges: module ranged from 1.5 mm to 5 mm; the angle of the tooth line inclination $\beta = 25^\circ$; face width of the gear ring ranged from 14 to 24 mm; and number of teeth ranged from 20 to 102) (Table 1). In Fig. 1, the relative depth of gear immersion in the oil bath is 0.55. It allows predicting the influence of the geometrical parameters of the gearing on the hydrodynamic power losses.

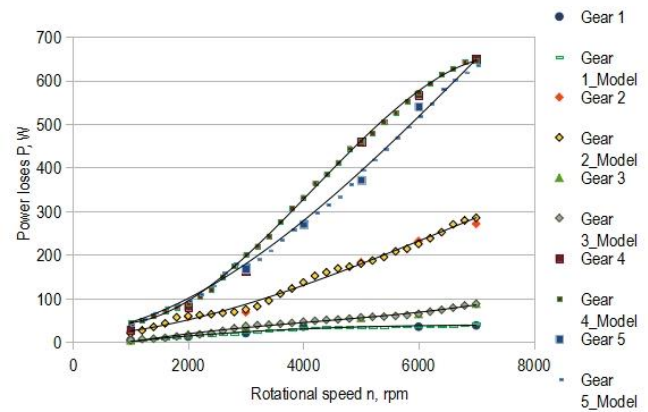


Fig. 1. Comparison of calculation results of the power losses due to hydrodynamic resistance to rotation of a toothed gear in the oil bath with experimental data

Tab. 1. Hydromechanical parameters of the gears

	Gear 1	Gear 2	Gear 2_Model	Gear 3	Gear 4	Gear 4_Model	Gear 5
Nominal pitch circle diameter, mm	96	153	153	90	159	159	100
Face width, mm	14	14	14	24	24	24	24
Module, mm	1,5	1,5	1,5	3	3	3	5
Number of teeth, n	64	102	102	30	53	53	20

4. DISCUSSION

Comparative analyses of the computational and experimental results yielded the following observations:

- The proposed method of calculating power losses due to hydromechanical resistance of the oil bath to rotation of the gear gives results with an error in the range of 1%–9% in relation to the experimental data;
- The change in hydrodynamic losses with a change in gear speed is practically subject to the law of the cubic parabola, but up to a certain speed (in Fig. 1, it is about 4,000 rev/min). A further increase in rotational speed leads to a decrease in the amount of oil in the space (disturbed mass balance: more oil is ejected from the space by centrifugal forces than the amount of oil entering the space through the space ends);
- At significant rotational speeds (in Fig. 1, it is from 5,000 rev/min to 7,000 rev/min), the amount of oil in the spaces decreases, and the power losses due to the hydrodynamic resistance in the oil bath, accordingly, are slightly reduced. Theoretical studies have made it possible to determine the

presence of two modes of oil motion in the tooth spaces of gears, which are characterised by the ratio of centrifugal, gravitational, hydrostatic, viscous and Coriolis forces.

5. CONCLUSIONS

When changing the face clearance from zero to the critical value, the power loss due to the hydrodynamic resistance of the toothed gear immersed into the oil bath is always less than similar losses, if the face clearance is greater than the critical value.

The dependence calculation Eq. (37) not only takes into account the influence of the geometrical parameters of the toothed gears immersed into the oil bath but also the structural characteristics, such as the depth of the toothed gear immersion and the face clearance between the casing walls and the rotating gear.

In order to determine the integral characteristics of energy dissipation and to develop a further engineering method for evaluating the energy efficiency of gearings, a mathematical model of the oil behaviour in the tooth spaces of rotating gears immersed into an oil bath has been developed.

The condition of the gear's maximum rotational speed at which lubrication by immersion into the oil bath becomes ineffective is established and the scheme of circulating greasing is found to be necessary.

Satisfactory coincidence of the theoretical and experimental results allows recommending the received analytical dependencies for practical calculations of high-speed gears.

Notation

b_i – effective face width
 h_i – tooth height at any point of the tooth
 ϕ_i – angle determined by the relative level of the oil bath
 m – module of the gearing
 r_i – radius to any point on the tooth profile curve
 x – profile offset factor
 z_i – number of teeth
 g – acceleration due to gravity
 α_i – operating pressure angle at any point of the involute of radius r_i
 α_a – pressure angle for addendum circle
 α_f – pressure angle for dedendum circle
 δ_i – inclined angle of the meshing line of directrices with respect to the pinion axis of rotation
 ρ_m – the density of the lubricant
 μ_m – dynamic viscosity
 ν_m – kinematic viscosity
 φ_i – angle of gear rotation in the process of meshing
 r_a – tip fillet radius
 r_f – root fillet radius
 ω_i – angular velocity
 δ – thickness of the boundary layer

REFERENCES

- Ahsan SN, Aureli M. Minimization of Hydrodynamic Power Losses in Oscillating Submerged Structures by a Novel Shape-Morphing Strategy. Volume 2: Mechatronics; Mechatronics and Controls in Advanced Manufacturing; Modeling and Control of Automotive Systems and Combustion Engines; Modeling and Validation; Motion and Vibration Control Applications; Multi-Agent and Networked Systems; Path Planning and Motion Control; Robot Manipulators; Sensors and Actuators; Tracking Control Systems; Uncertain Systems and Robustness; Unmanned, Ground and Surface Robotics; Vehicle Dynamic Controls; Vehicle Dynamics and Traffic Control. 2016; 2: 12-14.
- Akin LS, Mross JJ. Theory for the Effect of Windage on the Lubricant Flow in the Tooth Spaces of Spur Gears. *Journal of Engineering for Industry*. 1975;97(4):1266-1272.
- Amani A, Spitas C, Spitas V. Generalised non-dimensional multi-parametric involute spur gear design model considering manufacturability and geometrical compatibility. *Mechanism and Machine Theory*. 2017;109:250-277.
- Barone S. Gear Geometric Design by B-Spline Curve Fitting and Sweep Surface Modelling. *Engineering with Computers*. 2001;17(1):66-74.
- Blok H. Hydrodynamic effects on friction in rolling with slippage. *Biolwelle Joseph B. Rolling contact phenomena*. Amsterdam: Elsevier; 1962.
- Bolotovskiy I, Gurev B, Smirnov V, Shenderoy B. Cylindrical involute gears in external gearing. Moskva: Mashinostroyeniye (in Russian); 1974.
- Changenet C, Vexex P. A Model for the Prediction of Churning Losses in Geared Transmissions—Preliminary Results. *Journal of Mechanical Design*. 2006;129(1):128-33.
- Changenet C, Vexex P. Housing Influence on Churning Losses in Geared Transmissions. *Journal of Mechanical Design*. 2008;130(6).
- Changenet C, Oviedo-Marlot X, Vexex P. Power Loss Predictions in Geared Transmissions Using Thermal Networks—Applications to a Six-Speed Manual Gearbox. *Journal of Mechanical Design*. 2005;128(3):618-625.
- Chen C-F, Tsay C-B. Tooth profile design for the manufacture of helical gear sets with small numbers of teeth. *International Journal of Machine Tools and Manufacture*. 2005;45(12):1531-1541.
- Chen G, Li H, Liu Y. Double-arc harmonic gear profile design and meshing analysis for multi-section conjugation. *Advances in Mechanical Engineering*. 2019;11(5):168781401985065.
- Chen H, Zhang X, Cai X, Ju Z, Qu C, Shi D. Computerized design, generation and simulation of meshing and contact of hyperboloidal-type normal circular-arc gears. *Mechanism and Machine Theory*. 2016;96:127-145.
- Concli F, Gorla C. Analysis of the Oil Squeezing Power Losses of a Spur Gear Pair by Mean of CFD Simulations. Volume 2: Applied Fluid Mechanics; Electromechanical Systems and Mechatronics; Advanced Energy Systems; Thermal Engineering; Human Factors and Cognitive Engineering. 2012: 1-8.
- Daily JW, Nece RE. Chamber Dimension Effects on Induced Flow and Frictional Resistance of Enclosed Rotating Disks. *Journal of Basic Engineering*. 1960;82(1):217-230.
- Dawson PH. Windage Loss in Larger High-Speed Gears. *Proceedings of the Institution of Mechanical Engineers, Part A: Power and Process Engineering*. 1984;198(1):51-59.
- Dawson P. High speed gear windage GEC Review. *GEC Review*. 1988;43(3):164-167.
- Sheng W, Li Z, Zhang H, Zhu R. Geometry and design of spur gear drive associated with low sliding ratio. *Advances in Mechanical Engineering*. 2021;13(4):168781402110125.

18. Franulovic M, Markovic K, Vrcan Z, Soban M. Experimental and analytical investigation of the influence of pitch deviations on the loading capacity of HCR spur gears. *Mechanism and Machine Theory*. 2017;117:96-113.
19. Heingartner P, Mba D. Determination power losses in the helical gear mesh. *Gear technology*. 2005;22(5):32-37.
20. Hlebanja G. S-Gears for Wind Power Turbine Operating Conditions. *Machine Design*. 2012;4(3):123-130.
21. Gao Q, Ye J, Liu C. Design and modeling of noncircular gear with curvature radius function. *Journal of Computational Methods in Sciences and Engineering*. 2018;18(3):683-689.
22. Ioselevich G.B. *Machine parts*. Moskva: Mashinostroenie (in Russian); 1988.
23. Kapelevich A. Geometry and design of involute spur gears with asymmetric teeth. *Mechanism and Machine Theory*. 2000;35(1):117-130.
24. Karpov O, Nosko P, Fil P, Nosko O, Olofsson U. Prevention of resonance oscillations in gear mechanisms using non-circular gears. *Mechanism and Machine Theory*. 2017;114:1-10.
25. Senthil Kumar V, Muni D, Muthuveerappan G. Optimization of asymmetric spur gear drives to improve the bending load capacity. *Mechanism and Machine Theory*. 2008;43(7):829-858.
26. Lechner G, Naunheimer H. *Automotive Transmissions-Fundamentals, Selection, Design and Application*. 1st ed. Berlin: Springer; 1999.
27. Litvin F. *Gear theory*. Moskva: Nauka (in Russian); 1968.
28. Litvin F, Lu J. Computerized simulation of generation, meshing and contact of double circular-arc helical gears. *Mathematical and Computer Modelling*. 1993;18(5):31-47.
29. Litvin F, Lu J. Computerized design and generation of double circular-arc helical gears with low transmission errors. *Computer Methods in Applied Mechanics and Engineering*. 1995;127(1):57-86.
30. Litvin FL, Fuentes A, Zanzi C, Pontiggia M. Design, generation, and stress analysis of two versions of geometry of face-gear drives. *Mechanism and Machine Theory*. 2002;37(10):1179-1211.
31. Mann RW, Marston CH. Friction Drag on Bladed Disks in Housings as a Function of Reynolds Number, Axial and Radial Clearance, and Blade Aspect Ratio and Solidity. *Journal of Basic Engineering*. 1961;83(4):719-723.
32. Niemann G, Winter H. *Maschinenelemente*. 2nd ed. Berlin (in German): Springer; 2003. (Band 2: Getriebeallgemein, Zahnradgetriebe – Grundlagen, Stirnradgetriebe).
33. Pechersky M. An analysis of fluid flow between meshing spur gear teeth. MS thesis, Pennsylvania State University, State College, PA. 1987.
34. Polly J, Talbot D, Kahraman A, Singh A, Xu H. An Experimental Investigation of Churning Power Losses of a Gearbox. *Journal of Tribology*. 2018;140(3): 031102.
35. Reshetov D. *Detali mashin*. Moskva: Mashinostroenie (in Russian); 1989.
36. Seetharaman S, Kahraman A, Moorhead MD, Petry-Johnson TT. Oil Churning Power Losses of a Gear Pair: Experiments and Model Validation. *Journal of Tribology*. 2009;131(2):1-9.
37. Shishov V, Pankratov D, Muhvatyy O. The evaluation criteria of efficiency gearing transmission. *Visnik NTU KHPI (in Russian)*. 2001;12:27-33.
38. Stavitskiy V, Nosko P. Opredeleniye mekhanicheskogo kpd v zubchatom zatseplenii s uchetom usloviy ekspluatatsii. *Vestnik NTU «KHPI» (in Russian)*. 2011;51:152-164.
39. Stavitskiy V, Nosko P. Opredeleniye koeffitsiyenta poter' moshchnosti vsledstviye szhatiya maslovozdushnoy smesi mezhdub' yami tsilindricheskikh peredach. *Visnik Skhidnoukr. nats. u-tu im. V. Dalya (in Russian)*. 2011;5(2):313-318.
40. Stavitskiy V, Nosko P. Gidrodinamicheskoye soprotivleniye v vysokoskorostnykh zubchatykh peredachakh, Progressivni tekhnologii i sistemi mashinobuduvannya. *Mizhnarodny zb. naukovich prats' (in Russian)*. 2012;43:278-85.
41. Stavitskiy V, Nosko P, Likhodeyev S. Analiz sostavlyayushchikh poter' moshchnosti vsledstviye aerodinamicheskogo soprotivleniya vrashcheniyu zubchatykh koles, Progressivni tekhnologii i sistemi mashinobuduvannya. *Mizhnar. zb. naukovich prats' (in Russian)*. 2011;41:297-302.
42. Stavitskiy V, Nosko P, Fil P. Energeticheskaya effektivnost' vysokoskorostnykh zubchatykh peredach. Luhansk: vydavnytstvo SNU im. Dalia (in Russian); 2013.
43. Tkach P, Nosko P, Boyko G, Bashta O, Bashta A. Design of worm gears with optimal geometric parameters based on minimization of losses in gearing. *Problems of Friction and Wear*. 2018;1(78):75-84.
44. Tkach P, Nosko P, Bashta O, Boyko G, Tsybrii I, Gerasimova O. Gearing with increased teeth wear resistance. *Problems of Friction and Wear*. 2018;2(79):86-92.
45. Zhuravlev G. Evaluation of the Hertz solution applicability in problems of the gears teeth contact. *Mezhdunar. konf. Tehn. Mashinostroeniya (in Russian)*. 2001.
46. Zhou X, Walker P, Zhang N, Zhu B, Ruan J. Study of Power Losses in a Two-Speed Dual Clutch Transmission. *SAE Technical Paper Series*. 2014:1799.

Oleksandr Bashta:  <https://orcid.org/0000-0001-7914-897X>

Pavlo Nosko:  <https://orcid.org/0000-0003-4792-6460>

Yurii Tsybrii:  <https://orcid.org/0000-0002-7444-6035>

EXPERIMENTAL EVALUATION OF CIRCUIT BOARD COMPONENTS UNDER EXTREME CONDITIONS

Krzysztof SOKÓŁ^{*}, Piotr PTAK^{*}

^{*}Institute of Mechanic and Machine Design Foundations, Czestochowa University of Technology,
ul. J.H. Dąbrowskiego 69, 42-201 Czestochowa, Poland

krzysztof.sokol@pcz.pl, piotr.ptak@pcz.pl

received 12 May 2021, revised 10 October 2021, accepted 12 October 2021

Abstract: Designing products operating in harsh conditions is a challenging task. Years of experience, developed standards and good practices are crucial in achieving the intended result. The article shows a methodology for designing electronic systems based on the worst-case analysis (WCA) and comparing its outcomes with the experimental verification of an actual circuit through large-scale tests. The analysed diode-based semiconductor circuit is part of a temperature measuring system of industrial application. The objective of the design and analysis process is to achieve a reliable solution, which has all the required functionalities under actual, extreme operating conditions. The preliminary circuit design is developed using ideal components. The truth table, which represents customer requirements, is created to check the correct operation of the system. Simulation software, such as LTSpice, are used as the main tools to verify the correct functioning based on ideal or close-to-real component models. Next, based on the results of computer simulations, the WCA is conducted, considering all extreme (worst) operating environment parameters, such as, among others, ambient temperature or ageing. WCA results were verified through an experimental, large-scale measurement of the real system, with defined forward voltage as a function of the current flowing through the semiconductor at various ambient temperatures.

Key words: experimental test, mathematical model, semiconductor diodes, thermal chamber, WCA

1. INTRODUCTION

Worst-case analysis (WCA) is a popular tool for verifying a correctly designed system. This analysis is an effective tool to check a design, to ensure, with high probability that potential damage and imperfections are identified and eliminated before manufacturing and delivery to the customer. It is a qualitative assessment of a product's performance, taking into account the impact of external factors, such as the operating environment or component ageing. Besides analysing circuits, WCA often involves thermal stress and searching for extreme nominal value tolerances, failure variants or reliability prediction. The primary objective of the WCA is checking design correctness aimed at ensuring operation in accordance with the complete specification, throughout its service life and in the worst conditions and tolerances, such as ageing, initial deviations or temperature. Stress analysis is aimed at improving reliability by ensuring a sufficient margin, relative to permissible stress limits set out in the component documentation. A correctly conducted analysis mitigates overload conditions, which can contribute to a failure or reduce the change rate of parameters induced by thermal stress throughout the product's life cycle. The WCA should be conducted for all circuits covered by the design, regardless of their criticality. The WCA is an analytical technique that involves the observation of defined environmental conditions, such as external stresses. Operating conditions include electrical inputs/outputs, component quality, correlations between the parts and the impact of time on

subassembly parameters. WCA is a key tool in the process of developing a multi-system platform, which forms a complete product only as a whole. [1] discussed WCA methodologies based on National Aeronautics and Space Administration (NASA) experience, to develop a database containing worst variants for parts, sensitivity analysis and a mathematical approach to the extreme value analysis (EVA), root sum square (RSS) and the Monte Carlo analysis for solving circuit equations. These analyses have become an accepted industry standard over the last 8 years.

Scientists [2-9] showed the results of tests involving such methods as reverse engineering, which is required to find regions and prepare for analysing them. They also state worst-case execution time (WCET) analysis and discuss their accuracy. The authors also presented qualitative and quantitative data regarding the program structure of the regions. This information is suitable in terms of evaluating whether WCET analysis can provide useful results for this class of real codes, without excessive manual labour. A list of WCET analytical tool functions, which appeared during the project, was also presented.

Ferlet-Cavrois [10] described the worst deviation case for silicon on insulator (SOI) transistors in two technologies. It also includes experiments and simulations for the threshold shift analysis of an SOI transistor voltage. Lynch [11] analysed the worst output voltage ratio for resistor memory matrix having a finite resistance coefficient for bit elements. It was concluded that the resistance coefficient does not have to be high, and ratios >10 are usually sufficient. It also discusses trade-offs in terms of output

power and output voltage. Marcovitz [12] analysed and developed procedures for designing a transistor system coupled with a resistor and used in the mechanization of logic operations. The basis circuit consists of one transistor and several resistors. The circuit performs the OR function, followed by NO or AND, and then NO. Owing to the mechanization of these complex functions, it is possible to create any logical system. The first operational prerequisite for this circuit is that a transistor must be saturated if one or more inputs are of low status. The second requirement is transistor isolation if all inputs are high. A WCA is conducted for each of these requirements. Three solution types, namely, general purpose, indirect (flexible) purpose and special purpose were reviewed. Tian [13] demonstrated that the operations of an analytical and precise algorithm are complementary – the analytical algorithm is faster than the precise algorithm but has a higher interval spread error. It also discusses AC tolerance analysis, time-domain tolerance analysis and DC tolerance analysis techniques. Several examples and comparisons are given. In [14] the technique for characterising the behaviour of a DC-powered converter within the common mode (CM) was introduced for the first time. This characterization technique is based solely on measurements conducted on power converter terminals, without the requirement of in-depth knowledge regarding the converter structure, and describes CM behaviour in relation to the Thevenin equivalent circuit. Next, the analysis is used to determine the upper limit of CM potential within a system with at least one power converter. Finally, a model of the Thevenin equivalent circuit was generalised to a dual-port equivalent circuit, owing to which CM behaviour can be modelled at both the input and output of a power converter. Spence [15] provided an overview of concepts involving tolerance analyses and electronic system designing. They thoroughly discussed the approach towards statistical analyses. Such statistical methods as the Monte Carlo analysis were presented. Finally, they discussed several application examples for such analyses in terms of designs. Divekar [16] discussed statistical analyses simulating circuit performance variations caused by tolerance variations or other factors related to circuit manufacturing. The statistical circuit simulation procedure was illustrated via a simple system undergoing measurements. The measurement data are compared with the simulation results from worst-case and statistical analyses, without correlating model parameters and with model parameter correlations for devices used within the circuit. This comparison indicates a need to correctly take model parameter correlations into account. Riley [17] and Sokól et al. [18] focussed on the WCA in terms of using resistors in electronic systems. Hillebrand [19] reviewed the techniques and tools used to verify Verisoft software. Nassif [20] showed an approach towards WCA, which leads to more realistic estimates of the electronic device and circuit performance changes. Rafaila et al. [21] discussed experiment design concepts, and screening tests aimed at reducing the verification space size, whereas Maly et al. [22] and Nassif et al. [23] suggested a methodology for modelling random process fluctuations, together with its advantages and applications.

This research paper includes the results of studies focused on an electronic system that can be used, among others, as a temperature sensor or resistor calibrator. WCA and experimental measurements were used to determine the forward voltage as a function of the current flowing through the semiconductor at various ambient temperatures.

2. ANALYZED SYSTEM

The electronic system analysed by the authors is a module responsible for providing information on the engine operating temperature. The mathematical model of the analysed circuit is shown in Fig. 1 and described by Eq. (1). Diodes within the system act as a temperature sensor consisting of an actuator made up of two serially connected semiconductor diodes, contained in a single enclosure. The authors of the design decided to use two light-emitting diodes LEDs owing to the increased measurement accuracy. Two LEDs connected in series supply higher voltage to the output, which at the same time is the average value of two voltages. The application of two semi-conductors contained in a common enclosure enables ensuring the same operating conditions, smaller dimensions and minimizing the costs associated with the requirement to use subsequent LEDs in separate enclosures. A resistor limiting current consumption and a capacitor filtering the output voltage were also used within the analysed system. Semiconductor diodes are very popular, relatively inexpensive and accurate temperature measuring systems. A linear temperature coefficient, such as $-2 \text{ mV}/^\circ\text{C}$ for the operating temperature, makes LEDs an excellent solution for flexible and low-cost applications. A diode-based system can be simple, but its implementation may require a deeper analysis.

$$I = I_s - I_{D1} \exp\left(\frac{V - I_s R_{01}}{A_{01} V_T}\right) - I_{D2} \exp\left(\frac{V - I_s R_{01}}{A_{02} V_T}\right) - I_C \quad (1)$$

where: I – output current, I_s – current supplied by a generator, I_{D1} – diode 1 current, I_{D2} – diode 2 current, I_C – capacitor current, A_{01} , A_{02} – ideality factor corresponding to diodes 1 and 2, respectively, V_T – thermal voltage, V output voltage, resistance R_{01} and R_{02} .

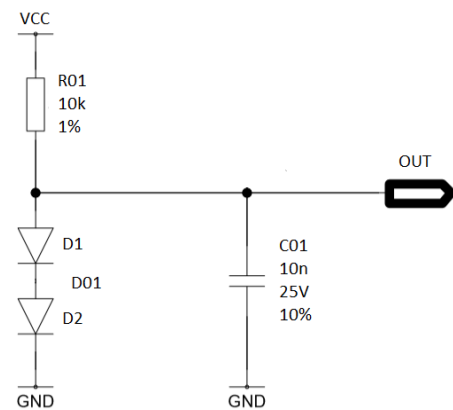


Fig. 1. Circuit diagram

Authors [24 – 26] have identified typical temperature measurement techniques and focused on the applications and advantages of silicon diodes acting as temperature sensors in various operating conditions. This article verified the system shown in Fig. 1 in terms of its use as a resistance calibrator in an unchanged version. R01 resistor in the analysed system is replaceable, which enables resistance measurements of this component (in this system, the resistor acts as a current limiter, hence inducing a determined voltage drop on the diodes). Voltage is read directly by the microcontroller’s ADC input. The output signal is filtered by the capacitor.

3. OPERATING CONDITIONS AND SELECTION OF COMPONENTS

The analysed system should perform all its functions in real operating conditions that can be encountered during the normal operation of the system. Requirements for the analysed module are as follows:

- Operating voltage VCC (5 V ± 0.25 V)
- Operating temperature (−40 °C; 150 °C)
- Flowing current (D01) (100 μA; 1500 μA)

Initial simulation of the system, conducted using the LTSpice tool, enabled proceeding to the stage of selecting suppliers and specific component models. The following system components were selected:

- Capacitor – Kemet C0603C103F3GACTU
- and the following LEDs were selected for further analysis:
 - Diode – ROHM BAV99HMFH (SOT23)
 - Diode – NXP BAV99W (SOT323)
 - Diode – Onsemi BAV99W (SOT323)

4. WORST-CASE ANALYSIS

The worst-case circuit analysis is an analysis technique, which determines circuit performance in the worst case scenario (extreme environmental and operating conditions). A series of calculations verifying the correct system functioning were conducted; however, this paper is limited to discussing temperature measurement.

For this case, it was assumed that the resistance of the R_{01} resistor is constant over the entire temperature range, which enabled focusing the calculations solely on the $I_F(V_F)$ forward current characteristics depending on the forward voltage, which was studied for the entire temperature range and a certain range of expected current flowing through a diode series.

The $I_F(V_F)$ forward current characteristics depending on the forward voltage of selected diodes are shown below. Analysing and comparing the technical documentation of electronic components from different manufacturers entail numerous difficulties for the designer. The greatest hindrance when comparing the parameters is the different conditions of the tests providing the data shown in the technical documentation on manufacturers' websites. Each manufacturer individually defines the test conditions for component verification, which provide the data in the form of a table or specification (Figs. 2–4).

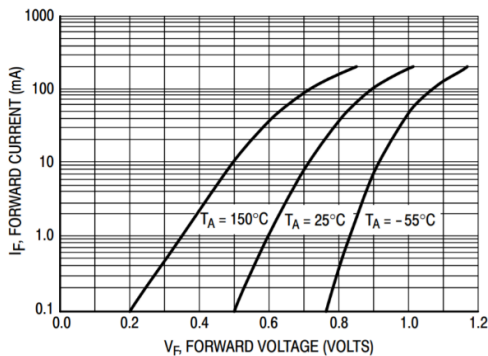


Fig. 2. Onsemi BAV99W $I_F(V_F)$ datasheet (<https://www.onsemi.com/pdf/datasheet/bav99wt1-d.pdf>)

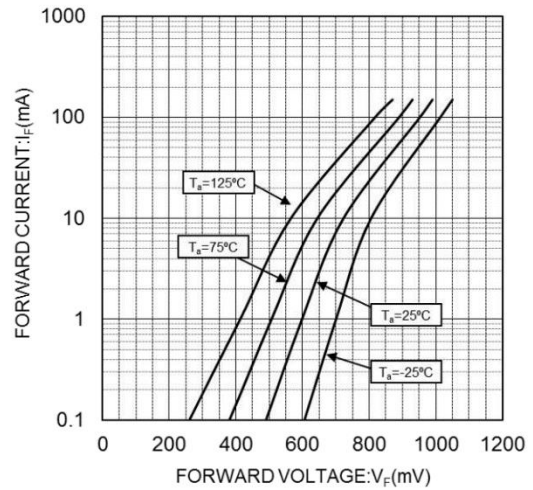


Fig. 3. ROHM BAV99HMFH $I_F(V_F)$ datasheet (<https://pl.mouser.com/datasheet/2/348/bav99hmfht116-e-1801281.pdf>)

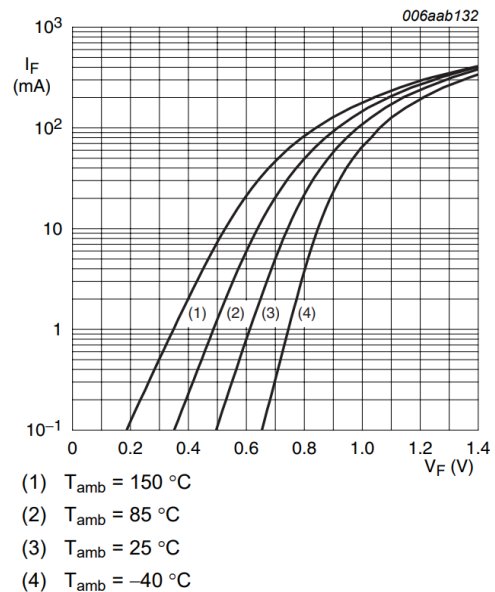


Fig. 4. NXP BAV99W $I_F(V_F)$ datasheet (https://www.elfadistelec.pl/Web/Downloads/_t/ds/bav99-series_eng_tds.pdf)

The technical documents made available by the component manufacturers very often include incomplete information regarding the conditions, in which the charts or tabular data were obtained. Very often, due to the specifics of a project, it is quite difficult to fully adopt the technical documentation data in a specific design. In many cases, this leads to a big problem in terms of how to supplement the calculations with component parameters, which do not fully correspond to the analysed situation in the designed system. Another difficulty is the manner of how the component vendors present the component parameters. The following types can be distinguished in this regard:

- Presentation of complete characteristics for a full range of temperatures and currents (Figs. 2–4) but without a statement whether they are nominal, minimum or maximum values. This forces an engineer to make assumptions and adopt a high safety factor for the calculations.
- Presentation of characteristics for one or two temperatures only, which significantly hinders the analysis involving the be-

haviour of the component in negative temperatures. As a result, based on two functions, one has to assume the hypothetical behaviour at a given temperature.

- Presentation of parameters for one ambient condition only, as a constant operating within the stated range.
- No information about a particular operating parameter of the component is given, despite the fact that such a parameter may be crucial in certain applications.

In the case of components such as resistors, capacitors or diodes, the operating conditions in the case of static characteristics are mainly limited to voltages, currents and ambient temperature, whereas in the case of simulating complex integrated circuits or dynamic analysis, the list of operating conditions during a simulation grows significantly, entailing issue in respect of a reliable functional verification of the system.

5. EXPERIMENTAL MEASUREMENTS AND TEST SETUP

Electronic systems often experience problems with the determination of certain boundary conditions, such as voltage and current levels or the ambient temperature and self-heating of individual components on printed circuit board (PCB). An approximate estimation of hard-to-determine boundary conditions, aimed at solving the issue via a direct method, may lead to significant errors. This paper presents an inverse method, which enables determining a transient temperature field as accurately as possible. This method is based on analysing a large-scale test in specific, repeatable environmental conditions. It can be applied when solving simple unidimensional problems, as well as simple and complex multi-dimensional problems.

The article presents the results of experimental tests involving a semiconductor diode from three different manufacturers. The conducted laboratory tests standardised the diode test conditions, which enabled a reliable comparison of their characteristics and their numerical analysis. The outcome of these analyses was a conclusion regarding the manufacturer ensuring the highest accuracy and linearity of the analysed characteristic.

LED series from three manufacturers were ordered for the laboratory tests. For the verification of the actual manufacturing spread to be as clear as possible, 136 pieces (128 used, 8 spares) from different stores were ordered, which allowed to potentially receive diodes from different manufacturing batches.

A dedicated PCB was designed for the study (Figs. 5 and 6), which enables correct and effective implementation of the laboratory tests.

Designed PCB is the result of a previously established measurement methodology (Fig. 7). It involves the possibly most accurate determination of voltage on diode pairs with a correctly designed PCB, which enables omitting the voltage drop on the channels and conduits directly connecting diode pairs with a scopecorder. For this purpose, the lengths of the used wires were the same, and the channels on the laminate were routed so that their lengths were the same.

Measurements of the forward voltage drop during the lifetime of three diode models were conducted on dedicated PCBs (Figs. 5 and 6). Every supplier had 128 enclosures. Each enclosure houses two LEDs, where the double voltage drop for both diodes was measured. All semiconductors were placed on two PCBs with an independent power supply.

Voltage was measured for the complete temperature range (measurement conducted for 9 different temperatures) and 15

current levels. LED voltage was measured during the tests using a scopecorder. It was decided to use this measuring device because of its modularity and multi-channel nature. This measuring device can be configured for multiple applications. It combines the advantages of a rapid oscilloscope and a traditional data recorder in a single portable instrument. Owing to the possibility of a scopecorder measuring 16 diodes simultaneously, the measurement was repeated until all LEDs were measured (for each temperature).



Fig. 5. PCB prepared for the development test. PCB, printed circuit board

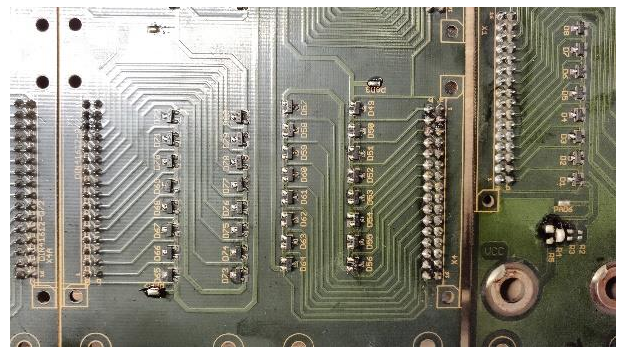


Fig. 6. PCB prepared for the development test (detailed view). PCB, printed circuit board

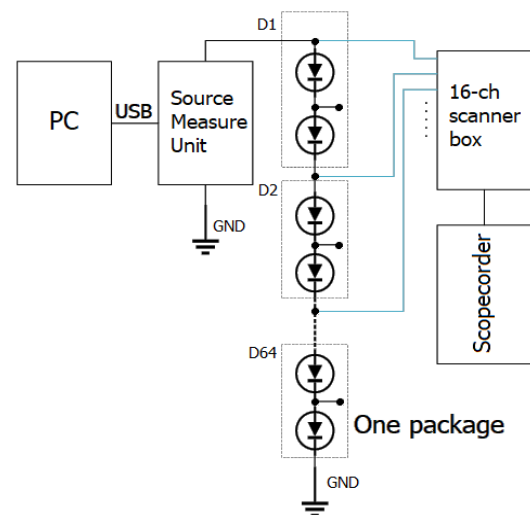


Fig. 7. Circuit diagram

The dedicated PCB was embedded in a specialized thermal chamber used to conduct all controlled climatic tests for a random period of time and on-going monitoring of interior conditions

(Fig. 8). Such climatic chambers are commonly used for testing the stability of medicinal products in the pharmaceutical industry but also in the construction industry, where, among others, it conditions concrete samples. It is also used in the automotive industry and the widely understood electronic engineering, for environmental testing of sub-assemblies and devices.



Fig. 8. PCBs in a thermal chamber. PCB, printed circuit board

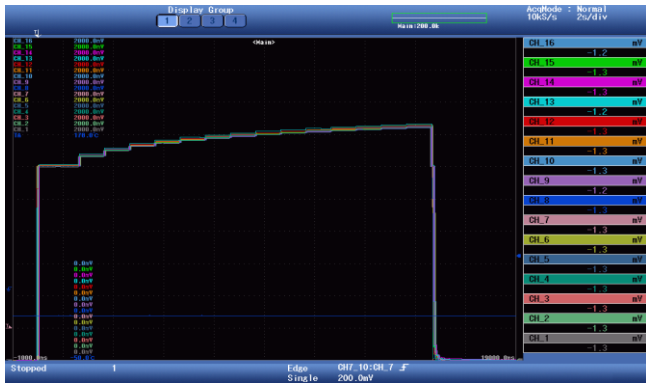


Fig. 9. Post-test scopecorder screen

Every diode pair was connected via a tape to a scopecorder recording the voltage as a function of time. A DC load power supply, controlled through a computer app, was connected to each of the printed boards. A procedure involving a computer setting a current excitation in the range of 100–1,500 μA , with an increment of 100 μA and increment duration of 1 s was conducted for each of the analysed temperatures. An example of obtained time waveforms from a scopecorder screen is shown in Fig. 9. They show voltage levels for a series of diodes, depending on the induced time-variable current flowing through them.

6. RESULTS

A series of data for analysis were obtained based on the conducted laboratory testing. The compiled data were analysed in terms of finding the optimal component for the project. For this purpose, the authors conducted a series of calculations enabling a comparison of all three LEDs. The first step involved calculating the average values for each of the tested diodes, in each of the tested currents, for a full range of temperatures Eq. (2).

$$n = \left(\sum_{i=1}^k n_i \right) / k \quad (2)$$

where: k – number of tested samples, n – arithmetic mean; and n_i – i th value in a dataset.

Next, the standard deviation was calculated according to Eq. (3), along with the previously calculated arithmetic mean Eq. (2). Efron [27] and Zięba [28] wrote about fitting methods, which involve algorithms for fitting various functions, a study of fitting quality and describe new statistical methods, such as the robust statistic, analysis of self-correlated data and Monte Carlo modelling applications.

$$\sigma = \sqrt{\frac{\sum_{i=1}^k (n_i - n)^2}{k - 1}} \quad (3)$$

where: σ – standard deviation.

The next step involved calculating the six sigma coefficient Eq. (4). The six sigma value was determined empirically. It was noticed that when processes are composed of hundreds of steps with the possibility of making an error in each of them, the probability that the entire process creates a good product at the first attempt depends on the product of probabilities of correct execution of each step. It was empirically established that even in the case of very complex processes, assuming six sigma at every stage, there was a high chance of obtaining a good product without corrections. This methodology was promoted by Harry et al. [29]. He derived them based on observation and practice. They are currently used as a change model since the production defects are not subject to the normal distribution in many cases. Standard deviation is not used to calculate potential defects in such a case, but the parameters of variabilities typical of other types of statistical distributions, which are discussed in greater detail in Yang et al. [30] and White [31].

$$\pm 6\sigma = n \pm 6\sigma \quad (4)$$

The measured and calculated parameters are shown in Figs. 10–12 and compared with manufacturers' datasheet. The next step involved selecting the range of expected current flowing through a diode to determine the graph linearity for a given range. Eq. (5) was used for this purpose. It enables determining a surface area formed by the mean (ideal) function of the voltage increase value $f(x)$ and the real value of this increase $g(x)$. The geometric interpretation of Eq. (5) is shown in Fig. 13.

$$|D| = \int_a^b [f(x) - g(x)] dx \quad (5)$$

where: x – test point, a – starting test point (100 μA), b – end test point (1,500 μA), $f(x)$ – ideal function and $g(x)$ – real-valued function.

The outcomes of the conducted calculations following formulas (2)–(5) are the results presented below. Figs. 10–12 contain the forward current as a voltage current function – $I_F(V_F)$ for each manufacturer. The blue colour in the graphs marks the mean value obtained from a series of measurements. The grey and yellow colours mark the plus and minus six sigma values, respectively. Orange colour curves correspond to the theoretical values from technical documentation. When analysing these graphs, it can be seen that the average measured, as well as theoretical datasheet values differ the most for Onsemi diodes under higher currents (Fig. 10).

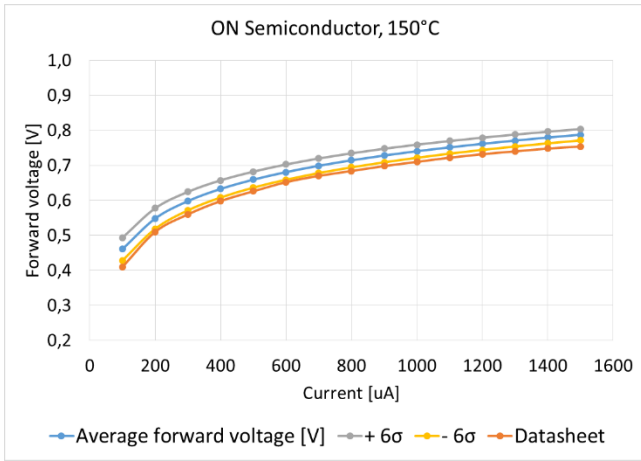


Fig. 10. Test results – Onsemi 150 °C

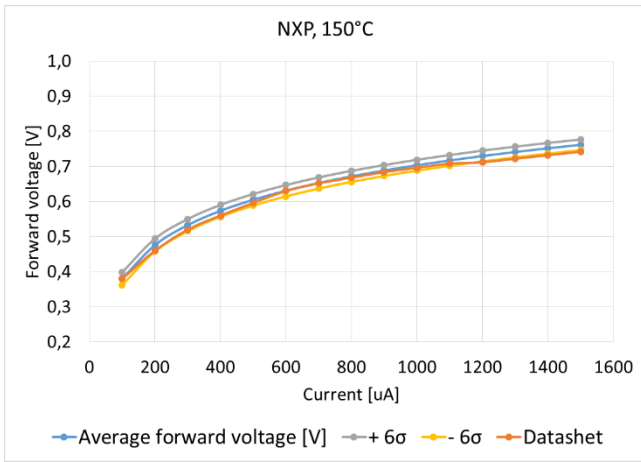


Fig. 11. Test results – NXP 150 °C

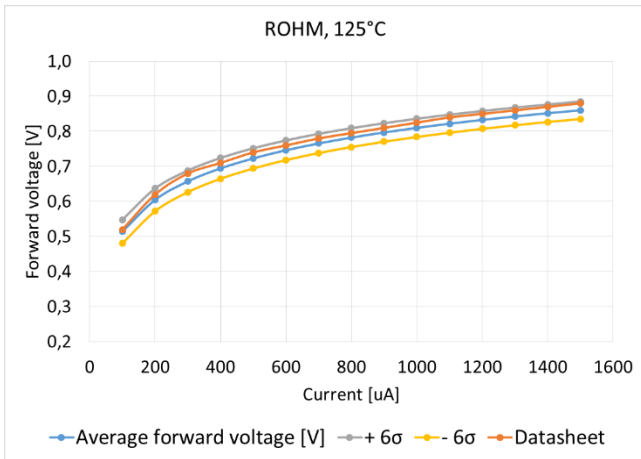


Fig. 12. Test results – ROHM 125 °C

The lowest average differences between the test and documentation can be observed for NXP LEDs, and amount to 13 mV, with 16 mV for ROHM and 42 mV for Onsemi. The observed differences can have several reasons. First, it should be noted that the manufacturer does not usually provide a formula for a function describing the curve. Second, please note that the I_F (V_F) function for each of the analysed diodes is not fully linear, which is confirmed both by manufacturer data, as well as laboratory measurements. On the other hand, each of the semiconductors is

characterized by the linearity of the current $>400 \mu\text{A}$. This statement is true for all three manufacturers at each of the tested temperatures. Finally, the authors show data (Tabs. 1–3) obtained based on Eq. (3), i.e., the standard deviation. The very low standard deviation in all tested diodes and conditions should be noted in this case. The average standard deviations obtained for all tested temperatures and currents are 4 mV, 2.2 mV and 1.9 mV for NXP, ROHM and Onsemi, respectively. Such results mean a very high repeatability for each manufacturer.

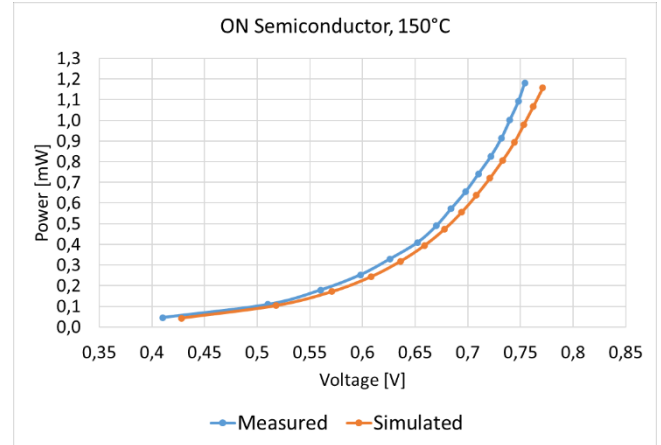


Fig. 13. Test results (P(U)) – Onsemi 150 °C

Tab. 1. Standard deviation – NXP

T [°C]	standard deviation [V]							
	I [μA]							
	100	300	500	700	900	1100	1300	1500
-40	0,004	0,005	0,005	0,005	0,005	0,005	0,005	0,005
-20	0,003	0,004	0,005	0,005	0,006	0,006	0,006	0,006
0	0,004	0,004	0,005	0,005	0,006	0,006	0,006	0,007
25	0,035	0,009	0,006	0,006	0,005	0,005	0,005	0,007
50	0,002	0,002	0,002	0,003	0,003	0,003	0,003	0,005
75	0,002	0,002	0,002	0,002	0,002	0,002	0,002	0,002
100	0,002	0,002	0,002	0,002	0,002	0,002	0,002	0,002
125	0,003	0,003	0,003	0,003	0,003	0,003	0,002	0,002
150	0,003	0,003	0,003	0,003	0,003	0,003	0,003	0,003

Tab. 2. Standard deviation – Onsemi

T [°C]	standard deviation [V]							
	I [μA]							
	100	300	500	700	900	1100	1300	1500
-40	0,001	0,001	0,001	0,001	0,001	0,002	0,002	0,002
-20	0,001	0,001	0,001	0,001	0,001	0,001	0,001	0,003
0	0,002	0,001	0,001	0,001	0,001	0,001	0,001	0,001
25	0,015	0,003	0,002	0,001	0,001	0,001	0,001	0,002
50	0,002	0,001	0,001	0,001	0,001	0,001	0,001	0,001
75	0,003	0,002	0,001	0,001	0,001	0,001	0,001	0,001
100	0,003	0,003	0,002	0,002	0,002	0,002	0,001	0,001
125	0,004	0,003	0,003	0,002	0,002	0,002	0,002	0,002
150	0,005	0,004	0,004	0,003	0,003	0,003	0,003	0,003

Fig. 14 shows a geometrical analysis of Eq. (5), which determines the surface area (D), representing the sum of deviations U for the entire analysed current range. The $g(x)$ function represents a real-valued function based on laboratory measurements (logarithmic function), while the $f(x)$ function is a linear-ideal function. The difference in the course of the $f(x)$ and $g(x)$ functions arises

from the difference between an ideal plot of the $g(x)$ straight line and the $g(x)$ function, which represents the laboratory test results. The resulting surface area (D) was created under the assumption that the starting and ending measurement points were common for them, which stems from the assumption and factor analysed during this test.

Tab. 3. Standard deviation – ROHM

T [°C]	standard deviation [V]							
	I [μA]							
	100	300	500	700	900	1100	1300	1500
-40	0,001	0,001	0,001	0,001	0,001	0,001	0,001	0,001
-20	0,001	0,001	0,001	0,001	0,001	0,001	0,001	0,003
0	0,002	0,002	0,002	0,002	0,001	0,002	0,002	0,003
25	0,010	0,003	0,002	0,002	0,002	0,002	0,002	0,002
50	0,003	0,002	0,002	0,002	0,002	0,002	0,002	0,003
75	0,003	0,003	0,003	0,002	0,002	0,002	0,002	0,002
100	0,003	0,003	0,003	0,003	0,003	0,003	0,003	0,003
125	0,003	0,003	0,003	0,003	0,003	0,003	0,003	0,003
150	0,003	0,003	0,003	0,003	0,003	0,003	0,003	0,004

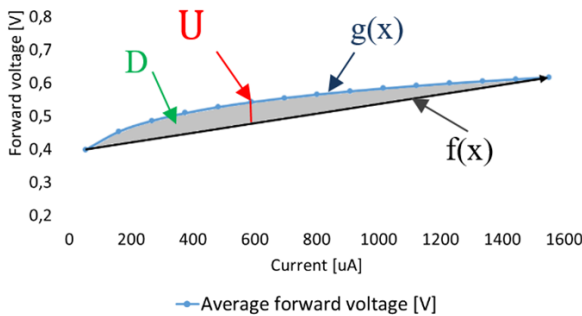


Fig. 14. Determination of the linearity coefficient (D)

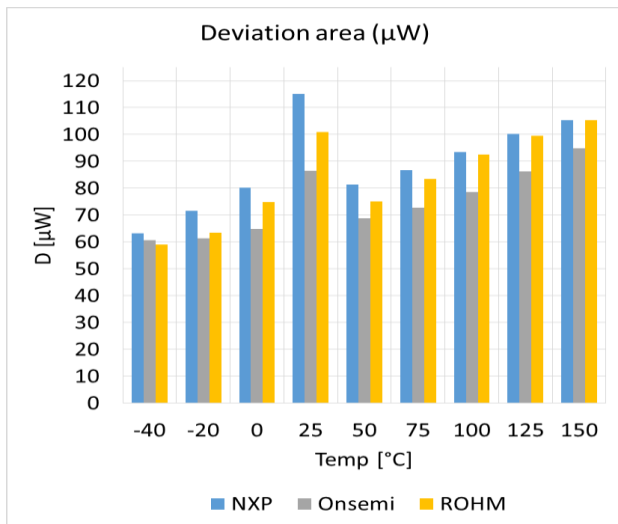


Fig. 15. Deviation area (D)

Fig. 15 shows the results obtained for each manufacturer, based on Eq. (3), for each of the nine analysed ambient temperatures – (blue – NXP, grey – Onsemi, yellow – ROHM). The higher the deviation area value, the higher the deviation from the linear, ideal course of $f(x)$ shown in Fig. 14.

Finally, the results of measurements were compared with datasheets. It was calculated that 98.9% of the tested elements

were in the range of \pm six sigma. Further calculations were made to better assess the phenomenon. The significance of the linear one-dimensional regression function was tested. The previously calculated means and standard deviations were used, and then the moment of correlation of the variables from the sample was calculated. Successively, the linear correlation coefficient was obtained, which characterizes the degree of linear dependence between random variables. For the analysed case, the correlation coefficient is 0.95 and the t factor for the analysed case is 67.94. Based on the results obtained for the moment of linear correlation and its coefficient, it was concluded that there is a very close relationship between the analysed data and the hypothesis that there is no correlation between the analysed variables should be rejected.

More about this analysis can be found [32, 33].

7. CONCLUSIONS

The article describes a methodology for analysing electronic circuits based on a module acting as a resistor calibrator, which can also work as a temperature sensor. The WCA, which is the key verifier of a correctly designed system, was expanded in this study with a deeper analysis, based on large-scale laboratory tests. The analysis of standard deviations, maximum deviations from the mean and obtained deviation areas for individual temperatures and manufacturers provided a much better picture of a component's behaviour under expected operating conditions, compared with manufacturer's documentation. It should be noted that the standard deviations for the measurement of 25 °C and 100 μA differ significantly from the rest of the results obtained. The reason for such a situation is the human factor that has serially influenced the measurements at this particular temperature and in this particular flowing current. These measurements should be disregarded when drawing conclusions for the entire study. The obtained results and comparisons for the rest of the measured and simulated data prove that such an approach is justified.

Based on the standard deviations, it can be concluded that the NXP diode slightly differs from the other two manufacturers, due to the complete current and temperature range. When analysing the deviation area, it can be noticed that Onsemi diodes exhibit lower deviations for almost all of the tested ambient temperatures than the semiconductor of other manufacturers. The average deviation area offset for all temperatures and current levels is 89 μW, 84 μW and 75 μW for NXP, ROHM and Onsemi, respectively.

All analysed diodes are characterized by very similar calculation results. It is difficult to unequivocally select the best manufacturer. However, ultimately, based on the conducted calculations, Onsemi diodes should be considered the best product. They exhibit the most linear I_F (V_F) operating range and the highest result repeatability, which is demonstrated by the results of standard deviation calculations.

REFERENCES

1. Smith W. M. Worst case circuit analysis-an overview (electronic parts/circuits tolerance analysis), Proc. Annu. Reliab. Maintainab. Symp. 1996; 326-334.

2. Anceaume A., Cabillic G., Chevochot P., Puaut I. A middleware support for distributed safety-critical real-time applications, In Proc. of the 18th Inter. Conf. Distrib. Comp. Syst. 1998; 344–351.
3. Colin A., Bernat G. Scope-tree: A program representation for symbolic worst-case execution time analysis, Proc. 14th Euromicro Conf. of Real-Time Syst. 2002; 50-59.
4. Colin A., Puaut I. Worst case execution time analysis for a processor with branch prediction, Real-Time Syst. 2000;18: 249-274.
5. Carlsson M., Engblom J., Ermedahl A., Lindblad J., Lisper B. Worst-case execution time analysis of disable interrupt regions in a commercial real-time operating system, Proc. Inter. Work. Real-Time Tools. 2002; 1-12.
6. Engblom J., Static properties of embedded real-time programs and their implications for worst-case execution time analysis, Proc. IEEE Real-Time Tech. Appl. Symp. 1999; 46-55.
7. Jacques S., Batut N., Leroy R., Gonther L. Aging test results for high temperature triacs during power cycling, Proc. IEEE Pwr. Electro. Spec. Conf. 2008; 2447-2452.
8. Lien W., Damrongplait N., Paredes J.H., Senesky D.G., Liu T.K., Pisano A.P. 4H-SiC N-Channel JFET for operation in high-temperature environments, IEEE J. Electron Devices Soc. 2014; 2(6): 4–7
9. Shwarts Y. M., Sokolov V. N., Shwarts M. M., Fedorov I. A., Venger E. F. Advanced silicon diode temperature sensors with minimized self-heating and noise for cryogenic applications, Proc. Inter. Euro. Conf. Adv. Semicond. Dev. Microsyst. 2000; 351-354.
10. Ferlet-Cavrois V., Colladant T., Paillet P., Leray J.L., Musseau O., Worst-case bias during total dose irradiation of SOI transistors, IEEE Trans. Nuc. Sci. 2000; 47(6): 2183 – 2188.
11. Lynch W. T. Worst-Case Analysis of a transistor memory matrix, IEEE Trans. Comput. 1969; 18(10): 940-942.
12. Marcovitz M., Seif E. Analytical design of resistor-coupled transistor logical circuit, IRE Trans. Elect. Comp. 1958; 7(2): 109-119.
13. Tian W., Ling X. T., Liu R.W. Novel methods for circuit worst-case tolerance analysis, IEEE Trans. Circuits Syst. I. Fundam. Theory Appl. 1996; 43(4): 272-278.
14. Donnelly T.J., Pekarek S.D., Fudge D., Vaks N., Zarate N. Predicting Worst Case Common-Mode behavior in power electronic based systems, IEEE Electr. Ship. Tech. Symp. 2019; 396-402.
15. Spence R., Soin R. S., Tolerance design of electronic circuits, Imperial College Press; 1988.
16. Divekar D.A. DC statistical circuit analysis for bipolar IC's using parameter correlations – an experimental example, IEEE T Comput Aid D. 2006; 101-103.
17. Riley J. C. The accuracy of series and parallel connections of four-terminal resistors, IEEE Trans. Instrum. Meas. 1967; 16(3): 258-268.
18. Sokół K., Ptak P. Experimental verification of mathematical models for failure estimation of electronic systems, Acta Phys. Pol. A 2020; 2(138): 207-209.
19. Hillebrand M., Paul T. Dealing with I/O devices in the context of pervasive system verification, Inter. Conf. Comp. Dsg. 2005; 309-316.
20. Nassif S.R., Strojwas A.J., Director S.W. A methodology for Worst-Case Analysis of integrated circuits, IEEE T Comput Aid D. 1986; 5(1): 104 – 113.
21. Rafaila M., Decker C., Grimm C., Pelz G. Simulation-based sensitivity and worst-case analyses of automotive electronics, IEEE Symp. Dsg. Diag. Elec. Circ. Syst., 2010; 309-312.
22. Maly W., Strojwas A.J. Statistical simulation of the IC manufacturing process, IEEE Trans. Comput.-Aided Design Integr. Circuits Syst. 1982; 1(3): 120-131.
23. Nassif S.R., Strojwas A.J., Director S.W. FABRICS II: A statistically based IC fabrication process simulator, IEEE Trans. Comput.-Aided Design Integr. Circuits Syst. 1984; 3(1): 40-46,
24. Lanchester P. C. Digital thermometer circuit for silicon diode sensors, Cryogenics 1989; 29 (12): 1156-1159.
25. Mansoor M., Haneef I., Akhtar S., De Luca A., Udrea F. Silicon diode temperature sensors — A review of applications, Sens. Actuator A Phys. 2015; 232 (1): 63-74.
26. Szymrka-Grzebyk A., Lipiński L. Linear diode thermometer in the 4–300 K temperature range, Cryogenics 1995; 35(4): 281-284.
27. Efron B., Tibshirani R. Statistical data analysis in the computer age, Science 1991; 253 (5018): 390-395.
28. Zięba A. Analiza danych w naukach ścisłych i technice [Data analysis in exact sciences and technology], Wydawnictwo Naukowe PWN; 2013.
29. Harry M., Ronald Lawson J. Six Sigma Producibility Analysis and Process Characterization, Addison-Wesley; 1992.
30. Yang K., El-Haik B. Design for six sigma: A Roadmap for Product Development, The MacGraw-Hill Companies; 2003.
31. White R. V. An Introduction to Six Sigma with a design example, Ann. Appl. Pwr. Elec. Conf. Exps. 1992; 28-35.
32. Majchrzak E., Mochnacki B. Metody numeryczne [Numerical methods], Wydawnictwo Politechniki Śląskiej; 2004.
33. Sorokin A. E. Experimental verification of a mathematical model for a heat store, Russ. Eng. Res. 2021; 41: 742–744.

Krzysztof Sokół:  <https://orcid.org/0000-0002-8661-1763>

Piotr Ptak:  <https://orcid.org/0000-0002-2477-0136>

DESIGN OF A FUZZY FRACTIONAL ORDER ADAPTIVE IMPEDANCE CONTROLLER WITH INTEGER ORDER APPROXIMATION FOR STABLE ROBOTIC CONTACT FORCE TRACKING IN UNCERTAIN ENVIRONMENT

Hongli CAO* 

* Key Laboratory of Advanced Transducers and Intelligent Control System of Ministry of Education, Taiyuan University of Technology, Taiyuan 030024, China

caohongli@tyut.edu.cn

received 30 June 2021, revised 17 September 2021, accepted 25 September 2021

Abstract: Current research in robot compliance control is unable to take both transient contact force overshoots and steady-state force tracking problems into account. To address this problem, we propose a fuzzy fractional order (FO) adaptive impedance controller to avoid the force overshoots in the contact stage while keeping force error in the dynamic tracking stage, where traditional control algorithms are not competent. A percentage gain is adopted to map FO parameters to integer order (IO) parameters by their natural properties, and a fuzzy logical controller is introduced to improve the system stability. The simulation results indicate that the proposed controller can be made more stable than and superior to the general impedance controller, and the force tracking results also have been compared with the previous control methods.

Key words: adaptive impedance control, contact interactions, fractional order, fuzzy logic, integer order approximation

1. INTRODUCTION

With the development of robot technology, establishing the contact between the robot's end-effector and the environment is becoming a vital part of tasks in robotic applications that involve assembly [1], precise handling or surface processing [e.g., polishing] [2], exoskeleton [3] etc. The main issue in contact establishment concerns the contact force magnitude that may take prohibiting values, which may directly lead to the failure of a task, with even more serious consequences [manipulated object or manipulator itself damaged] at the instant of contact. This force overshoot could be due to delays in measurement or communication, uncertainties regarding the robot/environment model and discontinuities in controller input. To solve this knotty problem, some compliance control methods are proposed by researchers [4].

Hybrid position/force control and impedance control are two main compliance control approaches which can be distinguished by the relationship between positions and force, which are usually used to solve the contact problem. Hybrid position/force control is determined based on formal models of the manipulator and task geometry to divide the task space into two separate subspaces: the position and the force subspaces as proposed by Robert [5, 6]. Different control laws are responsible for position control in the free space and for force control along the directions in which position is constrained. The second strategy is an impedance control which describes the relation between force and position, first introduced by Hogan [7]. In this method, neither the position nor the force is used for control, but a generalised impedance equation, which defines the target impedance between the motion and the interaction force/torque, is utilised. In many cases, impedance control outperformed the hybrid position/force control in

terms of controlling the dynamic contact between manipulators and the environment, as well as showing more robustness in an unknown stiffness environment [8]. To cope with the need for more complex tasks in practical robotic applications, a variety of studies have combined the concept of the hybrid force/position control (intuitive and easy implementation) and the impedance control (superior interactivity) scheme to form the hybrid impedance control [9-11]. Furthermore, due to the various uncertainties in the robot manipulator and the environment, adaptive hybrid impedance control was required to be a new stable force tracking impedance control scheme, capable of both tracking a desired force and of compensating for uncertainties in environment location and stiffness [12-14].

But at the same time, some advanced nonlinear control schemes are also applied to handle the uncertainties for complex tasks, such as robust impedance control [3], adaptive fuzzy control [15] and neural net-works control [16]. Moreover, to manage the application of industrial robots, the position-based impedance control was proposed, and the performance and stability were also analysed [17, 18]. Among these methods, fuzzy logic brings advanced and useful properties for the robust command of uncertain dynamic systems, which are prone to appearing in practical industrial robot applications, since it allows to interpret and combine several different actions of control by means of linguistic rules and taking advantage of the user experience. These outstanding properties of fuzzy control systems have been considered for designing robust controllers and precise motion planning schemes in the case of robotic plants [19, 20].

In addition to using integer order (IO) system models and methods to control robots, some researchers have also turned their eyes to other nonlinear control strategies – namely fractional order (FO) tools – due to the virtue of their inherent properties of

memory and heritage. From here, the impedance controller has IO and FO control distinction. The FO controller is widely used to enhance the closed-loop performance by improving trajectory tracking and transient and steady-state responses, and it guarantees the better control performance for both IO and FO systems [21]. Hence, the FO controller has been widely combined with advanced control techniques such as Proportion Integral Differential (PID) control, optimal control, adaptive control, (Sliding Mode Control) SMC etc. [22-24]. It also has been demonstrated that the FO controller is compatible with useful techniques for the modeling and control of advanced complex systems [25, 26], such as industrial automation control [27] and robotic applications [28-31], but then the problem of calculating the FO needs to be tackled.

Therefore, there are many methods proposed using the integer order approximation (IOA) to solve the FO derivative and integrator operators. However, it is quite difficult to determine the best among these methods due to the performance evaluation criteria having different emphases; examples for this phenomenon include the IOA effect, accuracy of the frequency response and accuracy of the time response applying only to certain situations. In the frequency domain, Oustaloup presents an approximation method based on the recursive distribution of poles and zeros in a limited frequency range to obtain an IO transfer function by using frequency response fitting [32], which is by far the most common method. Either way, it is still complex, and a reasonable balance needs to be struck between the practicality of robotic industrial applications and their calculation complexity. Fuzzy logic and FO techniques have been considered together for out-standing control applications, the aim being to improve the performance of classical schemes [33].

The above control schemes usually only consider one aspect of the force control problem; in actual robot applications, it is a very intractable problem to both maintain accurate force tracking and refrain from damaging the operating objects. Satisfying three indicators of force control: (1) maintaining force tracking error; (2) avoiding force overshoots; and (3) achieving fast response is still an open problem. Few researchers have considered all the indicators together, most confining themselves to only one aspect.

1.1. Contribution

In view of this, the contribution of this paper lies in the validation of the proposed controller, which uses fuzzy logic, FO tools and adaptive control to form a fuzzy FO adaptive impedance control (Fuzzy-FO-AIC) for dynamic force contact control in uncertain environments. The main goal of such a controller is to avoid the force overshoots in the contact stage while keeping force error in the dynamic tracking stage, where traditional control algorithms are not competent. The control scheme does not rely on the FO calculus; thus, a percentage control is adopted to convert it to IO calculations using its natural properties. This approximation method is simpler and more efficient than other IOA methods for robot compliance control problems. More-over, the Fuzzy-FO-AIC is presented here mainly in order to cater to a time-varying environment by adjusting the general impedance controller parameters using a fuzzy controller to achieve a dynamic update rate; its adaptability to time-varying dynamic environments is far superior to traditional impedance control. The stability and robustness of Fuzzy-FO-AIC and its effect on force overshoot suppression and force tracking performance during contact interactions with linear and nonlinear uncertain environments are investigated and com-

pared to previous impedance controls. It is expected that it would have a very significant impact on the film precision processing field of industrial robotic applications.

1.2. Outline

The paper is structured as follows. Section 'Preliminaries' reviews some preliminaries, control architecture and the problem. The Fuzzy-FO-AIC control scheme is proposed to solve the problem in Section 'Control Architecture'. Section 'Simulations' presents the simulation results to verify the superiority of the proposed control algorithm. Conclusions are presented in Section 'Conclusions'.

2. PRELIMINARIES

2.1. FO system

FO calculus, a generalisation of well-known IO calculus, allows differentiation and integration of arbitrary orders. Calculating a FO derivative/integral (differ-integral) is not trivial. In multiple mathematically well-founded definitions, one needs to choose the appropriate definition based on the application area. Among them, the Grunwald-Letnikov definition is usually used for calculating the FO. The Grunwald-Letnikov definition for FO operation is given as:

$$D^\alpha y(t) = \lim_{h \rightarrow 0} \frac{1}{h^\alpha} \sum_{i=0}^{\frac{t-a}{h}} C_i^\alpha y(t - ih) \quad (1)$$

where α is the order, h is the step size of the calculation, a is the window length and C_i^α can be calculated by following:

$$C_0^\alpha = 1, C_i^\alpha = C_{i-1}^\alpha \left(1 - \frac{\alpha+1}{i}\right), i = 1, 2, \dots \quad (2)$$

FO differ-integral is a linear operator, and it has a memory and relies on the whole history. In real-time implementation, it relies upon the short memory principle due to the forgetting factor. Therefore, the memory storage and calculation amount will be large, which will lead to some obstacles to practical application.

2.2. Contact control problem

For modelling the contact between robot and environment, we can consider one of the degrees of the robot system in which a mass interacts with a stiffness environment (Fig. 1). The contact procedure can be divided into three processes: (1) Free motion; (2) Instant contact; (3) Steady tracking. The corresponding contact force curves are shown in Fig. 1(b). It can be seen that a large force overshoot is produced in the collision stage. In the actual robotic application, if not controlled, too much oscillation and force overshoot will cause the system to be unstable and even worse consequences.

In addition to the above requirements, a superior force controller adapting to a variety of complex tasks should have the following characteristics: (1) Maintaining a high accuracy position tracking capability in Free-space (basic capabilities of modern industrial robots); (2) High speed, stable, smooth contact with the collision stage; (3) High precision force tracking capability in Steady-contact. In this study, the design of robot controller is mainly

aimed at the indicators of (2) and (3). As (1) is a basic capability of industrial robots and the impedance control strategy is built on (1), the following section gives a brief introduction.

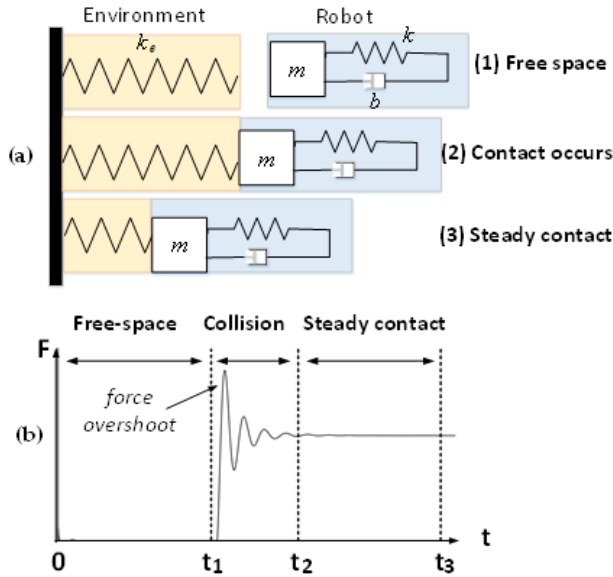


Fig. 1. Contact model of robot and environment

2.3. Position controlled robot

For position-based impedance control (also called admittance control in some researches) systems, hierarchical separation of position control and impedance control is a common structure nowadays (Fig. 2). The computed-torque method combined with a conventional proportional–differential (PD) controller can form a superior position controller, in which the actual end-effector’s position is equal to that commanded, with no tracking delay and error. Once such a position controller is available, the impedance controller can be built on it.

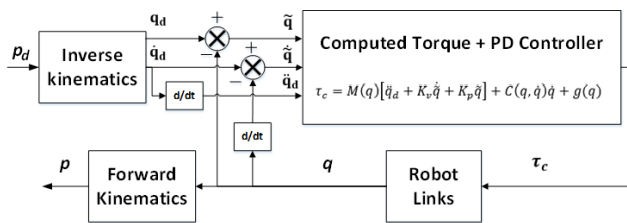


Fig. 2. Generic position controller that is applied to a robot manipulator (computed-torque + PD). PD, proportional–differential

3. CONTROL ARCHITECTURE

Fig. 3 shows the whole Fuzzy-FO-AIC control architecture. Firstly, the motion space and constraint space are planned according to the robot’s task definition. The robot is required to move its own end-effector with a desired position P_d , and interact with the environment. The generated interaction force F_e between robot and environment is measured by a force sensor, which is attached to the end-effector of the robot. The force error between the desired force F_d and the interaction force F_e is then sent to

the Fuzzy-FO-AIC to generate the corresponding position error e . Then, the robot’s servo motion controller transmits sufficient torque to its joints in order to closely achieve the reference position.

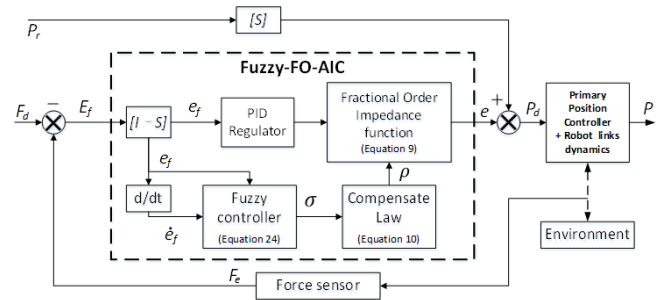


Fig. 3. Fuzzy FO adaptive hybrid impedance control architecture. FO, fractional order

3.1. Fractional order-adaptive impedance control (FO-AIC)

3.1.1. FO-AIC design

Inspired by the integer order adaptive impedance controller (IO-AIC) that is most commonly used in researches, the difference between FO controller and IO controller is that the 2-order term in IO-AIC is not an integer but a decimal. Hereby, FO-AIC is defined as:

$$Y(s) = \frac{1}{Z_{FO-AIC}(s)} = \frac{1}{m_d s^\alpha + b_d (s + \rho(s))} \quad (3)$$

$$\rho(s) = -\frac{\sigma}{b} e_f(s) \quad (4)$$

The range of α is defined as $1 < \alpha < 2$. Here, m_d and b_d are the desired parameters of impedance controller. Eq. (4) defines the adaptive compensation law; ρ is the damping compensation which is adjusted according to the force sensor information online. From an extreme point of view, for $\alpha = 1$, the controller acts like a pure damper due to the order being reduced to 1-order. On the other hand, when the integration order is at $\alpha = 2$, it becomes IO-AIC. Therefore, the effective mass and damping supplied by FO-AIC changes depending on the integration order α , while disruptive effects are present throughout the range. An important nature property of FO is, as α is decreased gradually from 2 to 1, the inertial energy storage characteristics of decay and energy dissipation characteristics dominate. To demonstrate the effect of α on the dynamical response of the FO-AIC, considering the frequency domain expression using the Euler transform, we obtain:

$$Z = m_d \omega^\alpha \cos\left(\frac{\alpha\pi}{2}\right) + b_d (j\omega + \rho(j\omega)) + j m_d \omega^\alpha \sin\left(\frac{\alpha\pi}{2}\right) \quad (5)$$

In Eq. (5), the effective mass and damping provided by FO-AIC are $m_d \omega^\alpha \sin(\alpha\pi/2)$ and $m_d \omega^\alpha \cos(\alpha\pi/2) + b_d (j\omega + \rho(j\omega))$, respectively, whereas these values are constant as m_d and b_d for IO-AIC. Hence, unlike in the IO case, the effective damping in FO-AIC is frequency-dependent and can be adjusted by altering the integration order α . This property of FO-AIC is of interest for robot force control tasks, as it can improve stability robustness of interactions in tasks involving contacts with

environment, as can be seen in Fig. 4. From the point of view of controllability, compared with IO-AIC, one more adjustable parameter can ensure the system stability using FO-AIC.

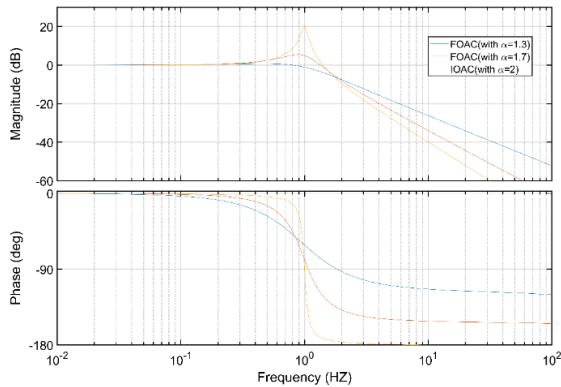


Fig. 4. Bode diagram analysis of FO-AIC and IO-AIC. FO-AIC, fractional order-adaptive impedance control; IO-AIC, integer order adaptive impedance controller

3.1.2. FO-AIC with IOA

From the natural property analysis of FO-AIC, we ascertain that the effective mass and damping are frequency-dependent, and can be adjusted by varying the integration order α . Based on this property, a natural idea was born – when taking two limits of FO, the FO-AIC becomes IO-AIC ($\alpha = 2$) and a pure damper controller ($\alpha = 1$), respectively. Hence, the new approximation controller can be formed by moving α from the order to the coefficient β ($\beta = \alpha - 1$). The coefficient β ($0 < \beta < 1$) connects the two IO controllers (IO-AIC and a pure damper) by controlling percentages of the output, which does the same thing as α :

$$Y(s) = \frac{1}{Z_{FO-AIC}(s)} = \frac{\beta}{m_d s^2 + b_d(s + \rho(s))} + \frac{(1-\beta)}{b_d(s + \rho(s))} \quad (6)$$

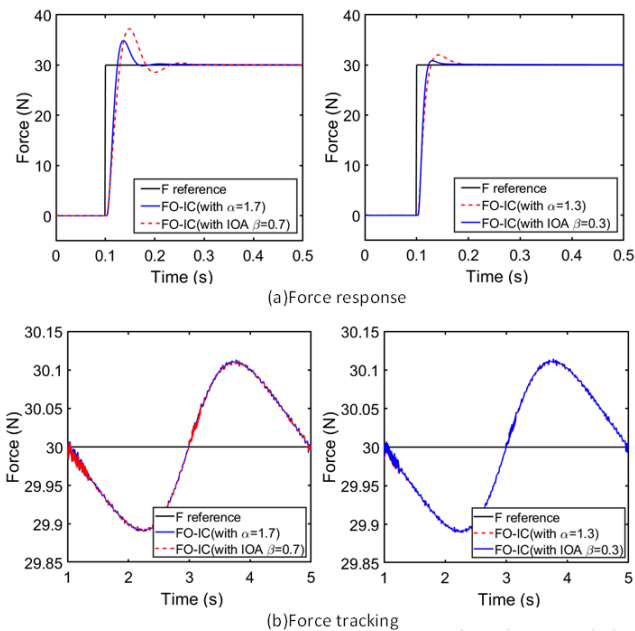


Fig. 5. IOA Effects of FO-AIC. FO-AIC, fractional order-adaptive impedance control; IOA, integer order approximation

From Eq. (3), it can be found that β is directly related to the mass and damping effect that the controller wants to present. Similar to contact tasks, it can improve stability and robustness by decreasing β in the collision stage (presents its damping characteristics) and increasing β in the steady force tracking stage (presents its compensation characteristics), when the robot contacts the environment.

Fig. 5 shows the IOA effects of FO-AIC. It can be seen that there is a certain error in the contact stage between the FO-AIC (with Oustaloup method) and FO-AIC with IOA; due to the fact that FO has a memory and relies on the whole history, the memory effect is removed and replaced by a percentage in FO-AIC with IOA. Nevertheless, considering the ease and analyzability of use, this error can be ignored. This means the new IOA methods can be used in robot force control.

3.2. Pre-PID regulator

To achieve the force tracking response speed, a pre-PID regulator is designed before FO-AIC, each part forming a PID-like FO-AIC to improve the force tracking performance, which can be expressed as:

$$\left(k_p + \frac{k_i}{s} + k_d s\right) e_f(s) = \frac{m_d s^2 + b_d(s + \rho(s))}{\beta} + \frac{b_d(s + \rho(s))}{1 - \beta} \quad (7)$$

where k_p , k_i and k_d are the positive gains of the pre-PID. Marking $\gamma = k_p + k_i/s + k_d s$, we obtain:

$$e_f(s) = \frac{m_d}{\gamma \beta} s^2 + \frac{b_d}{\gamma \beta (1 - \beta)} (s + \rho) \quad (8)$$

Compared with the general FO-AIC, it could be found that the desired mass and damp coefficient of the PID-like FO-AIC changes from m_d/β to $m_d/\gamma\beta$ and $b_d/\beta(1 - \beta)$ to $b_d/(\gamma\beta(1 - \beta))$, respectively. It means that the pre-PID parameter γ selection and β will affect the response speed and stability of the controller. To make this point clearer, we observe the response behavior of a second-order system by changing its parameters, as shown in Fig. 6.

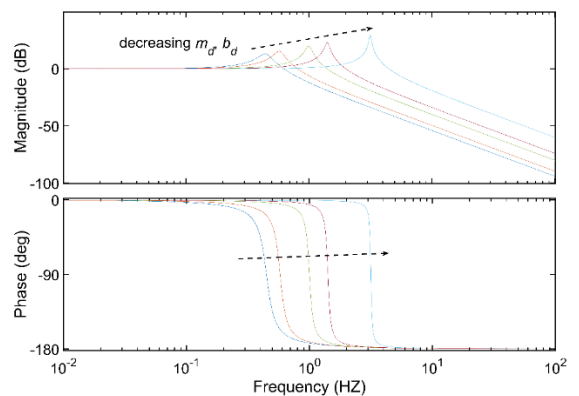


Fig. 6. Frequency response diagrams for decrease of inertia and damping

The selection of β has a great impact on the response of the system due to fact that it relates to the nature property of the system. Here, if we were to keep the coefficient β a constant value, and the impedance parameters are decreased simultaneously, then both the resonance amplitude and the resonant fre-

quency are increased. This indicates that if the pre-PID parameters are chosen reasonably, it can achieve a better expectation than the general controller, so that the contact force generated at the end-effector can quickly converge to the desired value.

3.3. Fuzzy logic design

It can be seen from Eq. (8) that the response of the FO-AIC is related not only to coefficient β and the pre-PID regulator γ but also to the compensation rate ρ . It is assumed that the position controller for the industrial robot has a high-bandwidth servo loop, and the model uncertainties (inertia, friction and Coriolis etc.) and some external disturbances can be suppressed by PD control. Therefore, the block for the primary position controller with robot-link dynamics in Fig. 2 is dropped; thus, $P_d \cong P$. Hence, the robot motion controller can be simplified to gain 1. The force sensor can be reduced to a linear stiffness environmental model. The whole of the robot control strategy is simplified in Fig. 7.

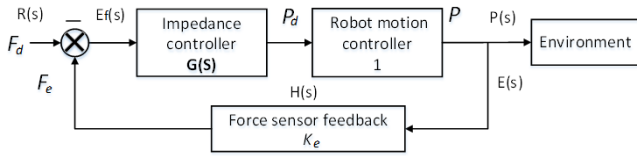


Fig. 7. The transfer function of the simple interaction model

The complete pre-PID, such as FO-AIC with IO approximation and the new design adaptive compensation rate in the time domain, can be represented as:

$$e_f(t) = \frac{m_d}{\gamma\beta} \ddot{\hat{e}}(t) + \frac{b_d}{\gamma\beta(1-\beta)} (\dot{\hat{e}}(t) + \rho(t)) \quad (9)$$

$$\rho(t) = \rho(t-T) + \sigma\gamma\beta(1-\beta) \frac{(f_d(t-T) - f_e(t-T))}{b_d} \quad (10)$$

Given that $\hat{p}_e = p_e - \delta p_e$ is the estimation of the environment location, the estimation position error can then be expressed as $\hat{e} = e + \delta p_e$. γ is the pre-PID regulator, and since we're just taking the proportional part here, $\gamma = k_p$ is equal to a constant. The initial conditions are given by $\rho(0) = 0$, and T is the sampling period (usually smaller is better). The update rate σ selection is associated with system stability and performance, which has been analysed in the forthcoming section, and it is used for designing the fuzzy logic controller.

3.3.1. Transient and steady-state analysis

According to the principle of dispersion, rewriting Eq. (10) and marking $c(t) = -e_f = f_d(t) - f_e(t)$, n elements of the ρ series can be expanded as:

$$\frac{b_d}{\gamma\beta(1-\beta)} \rho(t) = \frac{b_d}{\gamma\beta(1-\beta)} \rho(t-nT) + \sigma c(t-nT) + \dots + \sigma c(t-T) \quad (11)$$

Substituting Eq. (11) into Eq. (9) yields:

$$e_f(t) = \frac{m_d}{\gamma\beta} \ddot{\hat{e}}(t) + \frac{b_d}{\gamma\beta(1-\beta)} \dot{\hat{e}}(t) + \sigma(c(t-nT) + \dots + c(t-T)) \quad (12)$$

Taking the Laplace transform of Eq. (12),

$$E_f(s) = \left(\frac{m_d}{\gamma\beta} s^2 + \frac{b_d}{\gamma\beta(1-\beta)} s \right) \hat{E}(s) + \sigma(e^{-nTs} + \dots + e^{-Ts})(-E_f(s)) \quad (13)$$

where the sampling rate T is sufficient and n is a sufficiently large number. It is reasonable to assume that

$$\sum_{n=1}^{\infty} e^{-nTs} \cong (1-Ts)/Ts.$$

The steady transfer function can be rewritten as:

$$G(s) = \frac{\hat{E}(s)}{E_f(s)} = \frac{(\gamma\beta(1-\beta)(1-\sigma)Ts + \gamma\beta(1-\beta)\sigma)}{m_d(1-\beta)Ts^3 + b_dTs^2} \quad (14)$$

The force error transfer function $\Phi(s)$ for the whole closed-loop system is shown below:

$$\begin{aligned} \Phi(s) &= \frac{E(s)}{R(s)} = \frac{1}{1 + G(s)H(s)} \\ &= \frac{m_d(1-\beta)Ts^3 + b_dTs^2}{m_d(1-\beta)Ts^3 + b_dTs^2 + (\gamma\beta(1-\beta)(1-\sigma)k_eTs + \gamma\beta(1-\beta)\sigma)} \end{aligned} \quad (15)$$

Consider a complex dynamic environmental situation: a sine signal $r(t) = \sin\omega t$. Long division method is used to compute dynamic error of FO-AIC (taking the first three terms):

$$\begin{aligned} e_{ss}(t) &= \Phi(0)r(t) + \dot{\Phi}(0)\dot{r}(t) + \left(\frac{1}{2!}\right)\ddot{\Phi}(0)\ddot{r}(t) + \dots = \\ &= -\omega^2 \frac{2bT}{\gamma\beta(1-\beta)k_e^2\sigma} \sin\omega t + \dots \end{aligned} \quad (16)$$

It can be seen that, for a complex environment, the tracking error can be decreased by increasing the update rate σ .

For transient response analysis, since the collision time is short, n is no longer being an infinite amount. Hence, rewriting the compensation part of Eq. (10) and dividing both sides by the sampling time, we obtain:

$$\frac{\rho(t) - \rho(t-T)}{T} = \frac{\sigma\gamma\beta(1-\beta)}{b_d} \left(\frac{f_d(t-T) - f_e(t-T)}{T} \right) \quad (17)$$

In an extremely small period, it can be approximated that $c(t-T) \cong c(t) = -e_f$. The function representation between $\rho(t)$ and $c(t)$ can be written as follows:

$$\rho(t) = -\frac{\sigma\gamma\beta(1-\beta)}{b_d} e_f(t) \quad (18)$$

Substituting Eq. (18) into Eq. (9) and then performing a Laplace transformation, the transient response transfer function of the impedance controller is obtained as the following:

$$G(s) = \frac{\hat{E}(s)}{E_f(s)} = \frac{\gamma\beta(1-\beta)(1+\sigma)}{(1-\beta)ms^2 + bs} \quad (19)$$

The transient response transfer function $\Psi(s)$ for the whole closed-loop system is:

$$\Psi(s) = \frac{G(s)H(s)}{1 + G(s)H(s)} = \frac{\gamma\beta(1-\beta)(1+\sigma)k_e}{(1-\beta)ms^2 + bs + \gamma\beta(1-\beta)(1+\sigma)k_e} \quad (20)$$

The damping coefficient ζ about the oscillation form of the system can be calculated from Eq. (20) as:

$$\zeta = \frac{b}{2(1-\beta)\sqrt{m\gamma\beta(1+\sigma)k_e}} \quad (21)$$

In Eq. (21), it can be clearly seen that the system will present oscillation when σ increases, which indicates that the smaller σ having a better force overshoots the suppression effect.

Combining the transient response and steady-state tracking analysis, in general, keeping the σ unchanged is an inadvisable

choice. Therefore, a dynamic adaptive update rate based on fuzzy logic coupling into FO-AIC is introduced in the forthcoming section.

3.3.2. Fuzzy logic controller

Supposing $[-X_{ef}, X_{ef}]$, $[-X_{\dot{e}_f}, X_{\dot{e}_f}]$ and $[-Y_\sigma, Y_\sigma]$ are the basic domains of e_f , \dot{e}_f and σ , respectively, in this study, we set number 10 as the boundary for simplify. Based on the comparison between the effects of different types of membership functions on fuzzy controller performance, seven triangular type membership functions are chosen to demonstrate input and output of the proposed controller, as illustrated in Fig. 8. Seven linguistic values are described, namely positive big (PB), positive medium (PM), positive small (PS), zero (ZO), negative big (NB), negative medium (NM) and negative small (NS). The triangular membership function is used here mainly considering the computation speed. Similarly, the membership functions of the selected input and output are kept the same for the sake of calculation.

The fuzzy control rules generalise the relationships between the inputs and outputs. They are established based on the experiences and intuitions of the skilled workers. Both the error e_f and the error ratio \dot{e}_f have seven fuzzy subsets. Therefore, 49 fuzzy rules can be obtained according to the expertise, which are shown as Tab. 1.

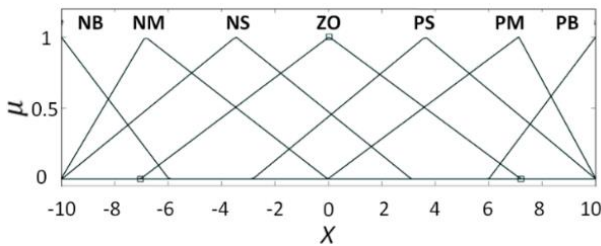


Fig. 8. Membership function of e_f , \dot{e}_f and σ

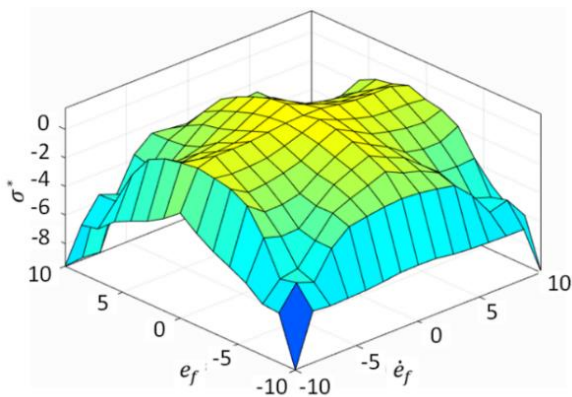


Fig. 9. Output curve-surface of fuzzy logic control

Tab. 1 can be applied as: if $e_f(i) = A_j$ and $\dot{e}_f(i) = B_j$, then $\sigma = C_j (j = 1, \dots, 49)$ and A_j and B_j are the fuzzy sets corresponding to $e_f(i)$ and $\dot{e}_f(i)$ in the j -th fuzzy rule, respectively. C_j is the fuzzy outputs corresponding to σ in the j -th fuzzy logical rule. The output membership grades for different fuzzy sets are derived from the rule table using the Mamdani fuzzy reasoning method, as seen in Fig. 9. The centre of gravity defuzzification

method is selected to defuzzify the output fuzzy set:

$$\sigma^* = \frac{\sum_{j=1}^n A_j(e_f)B_j(\dot{e}_f)\mu_j}{\sum_{j=1}^n A_j(e_f)B_j(\dot{e}_f)} \quad (22)$$

Tab. 1. Fuzzy Control Logic Rule Table

		\dot{e}_f						
		NB	NM	NS	ZO	PS	PM	PB
e_f	NB	NB	NB	NM	PM	NM	NB	NB
	NM	NB	NB	NM	PM	NM	NB	NB
	NS	NM	NM	NS	PS	NS	NM	NM
	ZO	NM	ZO	PM	PB	PM	ZO	NM
	PS	NM	NM	NS	PS	NS	NM	NM
	PM	NB	NB	NM	PM	NM	NB	NB
	PB	NB	NB	NM	PM	NM	NB	NB

NB, negative big; NM, negative medium; NS, negative small; PB, positive big; PM, positive medium; PS, positive small; ZO, zero.

In Tab. 1, n is the fuzzy rule number, and μ_j is the membership grade of the j -th fuzzy output, which takes values in $[0, 1]$. Suppose Q_σ is the quantification factors of σ undergoing conversion from the fuzzy domain to the basic domain, then Q_σ can be given by:

$$Q_\sigma = \frac{B_\sigma}{10} \quad (23)$$

Then, the precise values of σ can be denoted as:

$$\sigma = Q_\sigma \sigma^* \quad (24)$$

3.3.3. Sigma boundary and stability

To determine the σ boundary B_σ , a stability analysis is carried out in this section. Then, stability analysis is given according to the Routh criterion.

Substituting Eq. (10) into Eq. (9) yields:

$$e_f(t) = \frac{m_d}{\gamma\beta} \ddot{e}(t) + \frac{b_d}{\gamma\beta(1-\beta)} \dot{e}(t) + \frac{b_d}{\gamma\beta(1-\beta)} \rho(t-T) + \sigma(f_d(t-T) - f_e(t-T)) \quad (25)$$

Substituting the estimated position error $\hat{e}(t) = e(t) + \delta p_e(t)$, Eq. (25) is rewritten as:

$$e_f(t) = \frac{m_d}{\gamma\beta} [\ddot{e}(t) + \delta \ddot{p}_e(t)] + \frac{b_d}{\gamma\beta(1-\beta)} [\dot{e}(t) + \delta \dot{p}_e(t)] + \frac{b_d}{\gamma\beta(1-\beta)} \rho(t-T) + \sigma(f_d(t-T) - f_e(t-T)) \quad (26)$$

Reorganising Eq. (26) yields:

$$\frac{m_d}{\gamma\beta} \ddot{e}(t) + \frac{b_d}{\gamma\beta(1-\beta)} \dot{e}(t) - e_f(t) + \frac{b_d}{\gamma\beta(1-\beta)} \rho(t-T) + \sigma(f_d(t-T) - f_e(t-T)) = -\frac{m_d}{\gamma\beta} \delta \ddot{p}_e(t) - \frac{b_d}{\gamma\beta(1-\beta)} \delta \dot{p}_e(t) \quad (27)$$

According to the stiffness model between the robot and the environment, which is $f_e = k_e(p_e - p_d) = -k_e e$, after the

differential it becomes:

$$\dot{e} = -\dot{f}_e/k_e, \ddot{e} = -\ddot{f}_e/k_e \quad (28)$$

Substituting Eq. (28) into Eq. (27) yields:

$$\begin{aligned} & -\frac{m_d}{\gamma\beta} \ddot{f}_e(t) - \frac{b_d}{\gamma\beta(1-\beta)} \dot{f}_e(t) - k_e e_f(t) \\ & + \frac{b_d}{\gamma\beta(1-\beta)} k_e \rho(t-T) + \sigma k_e (f_d(t-T) - f_e(t-T)) \\ & = -k_e \left(\frac{m_d}{\gamma\beta} \delta \ddot{p}_e(t) + \frac{b_d}{\gamma\beta(1-\beta)} \delta \dot{p}_e(t) \right) \end{aligned} \quad (29)$$

Let $\hat{f}_e(t) = k_e \delta p_e(t)$; then, adding the term $\frac{m_d}{\gamma\beta} \dot{\hat{f}}_d(t) + \frac{b_d}{\gamma\beta(1-\beta)} \hat{f}_d(t)$ at both sides, Eq. (29) could be represented as:

$$\begin{aligned} & \frac{m_d}{\gamma\beta} (\ddot{\hat{f}}_d(t) - \ddot{\hat{f}}_e(t)) + \frac{b_d}{\gamma\beta(1-\beta)} (\dot{\hat{f}}_d(t) - \dot{\hat{f}}_e(t)) - k_e e_f(t) + \\ & \frac{b_d}{\gamma\beta(1-\beta)} k_e \rho(t-T) + \sigma k_e (f_d(t-T) - f_e(t-T)) = \\ & \frac{m_d}{\gamma\beta} (\ddot{\hat{f}}_d(t) - \ddot{\hat{f}}_e(t)) + \frac{b_d}{\gamma\beta(1-\beta)} (\dot{\hat{f}}_d(t) - \dot{\hat{f}}_e(t)) \end{aligned} \quad (30)$$

Marking $c(t) = f_d(t) - f_e(t)$ and $r(t) = f_d(t) - \hat{f}_e(t)$, Eq. (30) can be simplified as follows:

$$\begin{aligned} & \frac{m_d}{\gamma\beta} \ddot{c} + \frac{b_d}{\gamma\beta(1-\beta)} \dot{c} + \frac{b_d}{\gamma\beta(1-\beta)} k_e \rho(t-T) + \sigma k_e c(t-T) + \\ & k_e c = \frac{m_d}{\gamma\beta} \ddot{r} + \frac{b_d}{\gamma\beta(1-\beta)} \dot{r} \end{aligned} \quad (31)$$

Combining Eq. (11) and Eq. (31) yields:

$$\begin{aligned} & \frac{m_d}{\gamma\beta} \ddot{c} + \frac{b_d}{\gamma\beta(1-\beta)} \dot{c} + \sigma k_e (c(t - (n+1)T) + \dots + \\ & c(t-T)) + k_e c = \frac{m_d}{\gamma\beta} \ddot{r} + \frac{b_d}{\gamma\beta(1-\beta)} \dot{r} \end{aligned} \quad (32)$$

Laplace transform of Eq. (32) is:

$$\frac{c(s)}{r(s)} = \frac{(1-\beta)m_d s^2 + b_d s}{(1-\beta)m_d s^2 + b_d s + k_e \gamma\beta(1-\beta) + \sigma k_e \gamma\beta(1-\beta)(e^{-(n+1)Ts} + \dots + e^{-Ts})} \quad (33)$$

The stability of Eq. (33) can be guaranteed by the characteristic expressed as:

$$(1-\beta)m_d s^2 + b_d s + k_e \gamma\beta(1-\beta) + \sigma k_e (e^{-(n+1)Ts} + \dots + e^{-Ts}) = 0 \quad (34)$$

Assuming that n is a sufficiently large number, and that the sampling rate T is sufficient for $\sum_{n=1}^{\infty} e^{-nTs} \cong (1 - Ts)/Ts$, we substitute it into Eq. (34) to obtain:

$$(1-\beta)m_d Ts^3 + b_d Ts^2 + k_e T(\gamma\beta(1-\beta) - \sigma)s + \sigma k_e = 0 \quad (35)$$

According to the Routh criterion, the Routh array is presented as:

$$\begin{array}{l} s^3 \quad (1-\beta)m_d T \quad k_e T(\gamma\beta(1-\beta) - \sigma) \\ s^2 \quad b_d T \quad \sigma k_e \\ s^1 \quad \frac{b_d T^2 k_e (\gamma\beta(1-\beta) - \sigma) - (1-\beta)m_d T \sigma k_e}{b_d T} \quad 0 \\ s^0 \quad \sigma k_e \quad 0 \end{array} \quad (36)$$

To ensure the stability of the system, the coefficients of the first column and the coefficients of the characteristic equation must be positive, which is represented as:

$$\begin{cases} \frac{b_d T^2 (\gamma\beta(1-\beta) - \sigma) - (1-\beta)m_d T \sigma k_e}{b_d T} > 0 \\ k_e T(\gamma\beta(1-\beta) - \sigma) > 0 \\ \sigma k_e > 0 \end{cases} \quad (37)$$

Simplifying Eq. (37), the boundary of σ is:

$$0 < \sigma < \frac{b_d T \gamma\beta(1-\beta)}{(1-\beta)m_d + b_d T} \quad (38)$$

For a stable system, the steady-state error e_{ss} can be defined based on the Laplace transform. For convergence, the steady-state error can be calculated as:

$$\begin{aligned} e_{ss} &= \lim_{s \rightarrow 0} sE(s) = \\ & \lim_{s \rightarrow 0} s \left[\frac{(1-\beta)m_d Ts^2 + b_d Ts}{(1-\beta)m_d Ts^3 + b_d Ts^2 + k_e T(\gamma\beta(1-\beta) - \sigma)s + \sigma k_e} - 1 \right] r(s) \end{aligned} \quad (39)$$

When the input is a step function with the form as $r(s) = 1/s$, Eq. (39) yields a result as follows:

$$e_{ss} = \lim_{s \rightarrow 0} s(c(s) - r(s)) = -1 \quad (40)$$

The following conclusion can be reached from Eq. (40):

$$\lim_{s \rightarrow 0} s c(s) = 0, \lim_{t \rightarrow \infty} c(t) = 0 \quad (41)$$

Therefore, when $t \rightarrow \infty$, $f_e \rightarrow f_d$. The contact force converges to the desired force. Actually, even if $r(s)$ is a slope or sine input as in simulations and experiments, the force tracking error tends to zero, and this also can be proven.

3.4. Control effect analysis

For position-based impedance control systems, hierarchical separation of position control and impedance control is a common structure nowadays. This means that the stability of the whole system can be divided into two subsystems: impedance control and position control. It is a reasonable assumption that the position controller can achieve stable tracking in industrial robots. Therefore, we mainly study the stability of the impedance control part. The stability of the impedance control part is mainly composed of the following parts: pre-PID regulator, fuzzy controller and FO-AIC. Similarly, the performance of the controller is related to these three parts, which can be seen in Tab. 2. (The table is obtained by simulation analysis, based on the selection variable method.)

Tab. 2. The Control effect of pre-PID regulator, Fuzzy logic and FO-AIC

Index Controller		Force response (Tracking time)	Force overshoot (Collision force)	Force tracking (Tracking error)
Pre-PID	$k_p(\uparrow)$	High (\downarrow)	High (\uparrow)	Low (\downarrow)
Fuzzy logic	$\sigma(\uparrow)$	Low (\downarrow)	High (\uparrow)	High (\downarrow)
FO-AIC	α or $\beta(\downarrow)$	Low (\uparrow)	High (\downarrow)	Low (\uparrow)

FO-AIC, fractional order-adaptive impedance control.

As can be seen from Tab. 2, each part has its own emphasis and strengths on the performance indicators of force control. The pre-PID can quickly improve the response speed and ensure the tracking accuracy, but at the same time will introduce a large

overshoot. FO tools can greatly reduce overshoot of force control, but it is insufficient in response time and tracking accuracy. The σ can greatly affect the overshoot and tracking accuracy, and thus fuzzy logic is needed to determine dynamic adjustment based on the contact information. Therefore, in order to obtain a force controller with fast response, small overshoot and high tracking accuracy, all three parts are indispensable.

4. SIMULATIONS

To verify the theoretical findings and controller performance, a series of simulation studies are conducted and presented in this section. To test the performance and adaptability of various strategies in a dynamic continuous stiffness environment, the stiffness is designed as:

$$k_e = 4000 + 800 \sin\left(\frac{\pi}{2}t\right) \quad (42)$$

The motion process of the robot is as follows: first contacting the dynamic, uncertain surface to achieve a desired contact force, and then tracking the desired force.

4.1. FO order impacts simulation

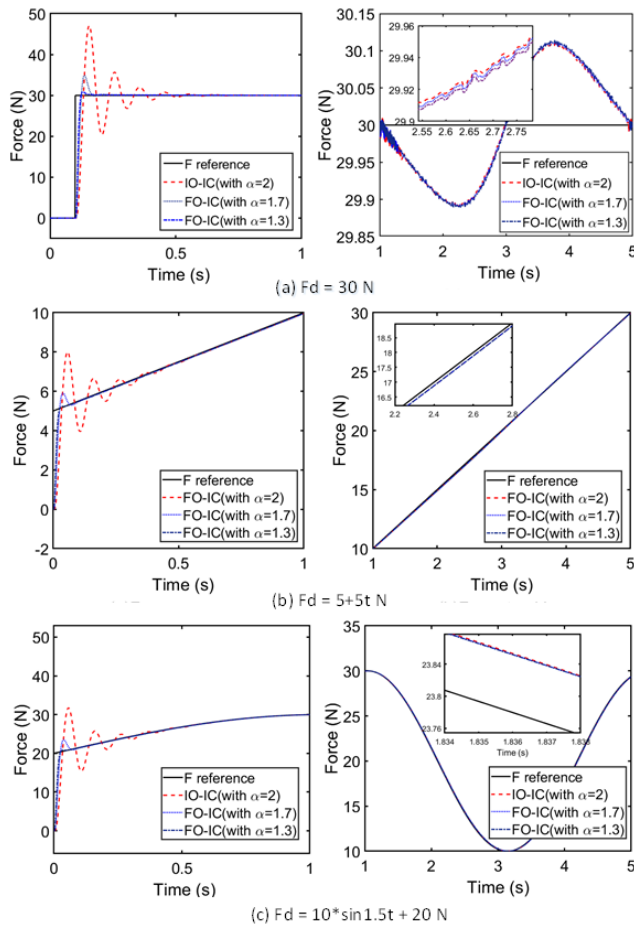


Fig. 10. Performance comparison of FO-AIC and IO-AIC for (a) constant force; (b) slope force; (c) sine force with dynamic stiffness. FO-AIC, fractional order-adaptive impedance control; IO-AIC, integer order adaptive impedance controller

Fig. 10 shows the simulation results of FO-AIC and IO-AIC for a constant force, a slope force and a sine force, respectively. 0~1s is the initial contact state, 1~5s are the tracking state. As can be seen in the contact stage, as the order decreases, the force overshoots also decrease, which indicates that the smaller the order, the smaller the collision force. Meanwhile, we can see that the force tracking has a slight improvement in the tracking stage, but not much. Therefore, the proposed FO-IC can greatly reduce force overshoots in the initial contact phase compared with IO-IC, and this effect has strong adaptability and robustness for various tasks.

4.2. 1-DOF robot contact force tracking simulation

The basic impedance parameters $m_d = 1 \text{Ns}^2/\text{m}$ and $b_d = 44 \text{Ns}/\text{m}$ are selected based on experiences (here referring to the benchmark). Modelling uncertainty is introduced in simulation implementations by considering the estimated mass $\hat{m}_r = 0.8 \text{kg}$ instead of the real mass $m_r = 1 \text{kg}$. The position controller is designed with high gains to achieve good position tracking, which is common in practice. The unmodelled friction F_f is assumed to have a form, with $c_v = 1.2 \text{Ns}/\text{m}$ and $F_c = 4 \text{N}$ as the coefficients of viscous and coulomb friction:

$$F_f = -\text{sign}(\dot{x})(c_v |\dot{x}| + F_c) \quad (43)$$

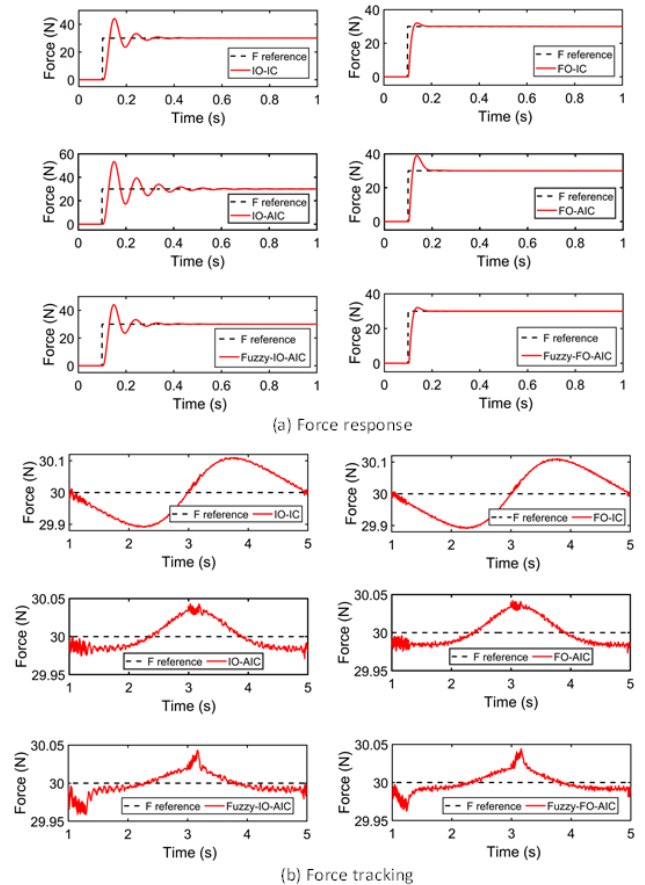


Fig. 11. Constant force control performance comparison of Fuzzy-FO-AIC with other controllers. Fuzzy-FO-AIC, fuzzy FO adaptive impedance control

Figs. 11 and 12 show the force response, overshoots and tracking performance of the classical control methods (IO-IC [7],

IO-AIC [12]), Fuzzy-IO-AIC [19], contrast controller (FO-IC [30], FO-AIC [21]) and the proposed Fuzzy-FO-AIC control strategies in different scenarios. (The FOs are all replaced by the FO with IOA.)

First, the transient response of the step and sine force are shown in Fig. 11 (a) and Fig. 12 (a) with a time range of 0-1 s, respectively. The contact force has a stronger vibration and force overshoots in IO-AIC at the initial contact stage, followed by Fuzzy-IO-AIC, IO-AIC and FO-AIC. However, both FO-IC and Fuzzy-FO-AIC have a superior force overshoots suppression ability. Lateral results' comparison show that FO tools have better vibration suppression than IO due to their natural damping effect. Longitudinal results' comparison shows that a smaller σ has a smaller force overshoot. Taken together, the Fuzzy-FO-AIC actually achieve the double damping effect, which indicates that this approach has the best force overshoots suppression ability.

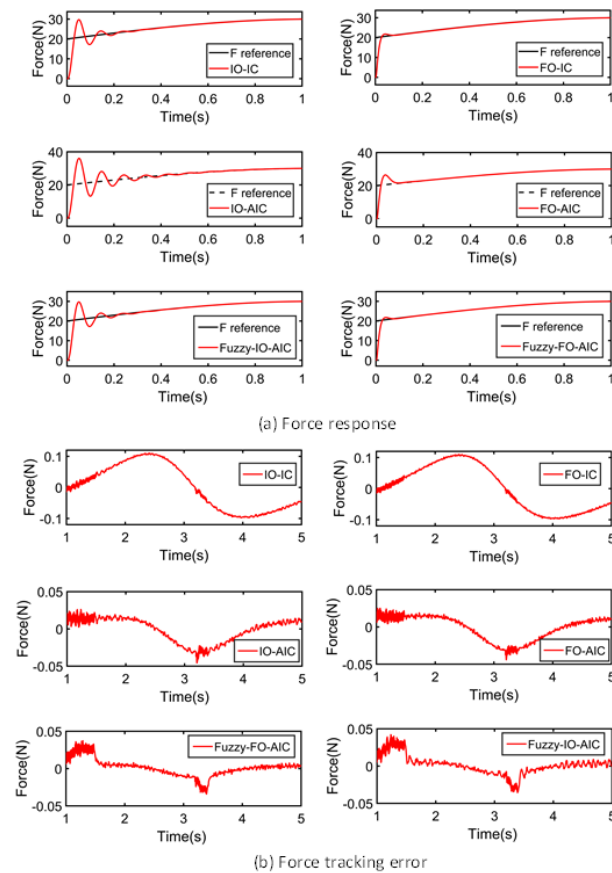


Fig. 12. Varying force control performance comparison of Fuzzy-FO-AIC with other controllers. Fuzzy-FO-AIC, fuzzy FO adaptive impedance control

Then, the corresponding steady force tracking performance is highlighted in Fig. 11(b) and Fig. 12(b) with a time ranging from 1 s to 5 s. Unlike the vibration collision phase, IO-IC and FO-IC have the worst tracking effect of all. IO-AIC, FO-AIC and their adaptive versions Fuzzy-IO-AIC, Fuzzy-FO-AIC have the best tracking effects since all their σ ups to the upper bound. Therefore, it can be concluded that the force tracking accuracy of either FO or IO depends only on the value of σ , the larger σ and the higher precision. In theory, the Fuzzy-IO-AIC and Fuzzy-FO-AIC controllers all can achieve more accurate force tracking effects owing to the fact that the σ boundary can be enlarged by the pre-PID regulator.

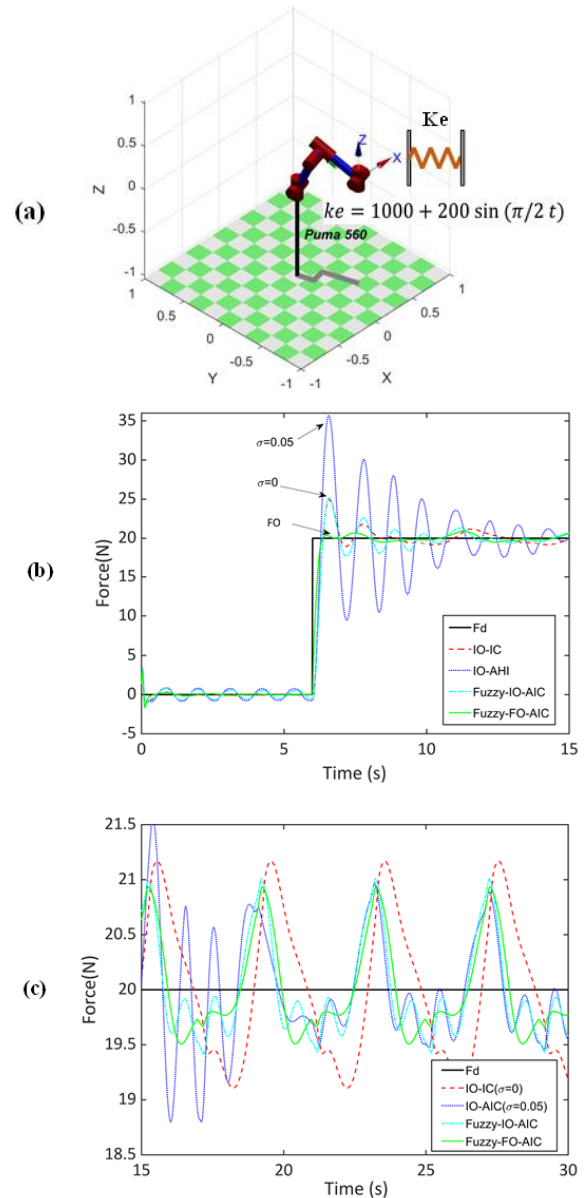


Fig. 13. 6-DOF robot force control grinding simulation

From the simulation results and analysis, we observe that introducing fuzzy adaptive σ can effectively balance the impact force and tracking requirements. Meanwhile, FO is used to further enhance control system stability. Hence, the Fuzzy-IO-AIC control strategy is the best choice of all to achieve a superior force controller, namely one with the characteristics of high force tracking and no overshoots.

4.3. 6-DOF robot dynamic contact simulation

The Fuzzy-FO-AIC is arranged in the form of a 6-DOF robot (PUMA560) for the polishing simulation study, with force control in the x-direction of the motion constraint, and motion control in the remaining directions, as indicated in Fig. 13(a). Basic cartesian impedance parameters are set: $m_d = 30 \text{ Ns}^2/\text{m}$ and $b_d = 120 \text{ Ns}/\text{m}$; and the approximation coefficient of FO is $\beta = 0.7$. The robot is controlled by inverse dynamics plus joint servo for motion tracking, with PD parameters $k_p = 1e^3$ and $k_d =$

35. The sampling period is 4 ms.

Fig. 13(b) shows the IO-IC, IO-AIC, Fuzzy-IO-AIC and Fuzzy-FO-AIC in the contact phase. It can be seen that IO-AIC also exhibits a large overshoot behaviour, and as the update rate decreases, the vibration overshoot has a great reduction in IO-IC and Fuzzy-IO-AIC, but does not disappear completely. In contrast, there is almost no overshoot in Fuzzy-FO-AIC. As can be seen from the steady-state tracking phase in Fig. 13(c), the IO-IC tracking accuracy is poor at about 10.5%, while the IO-AIC, Fuzzy-IO-AIC and Fuzzy-FO-AIC tracking accuracy improves at about 7%. The Fuzzy-FO-AIC demonstrates a transient and steady-state control performance that is much better than the current commonly used impedance control strategies. Essentially, fractional-order impedance can further improve the tracking accuracy to a certain extent by appropriately increasing the update rate due to its better stability.

5. CONCLUSIONS

The significance of the robot contact operation has been growing recently due to the introduction of interactive robots. Maintaining the high speed, stable, smooth contact and high precision force tracking indicators are some of the highly challenging aspects involved in force controller design. Additionally, these demands are among the most common issues in real robot application.

In this paper, the Fuzzy-FO-AIC is proposed to manage dynamic contact force tracking in an uncertain environment (e.g., polishing tasks). The need to adjust the dynamic update rate and maintain the superiority of FO control are highlighted. A fuzzy logic controller inferring the update rate on-line is applied and the stability and boundary are analysed. Meanwhile, an IO approximate method using percentage to simplify fractional control is also provided and verified through simulation. The simulation results all show that Fuzzy-FO-AIC can improve the dynamic force tracking performance, significantly in an uncertain environment, better than other previous controllers. In particular, FO control enables more effective control and provides more flexibility to adjust stability than IO, making it well suited for robotic applications involving force control. Furthermore, the reported methodology can be expanded to force control in other tasks where an unknown environment is easily distorted or manufacturing requires force control based on industrial robots.

REFERENCES

- Liang L, Chen Y, Liao L, Sun H, Liu YJR, Manufacturing C-I. A novel impedance control method of rubber unstacking robot dealing with unpredictable and time-variable adhesion force. 2021;67:102038.
- Cao H, He Y, Chen X, Zhao XJRTijorr, application. Smooth adaptive hybrid impedance control for robotic contact force tracking in dynamic environments. 2020.
- Mokhtari M, Taghizadeh M, Mazare MJR. Hybrid adaptive robust control based on CPG and ZMP for a lower limb exoskeleton. 2021;39(2):181-99.
- Dong Y, Ren T, Wu D, Chen KJJoI, Systems R. Compliance control for robot manipulation in contact with a varied environment based on a new joint torque controller. 2020;99(1):79-90.
- Raibert MH, Craig JJ. Hybrid position/force control of manipulators. 1981.
- Mason MTJIToS, Man., Cybernetics. Compliance and force control for computer controlled manipulators. 1981;11(6):418-32.
- Hogan N. Impedance control: An approach to manipulation: Part I—Theory. 1985.
- Komati B, Pac MR, Ranatunga I, Clévy C, Popa DO, Lutz P, editors. Explicit force control vs impedance control for micromanipulation. International Design Engineering Technical Conferences and Computers and Information in Engineering Conference; 2013: American Society of Mechanical Engineers.
- Wu J, Ni F, Zhang Y, Fan S, Zhang Q, Lu J, et al. Smooth transition adaptive hybrid impedance control for connector assembly. 2018.
- Akdoğan E, Aktan ME, Koru AT, Arslan MS, Atlihan M, Kuran BJM. Hybrid impedance control of a robot manipulator for wrist and forearm rehabilitation: Performance analysis and clinical results. 2018;49:77-91.
- Jung S, Hsia TC, Bonitz RGJIToCST. Force tracking impedance control of robot manipulators under unknown environment. 2004;12(3):474-83.
- Duan J, Gan Y, Chen M, Dai XJR, Systems A. Adaptive variable impedance control for dynamic contact force tracking in uncertain environment. 2018;102:54-65.
- Solanes JE, Gracia L, Muñoz-Benavent P, Esparza A, Miro JV, Tornero JJR, et al. Adaptive robust control and admittance control for contact-driven robotic surface conditioning. 2018;54:115-32.
- Lu Z, Goldenberg AAJITjorr. Robust impedance control and force regulation: Theory and experiments. 1995;14(3):225-54.
- Fateh MM, Khorashadizadeh SJND. Robust control of electrically driven robots by adaptive fuzzy estimation of uncertainty. 2012;69(3):1465-77.
- Li Y, Ge SS, Zhang Q, Lee THJICT, Applications. Neural networks impedance control of robots interacting with environments. 2013;7(11):1509-19.
- Cao H, Chen X, He Y, Zhao XJIA. Dynamic adaptive hybrid impedance control for dynamic contact force tracking in uncertain environments. 2019;7:83162-74.
- Xu WJJoDS, Measurement,, Control. Robotic time-varying force tracking in position-based impedance control. 2016;138(9):091008.
- Sheng X, Zhang XJM. Fuzzy adaptive hybrid impedance control for mirror milling system. 2018;53:20-7.
- Zhou Q, Li H, Shi PJIToFS. Decentralized adaptive fuzzy tracking control for robot finger dynamics. 2014;23(3):501-10.
- Nikdel N, Badamchizadeh M, Azimirad V, Nazari MAJIToIE. Fractional-order adaptive backstepping control of robotic manipulators in the presence of model uncertainties and external disturbances. 2016;63(10):6249-56.
- Zhong J, Li LJITocst. Tuning Fractional-Order λ^{μ} Controllers for a Solid-Core Magnetic Bearing System. 2015;23(4):1648-56.
- Padula F, Visioli AJICT, Applications. Optimal tuning rules for proportional-integral-derivative and fractional-order proportional-integral-derivative controllers for integral and unstable processes. 2012;6(6):776-86.
- Aguila-Camacho N, Duarte-Mermoud MAJIt. Fractional adaptive control for an automatic voltage regulator. 2013;52(6):807-15.

25. Shahri ESA, Alfi A, Machado JTJASC. Fractional fixed-structure H^∞ controller design using augmented lagrangian particle swarm optimization with fractional order velocity. 2019;77:688-95.
26. Haji VH, Monje CAJAsc. Fractional order fuzzy-PID control of a combined cycle power plant using Particle Swarm Optimization algorithm with an improved dynamic parameters selection. 2017;58:256-64.
27. Efe MÖJIToll. Fractional order systems in industrial automation—a survey. 2011;7(4):582-91.
28. Ahmed S, Wang H, Tian YJAJoc. Robust adaptive fractional-order terminal sliding mode control for lower-limb exoskeleton. 2019;21(1):473-82.
29. Efe MÖJITotloM, Control. Integral sliding mode control of a quadrotor with fractional order reaching dynamics. 2011;33(8):985-1003.
30. Feliu-Talegon D, Feliu-Battle V, Tejado I, Vinagre BM, HosseinNia SHJIt. Stable force control and contact transition of a single link flexible robot using a fractional-order controller. 2019;89:139-57.
31. Muñoz-Vázquez AJ, Gaxiola F, Martínez-Reyes F, Manzo-Martínez AJAsc. A fuzzy fractional-order control of robotic manipulators with PID error manifolds. 2019;83:105646.
32. Oustaloup A, Levron F, Mathieu B, Nanot FMJIToC, Theory SIF, Applications. Frequency-band complex noninteger differentiator: characterization and synthesis. 2000;47(1):25-39.
33. Wang Y, Luo G, Gu L, Li XJJoV, Control. Fractional-order nonsingular terminal sliding mode control of hydraulic manipulators using time delay estimation. 2016;22(19):3998-4011.

Acknowledgement: This work was supported by the National Key R&D Program of China (2017YFB1301400).

Hongli Cao:  <https://orcid.org/0000-0003-4324-3785>

USING HSM TECHNOLOGY IN MACHINING OF THIN-WALLED AIRCRAFT STRUCTURES

Paweł BAŁON^{*,**}, Edward REJMAN^{***}, Bartłomiej KIEŁBASA^{**}, Robert SMUSZ^{****}

^{*}SZEL-TECH, R&D Dep., Sołyka st. 16, 39-300 Mielec Poland

^{**}AGH University of Science and Technology, WIMiR, Al. Mickiewicza 30-B2, 30-059 Kraków, Poland

^{***}Rzeszów University of Technology, KKM, Al. Powstańców Warszawy 12, 35-959 Rzeszów, Poland,

^{****}Rzeszów University of Technology, ZT, Al. Powstańców Warszawy 12, 35-959 Rzeszów, Poland,

balonpawel@gmail.com, erejman@prz.edu.pl, bartek.kielbasa@gmail.com, robsmusz@prz.edu.pl

received 6 July 2021, revised 29 September 2021, accepted 5 October 2021

Abstract: Subtracting manufacturing technologies have entered that realm of production possibilities which, even a few years ago, could not be directly adapted to direct production conditions. The current machines, i.e. heavy, rigid cutting machines using high spindle speed and high feed speed, allow for manufacturing very thin and relatively long parts for use in the automotive or aerospace industry. In addition, the introduction and implementation of new 70XX aluminium alloys with high strength parameters, as well as monolithic diamond cutting tools for special machining, have had a significant impact on the introduction of high-speed machining (HSM) technologies. The main advantage of the applied manufacturing method is obtaining a very good smoothness and surface roughness, reaching even $S_z = 6-10 \mu m$ and $S_a < 3 \mu m$, and about four times faster and more efficient machining compared to conventional machining (for the beam part). Moreover, fixed and repeatable milling process of the HSM method, reduction of operational control, easy assembly of components and increase in the finishing efficiency compared to other methods of plastic processing (forming) are other benefits. The authors present a method using HSM for the manufacturing of aircraft parts, such as the chassis beam at the front of a commuter aircraft. The chassis beam assembly is made of two parts, front and rear, which – through a bolted connection – form a complete element replacing the previous part made using traditional technology, i.e., cavity machining, bending and plastic forming. The implementation of HSM technology eliminates many operations related to the construction of components, assembling the components (riveting) and additional controls during construction and assembly.

Key words: aviation, high-speed machining, milling, thin-walled parts, integral structures

1. INTRODUCTION

Aircraft constructions require meeting three basic criteria: adequate strength, rigidity and minimum weight of the structure. These features determine the cross-sectional areas and the minimum dimensions of the thickness of the structural elements. Small local buckling of the elements of an aircraft structure (frames, spars, ribs, etc.) is acceptable for different payload capacities and weight scenarios, but surpassing the load limits of components practically guarantees the structure's destruction, due to the low construction safety factor.

Therefore, the methodology behind the design and fabrication of airplane components requires constant improvements. Rapid progress in materials science and manufacturing systems permits the production of aggregate parts of complex shapes. Such integral assemblies make it possible to apply material properties in a more appropriate way and also enable a substantial boost in the mechanical parameters of their primary framework. The most vital benefit from implementing the aggregate parts is the cost savings from the minimisation of steps in manufacturing. Rib T-shape elements significantly increase strength and reduce the weight of the structure. Owing to this, a structure with substantially improved capacity limits can be manufactured by lowering thicknesses and utilising hardened longitudinal parts that are spaced appropriately [11].

The current trend in the development of subtracting manufac-

turing is the growth in the cutting velocity. A very large increase in cutting speed occurred with the introduction of new tool materials and tool coatings that increase durability [6]. It can be assumed that cutting speeds used during high-speed machining (HSM) are 5–10 times greater than conventional cutting speeds, which depend on the type of material being machined [13]. To define the HSM process, different values are used to characterise the cutting process. These values include cutting forces, friction force in the cutting zone, specific cutting energy and the ratio of the spindle motor power demand to its maximum rotational speed.

The growing interest in HSM, especially in the aviation industry, is associated with a number of benefits obtained after the implementation of cutting at high speeds. The effect of the increase in the rotational speed is a reduction in the machining time and, thus, an increase in machining efficiency. Other additional beneficial effects of the introduction of high-speed milling can include a reduction in the cutting forces needed, a reduction in the percentage of cutting heat penetrating through 88% of the work-piece, reduction in the roughness of the treated surface, as well as greater processing capabilities in thin-walled elements and more favourable chip forms.

It is assumed that HSM begins when increasing the cutting speed v_c results in a decrease in cutting forces, which can be expressed by the following expression:

$$\frac{\partial F}{\partial v_c} < 0, \text{ for HSM} \quad (1)$$

$$\frac{\partial F}{\partial v_c} > 0, \text{ for conventional treatment [9]} \quad (2)$$

High-speed milling was first used to produce small elements of aircraft constructions approximately 12 years ago. However, the use of this method for an entire assembly, such as the front chassis beam, is a great process and product achievement. The front chassis beam is a critical structural element of the aircraft, which is subjected to special supervision and control during the entire production process, not only due to its external dimensions of 3,000 × 500 mm but also due to the significant loads it bears during the touchdown phase of the aircraft's flight, where, in some significant cases, non-axial forces may occur. In the presented work, the authors, as part of the planned works for the project, developed and made a prototype of the chassis beam assembly using high-speed milling technology. This technology makes it possible to create elements that have a complicated shape with a small wall thickness of the reinforcing ribs.

In a series of preceding tests, the authors checked and demonstrated the application of the high-speed milling method for another construction part, i.e. the front beam of the aircraft [4]. It was proved that it is possible to obtain a minimum wall thickness of <0.6 mm for a ribbed plate without losing the required geometry of the structural element. Obtaining the minimum wall thickness of the ribbed plate allows for a significant reduction in product weight of up to 20% compared to conventional solutions. The use of the high-speed milling method to create integral parts additionally reduces the number of fastener elements necessary to connect the entire assembly.

Manufacture of the thin-surfaced parts comes with many technical problems related to distortions and alterations of the part resulting from its elasticity and plasticity. Vibrations can be caused by deformations of the ground part, and thus, flaws may occur in the structure's shape. In addition, permanent deformities can also generate geometric errors and cause interior stress in the outermost sheet, which are rather challenging to reduce and result in deformity of the post-machining part. This results in expanded fabrication expenses for production processes, particularly for thin-sided parts, resulting from low quantities and greater fabrication time [12].

The commonly used rule for choosing materials to be used in the manufacture of aircraft is the durability-to-weight relation. Elements are devised and the proper materials (aluminium, titanium, steel and composite) are chosen depending on the aircraft's capacities [5, 7]. Full block material, a forging, or a casting is used for workpieces. Composites, aluminium alloys and titanium alloys are the most commonly used materials for aircraft constructions. Considering the implementation of composite materials in aircraft structures, fatigue failure analysis needs to be taken into account [8]. Lately, intense corporate rivalries within the aviation industry have resulted in the rather rapid growth of contemporary fabrication processes.

Nowadays, many aircraft parts are fabricated for off-the-shelf sale from a full amount of material. The aggregate parts of aircraft usually demand deletion of up to 98% of the raw material during the course of manufacturing. To successfully fulfil such mass production processes, it is essential that the most economical methods be utilised so that the manufacturing can be profitable. High-speed milling technology creates or enhances this possibility. Furthermore, the fabricated workpieces are homogeneous and possess improved mechanical properties. The absence of joints fastened with rivets leads to a lower weight piece structure with a

better strength-to-weight ratio [1]. An aircraft beam structure made of stamped, bent and riveted sections is shown in Fig. 1. The same structure can be successfully made using the HSM technology, which vastly saves manufacturing time and labour intensity (Fig. 2).

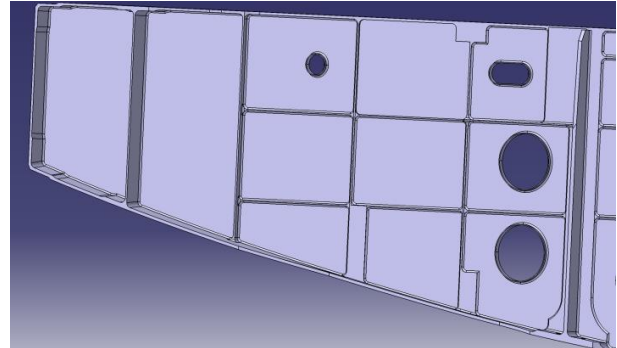


Fig. 1. Structure of aircraft beam designed for HSM made of stamped and bent sections. HSM, high-speed machining

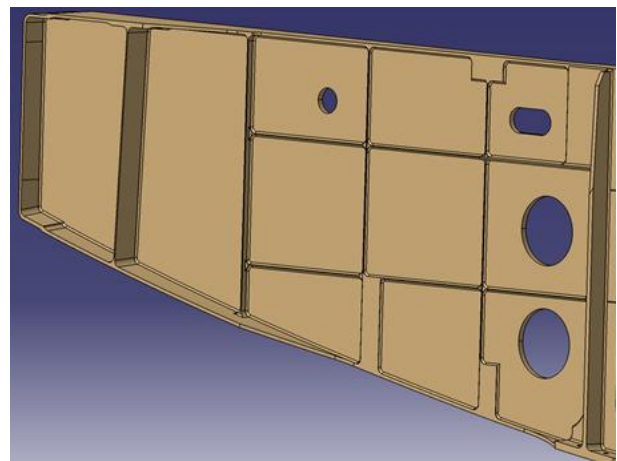


Fig. 2. Structure of aircraft beam designed for HSM milled using the HSM method. HSM, high-speed machining

The modern CAM systems do not just calculate a tool's pathway but are also utilised for its checking, authentication and optimisation with the goal of reducing the number of errors.

The essence of the aerospace industry sector is low-quantity manufacturing which necessitates elasticity immediately at the technological fabrication preparation phase, wherein unified CAD and CAM programmes are particularly helpful.

The design scheme for production of thin-sided complex assemblies made for the aeronautics industrial sector necessitates consideration of the standard conventions recommended for the programming of CNC machines, as well as the special features of thin-sided parts with a high proportion of wall height to wall thickness, especially whenever HSM is used. For this technology, it is crucial to select a proper fabrication procedure, particularly for flat, thin-sided aircraft parts, such as frameworks, beams, ribs, etc. In such cases, the wall's ratio of height-to-wall thickness is the normal parameter.

This relationship represents the elastic rigidity of the part and, specifically, the malformations that take place during production. To minimise wall bending, the most suitable amount of tool runs should be utilised. Additionally, the time of machine-to-part contact should be minimised by using a high cutting speed and a low

ratio of cut depth a_p to cut layer width a_e . The solidity of the tool and the machined wall is of great importance to the process. In areas where there is weaker support of the thin-sided piece, reverse milling should be used. For a height-to-thickness ratio $<15:1$, machining should be done for only one side of the part's surface, in non-overlapping passes. Grinding should be repeated for the reverse side and an allowance must be made for finish production [10, 17].

2. CHARACTERISTICS OF HSM METHODS

The aerospace industry uses thin-walled pocket constructions made of aluminium alloys, which ensures low mass and high stiffness. They constitute up to 60% of the product weight. As blanks for their production, plates of a certain plastically processed thickness are used above all. Due to significant weight loss of up to 98%, modern, high-performance machining methods, such as milling: HPC roughing and HSC finishing machining, are used when making thin-walled parts.

The main problem encountered during the machining of thin-walled structures is their elastic and plastic deformations, which occur during the milling of thin-walled elements. After removing the load, the wall resiliently returns to its original position. The tool-holder-spindle layout also resists elastic deformation. HSM of deep, thin-walled pocket constructions requires the use of tools with large overhangs, which increases the deformation of this system.

Elastic deformation of the tool and the workpiece, in addition to shape errors, may cause process instability, which affects the quality of the work surfaces. This lack of machining stability results in the development of vibrations and the so-called "chatter" of the machined wall.

Stabilisation of machining conditions can be achieved through the appropriate selection of cutting parameters or the use of tools with geometry that reduces the vibration tendency. In order to minimise the vibrations, tools with different blade pitches and variable helix angles are used. Due to different helix angles, successive cutting edges produce chips with variable cross-sections. This ensures reduced harmonic vibrations and reduced cutting forces, which allows the efficiency of the machining process to be increased.

Increasing the cutting speed to the range corresponding to the HSC machining results in lower cutting forces, which reduces the distortion of both the thin-walled elements and the tool. Reduction of the cutting forces, especially the component perpendicular to the machined surface, which has the greatest impact on wall deformation, can also be obtained by optimising the cutting parameters, i.e. feed f_z , depth a_p and cutting width a_e . Lower cutting resistance generates lower machining stresses, which reduces deformation of the workpiece and ensures higher quality and accuracy. Additionally, the rise in the cutting velocity has an advantageous effect on the surface quality, which is characterised by a greater regularity in machining marks and lower roughness and waviness in relation to the machined surfaces with classic cutting parameters.

When machining the high walls of the elements, it is advisable to apply the appropriate machining strategy. The experience of the authors allows distinguishing the following methods of processing:

- Method I – separate treatment of each side of the wall (recommended at a wall height-to-thickness ratio of $<15:1$),

- Method II – alternate processing of both sides of the wall for a constant level – (height-to-thickness ratio of $<30:1$),
- Method III – alternating machining of both sides of the wall with a level difference – (height-to-thickness ratio of $<30:1$),
- Method IV – alternating processing of both sides of the wall with a constant level and increasing wall thickness towards its base (height-to-thickness ratio of $>30:1$).

For roughing thin-walled elements, counter-rotational milling is recommended for all strategies. A finishing allowance of approximately 0.2–1.0 mm should be left for the finishing treatment, depending on the final wall thickness. However, these machining methods have some drawbacks as follows:

- Multiple tool passes introduce additional stresses of their own, which can have a significant influence on the formation and form of deformation of the machined walls.
- Making subsequent passes after previous machining marks may cause a regeneration effect and, thus, loss of stability of the treated wall.
- During machining of subsequent layers and contact of the cutting edge of the tool with the previously machined surface, it accelerates the tool wear and causes loss of quality in the machined surface.

The above factors make it increasingly advisable to finish the thin walls at their full height. However, this requires the use of tools with appropriate geometry characterised by different blade pitches and a variable or differing helix angle. Densely ribbed structures are often used in aviation structural elements. They have the form of thin-walled elements with complex geometry and a significant depth of recesses between the ribs. This type of machining requires the use of "slender" tools with large overhangs and therefore low stiffness. Providing high performance involves the deformation of both the machine and the part, which affects the accuracy of the shaped walls.

In the case of HSC machining, mainly monolithic diamond tools and heat-shrinkable holders are used to ensure secure and accurate fastening [2, 3]. In HSC machining, especially when the tool reach is increased, its dynamic balancing is decisive. Poor balancing, like the low stiffness of the tool, may cause it to lose its stability during operation and may adversely affect the spindle-bearing arrangement.

The HSM machining process requires the use of synthetic cooling and lubricating fluids, which are primarily characterised by good machining properties. The lubricating fluid used in the research-and-development (R&D) works was an emulsion called HYCUT ET 46 (Oemeta company).

3. EXPERIMENTAL PROCEDURE

In the authors' own research, the use of HSC machining in the production of aircraft construction components was addressed. In the production of the most heavily loaded components, aluminium alloys from the 70XX group are used. Rigid alloys are characterised by high plasticity, and their mechanical properties depend on the chemical composition of a given alloy. The increase in strength of these alloys is achieved by heat treatment. In addition, increase in strength is obtained by strengthening the work-up during cold forming in combination with precipitation hardening. Multi-component aluminium alloys with alloy additions such as Mg and Cu, known as zinc dural, show the highest strength properties among all aluminium alloys. In the hardened state, their yield point ranges from $R_{p0.2} = 600$ MPa to

$R_{p0.2} = 700$ MPa and tensile strength ranges from $R_m = 700$ MPa to $R_m = 780$ MPa. Heat treatment of 70XX alloys consists of recrystallising annealing at 390–430 °C and precipitation hardening. Saturation is carried out at a temperature of 465–480 °C. Ageing, however, is done at a temperature of 120–150 °C. In the shaping of aeronautical elements from aluminium alloys, the aim is to make milling the basic machining process used in their production.

The material used in the research was 7075 T6 aluminium alloy with tensile strength properties in the supersaturated state (Fig. 3). The chemical composition of the material is given below (Tab. 1, Tab. 2):

Tab. 1. Chemical composition of the 7075 T6 aluminium alloy [%]

Al	Mg	Cu	Mn	Zn	Si + Fe
89.72	1.6	0.09	0.11	0.03	2.5

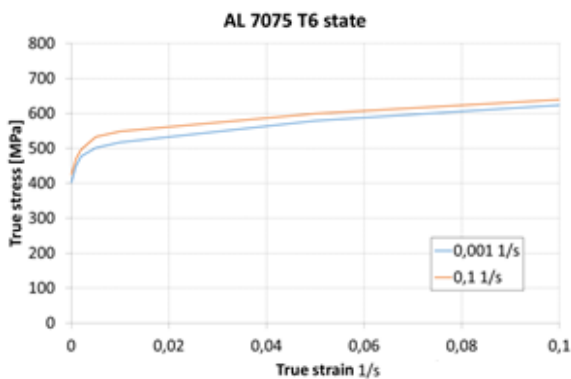


Fig. 3. Stretching chart of an aluminium alloy sample 7075 for the supersaturation condition T6

Tab. 2. Mechanical properties of the 7075 T6 aluminium alloy tested at a temperature of 21–22 °C

R_m	565 MPa
Yield strength $R_{p0.2}$	520 MPa
Young's modulus E	72 GPa
Poisson's ratio ν	0.33
Elongation	13,5%
Hardness (Fig. 4)	180 HV1

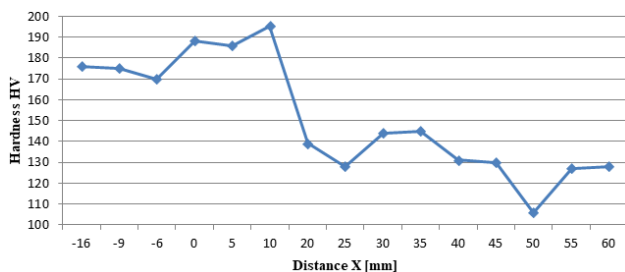


Fig. 4. Ageing at the temperature of 150 °C for 24 h with air cooling

Blocks with dimensions of 1,055 mm × 510 mm × 50 mm, with a total weight of 76 kg, were used as semi-completed products and were delivered in a solution state.

The size of the workpieces was 1017.5 mm × 354 mm × 48 mm. The thicknesses of the walls were 1 mm, 2 mm, 3 mm

and 5 mm. The biggest open, flat surfaces (devoid of ribs) were of size 338.5 mm × 108.8 mm × 1 mm. The ratio of the ribs' height to their thickness, h/g , was in the range between 9.6 and 28.5. The radius passing between the walls and the ribs was 1.5 mm. The roughing was carried out with a spindle having a rotational velocity of $n = 22,500$ rev/min (cutting tool $d = 12$ mm) and finishing $n = 45,000$ rev/min (cutting tool max $d = 6$ mm); this was meant to get the machining datum surfaces prepared for later operations. The workpiece was attached to the machining table using pressure clamps and the machining was done in a dual-phase process: shaping and finishing. Two parts were fabricated concurrently on the two machines, while equal and unequal machining processes of the pockets were used. For the first, the beam receptacles were positioned symmetrically to the part's axis and they were fabricated in an alternating fashion. For the unequal machining, the receptacles were ground intermittently in relation to the axis running through the symmetry of the beam. For such a method, internal malformations of the beam were roughly calculated after the machining phase.

Production of the two-sided beam receptacles required preparation of the machining foundations in which the supports needed to rest and position the part on the milling machine. Therefore, a rim with holes forming cylinders was created from the semi-finished material. The rim was a machining datum surface and the holes permitted the part to be fastened to the machine table (Fig. 5). The supports were only added on an as-needed basis and were excised after completion of the last beam fabrication operation.

Based on the presumption of the manufacturing documentation, the limits of the linear parameters of the beam are established by the norm BN-85/3813-79: Deviations of non-tolerated dimensions, shape and location for aviation products.

For the beam's sides, the tolerances are as follows:

- $g = 0.8$ –5 mm; deviations: ± 0.05 mm.
- For the rib height:
- $h = 11.9$ –40 mm; deviations: ± 0.1 mm.
- For the overall dimensions:
- 1,017.5 mm × 354 mm; dimensions: ± 0.3 mm.



Fig. 5. Chassis beam made using the HSM method with two integral parts. HSM, high-speed machining

The mechanical tooling of the beam was performed in two phases: pre-machining and finishing. The number of machine runs in all cases was determined by the wall measurements and the axial cut depth. The fundamental obligation of the machining process was to guarantee as minimal malformation of the ribs as possible and also to secure appropriate surface roughness during the finishing machining. In the fabricated beam, 1.5 mm finishing tolerances were used for large part surfaces and 0.1 mm on the rib walls with a thickness of 0.8–3 mm. To reduce the wall deform-

ity, the time needed to connect the tool and the part being machined had to be shortened. This was achieved by using high-speed cutting (i.e., high tool rotation speed). The later treatment, which established a high degree of machining precision of the smooth beam walls (the height-to-thickness ratio was maintained somewhere <30), was done to maintain a proper machining strategy. The most effective way was intermittent receptacle machining with a switch in machining sides and keeping the machining at equal amounts for each pocket. While machining thin sides, it is generally suggested that one grind in reverse. The weight of the complete, final frame was 4.65 kg (1.8 kg upper + 2.85 lower) and the weight of the initial material was 186 kg (76 kg + 110 kg), so the part's weight was 2.2% of the material started with; 97.8% of the semi-finished material was recycled into chips. This equals a "buy-to-fly" ratio (weight of the starting material to the weight of the final product) of 39. This technical process can be used for thin-sided structure manufacturing, wherein the chips' mass can be up to 97.8% of the starting material. It should be underscored that the beam's weight is 4.65 kg.

By introducing the HSM technology, in relation to classic milling methods, currently designed aircraft structures consist mainly of integral thin-walled elements, which were previously produced by plastic forming technologies and then joined using welding or riveting technologies. In the HSM technology, after machining, these parts are directly assembled in the semi-assembly or assembly process, bypassing the assembly into larger assemblies. Achieving high efficiency of HSM of high-strength aluminium alloys, especially in roughing, requires machine tools with high rigidity and high power on the machine spindle.

The time needed to manufacture the frame (including software preparation time) was 250 h (CAM software) and 300 h (time of milling). The manufacturing time of the beam can be minimised to 30 h for the production series by applying the successfully tested control system and the lessons learned through the mock-up processing. The roughing time of the beam is estimated to be around 20 h, and the finishing takes around 10 h, which comes to about 30 h in total to fabricate the frame using the HSM technique. A comparison of the HSM technology to the conventional machining process shows that about 4 times as many hours are necessary to fabricate the beam by traditional milling methods. The authors of the work, together with the industrial consortium, plan to develop the technological process and complete the construction of an entire integral beam of the aircraft front chassis using HSM technology, without the need to divide it into front and rear parts combined with bolts. This possibility results from the recent purchase of an appropriate machine tool. Moreover, for wall machining with a height-to-thickness proportion <15 , the effect of structural malformation defects on the geometric accuracy of the part is insignificant. In the case of narrower walls, this outcome becomes detectable and should be kept to a minimum through fine-tuning of the machining parameters, i.e., piece feed rate, milling extent, machining direction, etc.

4. QUALITY OF SURFACE

Inspection of the geometric dimensions and surface roughness of the processed beam allows us to draw a number of interesting conclusions. The surface quality after milling depends on the type of material to be machined and the geometry of the cutting tool. The cooling conditions have a substantial effect on the results of the treated surface. Cooling with emulsion significantly

improves the surface roughness. During milling of the above-mentioned beam, a surface roughness of $S_z = 6\text{--}10\ \mu\text{m}$ and $S_a < 3\ \mu\text{m}$ was obtained (Fig. 6).

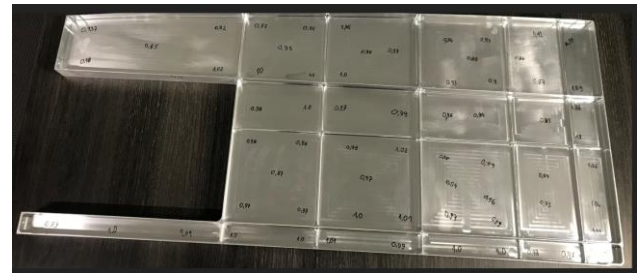


Fig. 6 Points of control measurements of wall thickness using CMM and micrometre methods

During milling with end milling cutters, with both conventional machining and with increased cutting speed, the best surface quality was obtained after machining with a diamond tool. The processing was carried out with a diamond milling cutter of $d = 12\ \text{mm}$ and $d = 6\ \text{mm}$, respectively. The milling width was $a_e = 10\ \text{mm}$ and $a_e = 5\ \text{mm}$, respectively. The choice of the diamond tool resulted from our own preliminary tests, where a tool with the carbide plate was used to chip off the cutting edge and this process subsequently destroyed the sample. This cannot be allowed when machining expensive integral parts. After machining of series 7075 alloys, the roughness of the machined surface was improved as seen by measuring the following parameters: S_a (arithmetic average of the roughness profile); S_z (the largest height of the profile). Increasing the feed above $f_z = 0.2\ \text{mm}$ per blade results in a significant increase in roughness.

The beam's specifications were assessed by an optic scanner in order to verify its geometry, linear measurements and spatial displacements (Fig. 7). This study helped us to ascertain the geometric parameters of specific beam details and to produce computerised and relief maps displaying the beam's stereometry. These maps mainly allowed assessment of the malformation potential of the large beam exterior. Such defects can occur due to internal tensions produced in the part throughout the mechanical treatment phase [15, 16, 17]. Dimension evaluation showed that the irregularities of the linear measurements were within the forecast tolerances. The deformities of the workpiece occur primarily near the shorter axis of symmetry, and the shifts are symmetrical in the direction of the longer axis of symmetry. The biggest relative displacement value is 0.31 mm. Precise measurements are assured by the optical scanner, with a margin of error of $\pm 0.25\ \text{mm}$. Nonetheless, this technique demonstrates – in a dependable way – what deformities should be foreseen in the machining of parts of a similar component. For an exacting assessment of the ribs' wall thicknesses, which are the most significant when considering structural durability, the walls were measured with a micrometer. The measurements were made at the ribs' points that were forecast to be most susceptible to malformations during the machining process – at the rib's base and at the rib's top.

To estimate the form, measurements and spatial displacements of the beam as a complete sub-assembly, the beam was evaluated on a control instrument that is used to study the beam present in current aircraft (Fig. 8). Research has shown that the beam measurements fall within the tolerances forecast in the technical documents. The measurements also met the local

standard BN-85/3813-79, which was utilised for verifying unacceptable distortions and shapes.

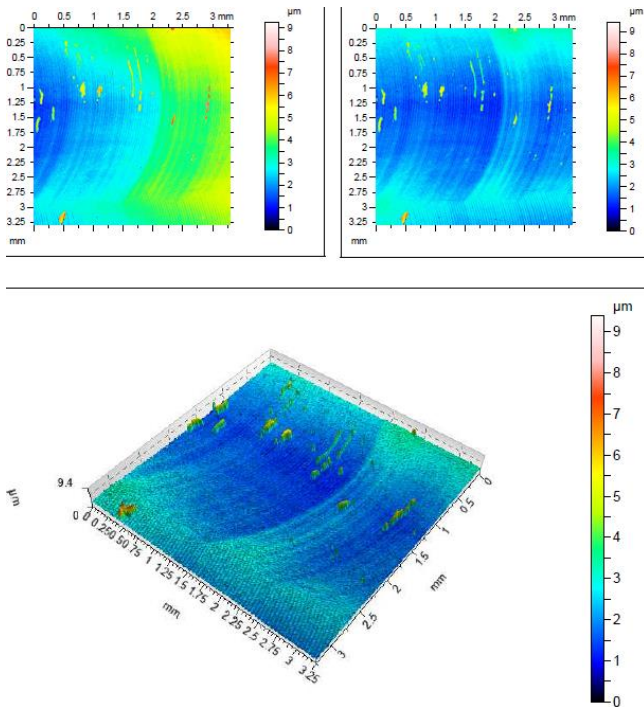


Fig. 7. Graphic representation of the roughness of the measured surface, $S_a = 0.275 \mu\text{m}$ – arithmetic means of discrepancy of the surface’s unevenness from the reference plane: (a) transition area between the machining marks; (b) homogeneous machining area; (c) view of the measurement zone

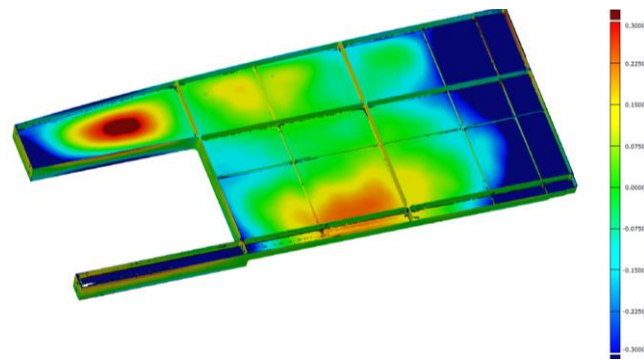


Fig. 8. The size of displacements of the beam elements measured by the GOM optical scanning method. The values of displacements reach positive and negative values due to the elastic stresses of the material after HSM treatment. The maximum brown values are due to wall thickness <math>< 1 \text{ mm}</math> of the pocket between the ribs with a relatively great height – 40 mm. HSM, high-speed machining

The application of HSM for thin-walled aircraft beams is achievable owing to the exactness of the workpiece and the machining potential of the Al7075 aluminium alloys. A suitable cutting parameter choice yields good surface waviness and roughness [1].

In the case of machined walls having a height-to-thickness ratio <math>< 30</math>, the effect of the structure’s deformity on the part’s parameter precision is negligible, and it still lands within the tolerances of the milling machine. For larger walls’ slenderness, this impact

starts to become noticeable and should be reduced by proper selection of the cutting velocity (workpiece feed rate, cutting depth).

Maintaining dimensional-shape precision throughout the machining process necessitates an appropriate choice of the technological bases to secure the mounting technique for the workpiece. In composite spatial components, some extra foundations ensuring mount solidity should be utilised and later removed during the final processes. The final HSM application permits the manufacturer to reduce the work machining hours.

The finished part is an integrated structure that replaces the same parts currently manufactured using plastic processing of individual parts (38) and then assembling those using fasteners. The entire manufacturing time for individual elements of the beam was >5 times that of the suggested HSM method. Augmenting the advantages resulting from the lowered manufacturing time of the beam, other benefits of the suggested technology are the quality and precision of the fabrication, in addition to the desirable roughness class of the part surfaces [18, 19].

During the machining process around the tip of the cutting tool, a plastic deformation of the workpiece is created, which, after removing the factor causing it, causes the formation of compressive residual stresses in the surface layer (Fig. 9). In addition, during cutting, heat is generated (related to, among others, friction), leading to large differences at temperature and thermal stresses exceeding the yield point of the material and, consequently, to tensile residual stresses in the surface layer. In fact, all these factors influence the state of residual stress, but their intensity may vary. However, it is assumed that after machining, the surface layer is dominated mainly by mechanical stress (pressure) and – acting in the opposite direction – thermal stress (temperature). The mechanical model corresponds mainly to machining, while the thermal model is characteristic of abrasive machining and the high-speed machining of HSC. The residual stress after machining occurs at depths of several tenths of a millimetre.

The residual stresses arising during the cutting process depend on many factors, including the following:

- depth of cut
- feed
- cutting speed
- the geometry of the cutting tool
- cooling conditions
- properties of the processed material and
- degree of wear of the cutting tool.

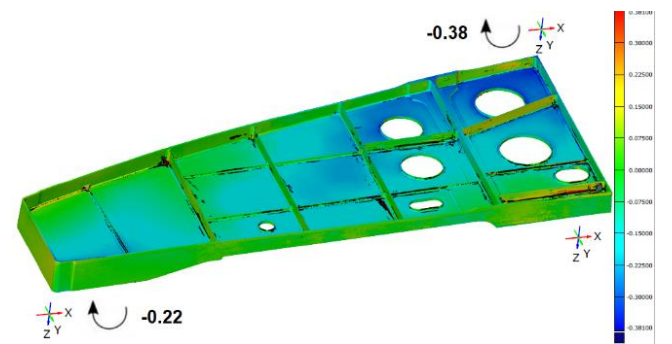


Fig. 9. The deformation of a thin-walled element caused during machining on a five-axis machine tool CNC measured in external points

5. SUMMARY

The tests of machined samples and elements of aircraft constructions made of alloy 7075 using the HSM method confirmed the overall suitability of this machining method in the manufacture of thin-walled airframe structures. First of all, HSM allows one to make components with a tolerance of 0.05 mm, which is satisfactory for such parts.

Application of the HSM method to thin-walled elements (thickness: 0.8–2.5 mm) results in changes in the state of the top layer (stresses, plastic deformations), followed by displacement of thin walls at the level of 0.6 mm, which should be considered during thin-wall machining of ribs and large free surfaces. This phenomenon can be partially counteracted by supporting the surfaces treated with elements of high stiffness.

The tests were conducted at a cutting velocity of $V_c = 830$ m/min for roughing and $V_c = 1,200$ m/min for finishing machining, respectively. In any case, the cutting process was very stable. No vibrations were observed, which caused a degradation of the surface quality of the worked part, especially surface undulation and roughness. Surface roughness of $R_a = 0.6\text{--}2$ μm was obtained, with higher values referring to the middle points of free surfaces (plate with dimensions of 300 mm \times 300 mm) and lower values with higher stiffness values. From the point of destination of the workpieces, such surface roughness is satisfactory. In comparison to the classic milling method, the HSM method gives results of 10% better surface quality at 5–10 times thinner wall thickness of the processed npockets, i.e. with a thickness of up to 0.6 mm. The proper choice of machining settings provides the desired roughness and waviness of the machined surface needed for the product grade for the aerospace industry. In addition, the use of HSM provides the production of thin-sided integral aircraft structures with sufficient accuracy, including the machining of high-strength aluminium alloys Al7075.

REFERENCES

- Adamski W. Manufacturing development strategies in aviation industry. *Advances in Manufacturing Science and Technology*. 2010; 34(3):73-84.
- Balon P, Rejman E, Smusz R, Szostak J, Kielbasa, B. Implementation of high speed machining in thin-walled aircraft integral elements. *DE GRUYTER Open Engineering*. 2018; 8:162-169.
- Balon P, Szostak J, Kielbasa B, Rejman E, Smusz R. Application of High Speed Machining Technology in Aviation. 21st International ESAFORM Conference on Material Forming. 2018.
- Balon P, Rejman E, Smusz R, Szostak J, Kielbasa, B. High Speed Milling in thin-walled aircraft structures. *Applied Computer Science*. 2018; 14(2):82-95.
- Burek J, Płodzień M. Wysoko wydajna obróbka części ze stopów aluminium o złożonych kształtach. *Mechanik*. 2012; 7:542-549.
- Calatoru VD, Balazinski W, Mayer JRR, Paris H, L'Esperance G. Diffusion wear mechanism during high-speed machining of 7475-T7351 aluminium alloy with carbide end mills. *Wear*. 2008; 265(11-12):1793-1800.
- Feld M. *Obróbka skrawaniem stopów aluminium*. Wydawnictwo Naukowo-Techniczne. Warsaw; 1984.
- Kielbasa B, Balon P, Świątoniowski A. Fatigue fracture analysis of composite plates with an elliptical hole. *Strength of Materials*. 2017; 49(4).
- Klonica M, Matuszak J, Pieško P, Włodarczyk M, Zaleski K, Kuczmaszewski J, Palka T, RusinekR, Zagórski I. *Obróbka skrawaniem stopów aluminium i magnezu*. Monografie – Politechnika Lubelska; 2015.
- Kuczmaszewski J, Pieško P, Zawada-Michałowska M. Influence of Milling Strategies of Thin-walled Elements on Effectiveness of their Manufacturing. *Procedia Engineering*. 2017; 182:381-186.
- Lundblad M. Influence of Cutting Tool Geometry on Residual Stress in the Workpiece, Proc. Third Wave AdvantEdge User's Conference. Atlanta, GA, Paper 7; 2002.
- Mativenga PT, Hon KKB. An experimental study of cutting force in high speed end milling and implications for dynamic force modeling. *Journal of Manufacturing Science and Engineering*. 2005; 127(2): 251-261.
- Pieško P, Zagórski I. Analiza porównawcza metod frezowania HSM, HPC oraz frezowania konwencjonalnego wysokokręgowych stopów aluminium. *Postępy Nauki i Techniki*. 2011; 7:219-226.
- Shih AJ, Yang HTY. Experimental and Finite Element Predictions of Residual Stresses Due to Orthogonal Metal Cutting. *Int. J. Num. Meth. Eng.* 1993; 36:1487-1507.
- Morey B. High-speed machining for aerospace. *Manuf. Eng.* 2008; 140(3).
- Shulz H, Dashchenko A. High speed machining Chapter 7, Manufacturing Technologies for Machines of the Future 21st Century Technologies.
- Dewes RC, Apsinwall DK. Review of Ultra High Speed Milling of Hardened Steels. *Journal of Materials Processing Technology*, 1997; 69(1-3);1-17.
- Hon KKB. The Impact of High Speed Machining on Computing and Automation. *International Journal of Automation and Computing*. 2006; 1: 63-68.
- Mativenga PT, Hon KKB. An Experimental Study of Cutting Force in High Speed End Milling and Implications for Dynamic Force Modelling. *Journal of Manufacturing Science and Engineering, Transactions of the American Society of Mechanical Engineers*, 2005; 127(2):251–261.

Acknowledgements: This research was conducted within the project More Affordable Small Aircraft Manufacturing; Airframe ITD grant agreement no. CS2-AIR-GAM-2014-2015-01 (Annex III), co-financed by Horizon 2020 Clean Sky 2, JTI-CS2-2015-CPW02-AIR-02-07. Partners: Instytut Lotnictwa, Szel-Tech Szeliga Grzegorz, Zakłady Lotnicze Margański&Mysłowski, PZL Mielec, CIRA, Eurotech, P.W. Metrol and Ultratech.

Paweł Balon:  <https://orcid.org/0000-0003-3136-7908>

Edward Rejman:  <https://orcid.org/0000-0003-4716-7613>

Bartłomiej Kielbasa:  <https://orcid.org/0000-0002-3116-2251>

Robert Smusz:  <https://orcid.org/0000-0001-7369-1162>

PALLET MOTION ON A MAGNETIC BRAKE ROLLER

Ildar SHARIFULLIN^{*}, Andrey NOSKO^{*}, Eugene SAFRONOV^{*}

^{*}Faculty of Robotics and Complex Automation, Department of Lifting and Transport Systems, Bauman Moscow State Technical University, 2-ya Baumanskaya 5/1, Moscow 105005, Russia

sharifullin@bmstu.ru, nosko@bmstu.ru, safonov@bmstu.ru

received 24 April 2021, revised 5 August 2021, accepted 24 September 2021

Abstract: The brake roller is one of the elements for the safe operation of gravity flow pallet racks. The brake roller of the magnetic (eddy current) type magnetic brake roller (MBR) is the most promising brake type. The working principle of the MBR is based on electromagnetic induction laws, according to which the braking of a conductor moving in the magnetic field is caused by the interaction of the conductor's eddy currents with the external magnetic field. In the paper, a mathematical model of the pallet motion on an MBR was developed. The equation of motion of the pallet on the MBR was derived. The calculation results were compared with the results of experimental studies of the pallet motion velocity on the MBR. For pallet speed under "drag peak" speed, the error of the mathematical model is $<7.7\%$, and the error starts increasing once over the "drag peak" speed. Additional investigation of the coefficient of magnetic viscosity for speeds greater than the "drag peak" speed is required.

Key words: pallet, rack, gravity flow rack, magnetic brake roller, coefficient of magnetic viscosity

1. INTRODUCTION

A warehouse is a complex comprised of a building, pallet racks, transport and lifting devices for storage and internal processing of incoming items, from acceptance to processing before shipping an item to a customer. The finished product warehouse maintains enough stocks to enable continuity of shipments. In logistics, warehouses are used to improve throughput. The goal is to optimise goods movement, which can be achieved by optimising the space used [1], reducing the total distance travelled by forklifts [2] and using automated storage and search systems [3].

Improving the efficiency of using storage space with constant volume is a task relevant to any company. The task can be solved by block storage or deep-lane storage [4, 5]. A pallet flow rack is one of such storage systems (Fig. 1) [6, 7]. As noted in a previous paper [8], the pallet flow rack reduces the forklift travel distance by 22–25% compared to single-deep racks.

A pallet flow rack can be subdivided into static and dynamic parts. The static element comprises standard rack elements providing stability in each direction and supports the dynamic elements. The dynamic part comprises a gravity flow rack and safety elements such as brake rollers and a stopping mechanism with a pallet separator [9].

Brake rollers are the main safety elements of gravity flow racks (GFRs) used in pallet racks for storing and moving pallets with cargo less than their own weight. The rollers are installed along the rack at a certain interval. Brake rollers are used to limit the speed of the pallet with cargo (further referred to simply as a pallet) [10]. In GFRs, centrifugal friction rollers are the most common. However, these rollers have many drawbacks, with the principal drawback being the wear of the brake friction lining, leading to changes in the roller braking characteristics.

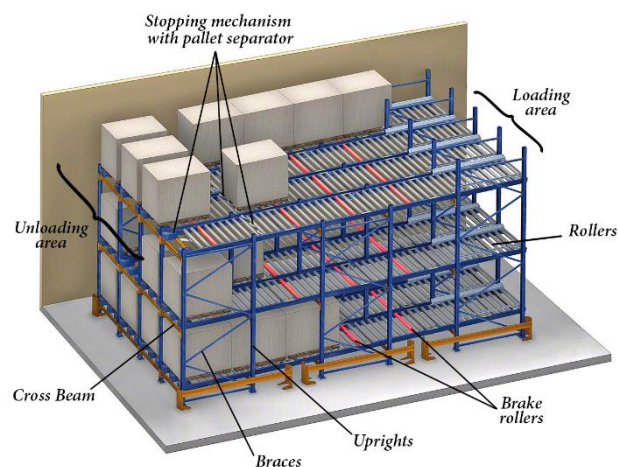


Fig. 1. Pallet flow rack

Analysis of different constructions of GFR brake rollers [11] revealed that magnetic (eddy current) brake rollers (MBRs) are the most promising brake roller type. Their main advantage is non-friction, contactless braking, meaning no wear of the roller brake lining.

The exploitation principle of such rollers is based on the laws of electromagnetic induction, whereby a conductor moving in the magnetic field is slowed down due to interaction between eddy currents in the brake conductor and the external magnetic field [12].

The paper aims to develop a mathematical model (further denoted as MM) of the pallet motion on an MBR and compare the results of experimental and analytical studies using this model. This paper reflects the Russian-language study of the authors [13].

2. MBR CONSTRUCTION AND EXPLOITATION FEATURES

Let us consider an MBR structure (Fig. 2) designed by the authors in Bauman Moscow State Technical University. The MBR comprises a brake insert 3 with a planetary multiplier 1 and an eddy current brake 2 installed on the insert axis 4.

The braking process in the MBR (Fig. 3) begins with torque transmission to the roller case (body of the brake insert 3). Then the torque is transmitted to a disc 5 (transparent display) via the multiplier. The disc starts moving in the magnetic field created by permanent magnets placed with alternating polarity and rigidly connected to the brake insert via an adaptor.

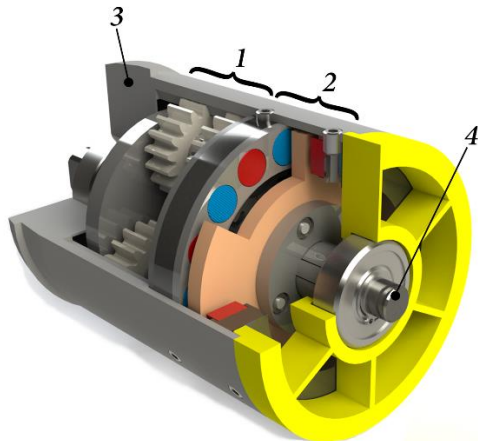


Fig. 2. General view of MBR (3D model in SolidWorks): 1 – planetary multiplier; 2 – magnetic (eddy current) brake; 3 – brake insert; 4 – axis. MBR, magnetic brake roller

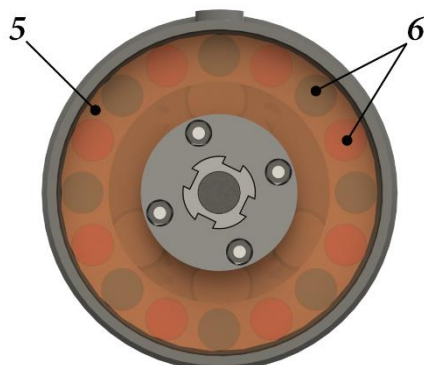


Fig. 3. Magnetic (eddy current) brake: 5 – disc (represented by transparent display), 6 – permanent magnets

Disc 5 is made of material with high specific conductivity, such as a copper or aluminium alloy. According to Lorentz law, eddy currents are generated on the disc surface, and a braking torque proportional to the external load (braking torque) is generated. Permanent magnets are made of Nd-Fe-B alloy. Such magnets have the best magnetic and electrical properties and enjoy a service life of ≥ 20 –25 years. Moreover, they have high coercive force, making MBRs almost immune to external magnetic fields [14].

In an MBR, the size of the air gap between the magnets 6 and the disc 5 is constant, while the braking torque is a function of their relative rotation speed.

3. MATHEMATICAL MODEL OF MBR

For developing the MM, the approaches used for centrifugal friction rollers [10, 15] and eddy current braking devices [16,17] were utilised. Fig. 4 shows the calculation diagrams of the GFR and BMR.

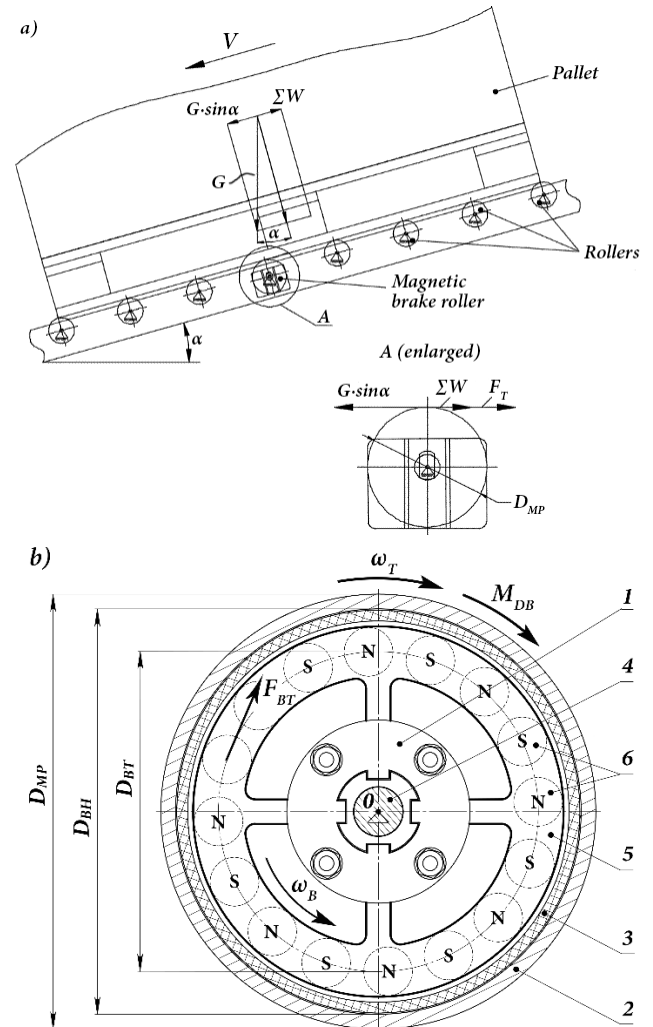


Fig. 4. Design schemes of (a) GFR and (b) MBR: 1 – a hub; 2 – shell MBR; 3 – brake insert; 4 – fixed axis of the brake insert; 5 – copper disc; 6 – permanent magnets. GFR, gravity flow rack; MBR, magnetic brake roller.

The main equation of motion governing the movement of the pallet on the MBR (Fig. 4a) is given by

$$M \frac{dv}{dt} = G \cdot \sin \alpha - \sum W - F_T = G \cdot (\tan \alpha - w) - F_T, \quad (1)$$

where M is the pallet mass, in kilograms; V is the pallet speed, in metres per second; G is the force of gravity acting on the pallet, in newtons; $\sum W$ is the sum of forces resisting the pallet motion on the GFR, in newtons; F_T is the MBR breaking force, in newtons; $w = \sum \frac{W}{G \cdot \cos \alpha}$ is the equivalent coefficient of resistance to pallet motion on a GFR [18]. As the GFR slope angle is small ($\alpha = 1.7 \dots 2.8^\circ$), one can assume that $\cos \alpha \cong 1$.

In its turn, the MBR rotation can be described by the main equation of rotary dynamics relative to the point O (Fig. 4b):

$$J_{MP} \frac{d\omega_T}{dt} = \sum M_O = M_{DB} - M_{T1} - M_{T2}, \quad (2)$$

where J_{MP} is the MBR moment of inertia, in kilogram metre squared; ω_T is the MBR angular velocity, in radians per second; M_{DB} is the drive torque acting on the MBR case, in newton-metres; M_{T1} and M_{T2} are the braking torques acting on the body and nave of the eddy current brake of the MBR reduced to its body, accordingly, in newton-metres.

Assuming that the pallet motion on the MBR is in the steady state ($\frac{dV}{dt} = 0$) and the pallet speed is $V = \frac{\omega_T \cdot D_{MP}}{2}$, where D_{MP} is the MBR diameter, we get

$$\frac{dV}{dt} = \frac{d(\frac{\omega_T \cdot D_{MP}}{2})}{dt} = 0; J_{MP} \frac{d\omega_T}{dt} = 0; M_{DB} - M_{T1} - M_{T2} = 0. \quad (3)$$

Thus, the MM of the pallet movement of the MBR can be represented as follows:

$$M_{DB} = M_{T1} + M_{T2}. \quad (4)$$

As the GFR slope angle α is small, the drive torque M_{DB} acting on the MBR body is equal to

$$M \frac{dV}{dt} = 0; F_T = G(\tan \alpha - w); M_{DB} = \frac{D_{MP} \cdot G \cdot (\tan \alpha - w)}{2}. \quad (5)$$

According to a previous study [15], the following assumption can be made for calculating the sum of forces $\sum W$ resisting the pallet motion on the GFR:

- there is no sliding of the pallet on the rollers;
- the movement of the pallet on the GFR is uniform, so the forces of inertia of the carrier rollers and pallet reach zero;
- the resistance caused by the GFR surface's unevenness is local and can be omitted in the calculations.

In this case, one should only consider the friction resistance in the supports of the carrier rollers and the rolling friction resistance of the GFR carrier rollers. The calculation of these factors is thoroughly described in [19-21].

The braking torque M_{T1} acting on the MBR case is given by

$$M_{T1} = F_{BT} \cdot \frac{D_{BT}}{2}, \quad (6)$$

where F_{BT} is the braking force of the eddy current brake (in newtons); $D_{BT}/2$ is the distance from the MBR rotation axis to the centre of the permanent magnets (in metres).

The braking torque M_{T2} acting on Nave 1 of the eddy current brake of the MBR reduced to its body is given by the following expression:

$$M_{T2} = F_{BT} \cdot \frac{D_{BT}}{2} \cdot u \cdot \eta_{MP}, \quad (7)$$

where u is the gear ratio of the MBR multiplier and η_{MP} is the MBR efficiency.

By substituting Eqs (5)–(7) in Eq. (4), we get

$$\frac{D_{MP} \cdot G \cdot (\tan \alpha - w)}{2} = F_{BT} \cdot \frac{D_{BT}}{2} + F_{BT} \cdot \frac{D_{BT}}{2} \cdot u \cdot \eta_{MP}. \quad (8)$$

Given that $G = M \cdot g$ (where $g = 9.81$ m/s² is the acceleration due to gravity), the braking force of the MBR eddy current brake is given by

$$F_{BT} = \frac{D_{MP} \cdot M \cdot g \cdot (\tan \alpha - w)}{D_{BT} \cdot (1 + u \cdot \eta_{MP})}. \quad (9)$$

On the other hand, according to [16,17, 22-29] the braking force of the eddy current brake is given by

$$F_{BT} = \beta \cdot \omega_{rel} \cdot \frac{D_{BT}}{2}, \quad (10)$$

where β is the coefficient of magnetic viscosity (in newton-second per metre); ω_{rel} is the angular velocity of the copper disc relative to the permanent magnets (in units per second).

So, for the considered MBR construction (Fig. 4b), $\omega_{rel} = \omega_T + \omega_B$, where $\omega_T = \pi \cdot n_T/30$ is the angular velocity of the MBR body (units per second); n_T is the rotation speed of the MBR body (in revolutions per minute); $\omega_B = \pi \cdot n_B/30$ is the angular velocity of the eddy current brake nave (units per second); n_B is the rotation speed of the eddy current brake body (in revolutions per minute). Because of the multiplier, $n_B = u \cdot n_T$.

As there is no slip between the pallet and the MBR (based on the studies conducted in [10, 15]), the MBR body rotation speed n_T is

$$n_T = \frac{60 \cdot V}{\pi \cdot D_{MP}}. \quad (11)$$

So, ω_{rel} can be represented as follows:

$$\omega_{rel} = \frac{\pi}{30} (u \cdot n_T + n_T) = \frac{2 \cdot V}{D_{MP}} (1 + u). \quad (12)$$

By substituting Eq. (12) in Eq. (10) and equalising Eqs (9) and (10), we get a formula for calculating the speed V of pallet motion on the MBR:

$$V = \frac{D_{MP}^2 \cdot g \cdot (\tan \alpha - w)}{D_{BT}^2 \cdot \beta \cdot (1 + u \cdot \eta_{MP}) \cdot (1 + u)} M. \quad (13)$$

By analysing Eq. (13), one can see that the coefficient of magnetic viscosity β and the gear ratio u are the main parameters defining the MBR braking capacity and, consequently, the speed of the pallet motion on the MBR. However, analysis of the influence of the gear ratio u will be carried out in further studies. In the proposed paper for the developed MBR design, it is possible to change the efficiency only by changing the number of magnets and the gap, thereby changing only the coefficient of magnetic viscosity β .

4. COEFFICIENT OF MAGNETIC VISCOSITY

According to [16, 17, 22, 23], the coefficient of magnetic viscosity is given by

$$\beta_1 = \frac{\pi \cdot \sigma}{4} D^2 d B^2, \quad (14)$$

$$\beta = n \cdot \beta_1, \quad (15)$$

where β_1 is the coefficient of magnetic viscosity for one magnet; n is the number of magnets; σ is the specific conductivity of the conductive body material (copper disc, Fig. 3), in siemens per metre; B is the magnetic induction, in teslas; D is the magnet cross-sectional diameter, in metres; d is the thickness of the conducting body (copper disc), in metres.

However, Eq. (14) does not consider the influence of the air gap between the copper disc and the magnets and their relative position (edge effect) on the coefficient of magnetic viscosity β and the braking force F_{BT} .

In this case, the coefficient of magnetic viscosity β is a com-

plex indicator governed by many parameters. It is hard to establish the theoretical relationships linking these parameters, so it is hard to make a justified choice of the structural parameters of the eddy current brake of the MBR.

Because of this fact, experimental studies were conducted in [30] to determine the coefficient of magnetic viscosity for one magnet, β_1 , under the operational condition of an MBR in a GFR. The following facts about the coefficient of magnetic viscosity β_1 were established:

- The coefficient decreases if the air gap between the conductive body and permanent magnets increases, and this relationship is exponential.
- The coefficient decreases if the rotation speed of the conductive body increases.
- The coefficient is invariant with the distance between the centres of the conductive body and the permanent magnet.
- The coefficient is reduced by the "edge effect" related to the air gap.

Considering the experimental studies on the coefficient of magnetic viscosity β_1 , the MBR shown in Fig. 2 was designed to ensure high brake torque for the operational conditions characteristic for GFR. Formula (13) can be rewritten as follows:

$$V = \frac{D_{MP}^2 \cdot g \cdot (\tan \alpha - w)}{D_{BT}^2 \cdot \beta_1 \cdot n \cdot (1 + u \cdot \eta_{MP}) (1 + u)} M. \quad (16)$$

5. COMPARISON OF CALCULATED AND EXPERIMENTAL RELATIONSHIP OF THE VELOCITY OF PALLET MOVEMENT ON THE MBR

Experimental investigations of the MBR were conducted for $n = 8$ and $n = 16$ permanent magnets on an experimental stand that allows simulating real operating modes of brake rollers of various designs used in the GFR for pallets [30]. Generally, the MBR diameter D_{MP} is chosen based on the structural constraints of the GFR and the gravity rack for pallets. In practice, tubes with diameter D_{MP} of 80 mm or 89 mm and wall thickness of 3 mm are the most common. In the developed construction (Fig. 2), $D_{MP} = 89$ mm and $D_{BH} = 83$ mm, and a two-stage multiplier with a gear ratio of 24 is used based on the analysis conducted in [31]. The efficiency η_{MP} of MBR can be calculated similarly to that of the centrifugal friction roller [10, 15]. In this case, according to experimental data [30], the coefficient of magnetic viscosity is $\beta_1 = 0.113$ N s/m for the considered MBR construction (Fig. 2). Initial data for calculating the speed V of the pallet movement on MBR are shown in Tab.1.

Tab. 1. Initial data for calculating the speed V of the pallet movement on MBR

Parameter	Value	Unit
Pallet mass, M	100 ÷ 1,000	kg
MBR diameter, D_{MP}	0.089	m
MBR length, L_{MP}	0.88	m
Distance from the MBR rotation axis to the centre of permanent magnets $D_{BT}/2$	0.03	m
Coefficient of magnetic viscosity, β_1	0.113	N·s/m

Equivalent coefficient of resistance to the pallet motion on the GFR surface, w	0.02	-
GFR slope angle, $\tan \alpha$	0.04	-

GFR, gravity flow rack; MBR, magnetic brake roller.

The percentage error of the theoretical calculation is given by

$$\varepsilon = \frac{|V_{Calc} - \bar{V}_{Exp}|}{\bar{V}_{Exp}} 100, \quad (17)$$

where V_{Calc} is the calculated speed of pallet motion on the MBR, in metres per second; \bar{V}_{Exp} is the average experimentally measured value of the pallet speed, in metres per second.

The results and a comparative analysis of the obtained calculation and experimental results of the investigation of the pallet speed V of motion on the MBR are shown in Tabs 2 and 3 and Fig. 5.

Tab. 2. Results of the calculated and experimental studies of the speed V (metres per second) of the pallet movement along the MBR

Pallet mass M , kg	Number of magnets, n			
	Calculation		Experiment	
	8	16	8	16
100	0.102	0.051	0.109	0.049
200	0.204	0.102	0.220	0.096
300	0.305	0.153	0.330	0.143
400	0.407	0.204	0.473	0.195
500	0.509	0.255	0.630	0.252
600	0.611	0.305	0.795	0.308
700	-	0.356	-	0.389
800	-	0.407	-	0.480
900	-	0.458	-	0.585
1,000	-	0.509	-	0.687

MBR, magnetic brake roller

Tab. 3. Comparative analysis of the results of calculated and experimental studies of the speed V of the pallet movement along the MBR

Pallet mass M , kg	Simulation error, %	
	Number of magnets, n	
	8	16
100	7.3	3.3
200	7.7	6.2
300	7.7	6.8
400	13.9	4.4
500	19.2	1.2
600	23.1	0.8
700	-	8.5
800	-	15.2
900	-	21.6
1,000	-	25.8

MBR, magnetic brake roller

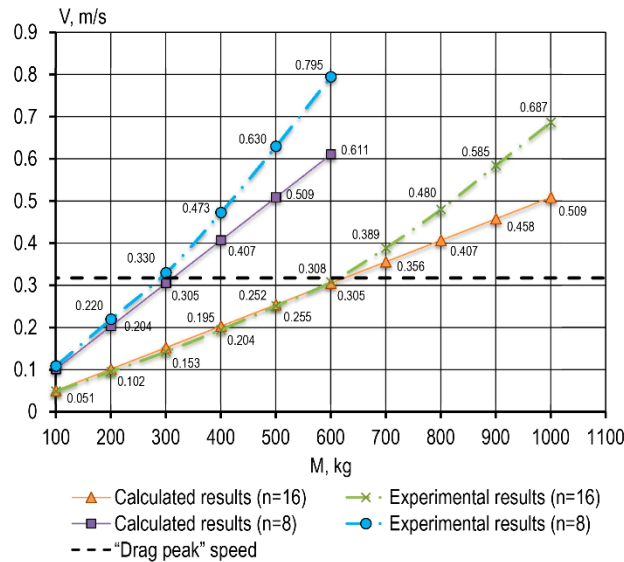


Fig. 5. Comparative analysis of the results of calculated and experimental studies of the speed V of pallet movement along the MBR with different numbers of permanent magnets n . MBR, magnetic brake roller

The comparison of experiments and calculations revealed that the error of the MM increases as the velocity of a pallet with mass M increases. The error is related to the assumption that the eddy current brake MBR is a linear viscous friction element [16, 17, 22, 23]. So, the calculated pallet speed is almost linear, as seen very well from Fig. 5. However, based on the results of multiple studies [32], one has to take into account the “drag peak” speed parameter given by the following expression:

$$\omega_{otn} = \frac{4}{\mu \cdot \sigma \cdot d \cdot D_{BT}} \quad (18)$$

where d is the thickness of the conducting body (copper disc, Fig. 3), in metres; μ is the magnetic permeability of the conductive body material, in henries per metre.

“Drag peak” speed is the angular velocity of a conducting body (copper disc) relative to permanent magnets over which the eddy currents generated on the conducting body surface do not reach their limit value, leading to reduced magnetic viscosity β and, consequently, reduced braking torque on an MBR.

By equalising Eqs. (12) and (18), we obtain a formula for calculating the pallet speed $[V]$ of motion on an MBR when the copper disc reaches the “drag peak” speed:

$$[V_{pk}] = \frac{2 \cdot D_{MP}}{\mu \cdot \sigma \cdot d \cdot D_{BT}(1+u)} \quad (19)$$

As seen from Fig. 5, the experimental velocity plots change their slope angle, while the difference between the calculated and experimental results starts increasing after the intersection with the “drag peak” speed line.

6. SUMMARY

A MM of the pallet motion on an MBR was developed.

An equation of the pallet motion on an MBR was derived.

The results of simulation and experimental studies of the pallet velocity moving on an MBR were compared. For pallet speed

less than $[V_{pk}]$, the error of the MM is $<7.7\%$, and the error starts increasing once exceeding $[V_{pk}]$.

Additional investigation of the coefficient of magnetic viscosity β_1 for speeds greater than the “drag peak” speed is required.

REFERENCES

- Derhami S, Smith JS, Gue KR. Optimising space utilisation in block stacking warehouses. *Int J Of Prod Res.* 2017; 55(21):6436-6452.
- Ghalekhondabi I, Masel DT. Storage allocation in a warehouse based on the forklifts fleet availability. *Journal Of Algorithms & Computational Technology.* 2018; 12(2):127-135.
- Heragu SS, Cai X, Krishnamurthy A, Malmberg CJ. Analytical models for analysis of automated warehouse material handling systems. *Int J Of Prod Res.* 2011; 49(22):6833-6861.
- Sulirova I, Zavodska L, Rakyta M, Pelantova V. State-of-the-art approaches to material transportation handling and warehousing. 12th International scientific conference of young scientists on sustainable modern and safe transport. *Procedia Engineering.* 2017; 192:857-862.
- Boywitz D, Boysen N. Robust storage assignment in stack- and queue-based storage systems. *Computers & Operations Research.* 2018; 100:189-200.
- Accorsi R, Baruffaldi G, Manzini R. Design and manage deep lane storage system layout. An iterative decision-support model. *Int J Adv Manuf Technol.* 2017; 92(1-4):57-67.
- Eo J, Sonico J, Su A, Wang W, Zhou C, Zhu Y, Wu S, Chokshi T. Structured comparison of pallet racks and gravity flow racks. *IIE Annual Conference and Expo.* 2015; 1971-1980.
- Wu S, Wu Ya, Wang Ya. A structured comparison study on storage racks system. *Journal of Residuals Science & Technology.* 2016; 13(8).
- Vujanac R, Miloradovic N, Vulovic S. Dynamic storage systems. *ANNALS of Faculty Engineering Hunedoara – International Journal of Engineering.* 2016; XIV:79-82.
- Safronov E, Nosko A. A Method to Determine Allowable Speed for a Unit Load in a Pallet Flow Rack. *Acta Mechanica et Automatica* 2019; 13(2):80-85.
- Safronov E, Sharifullin I, Nosko A. *Ustroystva bezopasnoy ekspluatatsii gravitatsionnykh rolikovykh konveyerov palletnogo tipa: Monografiya [Devices for safe operation of pallet type gravity roller conveyors: Monograph] Universitetskaya kniga Moscow (in Russian).* 2018.
- Kamenskaya NI, Sein VA, Zvereva MI. A Study of the Causes of Failure of Permanent Magnets from Cast Hard Magnetic Alloys *Met. Science and Heat Treatment.* 2017; 59:232-236.
- Sharifullin I, Nosko A, Safronov E. *Matematicheskaya model' protsessa dvizheniya pallyty po tormoznomu roliku magnitnogo tipa [Mathematical model of the motion pallet process on brake magnetic type roller]. The Russian Automobile and Highway Industry Journal.* 2020; 17(3):364-373 (in Russian).
- Ozolin AU, Skubov DU, Shtukin LV. *Sposoby tormozheniya padayushchego lifta s pomoshch'yu postoyannykh magnitov [Methods of braking a falling elevator with the help of permanent magnets] Nauchno-tekhnicheskkiye vedomosti Sankt-Peterburgskogo gosudarstvennogo politekhnicheskogo universiteta* 2008; 6(70):82-86 (in Russian).
- Safronov E, Nosko A. Influence of the brake lining position on the efficiency of the centrifugal friction roller. *IOP Conference Series: Materials Science and Engineering.* 2020; 709(2).
- Simeu E, Georges D. Modeling and control of an eddy current brake. *Control Engineering Practise.* 1996; 14(1):19-26.
- Ozolin AU, Skubov DU, Shtukin LV. *Issledovaniye vikhretokovogo diskovogo tormoza [Research eddy current disc brake]. Nauchno-tekhnicheskkiye vedomosti Sankt-Peterburgskogo gosudarstvennogo politekhnicheskogo universiteta.* 2009; 1(74):57-60 (in Russian).

18. Luskan' OA. Opredeleniye skorosti transportirovaniya shtuchnykh грузов na inertionnom rolikovom konveyer [Determining the speed of transportation of piece goods on an inertial roller conveyor]. Izv TulGU Pod'yemno-transportnyye mashiny i oborudovaniye. 2003; 4:84-89 (in Russian).
19. Zenkov RL, Ivashkov II, Kolobov LN. Mashiny nepreryvnogo transporta [Continuous transport machines]. Moscow (in Russian). 1997.
20. Luskan' OA. Teoreticheskiye osnovy peremeshcheniya грузов impul'snymi konveyerami [Theoretical Foundations of the Movement of Goods by Pulse Conveyors]. Saratov (in Russian). 2010.
21. Luskan' OA. Inzhenernyy raschet impul'snykh konveyerov [Engineering calculation of pulse conveyors]. Saratov (in Russian). 2011.
22. Hollowell TC, Kahl JT, Stanczak MD, Wang Y. Eddy Current Brake Design for Operation with Extreme Back-drivable Eddy Current Motor. Mechanical Engineering Undergraduates. 2010.
23. Andrew HC, Hayward V. Eddy Current Brakes for Haptic Interfaces: Design Identification and Control. IEEE/ASME Transactions on Mechatronics. 2008; 13(6):669-677.
24. Kerem K, Afzal S, Park EJ. Analytical modeling of eddy current brakes with the application of the time varying magnetic fields. Applied Mathematical Modeling. 2015; 1168-1179.
25. Kerem K, Park EJ, Afzal S. Improved braking torque generation capacity of an eddy current brake with time varying magnetic fields: A numerical study. Finite Elements in Analysis and Design. 2012; 59:66-75
26. Lee K, Park K. Modeling eddy currents with boundary conditions by using Coulomb's law and the method of images. IEEE Transactions on Magnetics. 2002; 38(2):1333-1340.
27. Heald MA. Magnetic braking: Improved theory. American Journal of Physics. 1988; 56(6):521-522.
28. Anwar S. A parametric model of an eddy current electric machine for automotive braking applications. IEEE Transactions on Control Systems Technology. 2002; 12(13):422-427.
29. Shin HJ, Choi JY, Cho HW, Jang SM. Analytical torque calculations and Experimental testing of permanent magnet Axial eddy current brake. IEEE Transactions on Magnetics. 2013; 49(7):4152-4155.
30. Sharifullin I, Nosko A, Safronov E, Kirillov D. Experimental study of eddy current braking applicable to gravity roller conveyor. Fundamental and Applied Problems of Engineering and Technology. 2020; 342(4-1):106-116.
31. Ghomri L, Sari Z. Mathematical modeling of the average retrieval time for flow-rack automated storage and retrieval systems. J Manuf Syst. 2017; 44:165-178.
32. Thompson MT. Permanent magnet electrodynamic brakes design principles and scaling laws. Online Symposium for Electrical Engineers. 2009.

Ildar Sharifullin:  <https://orcid.org/0000-0002-1930-2602>

Andrey Nosko:  <https://orcid.org/0000-0003-1382-4095>

Eugene Safronov:  <https://orcid.org/0000-0002-4250-7147>

THERMODYNAMIC CALCULATION OF A ROTARY ENGINE WITH EXTERNAL HEAT SUPPLY BASED ON THE IDEAL RALLIS CYCLE

Roman A. USENKOV[✉], Igor A. POPOV[✉], Yuri F. GORTYSHOV[✉],
Svetlana Y. KOKHANOVA[✉], Ravil A. LATYPOV[✉]

[✉]Department of Heat Engineering and Power Machinery, Kazan National Research Technical University named after A.N. Tupolev,
K. Marx Street 10, Kazan, Russia, 420111

[✉]Department of Power Engineering, "LLC Ravilmotors", Kazan, Russia

rausenkov@kai.ru, popov-igor-alex@yandex.ru, jurij.gortyshov@kai.ru, syakokhanova@kai.ru, ravilrotors@mail.ru

received 20 August 2021, revised 27 December 2021, accepted 28 December 2021

Abstract: The design and kinematic scheme of the operation of a rotary external combustion engine with offset shafts have been developed. Expressions are obtained that make it possible to calculate the values of the increasing and decreasing functions of the working volume of the hot and cold cavities with a change in the angle of rotation of the rotor. An expression is obtained for calculating the compression ratio in the cold cavity of a rotary heat engine with an external heat supply. An expression has been determined that makes it possible to calculate the total torque of a rotary external combustion engine. A comparative analysis of the torque values of a rotary heat engine with an external heat supply and a Wankel engine is carried out. An assessment of the efficiency of an external combustion engine with offset shafts is carried out. Based on the thermodynamic calculations using ideal Erickson and Rallis cycles for a rotary external combustion engine, the processes occurring inside the hot and cold cavities of a heat engine are described. The thermodynamic condition parameters at the characteristic points of the cycle are determined and expressions are obtained that determine the thermal efficiency of the ideal Erickson and Rallis cycles in relation to the considered external combustion engine. A method for calculating the ideal cycle for an external combustion engine with offset shafts is presented.

Key words: thermodynamic calculation, ideal cycle, work, heat, external combustion engine

1. INTRODUCTION

Nowadays, there is a strong demand for a heat engine with a higher thermal efficiency than that of existing power plants. Thus, this paper investigates the possibility of creating an alternative setup design, which is called a rotary external combustion engine.

The paper [1] considers Stirling piston engines with heat recovery, which operate according to the closed thermodynamic Stirling cycle, and piston heat engines with heat recovery, operating according to the Erickson open thermodynamic cycle. The design and operation of Stirling piston engines are discussed by Kruglov [2]. They are compared with existing designs of internal combustion engines. In the studies by Myshinsky and Ryzhkov-Dudonov [3] and Brodyansky [4], the principles of operation of various designs of a Stirling piston engine of external combustion are presented, and the main features of its thermodynamic cycle are considered. Campos et al. [5] consider the configuration of the Stirling engine, consisting of two cylinders, a regenerator and a sliding disk drive mechanism.

The paper presents a mathematical model that combines fundamental and empirical correlations. The feasibility of the Stirling engine operation using any external heat source is considered in Chen Duan et al. [6].

The results of studying the Stirling engine using three different methods, including the non-ideal adiabatic method, are presented in Toghyani et al. [7].

As shown in the literature [1–7], currently, the thermal efficien-

cy of piston-type heat engines with an internal heat supply has reached its limit (50–60%). Achieving a higher thermal efficiency is not possible due to the large amount of heat loss in a running engine.

The analysis of literary sources described above made it possible to draw the following conclusions:

- there is a need to create an alternative power plant, such as an external combustion engine;
- the existing designs of external combustion piston engines with a crank mechanism are very cumbersome and involve significant losses of mechanical energy; and
- new design options for external combustion engines are needed, such as a rotary heat engine.

In Khafizov et al. [8], the design of a rotary external combustion engine is presented; its operation is described using the ideal Stirling cycle.

In the Ali Shufat et al. [9], an analytical simulation of a beta-type Stirling engine powered by solar energy was carried out, as well as a simulation study based on the model equations. Pressure, power and engine speed were considered as the main parameters.

In Paul and Hoffmann [10], a method is presented for optimising the trajectories of pistons in an operating model of a Stirling engine and a comparison is made between the optimised trajectories of piston movement and harmonic trajectories to increase power and efficiency.

Hasanah et al. [11] investigate the influence of the distance to

the power crank of the Stirling engine on the angular speed of rotation of the wheels and the amount of generated electrical energy.

In Sirsath et al. [12], the influence of the temperature difference between the heat source and the radiator on the efficiency of three types of Stirling engines was established. It is shown that an increase in the temperature difference increases the efficiency of the engine.

In the study by Ladas and Ibrahim [13], a thermodynamic analysis of the cycle of a Stirling engine for a finite time is given, based on differential equations for the balance of mass and energy with the corresponding equations for the rate of heat transfer. The influence of the time of contact with the heating agent and regeneration on the output power and the efficiency of the Stirling engine is established.

In the study by Jana and Marekb [14], a mathematical model of time discretisation is presented, assuming that the cylinders are adiabatic spaces. The model makes it possible to optimise the dimensions of the main elements of the Stirling engine, such as heat exchanger, regenerator and cylinder and piston.

In Zhao et al. [15], a 3D simulation of fluid dynamics and heat transfer in an improved free piston Stirling engine was carried out. The turbulence model with improved wall treatment provides reasonable accuracy and stable convergence.

Podešva and Poruba [16] consider three types of mechanisms that analyse the movements of the piston and their behaviour. Special attention is given to the piston movement mode.

García et al. [17] compares the simulation results obtained on the basis of various thermodynamic models of Stirling engines, including the characteristics of both instantaneous and specified operating parameters.

Toghyani et al. [18] present the results of studies of the Stirling engine using three different methods, including the use of the non-ideal adiabatic method. The applied methods were compared, and the best results obtained were compared for similarity with the method of making decisions about the ideal solution.

The ideal Stirling and Erickson cycles are special cases of the ideal Rallis cycle, and therefore this cycle can also be used to describe the operation of a rotary heat engine with an external heat supply.

Currently, there is a problem of increasing the specific power of existing heat engines. To solve this problem, it is necessary to develop a new power plant, i.e. a rotary engine of external continuous combustion. Patents for one such plant are available in the literature [19, 20]. Stirling, Erickson and Rallis cycles can be used to describe the operation of a rotary external combustion engine. It should be noted that until now there has been no single methodology for the mathematical calculation of the mentioned cycles to describe the operation of heat engines.

There is a small number of studies that describe the operation of heat engines, which are based on the Rallis thermodynamic cycle. A patent describing one such heat engine is available in the literature [21].

The purpose of the study is a thermodynamic calculation of the ideal Rallis cycle, which quite accurately describes the thermal processes occurring in an external combustion engine.

2. DESCRIPTION OF THE HEAT ENGINE

Patents are available in the literature showing one of the options for a rotary external combustion engine [19, 20]. The dia-

gram of the heat engine is shown in Fig. 1.

The technical result is achieved due to the fact that a rotary external combustion engine contains a stator and a profiled rotor installed in it with the formation of cold 2 and hot 1 working cavities of variable volume 3. The rotor has a constant length of the largest section (a chord) in its various positions on two supporting working motor shafts.

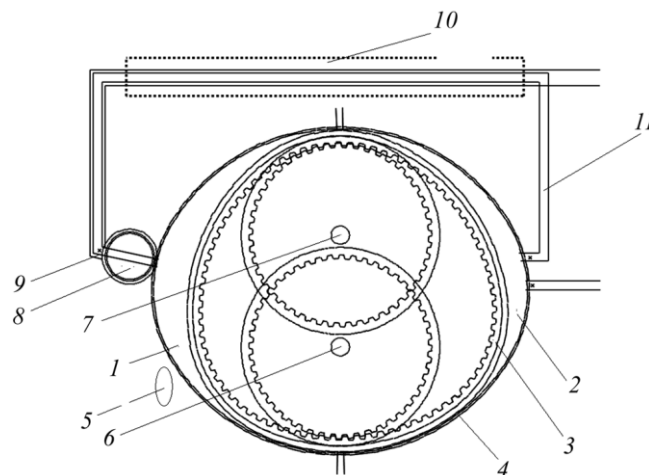


Fig. 1. Diagram of a rotary heat engine with an external heat supply: 1 is the hot cavity; 2 is the cold cavity; 3 is the rotor; 4 is the case; 5 is the external heat source; 6 is the first power take-off shaft; 7 is the second power take-off shaft; 8 is spool valve; 9 is the bypass pipelines; 10 is the recuperative heat exchanger; 11 is the inlet pipeline

The cold cavity is provided with inlet openings communicated with the inlet pipelines 11, as well as outlet openings that are communicated with the inlet openings of the hot cavity by the bypass pipelines 9.

The hot cavity is also provided with outlet openings connected with the exhaust pipelines, and the exhaust and bypass pipelines are located in the recuperative heat exchanger 10 with the possibility of transferring heat from the heated outlet pipelines of the next portion of the working fluid in the bypass pipelines.

The engine contains a spool cylindrical body 8, which is connected kinematically with the working shafts of the rotor and containing a gas distribution shaft, where, through radial bypass and outlet, openings are made to facilitate the possibility of connecting the bypass pipelines with the inlet openings of the hot cavity through bypass channels, as well as of connecting the hot cavity with the exhaust pipelines using outlet channels. In this case, the spool member 8 is installed with the possibility of connection between the holes and the pipelines during its rotation, synchronised with the rotation of the working rotor shafts 6 and 7, in the corresponding angular position of the rotor 3 relative to the stator.

Before entering the hot cavity, self-acting valves are installed with the ability to prevent the bypass of the working fluid from the hot cavity into the bypass pipeline.

The spool body 8 can be located around the hot cavity of the engine. The camshaft of the spool valve and the supporting rotor shafts are located in parallel. The spool valve shaft is connected to the rotor shafts with the ability to change its angular position relative to the angular position of the rotor shaft, depending on the engine operating mode.

Self-acting valves can be installed directly in the gas distribution shaft of the spool valve or in the bypass line in front of the

spool valve.

The design of the presented heat engine can be characterised as a rotary planetary engine with an external heat supply. This engine has hot 1 and cold 2 cavities of variable volume, which are formed by the working surfaces of the rotor 3 and the case 4. In these cavities, thermodynamic processes are implemented forming a direct Rallis cycle.

Air is supplied to the cold cavity through the inlet pipeline 11, and the air is removed from the hot cavity into the environment through the exhaust pipeline. Also, the air gives up its heat to the working fluid in the recuperative heat exchanger 10.

The working fluid (a portion of air) enters the cold cavity 2 through the inlet pipeline 11 and the inlet hole. Next, inside the cold cavity 2, due to the rotation of the rotor 3, the working fluid is compressed with the removal of heat from heated air through the wall of the case into the environment. Then a portion of air from the cold cavity enters the pipeline connecting the two cavities. The working fluid receives heat from the air leaving the hot cavity inside the recuperative heat exchanger 10.

In the hot cavity, the working fluid expands due to the supply of heat through the wall of the engine case from an external heat source. In this case, a certain torque is imparted to the rotor, due to which the air moves through the exhaust pipe from the hot cavity to the recuperative heat exchanger, and then is expelled into the environment. In this case, along the route, the air relinquishes its heat to the working fluid moving from the cold cavity 2 to the hot cavity 1 in the recuperative heat exchanger. Due to the rotation of the rotor 3, two power take-off shafts acquire a certain torque. Next, the processes taking place inside the engine are repeated.

The kinematic scheme of a rotary engine with an external heat supply is shown in Fig. 2.

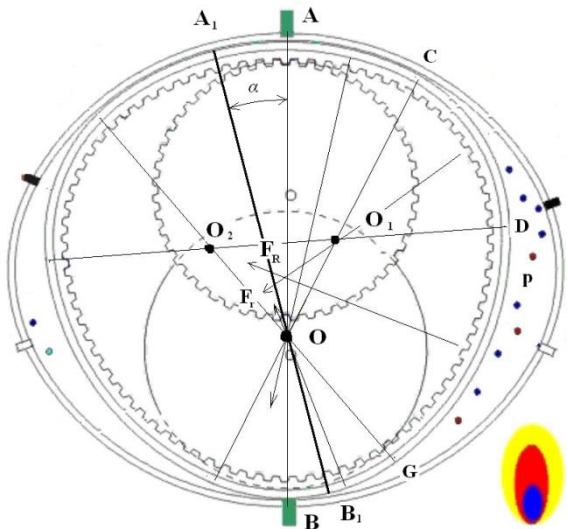


Fig. 2. Kinematic and dynamic analysis of the operation of a rotary heat engine with an external heat supply

The analysis of the diagram (Fig. 2) allows us to conclude that the instantaneous centre of rotation O , which coincides at the initial moment of time with one of the centres of curvature of the regular polycircle, is motionless during the stroke of changing the working volume and is located on the diametrical line AB . A line connects the points of contact of the rotor with the radial seal plates.

The full stroke of the rotary heat engine is carried out when the angle of rotation of the rotor changes from 0 to $\frac{\pi}{k}$ (where k is the number of “angles” of the polycircle).

In this case, the volumes of the hot and cold cavities change synchronously, continuously and monotonously in antiphase. If the working volume of the hot cavity increases from the minimum value V_{min} to the maximum value V_{max} , then the working volume of the cold cavity decreases from the maximum value V_{max} to the minimum value V_{min} . In the next cycle, the nature of the change in the working volumes in the cold and hot cavities is reversed.

At the end of the stroke, the instantaneous centre of rotation of the rotor abruptly moves along the diametrical line AB to the opposite position located at a distance r from the point A .

Thus, in the developed heat engine, there is a change in the position of the instantaneous axis of rotation of the rotor. In this case, the working contours of the rotor are regular polycircles.

From Fig. 2 it follows that the increment in the area of the contour of the working cavity between the points of contact of the rotor with the radial sealing plates when the rotor is turned through an angle α is equal to the difference in the surface areas of the sectors A_1OA and B_1OB .

Expressions were obtained that make it possible to calculate the values of the increasing V_1 and decreasing V_2 functions of the working volume of the hot and cold cavities when changing the angle α from 0 to $\frac{\pi}{k}$:

$$V_1 = H(R^2 - r^2)\frac{\alpha}{2}, \tag{1}$$

$$V_2 = H(R^2 - r^2)\frac{\frac{\pi}{k} - \alpha}{2}, \tag{2}$$

where: H is rotor width or distance between closing end planes; R is the radius of the large segment of the outer envelope of the rotor; r is the radius of the smaller segment of the outer envelope of the rotor; and k is the number of “angles” of the polycircle.

An expression was determined that allows calculating the working volumes of the hot and cold cavities depending on the change in the angle of rotation of the rotor:

$$V_{max} = V_{min} + H(R^2 - r^2)\frac{\pi}{2k}. \tag{3}$$

A relation was obtained for calculating the compression ratio in the cavity of a rotary heat engine with an external heat supply:

$$\varepsilon = 1 + \frac{H(R^2 + r^2)\pi}{2kV_{min}}. \tag{4}$$

The number of strokes per one complete revolution of the rotor j is determined by the angular length $\frac{\pi}{k}$ of one stroke and the number of working cavities in a rotary heat machine:

$$j = 6k, \tag{5}$$

where k is the number of “angles” of the polycircle.

With the number of “angles” of the polycircle of $k = 3$, the number of strokes per one complete revolution of the rotor is $j = 18$. Thus, during one complete revolution of the rotor shaft, 18 strokes occur in the hot and cold cavities of a rotary heat machine with an external heat supply, or in fact 18 thermodynamic processes are implemented.

From Fig. 2 it follows that the value M_1 of the rotor torque relative to the centre of rotation O is equal to the sum of the two values of the torques M_R and M_r , generated by the forces F_R and F_r , respectively. The resulting action of the forces determines the magnitude of the pressure p with which the working fluid acts on

the corresponding sections of the working cylindrical surface of the rotor, limited by the generators at the points C, D and G .

The action of the force F_R is directed along the bisector of the angle GO_2D :

$$|F_R| = pH |DG| = pHR \frac{\pi}{3}. \quad (6)$$

Let us determine the ratio for calculating the arm of the force F_R relative to the centre of rotation O and obtain an expression for determining the magnitude of the torque M_R :

$$\frac{OO_1}{2} = \frac{R-r}{2} \Rightarrow M_R = pH(R-r) \frac{\pi R}{6}. \quad (7)$$

The force F_r is directed along the bisector of the angle CO_1D :

$$|F_r| = pH |CD| = pHr \frac{\pi}{3}. \quad (8)$$

Let us determine the ratio for calculating the arm of the force F_r and obtain an expression for determining the magnitude of the torque M_r :

$$\frac{OO_2}{2} = \frac{R-r}{2} \Rightarrow M_r = pH(R-r) \frac{\pi r}{6}. \quad (9)$$

It should be noted that the torques $M_{AC} = M_{BG} = 0$, since the direction of action of the resulting forces F_{AC} and F_{BG} pass through the centre of rotation O .

Let us determine the total torque of a rotary heat machine with an external heat supply

$$M_1 = M_R + M_r = pH(R^2 - r^2) \frac{\pi}{6} = p(V_{max} - V_{min}) = pV, \quad (10)$$

where H is the rotor width or distance between closing end planes; R is the radius of the large segment of the outer envelope of the rotor; r is the radius of the smaller segment of the outer envelope of the rotor; and p is the value of pressure with which the working fluid acts on the corresponding sections of the working cylindrical surface of the rotor.

We present the results of a comparative analysis of the torque values of a rotary heat engine with an external heat supply M_1 and a Wankel engine M_2 .

Let us assume that the initial conditions for the generation of the working fluid, the working volumes $V = V_{max} - V_{min}$, and the dynamics of the pressure change p for the two compared engines are identical.

For a Wankel engine with a triangular rotor, the working volume V is determined as:

$$V = \sqrt{3}arH = \sqrt{3}nRH, \quad (11)$$

where R is the radius of the rolling circle in the procedure for synthesising the epitrochoid of the stator working contour; r is the radius of the circle being rolled in the procedure for synthesising the epitrochoid of the stator working contour; H is the width of the rotor along the generatrix of the cylinder; $a = c \cdot R$ is the producing radius of the epitrochoid of the stator working contour; and c is the coefficient of elongation of the epitrochoid of the stator working contour.

Thus, the torque of the Wankel engine will be determined as:

$$M_2 = p\sqrt{3}arH |\sin 2\psi| = p\sqrt{3}nRH |\sin 2\psi| = p\sqrt{3}V \left(\frac{r}{R}\right) |\sin 2\psi|, \quad (12)$$

where ψ is the angle between the line of action of the resulting driving force of the working fluid pressure and the crank of the eccentric shaft.

To carry out a comparative analysis of the values of the tor-

ques M_1 and M_2 for the two engines, it is necessary to fix the values of the simplex $\frac{r}{R}$, as well as the value $\sin 2\psi$.

Supposing that $\frac{r}{R} = \frac{2}{3}$, and the value $\sin 2\psi = \frac{1}{2}$, then the expression in Eq. (12) will take the following form:

$$M_2 = \frac{2\sqrt{3}}{3} \cdot \frac{1}{2} \cdot pV = 0.577pV. \quad (13)$$

To compare the values of the torque of a rotary heat engine with an external heat supply M_1 and a Wankel engine M_2 , we divide the expression in Eq. (10) by the relation in Eq. (13) and obtain:

$$\frac{M_1}{M_2} = \frac{pV}{0.577pV} = 1.73. \quad (14)$$

Thus, the torque of the proposed rotary heat engine with an external heat supply is 1.73 times higher than the torque of the Wankel engine.

The originality of the design of the proposed rotary heat machine with an external heat supply lies in the fact that the rotor moves not on gears, but on solid roller wheels.

The roller wheels are installed in parallel to the gears and roll on the smooth inner surface of the rotor with less friction than the gear transmission. Moreover, the radius of the roller wheels and the gears is less than the radius of the small segment of the rotor gear rim, as a result of which, when the instantaneous axis of rotation of the rotor is changed, a complete "head-on" blow of the small segment against the gears does not occur, and the transfer of the rotor torque to the shafts will be quite smooth.

For the supply and removal of the working body in a rotary heat engine with external fuel combustion, there are inlet and outlet pipelines. On the inner surface of the profiled rotor, shaped as a curved figure, there is a gear rim and a synchronisation mechanism made in the form of gears mounted on two shafts with the possibility of their interaction with the gear rim of the rotor.

The rotary heat engine is equipped with round roller wheels, and the rotor itself contains smooth grooves for them on the inner surface, with the support of which the rotor rolls inside the case with the least friction. Roller wheels have a smaller radius than the one of the inner envelope of the small segment of the rotor, and they can be installed symmetrically to the gears on both shafts or on their axle shafts attached to the end walls of the rotary heat engine.

The gears contain at least one tooth less than six times the number of teeth on the small rotor segment. For permanent engagement of the gears with the rotor gear rim, both shafts are parallelly displaced in opposite directions.

When the position of the rotor changes inside the case, the volumes of the hot cavity and the cold cavity change. The outer and inner envelopes of the rotor have a profile, which is formed by three pairs of opposite large and small segments (sectors of 60°) of circles with centres at the vertices of an equilateral triangle.

Such a profile of the outer and inner envelope, when the rotor moves inside the case, ensures the immobility of the compression plates, which are made of fluoroplastic, and creates a constant engagement of the gear rim with two gears of the power take-off shafts.

3. THERMODYNAMIC ANALYSIS

In the presented article, a specific thermodynamic cycle is determined, which most accurately describes the processes occurring inside a rotary engine with an external heat supply. For this, a

thermodynamic analysis of the processes occurring inside the heat engine was carried out using the Erickson and Rallis ideal cycles.

When carrying out thermodynamic analysis, it is assumed that thermodynamic cycles are reversible and closed and that the working body is 1 kg of ideal gas.

Let us carry out a thermodynamic analysis of the operation of a rotary heat engine using the Erickson ideal cycle. It consists of two isotherms and two isobars (Fig. 3).

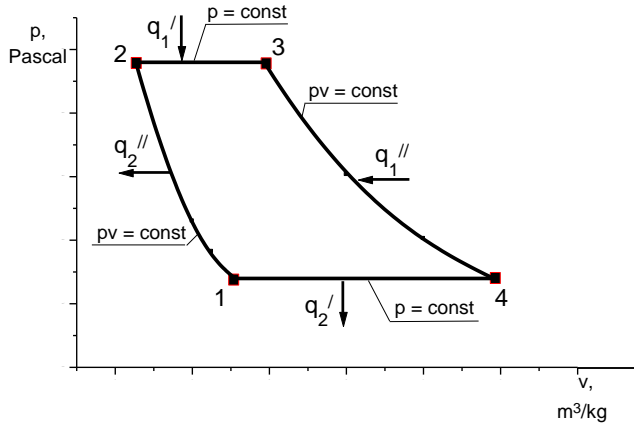


Fig. 3. Diagram of the ideal Erickson cycle in p, v – coordinates

An ideal gas with initial parameters p_1, v_1 and T_2 is compressed along the isotherm 1 – 2 to point 2 with heat removal of $q_2'' = RT_2 \ln \frac{v_1}{v_2}$ to a cold source. The isobar 2 – 3 imparts the amount of heat of $q_1' = c_p(T_1 - T_2)$ from an external hot source to the working fluid. From the point 3, the working fluid expands along the isotherm 3 – 4 with the heat supply of $q_1'' = RT_1 \ln \frac{v_4}{v_3} = RT_1 \ln \frac{v_1}{v_2}$ from an external hot source. Finally, along the isobar 4 – 1, the working fluid returns to its original state, while the amount of heat of $q_2' = c_p(T_1 - T_2)$ is removed to the cold source.

The characteristics of the cycle are compression ratio $\varepsilon = \frac{v_1}{v_2}$, and preliminary expansion ratio $\rho = \frac{v_3}{v_2}$.

Let us determine the parameters of the working fluid at all characteristic points of the Erickson cycle:

at point 1:

- pressure p_1 is given;
- absolute temperature T_2 is given;
- specific volume v_1 :

$$v_1 = \frac{RT_2}{p_1}, \quad (15)$$

at point 2:

- specific volume v_2 :

$$\varepsilon = \frac{v_1}{v_2} \Rightarrow v_2 = \frac{v_1}{\varepsilon}, \quad (16)$$

- absolute temperature T_2 is known and does not change, since the process 1 – 2 is isothermal;
- pressure p_2 :

$$p_2 v_2 = RT_2 \Rightarrow p_2 = \frac{RT_2}{v_2}, \quad (17)$$

at point 3:

- pressure $p_3 = p_2$, since the process 2 – 3 is isobaric;

- specific volume v_3 :

$$\frac{v_3}{v_2} = \rho \Rightarrow v_3 = v_2 \rho = \frac{v_1}{\varepsilon} \rho; \quad (18)$$

- absolute temperature T_1 :

$$p_3 v_3 = RT_1 \Rightarrow T_1 = \frac{p_3 v_3}{R}, \quad (19)$$

at point 4:

- absolute temperature T_1 is known and does not change, since the process 3 – 4 is isothermal;

- pressure $p_4 = p_1$, since the process 4 – 1 is isobaric;

- specific volume v_4 :

$$p_1 v_4 = RT_1 \Rightarrow v_4 = \frac{RT_1}{p_1}. \quad (20)$$

The expression that determines the thermal efficiency of the Erickson cycle takes on the following appearance:

$$\eta_t = 1 - \frac{q_2}{q_1} = 1 - \frac{c_p(T_1 - T_2) + RT_2 \ln \frac{v_1}{v_2}}{c_p(T_1 - T_2) + RT_1 \ln \frac{v_4}{v_3}}. \quad (21)$$

The presented algorithm made it possible to thermodynamically calculate the ideal cycle of a rotary heat engine with external fuel combustion in accordance with the following technical specifications: for the ideal Erickson cycle, the thermodynamic condition parameters p_i, v_i and T_i are determined at all characteristic points of the cycle, together with considering the specific supplied q_1 and removed q_2 heat, thermal efficiency of the cycle η_t and construction of this cycle in p, v – coordinates, given that the pressure is set at $p_1 = 1.7 \cdot 10^5$ Pa, the absolute temperature is $T_2 = 300$ K, the compression ratio is $\varepsilon = \frac{v_1}{v_2} = 2$ and the preliminary expansion ratio is $\rho = \frac{v_3}{v_2} = 2.34$. The working fluid is air with the gas constant of $R = 287 \frac{J}{kg \cdot K}$. We assume the heat capacity of the working fluid constant: $c_p = 1010 \frac{J}{kg \cdot K}, c_v = 721 \frac{J}{kg \cdot K}$.

The results of the calculation are presented in Tab. 1.

Tab. 1. Thermodynamic condition parameters of the ideal Erickson cycle

Condition parameters	Point 1	Point 2	Point 3	Point 4
p_i, Pa	$1.7 \cdot 10^5$	$3.4 \cdot 10^5$	$3.4 \cdot 10^5$	$1.7 \cdot 10^5$
$v_i, m^3/kg$	0.506	0.253	0.592	1.185
T_i, K	300	300	701.9	701.9

Supplied specific heat, $q_1, J/kg$:

$$q_1 = q_1' + q_1'' = c_p(T_1 - T_2) + RT_1 \ln \frac{v_4}{v_3} = 1010 \cdot (701.9 - 300) + 287 \cdot 701.9 \ln \frac{1.185}{0.592} = 5.45 \cdot 10^5 \frac{J}{kg}$$

Removed specific heat, $q_2, J/kg$:

$$q_2 = q_2' + q_2'' = c_p(T_1 - T_2) + RT_2 \ln \frac{v_1}{v_2} = 1010 \cdot (701.9 - 300) + 287 \cdot 300 \ln \frac{0.506}{0.253} = 4.65 \cdot 10^5 \frac{J}{kg}$$

Useful specific heat $q, J/kg$:

$$q = q_1 - q_2 = 8 \cdot 10^4 \frac{J}{kg}$$

Thermal efficiency of the Erickson cycle:

$$\eta_t = \frac{q_1 - q_2}{q_1} \cdot 100 \% = 14.7 \%$$

The efficiency of any engine can be assessed using the thermal efficiency of the direct Carnot cycle.

The efficiency of any engine can be assessed using the thermal efficiency of the direct Carnot cycle.

$$\eta_t = \frac{T_1 - T_2}{T_1} \cdot 100 \% = \frac{701.9 - 300}{701.9} \cdot 100 \% = 57.25 \%$$

We now proceed to represent this cycle as a graph using points in the p, v -coordinates (Fig. 4).

As a result, the overall thermal efficiency of an engine with an external heat supply operating according to the ideal Erickson cycle for one full rotor revolution will be 44.1 %.

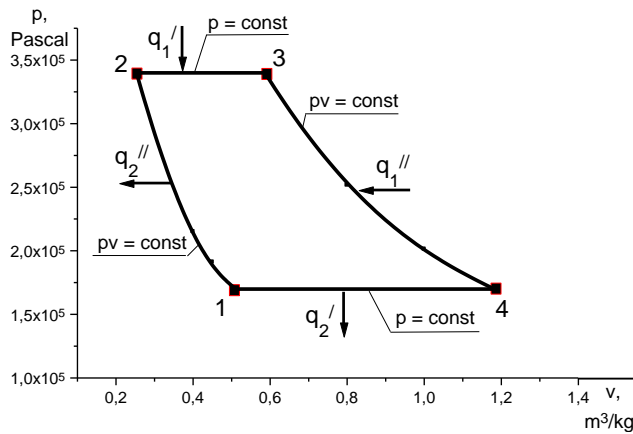


Fig. 4. Results of calculating the ideal Erickson cycle in p, v -coordinates

We then carry out a thermodynamic analysis of the heat engine operation using the ideal Rallis cycle. It consists of two isotherms, two isochores and two isobars (Fig. 5).

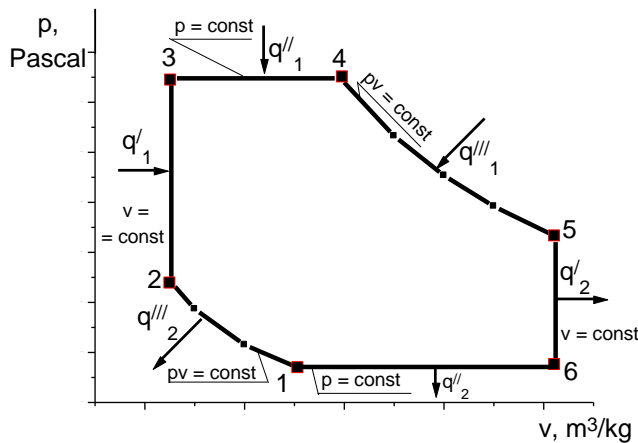


Fig. 5. Diagram of the ideal Rallis cycle in p, v -coordinates

The presented p, v -diagram of the ideal Rallis cycle allows one to determine the thermodynamic condition parameters at all reference points of the presented direct cycle.

An ideal gas with initial parameters p_1, v_1 and T_2 is compressed along the isotherm 1 – 2 to point 2 with heat removal of $q_2''' = RT_2 \ln \frac{v_1}{v_2}$ to a cold source. The isochor 2 – 3 imparts the amount of heat of $q_1' = c_v(T_3 - T_2)$ from exhaust gases in a recuperative heat exchanger to the working fluid. The isobar 3 – 4

imparts the amount of heat of $q_1'' = c_p(T_1 - T_3)$ from an external hot source to the working fluid. From the point 4, the working fluid expands along the isotherm 4 – 5 with the heat supply of $q_1''' = RT_1 \ln \frac{v_5}{v_4}$ from an external hot source. Along the isochore 5 – 6, the working fluid moves to the point 6 and at the same time the amount of heat of $q_2' = c_v(T_1 - T_6)$ is removed from the exhaust gases to the working fluid in the recuperative heat exchanger. Finally, along the isobar 6 – 1, the working fluid returns to its original state, while the amount of heat of $q_2'' = c_p(T_6 - T_2)$ is removed to the cold source.

The characteristics of the cycle are compression ratio $\varepsilon = \frac{v_1}{v_2}$, pressurisation ratio $\lambda = \frac{p_3}{p_2}$, preliminary expansion ratio $\rho = \frac{v_4}{v_3}$, and expansion ratio $\sigma = \frac{v_5}{v_4}$.

Let us determine the parameters of the working fluid at all characteristic points of the Rallis cycle:

at point 1:

- pressure p_1 is given;
- absolute temperature T_2 is given;
- specific volume v_1 :

$$v_1 = \frac{RT_2}{p_1}, \tag{22}$$

at point 2:

- specific volume v_2 :

$$\varepsilon = \frac{v_1}{v_2} \Rightarrow v_2 = \frac{v_1}{\varepsilon}, \tag{23}$$

- absolute temperature T_2 is known and does not change, since the process 1 – 2 is isothermal;

- pressure p_2 :

$$p_2 v_2 = RT_2 \Rightarrow p_2 = \frac{RT_2}{v_2}, \tag{24}$$

at point 3:

- specific volume v_3 equals $v_3 = v_2 = \frac{v_1}{\varepsilon}$, since the process 2 – 3 is isochoric;
- pressure p_3 :

$$\frac{p_3}{p_2} = \lambda \Rightarrow p_3 = p_2 \lambda; \tag{25}$$

- absolute temperature T_3 :

$$p_3 v_2 = RT_3 \Rightarrow T_3 = \frac{p_3 v_2}{R}; \tag{26}$$

at point 4:

- pressure $p_4 = p_3$, since the process 3 – 4 is isobaric;
- specific volume v_4 :

$$\frac{v_4}{v_3} = \rho \Rightarrow v_4 = v_3 \rho; \tag{27}$$

- absolute temperature T_1 :

$$p_3 v_4 = RT_1 \Rightarrow T_1 = \frac{p_3 v_4}{R}; \tag{28}$$

at point 5:

- absolute temperature T_1 is known and does not change, since the process 4 – 5 is isothermal;
- specific volume v_5 :

$$\frac{v_5}{v_4} = \sigma \Rightarrow v_5 = v_4 \sigma; \tag{29}$$

- pressure p_5 :

$$p_5 v_5 = RT_1 \Rightarrow p_5 = \frac{RT_1}{v_5}, \tag{30}$$

at point 6:

- pressure $p_6=p_1$, since the process 6 – 1 is isobaric;
- absolute temperature T_6 :

$$\frac{p_5}{p_1} = \frac{T_1}{T_6} \Rightarrow T_6 = \frac{p_1 T_1}{p_5} \quad (31)$$

- specific volume $v_6=v_5$, since the process 5 – 6 is isochoric.

The expression that determines the thermal efficiency of the Rallis cycle assumes the following form:

$$\eta_t = 1 - \frac{q_2}{q_1} = 1 - \frac{c_v(T_1-T_6)+c_p(T_6-T_2)+RT_2 \ln \frac{v_3}{v_2}}{c_v(T_3-T_2)+c_p(T_1-T_3)+RT_1 \ln \frac{v_5}{v_4}} \quad (32)$$

The presented algorithm made it possible to thermodynamically calculate the ideal cycle of a rotary heat engine with external fuel combustion in accordance with the technical task: for the ideal Rallis cycle, we determine the thermodynamic condition parameters p_i , v_i and T_i at all characteristic points of the cycle, the specific supplied q_1 and removed q_2 heat and thermal efficiency of the cycle η_t , and construct this cycle in p, v – coordinates, if the pressure is set at $p_1=1.7 \cdot 10^5$ Pa, the absolute temperature is $T_2 = 300$ K, the compression ratio is $\varepsilon = \frac{v_1}{v_2} = 2$, the pressurisation ratio is $\lambda = \frac{p_3}{p_2} = 2.2$, the preliminary expansion ratio is $\rho = \frac{v_4}{v_3} = 2.34$ and the expansion ratio is $\sigma = \frac{v_5}{v_4} = 1.73$. The working fluid is air with the gas constant of $R = 287 \frac{J}{kg \cdot K}$. We assume the heat capacity of the working fluid constant: $c_p = 1010 \frac{J}{kg \cdot K}$, $c_v = 721 \frac{J}{kg \cdot K}$. The results of the calculation are presented in Tab. 2.

Tab. 2. Thermodynamic condition parameters of the ideal Rallis cycle

Condition parameters	Point 1	Point 2	Point 3	Point 4	Point 5	Point 6
p_i , Pa	$1.7 \cdot 10^5$	$3.4 \cdot 10^5$	$7.5 \cdot 10^5$	$7.5 \cdot 10^5$	$4 \cdot 10^5$	$1.7 \cdot 10^5$
v_i , m^3/kg	0.506	0.253	0.253	0.592	1.024	1.024
T_i , K	300	300	659.9	1544	1544	606.5

Supplied specific heat, q_1 , J/kg:

$$\begin{aligned} q_1 &= q'_1 + q''_1 + q'''_1 = c_v(T_3 - T_2) + c_p(T_1 - T_3) + RT_1 \ln \frac{v_5}{v_4} \\ &= 721 \cdot (659.9 - 300) + 1010 \cdot (1544.3 - 659.9) + 287 \\ &\quad \cdot 1544.3 \ln \frac{1.024}{0.592} = 1.39 \cdot 10^6 \frac{J}{kg} \end{aligned}$$

Removed specific heat, q_2 , J/kg:

$$\begin{aligned} q_2 &= q'_2 + q''_2 + q'''_2 = c_v(T_1 - T_6) + c_p(T_6 - T_2) + RT_2 \ln \frac{v_1}{v_2} \\ &= 721 \cdot (1544.3 - 606.5) + 1010 \cdot (606.5 - 300) + 287 \cdot 300 \ln \frac{0.506}{0.253} = 1.04 \cdot 10^6 \frac{J}{kg} \end{aligned}$$

Useful specific heat q , J/kg:

$$q = q_1 - q_2 = 3.5 \cdot 10^5 \frac{J}{kg}$$

Thermal efficiency of the Rallis cycle:

$$\eta_t = \frac{q_1 - q_2}{q_1} \cdot 100 \% = 25 \%$$

The efficiency of any engine can be assessed using the thermal efficiency of the direct Carnot cycle.

$$\eta_t = \frac{T_{max} - T_{min}}{T_{max}} \cdot 100 \% = \frac{1544.3 - 300}{1544.3} \cdot 100 \% = 80.57 \%$$

We make a graph of this cycle by points in p, v – coordinates (Fig. 6).

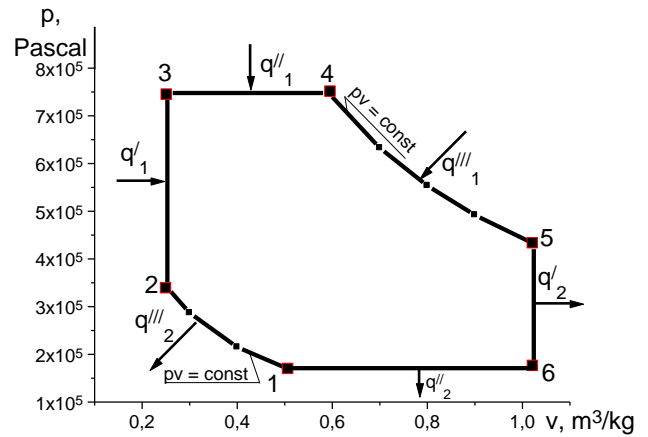


Fig. 6. Results of calculating the ideal Rallis cycle in p, v – coordinates

Thus, the overall thermal efficiency of an engine with an external heat supply operating according to the ideal Rallis cycle for one full rotor revolution will be 75%. The closer the thermal efficiency of the power plant is to the thermal efficiency of the direct Carnot cycle, the more perfect the power plant. An analysis of thermodynamic processes occurring inside a rotary heat engine with external heat supply made it possible to establish that the cycle that most accurately describes its work is the ideal Rallis cycle.

It should be noted that the ideal Stirling and Erickson cycles are special cases of the ideal Rallis cycle.

4. DISCUSSION

The Rallis cycle is designed to work only with a gaseous working fluid. In order for the dimensions of the engines at a given power to be acceptable, and the external and internal heat exchange of the working fluid under these conditions to be efficient enough, the pressure in the heat engine must be significantly higher than the atmospheric pressure. In this case, the working fluid must have a low viscosity and the highest possible thermal conductivity.

The conducted thermodynamic analysis showed that this cycle is a direct cycle, as a result of which heat turns into work. The advantage of this cycle is the fact that it allows operation in a wide temperature range of hot and cold sources at relatively small values of the ratio of the compression and expansion pressures.

5. CONCLUSION

The proposed rotary heat engine with external heat supply will facilitate:

- a reduction in the dimensions and weight of the power plant due to the small number of interacting units; and
 - an increase in the efficiency of the engine by reducing the friction of the rotor against the case and shaft gears.
- The use of solid roller wheels will facilitate:
- an increase in the specific power of the rotary external combustion engine; and
 - an increase in the performance of the power unit due to the possibility of using the power plant at increased rotor speed.

To reduce the forces of inertia and ensure constant meshing of the gears with the rotor gear rim, both shafts are displaced in opposite directions. The design feature of the presented power plant is the ability to replace two power take-off shafts without dismantling the rotor.

The carried out thermodynamic calculation made it possible to determine the main condition parameters at the characteristic points of the ideal Rallis cycle and to describe the operation of a heat engine with external combustion of fuel fairly accurately. The overall thermal efficiency of the power plant for one full revolution of the rotor was 75%, which indicates the possibility of using this engine as a power plant for driving motor vehicles.

The practical significance of the proposed rotary heat engine with an external heat supply lies in the fact that it can be used not only to obtain mechanical and electrical energy but also to generate heat energy in heaters in air heating systems and forced ventilation systems with mechanical air induction. Maintaining permissible microclimate conditions in the working area of large buildings can be ensured using the proposed heat engine.

REFERENCES

1. Walker G. Stirling cycle machines. Moscow: Energy; 1978. (In Russ.).
2. Kruglov MG. Stirling Engines. Moscow: Machinery engineering; 1977. 150. (In Russ.).
3. Myshinsky EL., Ryzhkov-Dudonov M.A. Marine piston external combustion engines (Stirling engines). Leningrad: Shipbuilding; 1976. 76. (In Russ.).
4. Brodyansky VM. Stirling Engines: Collection of articles. Moscow: World; 1975. 446. (In Russ.).
5. Campos MC., Vargas JVC., Ordóñez JC. Thermodynamic optimization of a Stirling engine. *Energy*. 2012;44(1):902–910.
6. Chen D, Xinggang W, Shuiming S, Changwei J, Huawei C. Thermodynamic design of Stirling engine using multi-objective particle swarm optimization algorithm. *Energy Conversion and Management*. 2014;84:88–96.
7. Somayeh T, Alibakhsh K, Mohammad HA. Multi-objective optimization of Stirling engine using non-ideal adiabatic method. *Energy Conversion and Management*. 2014;80:54–62.
8. Khafizov CA., Usenkov RA., Khalyullin FK., Latypov RA. The thermodynamic calculation of offset shafts rotary engine ideal cycle with external heat supply. *International Journal of Mechanical and Production Engineering Research and Development*. 2019;9(4):1109–1116.
9. Salem AAS, Erol K, Khaled MEH, Aybaba H. A numerical model for a Stirling engine. *Journal of Energy Systems*. 2018;2(1):1–12. DOI: 10.30521/jes.379164.
10. Paul R, Hoffmann KH. Cyclic Control Optimization Algorithm for Stirling Engines. *Symmetry*. 2021;13(873). DOI: 10.3390/sym13050873.
11. Uswatun H, Rahmatsyah, Eva M. Development of Stirling Engine Based Thermodynamics Tools. *IOP Conf. Series: Journal of Physics: Conf. Series*. 2020;1485. DOI: 10.1088/1742-6596/1485/1/012015.
12. Pratik S, Sumit R, Swapnil P, Nikhil P, Rajan P A Review on Stirling. *Engine Performance*. 2019;6(4):648–650.
13. Ladas HG., Ibrahim OM. Finite-time view of Stirling engine. *Energy*. 1994;19(8):837–843.
14. Wrona J, Prymon M. Mathematical Modelling of the Stirling engine. *Procedia Engineering*. 2016;157:349–356.
15. Wandong Z., Ruijie L, Hailing L, Ying Z, Songgang Q. Numerical analysis of fluid dynamics and thermodynamics in a Stirling engine. *Applied Thermal Engineering*. 2021;189:116727. DOI: 10.1016/j.applthermaleng.2021.116727.
16. Podešva J, Poruba Z. The Stirling engine mechanism optimization. *Perspectives in Science*. 2015. DOI: 10.1016/j.pisc.2015.11.052.
17. Garcia MT, Trujillo EC, Godiño JAV, Martínez DS. Thermodynamic Model for Performance Analysis of a Stirling Engine Prototype Energies. 2018;11;2655. DOI: 10.3390/en11102655.
18. Somayeh T, Alibakhsh K, Mohammad HA. Multi-objective optimization of Stirling engine using non-ideal adiabatic method. *Energy Conversion and Management*. 2014;80:54–62. DOI: 10.1016/j.enconman.2014.01.022.
19. Engine with external heat supply. Patent 2319848 Rus. Federation. No. 2006118599/06. 2008;8. 8 p. (In Russ.).
20. Rotary piston machine. Patent 2637301 Rus. Federation. No. 2016146956. 2017;34. 8 p. (In Russ.).
21. Heat engine implementing the Rallis cycle. Patent 2637301 Rus. Federation. No. 2016146956. 2015;16. 7 p. (In Russ.).

Acknowledgements: The work has been carried out as part of the implementation of the Agreement with the Ministry of Education of the Russian Federation (№ 075-03-2020-051/3).

Roman A. Usenkov:  <https://orcid.org/0000-0002-7119-8048>

Igor A. Popov:  <https://orcid.org/0000-0002-1700-7896>

Yuri F. Gortyshov:  <https://orcid.org/0000-0002-3225-9530>

Svetlana Y. Kokhanova:  <https://orcid.org/0000-0003-3788-7285>

Ravil A. Latypov:  <https://orcid.org/0000-0002-4536-8269>

FUZZY SYNERGETIC CONTROL FOR DYNAMIC CAR-LIKE MOBILE ROBOT

Zoulikha BOUHAMATOU^{*}, Foudil ABEDSSEMED^{*}

^{*}Department of Electronics, Faculty of Technology, University Mostefa Ben Boulaïd, Batna2, Algeria

z.bouhamatou@univ-batna2.dz, f.abdessemmed@univ-batna2.dz

received 25 May 2021, revised 27 September 2021, accepted 17 October 2021

Abstract: This paper aims to present the dynamic control of a Car-like Mobile Robot (CLMR) using Synergetic Control (SC). The SC control is used to make the linear velocity and steering velocity converge to references. Lyapunov synthesis is adopted to assure controlled system stability. To find the optimised parameters of the SC, the grey wolf optimiser (GWO) algorithm is used. These parameters depend on the best-selected fitness function. Four fitness functions are selected for this purpose, which is based on the integral of the error square (ISE), the integral of the square of the time-weighted error (ITSE), the integral of the error absolute (IAE) and the integral of the absolute of the time-weighted error (TIAE) criterion. To go further in the investigation, fuzzy logic type 2 is used to get at each iteration the appropriate controller parameters that give the best performances and robustness. Simulations results are conducted to show the feasibility and efficiency of the proposed control methods.

Key words: CLMR, Synergetic Control, Lyapunov stability, GWO, Fuzzy Logic type2

1. INTRODUCTION

In recent years, many works have been done on self-driving cars. This is mainly due to the increasing number of accidents on the road caused especially by inattention. How we drive is inefficient and becomes a real problem as we get old or we get more infirm. The way technology is evolving has brought many solutions to rolling vehicles. To end up with a smart vehicle, we should equip it with different sensors, a robust computing platform and robust control algorithms that execute in real time. In fact, the research in control focuses on the robustness of control laws and their influence on external disturbance, as well as on vehicle's response speed to execute the task and perform the desired objectives. Therefore, the recent works on control are oriented to these kinds of systems. The controller is to regulate some of the states of the vehicle such as velocity and rotation rate by sensing the current state variables and generating actuator signals to satisfy the objectives provided. Within this aspect, different techniques have been proposed. To obtain a stable movement of trajectory tracking we can find a lot of works applied to indoor and outdoor mobile robots. Dung et al. [4] developed an adaptive sliding mode control, they use this control to achieve the mobile robot tracking a smooth curved reference, with a desired constant velocity. Yeh et al. [20] presented an adaptive fuzzy sliding-mode control for trajectory tracking under disturbances for a car-like mobile robot (CLMR). They presented three dynamic controllers, namely Adaptive Sliding Mode Control (ASMDC), and Adaptive Fuzzy Sliding Mode Control (AFSMDC), which are proposed to reduce the effect of the problem of uncertainties and external disturbances. Peng and Shi [16] solved the problem of uncertainties and external disturbances in a non-holonomic wheeled mobile robot, where the uncertainties are approximated by a fuzzy logic system and an adaptive fuzzy integral terminal sliding mode con-

troller is used for velocity controller. An adequate control law is presented in Benaziza et al. [2]. It is based on Global Terminal Sliding Mode (GTSM) with fuzzy control. The objective of this control is to eliminate the disturbances of the angular and linear velocities, respectively. Moreover, an exponential reaching law is presented in a dynamic model to eliminate the uncertainties. Ibrahim [8] proposed a robust sliding mode controller for trajectory tracking for the non-holonomic robot. In his study, two stages of the proposed control strategy are presented. The first one uses the steering controller for the kinematics model and the second is a robust sliding mode control technique for the velocity. Mallem et al. [12] proposed a dynamic control RBF Global Fast Sliding mode for a mobile robot, for which the main task is making the linear and angular velocities converge to references in finite time. The system injected by disturbances. To stabilise the velocity errors and estimate the non-linear function of the robot, the RBF-GFSM approach is used, which combines the RBF neural network and Global Fast Sliding mode.

Sliding Mode Control (SMC) has been widely used in mobile robot control and great effort has been made to reduce its main inconvenience: chattering. Many approaches have been proposed to eliminate chatter, including synergistic control of the system and decoupling, but it is used for several advantages. First, it is well suited for digital implementation. The second advantage is that the control operates at the constant switching frequency and therefore avoids chattering problems.

As there is not much application of this type of control in the robot, Liu and Hsiao [11] proposed a finite time synergetic control (FTSC) for controlling robot manipulators. This technique was extracted from the use of synergetic theory and a terminal attractor technique. Their control scheme demonstrates its advantage in the finite-time convergence and chattering-free phenomena. Podvalny and Vasiljev [17] deployed a SC to solve the problem of synthesis of a multirotor unmanned aerial vehicle (UAV) regulator.

Veselov et al. [19] solved the problem of a group of mobile robots using the principles and methods of synergistic control theory. Sklyarov et al. [18] presented the explanation of using new non-linear approaches to design control systems for omnidirectional mobile robots, the synergetic control theory (SCT). Bhattacharyya et al. [3] proposed a brain-machine interfacing (BMI) paradigm for controlling the direction of end-point movement of a 3-degrees of freedom (DOF) robot arm, and they use a synergetic algorithm to manage a peripheral redundancy in multi-DOF joints towards energy optimality. Humaidi et al. [7] developed a SCT for controlling a one-link robot arm actuated by pneumatic artificial muscles (PAMs) in opposing bicep/tricep positions. A terminal SC is applied to a nonlinear helicopter model to control the nonlinear fifth-order helicopter model, which controls height and angle [6].

Moreover, when it comes to looking for the best performances that the system can achieve, some parameters should be well determined according to certain predefined criteria. This can always be obtained by intelligent optimisation algorithms. One of these algorithms is grey wolf optimiser (GWO). It is an evolutionary algorithm that uses a population of candidate solutions to develop an optimal solution to the problem. Mirjalili et al. [14] proposed this algorithm in 2014. It was originally inspired by the living world, more precisely by the social behaviour of animals evolving in swarms, inspired by grey wolves (*Canis lupus*). The GWO algorithm mimics the leadership hierarchy and hunting mechanism of grey wolves in nature. GWO has gained increasing popularity among researchers and practitioners as a robust and effective technique for solving difficult optimisation problems [5, 6, 9, 13, 15].

In this paper, we present a SC law to command successfully a CLMR. In fact, it seems reasonable to work on controlling autonomous driving vehicles by taking a CLMR. This is accomplished by making the velocity and the rotational rate of the car-like mobile robot converge to their references in presence of disturbances. The asymptotic stability is guaranteed by Lyapunov theory, for which certain parameters need to be well chosen to achieve the best performances. To obtain the optimised parameters, the grey wolf optimiser (GWO) algorithm is employed for this purpose.

The paper is organised as follows, in section two, the kinematic and dynamic model of the CLMR is introduced. Section 3 introduces the basics of SCT for nonlinear systems. It is reviewed briefly with stability proved for closed-loop control systems. Section 4, GWO is applied to determine the optimal parameters of SC. Section 5, propose a Fuzzy Logic type2 Synergetic Control for an uncertain CLMR system with external disturbances. In Section 6, simulations are performed to examine the feasibility and effectiveness of the approach. A conclusion is drawn in Section 7.

2. KINEMATICS AND DYNAMICS MODELS

This section aims to describe the kinematic and dynamic model of a CLMR. The geometry of the CLMR is shown in Fig. 1.

2.1. Kinematics model

The state of the robot's motion is represented by the vector q such that: $q = [x \ y \ \theta \ \psi \ \varphi]^T$, where (x, y) are the coordinates of the center of the two rear wheels. θ : indicates the heading direction of the CLMR concerning the x -axis, ψ is the

steering angle of the front wheels, and φ denotes the angular velocity of the wheels. The kinematic model of the CLMR is given by,

$$\begin{bmatrix} \dot{x} \\ \dot{y} \\ \dot{\theta} \\ \dot{\psi} \\ \dot{\varphi} \end{bmatrix} = \begin{bmatrix} \cos(\theta) \\ \sin(\theta) \\ \tan(\psi)/d \\ 0 \\ \frac{1}{a} \end{bmatrix} \begin{bmatrix} v \\ i\psi \end{bmatrix} = S(q)V \quad (1)$$

where: $S(q) \in \mathbb{R}^{5 \times 2}$ and $V \in \mathbb{R}^2$ are the full rank velocity transformation matrix and velocity vector, respectively. $i\psi \in \mathbb{R}$ denotes the steering velocity of the front wheels, d is the distance between the front and rear wheels, and a is the radius of the wheels.

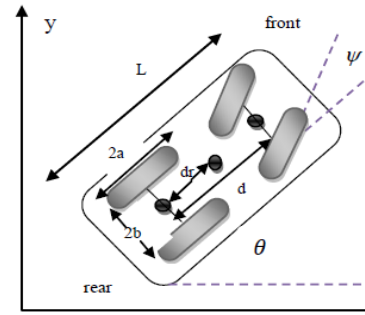


Fig. 1. The kinematics model of a non-holonomic CLMR, Car-like mobile robot

The linear velocity of the CLMR, $v(t) \in \mathbb{R}$, is obtained as:

$$v(t) = \sqrt{\dot{x}^2 + \dot{y}^2} \quad (2)$$

Here, we have two non-holonomic constraints, one for each wheel pair, that is:

$$\dot{x} \sin \theta - \dot{y} \cos \theta = 0 \quad (3)$$

$$\dot{x} \sin(\theta + \varphi) - \dot{y} \cos(\theta + \varphi) - \rho \dot{\theta} \cos \varphi = 0 \quad (4)$$

The two constraints can be rewritten as $H(q)\dot{q} = 0$, and therefore,

$$H(q)S(q)V = 0 \quad (5)$$

Such that

$$H(q) \begin{bmatrix} \sin \theta & -\cos \theta & 0 & 0 & 0 \\ \sin(\theta + \varphi) & -\cos(\theta + \varphi) & \rho \cos \varphi & 0 & 0 \end{bmatrix} \quad (6)$$

2.2. The dynamic model of the CLMR

The robot dynamic model of the non-holonomic mobile robot deals with the derivation of the dynamic equations of the robot motion. In this case, we use the methodologies of the Lagrange formula,

$$\frac{d}{dt} \left(\frac{\partial L}{\partial \dot{q}_i} \right) - \frac{\partial L}{\partial q_i} = \bar{N}(q)\tau + H^T(q)\lambda \quad (7)$$

L is the Lagrangian function defined by:

$$L = K - P \quad (8)$$

Here, K is the total kinetic energy, and P is the total potential energy of the robot. The Lagrangian L is equal to K since the robot is moving on a horizontal plane and so the potential energy P is zero.

$$\frac{d}{dt} \left(\frac{\partial K}{\partial \dot{q}_i} \right) - \frac{\partial K}{\partial q_i} = \bar{N}(q)\tau + H^T(q)\lambda \quad (9)$$

Where $i = 1, \dots, 5$ and λ is a Lagrange multiplier associated with the constraints, τ is the torque input vector. The kinetic energy of CLMR can be described as:

$$K = K_p + K_{fw} + K_{rw} \quad (10)$$

where K_p, K_{fw}, K_{rw} denote the kinetic energy of the body, front wheels and rear wheels of CLMR. According to Lagrange mechanics, the following matrices are adopted for CLMR models [2].

$$\bar{M}(q)\ddot{q} + \bar{V}_m(q, \dot{q})\dot{q} = \bar{N}(q)\tau + H^T\lambda \quad (11)$$

where: $\bar{M}(q) \in \mathbb{R}^{5 \times 5}$ is a symmetric positive definite inertia trix, $\bar{V}_m(q, \dot{q}) \in \mathbb{R}^{5 \times 5}$ is the centripetal and Coriolis matrix, $\bar{N}(q) \in \mathbb{R}^{5 \times 2}$ is the input transformation matrix, $H(q) \in \mathbb{R}^{5 \times 2}$ is a matrix associated with the nonholonomic constraints, and \dot{q} and \ddot{q} denote the velocity and acceleration vectors, respectively. The matrices in (11) are found to be,

$$\bar{M}(q) = \begin{bmatrix} m & 0 & -m\sin\theta & 0 & 0 \\ 0 & m & m\cos\theta & 0 & 0 \\ -m\sin\theta & m\cos\theta & I_\theta & 2I_w & 0 \\ 0 & 0 & 2I_w & 2I_w & 0 \\ 0 & 0 & 0 & 0 & 8I_w \end{bmatrix}$$

$$\bar{V}_m(q, \dot{q}) = \begin{bmatrix} 0 & 0 & -m\dot{\theta}\cos\theta & 0 & 0 \\ 0 & 0 & -m\dot{\theta}\sin\theta & 0 & 0 \\ 0 & 0 & 0 & 0 & 0 \\ 0 & 0 & 0 & 0 & 0 \\ 0 & 0 & 0 & 0 & 0 \end{bmatrix}$$

$$\bar{N}(q) = \begin{bmatrix} \cos\theta & \sin\theta & d\sin\psi\cos\psi & 0 & 1 \\ 0 & 0 & 0 & 1 & 0 \end{bmatrix}^T$$

The general dynamic model of mobile robot with unknown disturbances can be described by the following equation:

$$\bar{M}(q)\ddot{q} + \bar{V}_m(q, \dot{q})\dot{q} = \bar{N}(q)\tau + \tau_d + H^T\lambda \quad (12)$$

where τ_d is a denoted bounded unknown disturbance including unstructured but not modelled dynamically. It would be more suitable to express the dynamic equations of motion in terms of internal velocities. Substituting (1) and its differentiation in (12) and pre-multiplying by $S^T(q)$, results in Equation (13).

$$M(q)\dot{V} + V_m(q, \dot{q})V = N(q)\tau + \tau_{vd} \quad (13)$$

Where, $M = S^T \bar{M} S \in \mathbb{R}^{2 \times 2}$, $V_m = S^T [\bar{M} \dot{S} + \bar{V}_m S] \in \mathbb{R}^{2 \times 2}$, $N(q) = S^T \bar{N} \in \mathbb{R}^{2 \times 2}$; $\tau_{vd} = S^T * \tau_d \in \mathbb{R}^{2 \times 2}$.

The dynamic Equation (13) of the non-holonomic CLMR can be rewritten as:

$$\dot{V}(t) = -AV(t) + B\tau(t) + d \quad (14)$$

where, $A = M^{-1}V_m$, $B = M^{-1}N$, $d = M^{-1}\tau_{vd}$. In case of no disturbances ($d = 0$), Equation (14) reduces to

$$\dot{V}(t) = -AV(t) + B\tau(t) \quad (15)$$

3. SC DESIGN OF THE CAR LIKE MOBILE ROBOT

In this section, the SC method is used in designing a dynamic tracking controller. The objective is to control the velocity and

rotation rate to track the desired references.

SC system is an invariant-manifold-based control method and can be applied for controlling nonlinear dynamic systems. In the sequel, we present the basics of SC synthesis for a nonlinear dynamic system described by:

$$\dot{v} = f(v, u, t) \quad (16)$$

where v is the state vector, u is the control input vector, and t is time. The design process of SC algorithm for a nonlinear dynamic system can be summarised in the following steps as follows:

- Define the macro variable $\sigma(v, t)$, as a function of the system state. This macro variable will be used to determine a stabilising control law.

$$u(v) = u(v, \sigma(v)) \quad (17)$$

The system is forced by the controller to operate on the manifold: $\sigma = 0$.

- Design a control law that would drive the system states onto the specified manifold and remain on it with an evolution constraint, which can be stated as a set of the dynamic evolution of macro-variables written as Equation (18):

$$T\dot{\sigma}(v, t) + \sigma(v, t) = 0 \quad (18)$$

where $T = [T1, T2]^T$ is the rate of convergence vector of the macro-variables to manifolds $\sigma = 0$, and $\dot{\sigma}$ is the derivative of the aggregated macro variable by time.

- Solve the system (17) with the evolution condition (18) to obtain the control law.

To solve the differential Equation (18), we select a PI-type of the macro variable for v_c and ψ_c . By doing so, the tracking errors would converge effectively. Hence, the macro variables defined are expressed as:

$$\sigma(v, t) = \begin{bmatrix} \sigma_v(t) \\ \sigma_\psi(t) \end{bmatrix} = \begin{bmatrix} k_1 e_v + \int_0^t e_v(t) dt \\ k_2 e_\psi + \int_0^t e_\psi(t) dt \end{bmatrix} \quad (19)$$

The derivation of the macro variable $\sigma(t)$ is:

$$\dot{\sigma}(v, t) = \begin{bmatrix} \dot{\sigma}_v(t) \\ \dot{\sigma}_\psi(t) \end{bmatrix} = \begin{bmatrix} k_1 \dot{e}_v + e_v \\ k_2 \dot{e}_\psi + e_\psi \end{bmatrix} \quad (20)$$

In a more compact form, we write:

$$\dot{\sigma}(v, t) = k\dot{e} + e \quad (21)$$

where $k = [k_1, k_2]^T$ is the vector of positive coefficients and the vector of errors is $e = [e_v \ e_\psi]^T$, e_v is the linear velocity error and e_ψ is the steering velocity error. It is obvious that the tracking errors converge to if the parameters (k_1, k_2) are selected properly. The control law τ is obtained by letting $\dot{\sigma}(t)$ equal to zero. This is necessary for the state trajectory to stay on the synergetic surface. Since $T\dot{\sigma} + \sigma = 0$, therefore:

$$\dot{\sigma} = \frac{-\sigma}{T} \quad (22)$$

Substituting (22) in (21), yields

$$\dot{e} = -\frac{e}{k} - \frac{\sigma}{T} \quad (23)$$

The velocities errors are defined as:

$$e = V_d - V \quad (24)$$

For which the derivative is obtained:

$$\dot{e} = \dot{V}_d - \dot{V} \quad (25)$$

According to Equation (15), the system dynamic error is obtained as :

$$\dot{e} = \dot{V}_d(t) + AV(t) - B\tau(t) \quad (26)$$

Upon solving Eq. (26) for τ while taking into account Equation (23), the SC for the car like mobile robot law can be found as:

$$\tau(t) = B^{-1} \left[\frac{e}{k} + \frac{\sigma}{kT} + \dot{V}_d(t) + AV(t) \right] \quad (27)$$

where k is a diagonal matrix whose elements are k_1 and k_2 . By a suitable selection of the design parameters k_1 and k_2 , the final system can attain a suitable performance. Stability can be evaluated using the following Lyapunov function candidate

$$L_1 = \frac{1}{2} \sigma^T \sigma \quad (28)$$

This leads, after differentiation and using Eq. (21), to:

$$\dot{L}_1 = \sigma^T (k\dot{e} + e) \quad (29)$$

Written finally as,

$$\dot{L}_1 = -\frac{\sigma^T \sigma}{T} < 0 \quad (30)$$

Therefore, \dot{L}_1 is confirmed negative and consequently, the velocity tracking error will exponentially converge to zero.

4. GWO OF PARAMETERS

Grey Wolf Optimisation (GWO) is a smart swarm technique developed by Mirjalili et al. (2014), which mimics the leadership hierarchy of wolves which are well known for their group hunting. This algorithm mimics the social leadership hunting behavior of gray wolves in the wild. In this algorithm, the population is divided into four groups: alpha (α), beta (β), delta (δ) and omega (ω). The first three strongest wolves are considered α , β and δ which guide the other wolves (ω) to promising areas of the search space.

4.1. 4.1. Objective function

The objective function should be well chosen in order to find the unknown parameters of the designed control law leading to improve the performances of the control loop, such as the dynamic precision, the overshoot and the static error. The objective function considered is based on an error criterion, which is often the case when evaluating controller performances, for our applications, we have carried out a series of tests. In the end, our choice fell on two criteria namely: The integral of the error square (ISE), the integral of the square of the time-weighted error (ITSE), the integral of the error absolute (IAE) and the integral of the absolute of the time-weighted error (ITAE):

$$ISE = \int_0^t e(t)^2 dt \quad (31)$$

$$ITSE = \int_0^t t e(t)^2 dt \quad (32)$$

$$IAE = \int_0^t |e(t)| dt \quad (33)$$

$$ITAE = \int_0^t t |e(t)| dt \quad (34)$$

4.2. GWO basic algorithm

This algorithm imitates the hunting mechanism of gray wolves in nature, this kind of wolves mostly prefer to live in groups. Where the group can consist of 5–12 wolves. Or in the GWO strategy, each individual in the group has a specific role. Moreover, one of the interesting realities of the social life of these wolves is a very strict social hierarchy structure in the group; the main stages of the hunting of this type of wolves are:

- Tracking, chasing and approaching the prey
- Pursuing, encircling and harassing the prey until it stops moving
- Attack towards the prey

When designing GWO the social hierarchy of wolves, we consider the alpha (α) the fittest solution, the second and third-best solutions are beta (β) and delta (δ), respectively. The rest of the candidate solutions are assumed to be omega. In the GWO algorithm, the hunting (optimisation) is guided by α , β and δ . The (ω) wolves follow these three wolves.

4.2.1. Encircling prey

Describe the grey wolves encircle prey during the hunt by the following equations:

$$\vec{D} = |\vec{C} \cdot \vec{X}_p(t) - \vec{X}(t)| \quad (35)$$

$$\vec{X}(t+1) = \vec{X}_p(t) - \vec{A} \cdot \vec{D} \quad (36)$$

where: t indicates the current iteration, \vec{A} and \vec{C} are coefficient vectors. \vec{X}_p is the position vector of the prey, \vec{X} indicates the position vector of a grey wolf. The vectors are calculated as follows:

$$\vec{A} = 2\vec{a} \cdot \vec{r}_1 - \vec{a} \quad (37)$$

$$\vec{C} = 2\vec{r}_2 \quad (38)$$

where components of \vec{a} are linearly decreased from 2 to 0 over the course of iterations and r_1, r_2 are random vectors in $[0, 1]$.

4.2.2. Hunting

To search and identify the location of the prey and its surroundings. It is generally via Alpha, Beta and Delta which can also participate from time to time. However, the ideal location of prey does not have any idea of it remains. To mathematically simulate the hunting behavior of grey wolves, we assume that alpha (best candidate solution) beta and delta have better knowledge of the likely location of prey. Therefore, we save the three best solutions obtained so far and force other agents (including omegas) to update their sites according to the position of the best search agents.

$$\vec{D}_\alpha = |\vec{C}_1 \cdot \vec{X}_\alpha(t) - \vec{X}(t)|, \vec{D}_\beta = |\vec{C}_2 \cdot \vec{X}_\beta(t) - \vec{X}(t)|, \vec{D}_\delta = |\vec{C}_3 \cdot \vec{X}_\delta(t) - \vec{X}(t)| \quad (39)$$

$$\vec{X}_1 = \vec{X}_\alpha - \vec{A}_1 \cdot (\vec{D}_\alpha), \vec{X}_2 = \vec{X}_\beta - \vec{A}_2 \cdot (\vec{D}_\beta), \vec{X}_3 = \vec{X}_\delta - \vec{A}_3 \cdot (\vec{D}_\delta) \quad (40)$$

$$\vec{X}(t + 1) = \frac{\vec{X}_1 + \vec{X}_2 + \vec{X}_3}{3} \quad (41)$$

where: $\vec{X}_\alpha, \vec{X}_\beta, \vec{X}_\delta$ represents the position of the alpha, beta and delta respectively. X indicates the position of the current position. $\vec{C}_1, \vec{C}_2, \vec{C}_3$: Are random vectors.

4.2.3. Attacking prey (exploitation)

The proceeding of the hunt is finished when the prey stops moving which is then attacked by the grey wolves. In the mathematical model, the approaching towards the prey is made by a decrease in the value of a . Note that the fluctuation range of \vec{A} is also decreased by a . \vec{A} is a random value in the interval $[-a, a]$, and for each iteration, the value of a is decreased from 2 to 0. When random values of \vec{A} is in the interval $[-1, 1]$, the next search agent position is between its current position and the position of the prey. For A value of $|A| < 1$ forces the wolves to attack towards the prey.

4.3. Algorithm process

- The GWO algorithm works according to the following steps:
- Step 1: Initialise a random wolf population based on the upper and lower limits of the variables.
 - Step 2: Calculate the corresponding objective value for each Wolf.
 - Step 3: Choose the first three best wolves and save them under α, β and δ .
 - Step 4: Update the position of the rest of the population (wolves) using Equations (39), (40), and (41).
 - Step 5: Update of parameters a, A and C .
 - Step 6: Go to the 2nd step if the final criterion is not satisfied.
 - Step 7: Returns the position of α as the approximate optimal optimum.
- Fig. 2 resumes the control strategy proposed in this work.

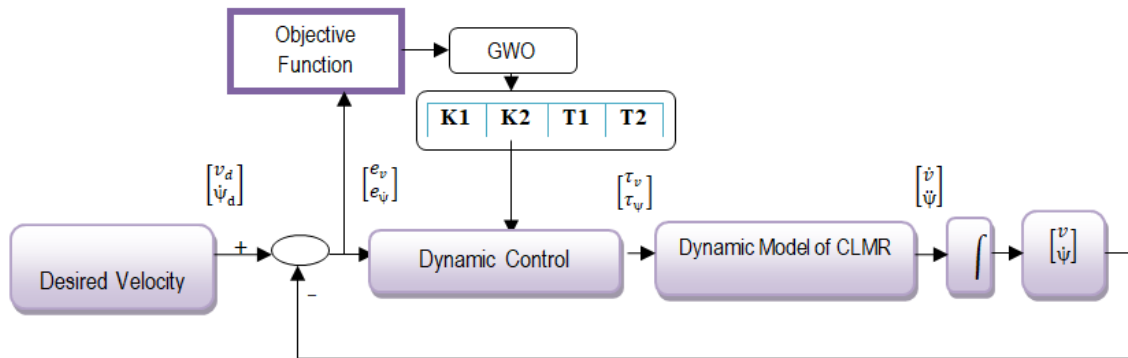


Fig. 2. The system architecture of the closed-loop system

5. FUZZY LOGIC TYPE 2 PARAMETERS FINDING

Even though the GWO algorithm gives the parameters that are relatively suitable for the controller and can be viewed as a means to find the best choice than using trial and error, we remarked that the tracking is not as good as it was expected when disturbances are present. In this section, we use fuzzy logic type 2 to estimate the parameters $[T_1, T_2, k_1, k_2]^T$ at each sampling time to reject as much as possible the effect of the external disturbances. In the presence of disturbances, the term d is added and Equation (14) presents, in this case, the system with added disturbances:

$$\dot{V}(t) = -AV(t) + B\tau(t) + d \quad (42)$$

In this equation the vector of disturbances is d , such that: $d = [dv \ d\dot{\psi}]$. The elements of this vector are bounded, i.e., $|dv| < \zeta_v, |d\dot{\psi}| < \zeta_{\dot{\psi}}$. dv and $d\dot{\psi}$ represent the perturbations of linear and steering Velocities and ζ_v and $\zeta_{\dot{\psi}}$ are positive constants. In our study, we define dv and $d\dot{\psi}$ as:

$$\begin{cases} dv = \sin t(\pi t) \\ d\dot{\psi} = \cos t(\pi t) \end{cases} \quad (43)$$

The fuzzifier is built using three Gaussian membership functions for both input variables and three Gaussian membership

functions for each of the four output variables as is depicted in Figs. 3–6. The following linguistic variables are assigned to each of the input and output fuzzy membership functions N, Z and of output S, M and B . Where the meaning of each linguistic variable should be clear from its mnemonic; in fact, N stands for negative, Z stands for Zero, P stands for positive, S stands for small, M stands for Mean and B stands for Big.

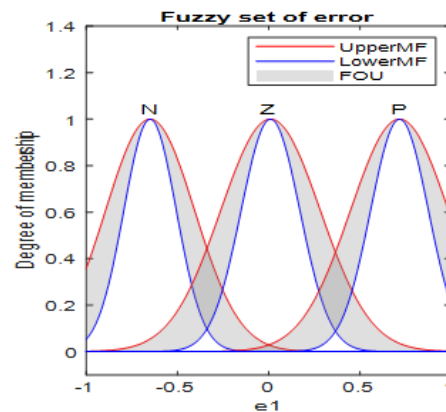


Fig. 3. Fuzzy sets of input function (e_v)

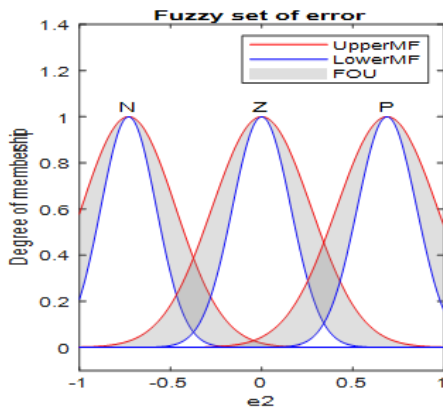


Fig. 4. Fuzzy sets of input function (e_{ψ})

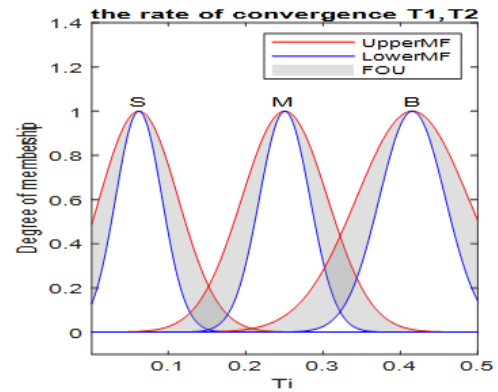


Fig. 6. Fuzzy sets of output function (T_i)

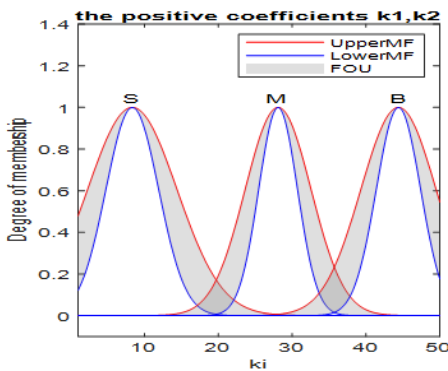


Fig. 5. Fuzzy sets of output function (K_i)

Fig. 7 shows the block diagram used for this purpose. In this system, the fuzzy inputs are the linear and steering velocity errors e_v and e_{ψ} while the fuzzy outputs are the SC parameters k_1, k_2, T_1 and T_2 .

The derivation of the rules obeys many techniques such as that of the experience and skilled operator. In our case, we made use of the knowledge of the behavior of the systems towards the values of the different parameters, taking into consideration that $k_i \geq 0$ and $T_i \geq 0, i = 1, 2$.

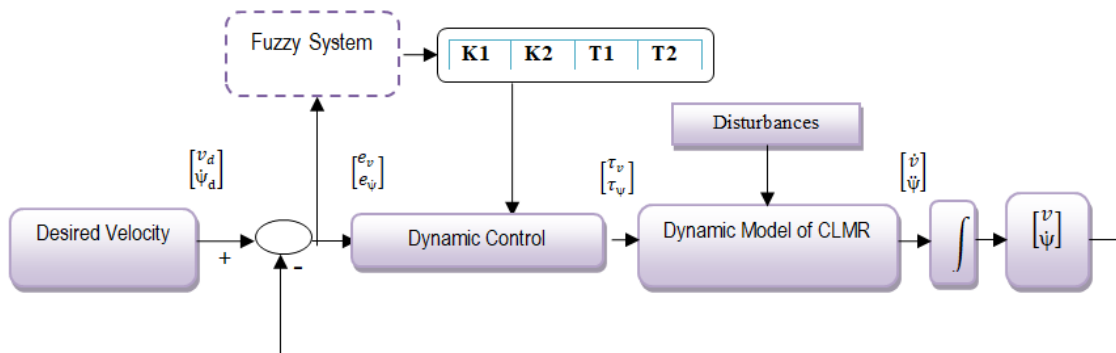


Fig. 7. The system architecture of the closed-loop system by fuzzy logic

Thus the parameters are gauged by the following fuzzy inference mechanism:

- If e_v is N and if e_{ψ} is N then k_1 is S, and k_2 is S and T_1 is S and T_2 is S.
- If e_v is N and if e_{ψ} is Z then k_1 is S, and k_2 is M and T_1 is S and T_2 is M.
- If e_v is N and if e_{ψ} is P then k_1 is S, and k_2 is B and T_1 is S and T_2 is B.
- If e_v is Z and if e_{ψ} is N then k_1 is M, and k_2 is S and T_1 is M and T_2 is S.
- If e_v is Z and if e_{ψ} is Z then k_1 is M, and k_2 is M and T_1 is M and T_2 is M.
- If e_v is Z and if e_{ψ} is P then k_1 is M, and k_2 is B and T_1 is M and T_2 is B.

- If e_v is P and if e_{ψ} is N then k_1 is B, and k_2 is S and T_1 is B and T_2 is S.
- If e_v is P and if e_{ψ} is Z then k_1 is B, and k_2 is M and T_1 is B and T_2 is M.
- If e_v is P and if e_{ψ} is P then k_1 is B, and k_2 is B and T_1 is B and T_2 is B.

6. SIMULATION RESULTS

A simulation study has been conducted to assess the effectiveness of the proposed control. The SC performances are evaluated. The control objective is to make the linear and steering velocities converge to the desired references. To investigate the effectiveness of the proposed methodologies, numerical simulations were carried out for the SC without disturbance. To test the

robustness of the approaches, disturbances were added in the second scenario of the simulation.

Let us consider:

- The desired linear velocity: $V_d = 1.0m.s^{-1}$ and the desired steering velocity: $\dot{\psi}_d = 1.0 rad.s^{-1}$.

The mobile robot parameters are given in Tab. 1.

Tab. 1. Parameters used in the simulation

Mobile Robot			
$I_{\theta}(Kg.m^2)$	$I_w(Kg.m^2)$	m (kg)	d(m)
1.35	$5 \cdot 10^{-3}$	25	0.2

This part presents the results of simulations of SC to judge the performances achieved by the manual gain, GWO algorithm and fuzzy logic type 2. We have used some metrics for this purpose to evaluate the mean linear velocity and the mean steering velocity errors. The tracking of the linear and steering velocities with the best gains are depicted in Figs. (8) and (9). The controller is tuned to have the fastest response. In these figures, one can figure out how fast is the response of the mobile robot to reach the reference velocities. To highlight this aptitude, trajectories errors are added in Figs. (10) and (11) while figures (12) and (13) present the control torques (14) and (15) present the macro-variable function.

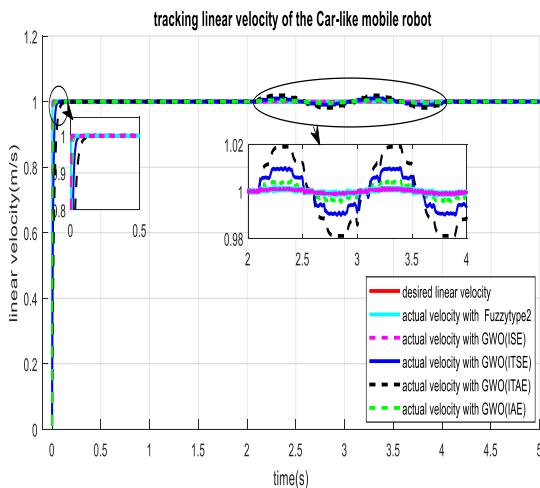


Fig. 8. Linear velocity

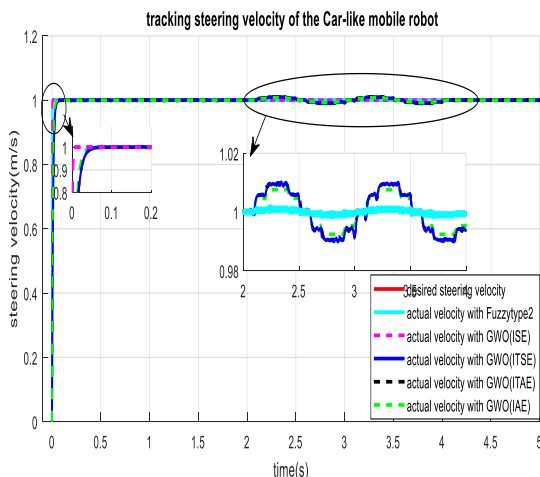


Fig. 9. Steering velocity

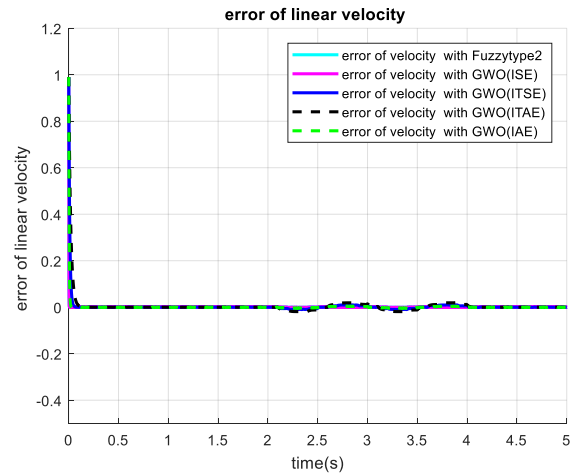


Fig. 10. Tracking error of linear velocity

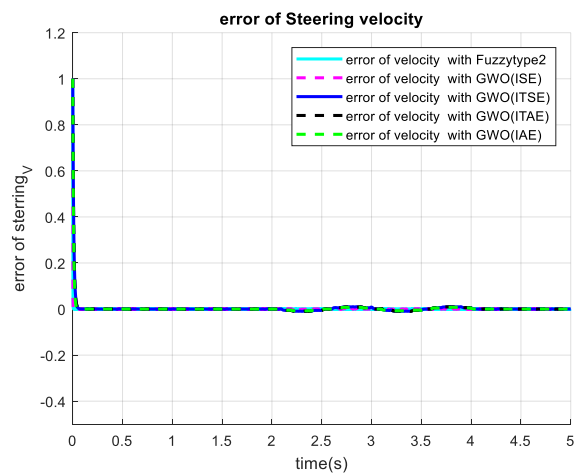


Fig. 11. Tracking error of steering velocity

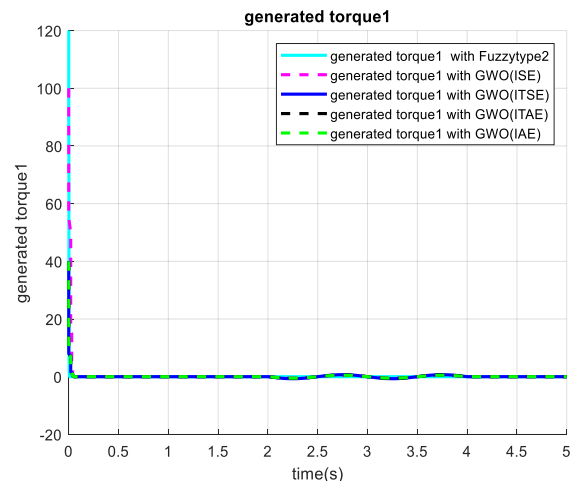


Fig. 12. Generated torque1

We should point out that the SC law used the best optimal parameters found by the GWO algorithm and fuzzy logic type2.

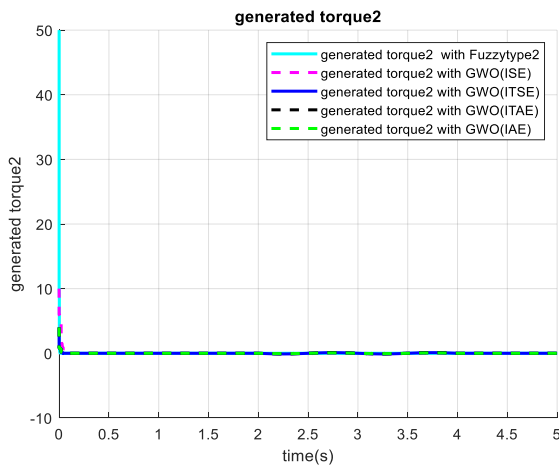


Fig. 12. generated torque2

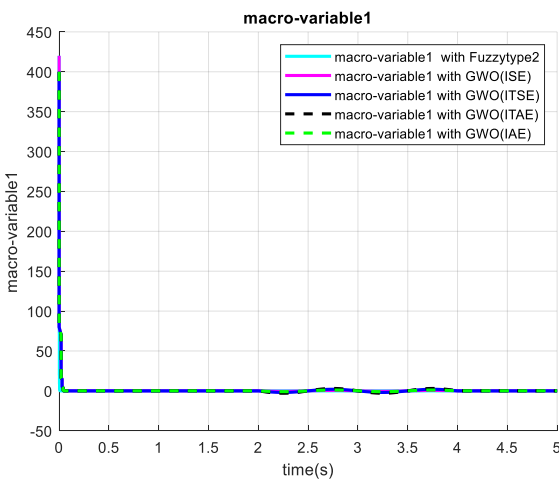


Fig. 14. Macro-variable1

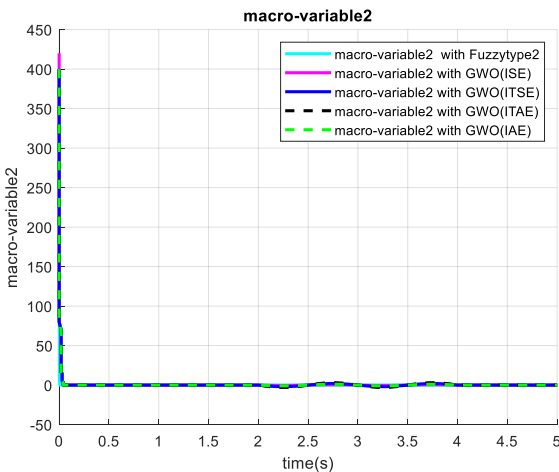


Fig. 15. Macro-variable2

Tab. 2. GWO parameters of synergetic

Objective function	IAE	ITAE	ISE	TISE
Gain	$k_1 = 480$ $k_2 = 480$	$k_1 = 401$ $k_2 = 500$	$k_1 = 455$ $k_2 = 350$	$k_1 = 455$ $k_2 = 497$
The rate of convergence	$T_1 = 0.011$ $T_2 = 0.00$	$T_1 = 0.01$ $T_2 = 0.0$	$T_1 = 0.02$ $T_2 = 0.01$	$T_1 = 0.004$ $T_2 = 0.008$

In fact, after execution of the algorithm for 25 generations, using the hyper-parameters of the GWO given in Table 2, we report in Table 3 the resulting optimum values of the gains and the rate of convergences for two chosen objective functions given by expressions (31), (32), (33) and (34). As for the sake of comparison, we start our simulation by trial and error on the unknown parameters. We tried to fix them manually and look for the best performances as it is depicted in Tab. 2. For each set of the parameters: k_1, k_2, T_1 and T_2 , we compare the different metrics defined in the first column of Tab. 3. As one can notice, the time taken for the robot to start tracking the desired velocities is within 0.5 s with a convergence time of about 3 s. The rising time of the steering velocity is decreased when its rate of convergence is reduced and the value of the gain is increased. However, the time of convergence and the mean errors of velocities become small as well as the mean error of the steering velocity. From Tab. 3, we can see that the best parameters are those given in column three, compromised by the time of convergence. We notice also that the time taken for the robot to start tracking the desired velocities is very fast with a convergence time of almost 3 s. The rising time of the steering velocity can decrease when its rate of convergence is reduced and the gain is increased. However, one can remark that the values plugged in this table were very hard to find by trial and error. Therefore, we cannot assert that these parameters are the best ones to span the whole parameter space and choose the values that can give the best performances automatically. In this case, we ran the GWO algorithm and recorded the performances found and plugged them in Table II. To observe the effect of the parameter values, a comparison between the results obtained using manual trials, the GWO algorithm and those of Fuzzy logic type 2. As it can be seen, that the Fuzzy logic type 2 and the value of GWO obtained from the integral of the error absolute achieved the best records.

Moreover, to test the robustness of each of the approaches, we inject some disturbances into the system. By trial error, we adjust manually the parameters until we observe that the velocities approach as close as possible their references. Despite the optimum parameters found by the integral of the square of the time-weighted error TISE of the GWO algorithm, it remains to enable to eliminate residual disturbances. To arrive at a satisfactory objective. The SC based on fuzzy logic type 2 parameter finding has solved the problem. In fact, the ability to find the appropriate parameter values at each sampling time helped in reducing enormously the effect of disturbances, where, one can observe an excellent response of tracking the forward and steering velocities.

It can be seen that the system operates on the manifold $\psi = 0$. The convergence rate of the dynamical system is determined by the value of the parameter T , the smaller the T value, the higher the convergence rate, the figures of simulation demonstrate that the convergence rate can be controlled.

Tab. 3. Mean error of synergetic control

	Manual gain			GWO				Fuzzy logic Type 2
Gain	$k_1 = 10$ $k_2 = 10$	$k_1 = 500$ $k_2 = 500$	$k_1 = 500$ $k_2 = 500$	$k_1 = 480$ $k_2 = 480$	$k_1 = 401$ $k_2 = 500$	$k_1 = 451$ $k_2 = 350$	$k_1 = 455$ $k_2 = 497$	
The rate of convergence	$T_1 = 0.1$ $T_2 = 0.1$	$T_1 = 0.1$ $T_2 = 0.1$	$T_1 = 0.01$ $T_2 = 0.01$	$T_1 = 0.011$ $T_2 = 0.001$	$T_1 = 0.01$ $T_2 = 0.01$	$T_1 = 0.02$ $T_2 = 0.01$	$T_1 = 0.004$ $T_2 = 0.003$	
Mean linear velocity error (m/s)	0.0646	0.0561	0.0123	0.0048	0.0014	0.0194	0.0042	0.002
Mean steering velocity error (m/s)	0.0654	0.0561	0.0120	0.0014	0.0049	0.0131	0.0036	0.002
Time of convergence (s)	3	3	3	9	9	3	7	30
Rising time of linear velocity (s)	0.5	0.5	0.08	0.01	0.05	0.2	0.03	0.01
Rising time of steering velocity(s)	0.5	0.5	0.08	0.08	0.06	0.1	0.02	0.02

7. CONCLUSION

In this paper, an optimised SC is proposed. The SC is designed to track the forward and steering velocities of a CLMR. The control law obtained involved parameters that should be well tuned to get the best performances. The tuning has been performed using the GWO optimisation algorithm and fuzzy logic type 2. The simulation confirmed a rapid convergence of the control law. Moreover, applying this control law helps in avoiding the chattering problem while assuring asymptotical stability. To arrive at the best performances, we used the GWO algorithm and fuzzy logic type 2 to get the optimised parameters of the control law. The SC law based on fuzzy adaptive parameters can choose the appropriate values of the parameters to best remove the external disturbances, which demonstrates its robustness. The results obtained are very satisfactory and promise a lot in the use of this control law in driving an autonomous vehicle in real-time conditions.

These control laws of linear and steering velocity can assure the asymptotical stability of the system by applying the Lyapunov theory, and proves that the controller is stable for any combination of the error states. The advantage of this control law is to eliminate the disturbances due to the dynamic model, such that the error states of the robot converge to zero.

REFERENCES

- Ahifar A, Ranjbar AN, Rahmani Z. Finite Time Terminal Synergetic Controller for Nonlinear Helicopter Model. 2019; 32(2):236–241.
- Benaziza W, Slimane N, Mallem A. Disturbances elimination with fuzzy sliding mode control for mobile robot trajectory tracking. *Advances in Electrical and Electronic Engineering*. 2018; 16(3):297–310. <https://doi.org/10.15598/aeec.v16i3.2767>
- Bhattacharyya S, Shimoda S, Hayashibe M. A Synergetic Brain-Machine Interfacing Paradigm for Multi-DOF Robot Control. *IEEE Transactions on Systems Man and Cybernetics: Systems* 2016; 46(7):957–968. <https://doi.org/10.1109/TSMC.2016.2560532>

- Dung NM, Duy VH, Phuong NT, Kim SB, Oh MS. Two-wheeled welding mobile robot for tracking a smooth curved welding path using adaptive sliding-mode control technique. *International Journal of Control Automation and Systems*. 2007; 5(3):283–294.
- Elhariri E, El-Bendary N, Hassanien AE, Abraham A. Grey wolf optimization for one-against-one multi-class support vector machines. 2015 7th International Conference of Soft Computing and Pattern Recognition (SoCPar). 2015; 7–12. <https://doi.org/10.1109/SOCPAR.2015.7492781>
- Gupta S, Deep K. Cauchy Grey Wolf Optimiser for continuous optimisation problems. *Journal of Experimental & Theoretical Artificial Intelligence*. 2018; 30(6):1051–1075 <https://doi.org/10.1080/0952813X.2018.1513080>.
- Humaidi AJ, Ibraheem IK, Azar AT, Sadiq ME. A New Adaptive Synergetic Control Design for Single Link Robot Arm Actuated by Pneumatic Muscles. *Entropy*. 2020; 22(7). <https://doi.org/10.3390/e22070723>
- Ibrahim AEB. Wheeled Mobile Robot Trajectory Tracking using Sliding Mode Control. 2016. <https://doi.org/10.3844/jcssp.2016.48.55>
- Kamalova A, Navruzov S, Qian D, Lee SG. Multi-Robot Exploration Based on Multi-Objective Grey Wolf Optimizer. *Applied Sciences*. 2019; 9(14). <https://doi.org/10.3390/app9142931>
- Kolesnikov A, Veselov G, Kolesnikov A. Modern applied control theory: synergetic approach in control theory. *TRTU Moscow Taganrog*. 2000; 4477–4479.
- Liu CH, Hsiao MY. A finite time synergetic control scheme for robot manipulators. *Computers and Mathematics with Applications*. 2012; 64(5):1163–1169. <https://doi.org/10.1016/j.camwa.2012.03.058>
- Mallem A, Slimane N, Benaziza W. Dynamic Control of Mobile Robot Using RBF Global Fast Sliding mode. *IAES International Journal of Robotics and Automation (IJRA)*. 2018; 7(3):159. <https://doi.org/10.11591/ijra.v7i3.pp159-168>
- Mesquita EDEM, Sampaio RC, Vicente H, Ayala H, Llanos CH. Recent Meta-Heuristics Improved by Self-Adaptation Applied to Non-linear Model-Based Predictive Control. 2020; 118841–118852.
- Mirjalili S, Mirjalili SM, Lewis A. Grey Wolf Optimizer. *Advances in Engineering Software*. 2014; 69:46–61. <https://doi.org/https://doi.org/10.1016/j.advengsoft.2013.12.007>
- Mittal N, Singh U, Sohi BS. Modified Grey Wolf Optimizer for Global Engineering Optimization. *Applied Computational Intelligence and Soft Computing*. 2016; 1–16. <https://doi.org/10.1155/2016/7950348>

16. Peng S, Shi W. Adaptive fuzzy integral terminal sliding mode control of a nonholonomic wheeled mobile robot. *Mathematical Problems in Engineering*. 2017. <https://doi.org/10.1155/2017/3671846>
17. Podvalny SL, Vasiljev EM. Synergetic control of UAV on the basis of multi-alternative principles. *International Russian Automation Conference RusAutoCon*. 2018; 1–6. <https://doi.org/10.1109/RUSAUTOCON.2018.8501727>
18. Sklyarov AA, Veselov GE, Sklyarov SA, Pohilina TE. Synthesis of the synergetic control law of the transport robotic platform. *Proceedings of 2017 IEEE 2nd International Conference on Control in Technical Systems CTS*. 2017; 285–288. <https://doi.org/10.1109/CTS.2017.8109547>
19. Veselov G, Sklyrov A, Mushenko A, Sklyrov S. Synergetic Control of a Mobile Robot Group. *Proceedings - 2nd International Conference on Artificial Intelligence Modelling and Simulation AIMS*. 2014; 155–160. <https://doi.org/10.1109/AIMS.2014.22>
20. Yeh YC, Li THS., Chen CY. Adaptive fuzzy sliding-mode control of dynamic model based car-like mobile robot. *International Journal of Fuzzy Systems*. 2009; 11(4):272–286. <https://doi.org/10.30000/IJFS.200912.0006>

Zoulikha Bouhamatou:  <https://orcid.org/0000-0002-3985-0147>

Foudil Abedssem:  <https://orcid.org/0000-0003-0935-3147>

MULTI-OBJECTIVE OPTIMISATION OF THE ELECTRIC WHEELCHAIR RIDE COMFORT AND ROAD HOLDING BASED ON JOURDAIN'S PRINCIPLE MODEL AND GENETIC ALGORITHM

Mohamed BELHORMA[✉], Aboubakar Seddik BOUCHIKHI[✉]

^{*}Faculty of Technology; Department of Mechanical Engineering, Mechanics of Structures and Solids Laboratory,
University of Sidi Bel Abbas, BP 89, Cité Ben Mhidi, Sidi Bel Abbas 22000, Algeria

medbelhorma@hotmail.com, asbouchikhi@yahoo.fr

received 23 March 2021, revised 15 November 2021, accepted 30 November 2021

Abstract: The paper addresses the multi-body modelling of an electric wheelchair using Jourdain's principle. First, a description of the adopted approach was presented. Next, the mathematical equations were developed to obtain the dynamic behaviour of the concerned system. The numerical computation was performed with MATLAB (matrix laboratory: a high performance language of technical computing) and validated by MBD (Multi-Body Dynamics) for Ansys, a professional multi-body dynamics simulation software powered by RecurDyn. Afterwards, the model was treated as an objective function included in genetic algorithm. The goal was to improve the ride quality and the road holding as well as the suspension workspace. The multi-objective optimisation aimed to reduce the Root-Mean-Square (RMS) of the seat's vertical acceleration, the wheels load and the workspace modulus by varying the bodies' masses, the spring-damper coefficients and the characteristics of the tires. Acceptable solutions were captured on the Pareto fronts, in contrast to the relatively considerable processing time involved in the use of a random road profile generated by the power spectral density (PSD). During the process, the compatibility and the efficiency of Jourdain's equations were inspected.

Key words: multi-body systems, Jourdain's principle, electric wheelchair, multi-objective optimisation, genetic algorithm

1. INTRODUCTION

Recent systems are complex and consist of many bodies interconnected by joints and elements of force. These systems are called multi-body systems in the literature. The dynamic equations that generate the motion of these systems are highly non-linear and thus in most cases cannot be solved by a closed analytical form, making the numerical solution of the resulting equations indispensable. Therefore, a proper choice of the formalism of multi-body modelling can improve numerical efficiency.

In 1909, Jourdain [16] had an intention to find a bridge between d'Alembert's principle and the Gauss principle of least constraint, and he did so by publishing a paper about a third principle of mechanics. This generalised form of d'Alembert's principle uses virtual velocities instead of virtual displacements, and is applied to systems with differential nonholonomic constraints [27]. Papastavridis [22] has demonstrated that Jourdain's principle results naturally from the total time differentiation of Lagrange's principle and produces the correct equations of motion independently of any commutation assumptions. Inexplicably, this principle seems to be very little known, and also appears prone to be confused with Kane's equations [17] presented in 1961 as "a general method for obtaining the differential equations of nonholonomic systems". Some authors state that Kane's equations are merely a reformulation of the concepts Appell and Jourdain developed earlier, due to which Piedboeuf [24] has reviewed both Jourdain's principle and Kane's equations and demonstrated that the latter can be expressed as easily the former. Henceforth,

Jourdain's principle will be applied in modelling dynamical behaviour of mechanical systems such as a powered wheelchair.

Electric wheelchairs are helpful for people unable to use a manual wheelchair, especially for larger distances or over rough terrain. In case a wheelchair is provided with a suspension, as shown in the example of Fig. 1, it will have an increased performance.



Fig. 1. The KARMAN XO-202 electric wheelchair [12]

To improve its performance, an electric-powered wheelchair may be subject to different types of studies. Vingback et al. [34] have used a motion base simulator to facilitate fast and cost-efficient development and adjustment of wheel suspension systems and parameters for increasing the ride comfort of wheelchair-seated passengers. Wang et al. [35] have compared the vibration isolation performances of the convalescent-wheelchair robot with and without a vibration-reducing device, and conducted

the sensitivity analysis of the vibration responses to the important dynamic parameters. Although there exist many works dealing with the development of active and semi-active suspension systems, such as the researches of Van der Sande et al. [33], Anandan and Kandavel [2] and others [4, 8, 20, 29, 31] on multi-objective optimisation related to passenger comfort and road holding of ground vehicles, few dealt with multi-objective optimisation of electric wheelchairs. The focus was on improving control automatism using genetic algorithms, in contrast with the studies of Sankardoss and Geethanjali [28], Ahmad et al. [1] and Dad et al. [5]. However, there is a lack of powered wheelchair design optimisation that combines evolutionary algorithms and Jourdain's equations.

This article will provide a clear description of the multi-body modelling of an electric wheelchair according to Jourdain's principle, from the generation of equations of motion to the numerical computation. Of particular interest are the interaction between the first-order ordinary differential equations (ODEs) and the non-linearity of the forces applied by the suspension as well as the random road effect produced by the power spectral density (PSD). The validated model will be injected into an optimisation program in order to investigate its efficiency, robustness and rapidity as a function with multiple objectives. The choice will be on the genetic algorithm in the MATLAB Optimisation Toolbox to improve ride quality and road holding. The multi-objective optimisation will aim to reduce the Root-Mean-Square (RMS) of the seat's vertical acceleration, the tires load and the suspension workspace modulus by varying the bodies' masses, the spring-damper coefficients and some parameters of the tires. The dominant objectives will be extracted, and the influence of the normalised variables will be examined. The reader will notice the frequent use of the predefined functions of MATLAB, both in modelling and optimisation, the aim of which is to benefit from a combination between these tools and first-order differential equations by having a straightforward process.

2. JOURDAIN'S PRINCIPLE OF VIRTUAL POWER

According to Rill [26], a right-handed Cartesian coordinate system is fixed to the body in its centre of mass (CoG: Centre of Gravity). The position and the orientation of body i with respect to the inertial reference frame 0 (RF0) is determined by the position vector r and the rotation matrix A , respectively.

$$r_{0i,0} = r_{0i,0}(y) \quad (1)$$

and

$$A_{0i,0} = A_{0i,0}(y) \quad (2)$$

where the generalised coordinates y_1, y_2, \dots, y_n are collected in the vector y . The velocity of body i in RF0 is

$$v_{0i,0} = \frac{d}{dt} r_{0i,0}(y) = \sum_{m=1}^f \frac{\partial r_{0i,0}(y)}{\partial y_m} \dot{y}_m = v_{0i,0}(y, \dot{y}) \quad (3)$$

The time derivative of $A_{0i,0} \cdot A_{0i,0}^T$ is a skew-symmetric matrix

$$\tilde{\omega}_{0i,0} = \begin{bmatrix} 0 & -\omega_{0i,0}(3) & \omega_{0i,0}(2) \\ \omega_{0i,0}(3) & 0 & -\omega_{0i,0}(1) \\ -\omega_{0i,0}(2) & \omega_{0i,0}(1) & 0 \end{bmatrix} \quad (4)$$

where the vector of angular velocity

$$\omega_{0i,0} = [\omega_{0i,0}(1), \omega_{0i,0}(2), \omega_{0i,0}(3)]^T \quad (5)$$

For simplification, we replace by z , where $z = K(y)\dot{y}$, $z = z(y, \dot{y})$, $v_{0i,0}(y, z)$ and $\omega_{0i,0}(y, z)$. The time derivative of velocities yields to

$$a_{0i,0} = \sum_{m=1}^f \frac{\partial v_{0i,0}(y,z)}{\partial y_m} \dot{y}_m + \sum_{m=1}^f \frac{\partial v_{0i,0}(y,z)}{\partial z_m} \dot{z}_m \quad (6)$$

$$\alpha_{0i,0} = \sum_{m=1}^f \frac{\partial \omega_{0i,0}(y,z)}{\partial y_m} \dot{y}_m + \sum_{m=1}^f \frac{\partial \omega_{0i,0}(y,z)}{\partial z_m} \dot{z}_m \quad (7)$$

The motion of one rigid body is described by Newton–Euler equations

$$m_i \cdot a_{0i,0} = F_{i,0} \quad (8)$$

$$\Theta_{i,0} \cdot \alpha_{0i,0} + \omega_{0i,0} \times \Theta_{i,0} \cdot \omega_{0i,0} = T_{i,0} \quad (9)$$

where m_i is the mass of body i and $\Theta_{i,0}$ is the corresponding inertia tensor. The forces and torques for constrained systems are devoted to ones applied on body i and others provided by constraints

$$F_{i,0} = F_{i,0}^a + F_{i,0}^c \quad (10)$$

$$T_{i,0} = T_{i,0}^a + T_{i,0}^c \quad (11)$$

The partial velocities and partial angular velocities are arranged in the $3 \times f$ Jacobian matrices of translation and rotation, as under:

$$\frac{\partial v_{0i,0}}{\partial z} = \left[\frac{\partial v_{0i,0}(y,z)}{\partial z_1}, \frac{\partial v_{0i,0}(y,z)}{\partial z_2}, \dots, \frac{\partial v_{0i,0}(y,z)}{\partial z_f} \right] \quad (12)$$

$$\frac{\partial \omega_{0i,0}}{\partial z} = \left[\frac{\partial \omega_{0i,0}(y,z)}{\partial z_1}, \frac{\partial \omega_{0i,0}(y,z)}{\partial z_2}, \dots, \frac{\partial \omega_{0i,0}(y,z)}{\partial z_f} \right] \quad (13)$$

Using the Jacobian matrices, the accelerations are obtained as:

$$a_{0i,0} = \frac{\partial v_{0i,0}}{\partial z} \dot{z} + a_{0i,0}^R \quad (14)$$

$$\alpha_{0i,0} = \frac{\partial \omega_{0i,0}}{\partial z} \dot{z} + \alpha_{0i,0}^R \quad (15)$$

The remaining terms in the accelerations are presented by R . It should be mentioned that the reaction terms are vanished. The first-order differential equation is $M(y)\dot{z} = q(y, z)$, where $f \times f$ mass matrix is defined by

$$M(y) = \sum_{i=1}^k \left[\frac{\partial v_{0i,0}^T}{\partial z} m_i \frac{\partial v_{0i,0}}{\partial z} + \frac{\partial \omega_{0i,0}^T}{\partial z} \Theta_{i,0} \frac{\partial \omega_{0i,0}}{\partial z} \right] \quad (16)$$

and the $f \times 1$ vector of generalised forces is given by

$$q(y, z) = \sum_{i=1}^k \left[\frac{\partial v_{0i,0}^T}{\partial z} H_1 + \frac{\partial \omega_{0i,0}^T}{\partial z} H_2 \right] \quad (17)$$

where

$$H_1 = F_{i,0}^a - m_i \cdot a_{0i,0}^R \quad (18)$$

and

$$H_2 = T_{i,0}^a - \Theta_{i,0} \cdot \alpha_{0i,0}^R - \omega_{0i,0} \times \Theta_{i,0} \cdot \omega_{0i,0} \quad (19)$$

3. DYNAMICAL MODEL OF THE ELECTRIC WHEELCHAIR

3.1. Kinematics

The Non-Linear Two-Dimensional Electric Wheelchair (NL2D-EWC), presented in Fig. 2, consists of four rigid bodies: Chassis

or Sprung mass (S), Control arm (C), Front Tire (FT) and Rear Tire (RT). The motion of the system is described by four generalised coordinates $y = (z \ \gamma \ \beta \ \varphi)^T$ representing the vertical displacement of the Sprung mass, the rotation angle of the Control arm about the revolute joint Bc, the rotation angle of the FT about the revolute joint Bf and the rotation angle of the RT about the revolute joint Br, respectively. The tires' deflections r_{sf} and r_{sr} , and the step inputs u_f and u_r of the road, are illustrated in Fig. 2.

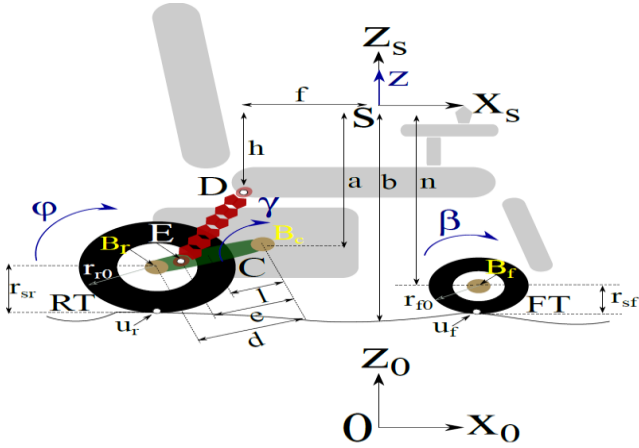


Fig. 2. The NL2D-EWC. FT, front tire; NL2D-EWC, non-linear two-dimensional electric wheelchair; RT, rear tire

The position, velocity and acceleration of the Sprung mass' CoG are

$$p_s = \begin{pmatrix} 0 \\ 0 \\ b+z \end{pmatrix}, v_s = \begin{pmatrix} 0 \\ 0 \\ \dot{z} \end{pmatrix}, a_s = \begin{pmatrix} 0 \\ 0 \\ \ddot{z} \end{pmatrix} \quad (20)$$

The distance b between the Sprung mass' CoG and the ground, and the parameters $l, d, a, n, r_{ro}, r_{fo}, h, f, d_2$ and e are shown in Fig. 2. The NL2D-EWC is not considered as a pitch-plane model because there is no orientation for the Sprung mass. Therefore, the rotation matrix that describes the orientation of the Control arm with respect to the Sprung mass' Reference Frame (SRF) is the same that describes it in RF0.

$${}^s_c A = {}^c_0 A = \begin{bmatrix} \cos\gamma & 0 & \sin\gamma \\ 0 & 1 & 0 \\ -\sin\gamma & 0 & \cos\gamma \end{bmatrix} \quad (21)$$

and the angular velocity and angular acceleration are

$$\omega_c = \begin{pmatrix} 0 \\ \dot{\gamma} \\ 0 \end{pmatrix}, \text{ and } \alpha_c = \begin{pmatrix} 0 \\ \ddot{\gamma} \\ 0 \end{pmatrix} \quad (22)$$

The position vector is

$$p_c = \begin{pmatrix} 0 \\ 0 \\ b+z \end{pmatrix} + \begin{pmatrix} 0 \\ 0 \\ -a \end{pmatrix} + \begin{pmatrix} -l \cos\gamma \\ 0 \\ l \sin\gamma \end{pmatrix} \quad (23)$$

The first two parts characterise the position of the revolute joint Bc. The first and second derivatives yield to

$$v_c = \begin{pmatrix} 0 \\ 0 \\ \dot{z} \end{pmatrix} + \begin{pmatrix} l \dot{\gamma} \sin\gamma \\ 0 \\ l \dot{\gamma} \cos\gamma \end{pmatrix} \quad (24)$$

and the acceleration

$$a_c = \begin{pmatrix} 0 \\ 0 \\ \dot{z} \end{pmatrix} + \begin{pmatrix} l \ddot{\gamma} \sin\gamma \\ 0 \\ l \ddot{\gamma} \cos\gamma \end{pmatrix} + \begin{pmatrix} l \dot{\gamma}^2 \cos\gamma \\ 0 \\ -l \dot{\gamma}^2 \sin\gamma \end{pmatrix} \quad (25)$$

The orientation of the FT with respect to the RF0 is determined by

$${}^{FT}_0 A = \begin{bmatrix} \cos\beta & 0 & \sin\beta \\ 0 & 1 & 0 \\ -\sin\beta & 0 & \cos\beta \end{bmatrix} \quad (26)$$

and the momentary position is determined by

$$p_{FT} = \begin{pmatrix} 0 \\ 0 \\ b+z-n \end{pmatrix} \quad (27)$$

then the velocity and acceleration are given by

$$\omega_{FT} = \begin{pmatrix} 0 \\ \dot{\beta} \\ 0 \end{pmatrix}, \alpha_{FT} = \begin{pmatrix} 0 \\ \ddot{\beta} \\ 0 \end{pmatrix} \quad (28)$$

and

$$v_{FT} = \begin{pmatrix} 0 \\ 0 \\ \dot{z} \end{pmatrix}, a_{FT} = \begin{pmatrix} 0 \\ 0 \\ \ddot{z} \end{pmatrix} \quad (29)$$

for the RT

$${}^{RT}_0 A = \begin{bmatrix} \cos\varphi & 0 & \sin\varphi \\ 0 & 1 & 0 \\ -\sin\varphi & 0 & \cos\varphi \end{bmatrix} \quad (30)$$

$$p_{RT} = \begin{pmatrix} 0 \\ 0 \\ b+z-a \end{pmatrix} + \begin{pmatrix} -d \cos\gamma \\ 0 \\ d \sin\gamma \end{pmatrix} \quad (31)$$

The velocity and acceleration are

$$\omega_{RT} = \begin{pmatrix} 0 \\ \dot{\varphi} \\ 0 \end{pmatrix}, \alpha_{RT} = \begin{pmatrix} 0 \\ \ddot{\varphi} \\ 0 \end{pmatrix} \quad (32)$$

and

$$v_{RT} = \begin{pmatrix} 0 \\ 0 \\ \dot{z} \end{pmatrix} + \begin{pmatrix} d \dot{\gamma} \sin\gamma \\ 0 \\ d \dot{\gamma} \cos\gamma \end{pmatrix} \quad (33)$$

$$a_{RT} = \begin{pmatrix} 0 \\ 0 \\ \dot{z} \end{pmatrix} + \begin{pmatrix} d \ddot{\gamma} \sin\gamma \\ 0 \\ d \ddot{\gamma} \cos\gamma \end{pmatrix} + \begin{pmatrix} d \dot{\gamma}^2 \cos\gamma \\ 0 \\ -d \dot{\gamma}^2 \sin\gamma \end{pmatrix} \quad (34)$$

According to Eqs (6) and (7) from the Jacobians, the partial velocities can be extracted from corresponding generalised velocities.

3.2. Applied forces

The complete force vector is populated from each body's gravitational forces and translational forces of the spring-damper unit; finally, the tires' longitudinal and vertical forces as it resumed is presented in Fig. 3 and Tab. 1. Translational springs are force elements in rigid-body systems. The force F_s of a non-linear spring is defined by Hahn [11] as

$$F_s = K_s \cdot \frac{r_{DE,0}}{|r_{DE,0}|} \cdot (|r_{DE,0}| - l_0) \quad (35)$$

with a positive constant K_S as the stiffness coefficient, l_0 as the undeformed length of the spring and $r_{DE,0}$ as the vector of the attachment points of the spring on the Sprung mass and the Control arm, the modulus of which is its deformed length. The force F_S of the spring acts on both bodies in opposite directions where $\text{sign}(F_S)$ on the Sprung mass = $-\text{sign}(F_S)$ on the Control arm:

- For $|r_{DE,0}| - l_0 > 0$ the spring is under tension and the two bodies are pulled.
- For $|r_{DE,0}| - l_0 < 0$ the spring is under compression and the two bodies are pushed.

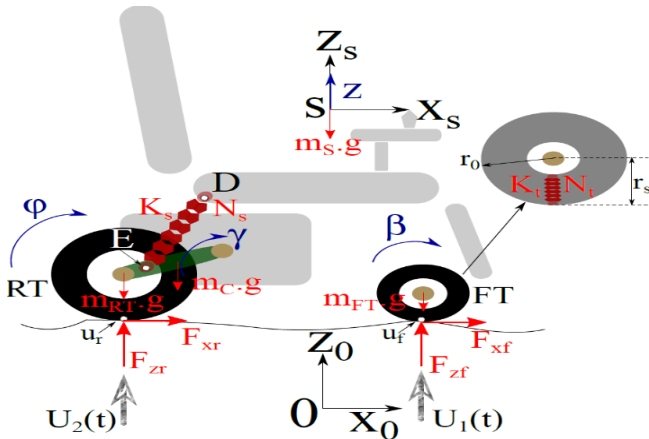


Fig. 3. Contact pressure distribution: a) gap distance effect; b) gap orientation effect Forces acting on the NL2D-EWC. FT, front tire; NL2D-EWC, non-linear two-dimensional electric wheelchair; RT, rear tire.

For the translational damper, Hahn [11] defines the force F_D as

$$F_D = N_S \cdot \frac{r_{DE,0}}{|r_{DE,0}|} \cdot |\dot{r}_{DE,0}| \quad (36)$$

while N_S is the suspension damping, $\dot{r}_{DE,0}$ represents the first derivative of the deformable length, and the sign convention is as follow:

- For $\dot{r}_{DE,0} > 0$ the damper forces exhibit a pull on the bodies.
- For $\dot{r}_{DE,0} < 0$ the two bodies move towards each other, and the damper forces exhibit a push on the bodies.

Finally, the primary force of the spring-damper unit can be found as

$$F_{SD} = F_S + F_D \quad (37)$$

According to Pacejka and Besselink [21], the normal load F_z of the wheel can be calculated as a linear function of the radial tire deflection measured by the reduction of the tire radius from the unloaded value r_0 to the loaded static radius r_s . As long as the tires are in contact with the actuator in u_k ($k := front, rear$), the vertical tire force is

$$F_{zk} = -c_{zk} \cdot (r_{0k} - r_{sk}), \quad k := front, rear \quad (38)$$

where

$$r_{sf} = b + z - n - U_1 \quad (39)$$

$$r_{sr} = b + z - a + d \cdot \sin\gamma - U_2 \quad (40)$$

The constant c_z characterises the compliance of the tires in the vertical direction. $U_1(t)$ and $U_2(t)$ are the inputs of the actuator in the points u_k at a certain time t_{step} . In the following pro-

cesses, the simulation of the road's profile will take the three forms shown in Fig. 4.

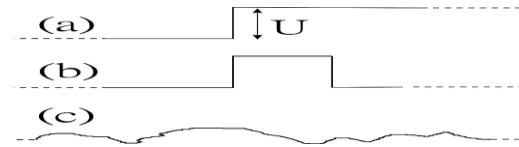


Fig. 4. Road's profiles: (a) Step, (b) Bump, (c) Random road

In the presence of adhesion in the contact area, Rill [26] defines the longitudinal tire force as

$$F_{xf} = -c_{xf} \cdot (r_{sf} \cdot \beta) - d_{xf} \cdot (r_{sf} \cdot \dot{\beta}) \quad (41)$$

$$F_{xr} = -c_{xr} \cdot (d \cdot (1 - \cos\gamma) - r_{sr} \cdot \varphi) - d_{xr} \cdot (d \cdot \sin\gamma \cdot \dot{\gamma} - r_{sr} \cdot \dot{\varphi}) \quad (42)$$

The constants c_{xk} and d_{xk} ($k := front, rear$) model the tires' longitudinal compliance and damping. It must be noted that for the rear wheel, the suspension damping affects the translational motions, and the rotation is determined by the longitudinal tire force only.

3.3. Equations of motion

Jourdain's principle is resumed in two first-order ODEs.

$$M = \begin{bmatrix} m_s + m_c + m_{FT} & (l \cdot m_c + d \cdot m_{RT}) \cos\gamma & 0 & 0 \\ (l \cdot m_c + d \cdot m_{RT}) & \Theta_c + l^2 \cdot m_c + d^2 \cdot m_{RT} & 0 & 0 \\ 0 & 0 & \Theta_{RT} & 0 \\ 0 & 0 & 0 & \Theta_{FT} \end{bmatrix} \quad (43)$$

$$q = \begin{pmatrix} F_{zr} + F_{zf} - m \cdot g + (l \cdot m_c + d \cdot m_{RT}) \cdot \sin\gamma \cdot \dot{\gamma} \\ F_{SD} - (l \cdot m_c + d \cdot m_{RT}) \cdot \cos\gamma \cdot g + d \cdot (F_{xr} \cdot \sin\gamma + F_{zr} \cdot \cos\gamma) \\ -r_{sr} \cdot F_{xr} \\ -r_{sf} \cdot F_{xf} \end{pmatrix} \quad (44)$$

where

$$m = (m_s + m_c + m_{RT} + m_{FT}) \quad (45)$$

3.4. Numerical computation

While the analytical techniques of Newton, D'Alembert, Lagrange and Jourdain were developed centuries ago, these classical approaches have proven to be suitable for implementation on high-speed digital computers when used with matrix and numerical methods. The application of those methods results in a group of differential equations that may be expressed in a very matrix form and might be solved using numerical and computer methods [30]. As proved previously, two ODEs sum up Jourdain's principle and they read as

$$\dot{y} = x \quad (46)$$

$$M \cdot \dot{x} = q \quad (47)$$

Kane and Levinson [18] have concluded that the process proposed here may be expected to lead to computational algorithms involving fewer arithmetic operations than algorithms generated by employing the best available Lagrangian and Newton-Euler

approaches. The MATLAB function ode45 solves the ODEs in Eqs (43) and (44). To recover the accelerations, after the integration process is completed, knowing the coordinates and velocities at every reported time step, we recomputed the accelerations by reconstructing the equations of motion. The results will be validated next.

4. COMPARATIVE ANALYSIS OF THE MODEL

4.1. Data setting

The parameters, the geometric constants and the initial values are collected in Tabs 1, 2 and 3 in order to perform the NL2D-EWC model.

Tab. 1. Model's parameters

Designation, (symbol)	Value	Unit
Sprung mass with/without user's weight, (m_s)	130/50	kg
Mass of the control arm, (m_c)	2	kg
Mass of the rear wheel, (m_{RT})	8	kg
Mass of the front wheel, (m_{FT})	4	kg
Inertia of the control arm, (Θ_c)	0.6	kg.m ²
Inertia of the rear wheel, (Θ_{RT})	0.5	kg.m ²
Inertia of the front wheel, (Θ_{FT})	0.5	kg.m ²
Suspension stiffness, (K_s)	10,000	N/m
Suspension damping, (N_s)	2,150	N.s/m
Longitudinal RT stiffness, (c_{xr})	20,000	N/m
Longitudinal RT damping, (d_{xr})	1,500	N.s/m
Vertical RT stiffness, (c_{zr})	98,700	N/m
Longitudinal FT stiffness, (c_{xf})	200,000	N/m
Longitudinal front tire damping, (d_{xf})	1,500	N.s/m
Vertical front tire stiffness, (c_{zf})	98,700	N/m
Gravity, (g)	9.81	m/s ²

FT, front tire; RT, rear tire.

Tab. 2. Constants of the NL2D-EWC

Designation,(symbol)	Value (m)
Distance between the joint Bc and the Control arm CoG, l	0.210
Distance between joint Bc and joint Br, d	0.266
Distance between Sprung mass CoG and joint Bc, a	0.383
Distance between Sprung mass CoG and the ground, b	0.574
Distance between Sprung mass CoG and joint Bf, n	0.489
RT radius, rr_0	0.173
FT radius, rf_0	0.085
Vertical position of spring attachment D, h	0.087
Longitudinal position of spring attachment D, f	1.37
Distance between Front Tire centre and joint Bc, d_2	0.3
Distance between joint Bc and spring attachment E, e	0.28

FT, front tire; RT, rear tire; NL2D-EWC, non-linear two-dimensional electric wheelchair

Tab. 3. Initial values

Designation	Value	Unit
z_0	0	m
γ_0	0	rad
ϕ_0	0	rad
β_0	0	rad
\dot{z}_0	0	m/s
$\dot{\gamma}_0$	0	rad/s
$\dot{\phi}_0$	0	rad/s
$\dot{\beta}_0$	0	rad/s

4.2. Model's implementation in MBD for Ansys/RecurDyn

To validate the mathematical model developed in MATLAB, a Three-Dimensional Electric Wheelchair (3D-EWC) was built in MBD for Ansys, a professional multi-body dynamics simulation software powered by RecurDyn. The 3D-EWC appearing in Fig. 5(a) was inspired from the KARMAN's XO-202 electric wheelchair, but some differences exist concerning the design, the measurements and the objective. The seat of the model is not supposed to stand up as the KARMAN's does.

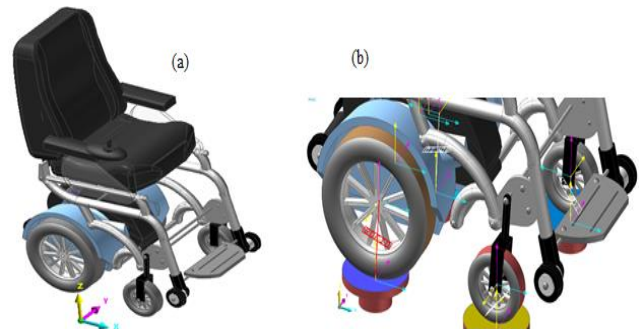


Fig. 5. (a) The 3D-EWC, (b) Tire/Actuator contact: Test-rig. 3D-EWC, three-dimensional electric wheelchair

For the designations shown in the previous tables, the NL2D-EWC and the 3D-EWC have the same values but it is clear that the 3D model has a larger geometry. When the tire-road interaction is simulated by either a bumped road or a test-rig, as shown in Fig. 5(b), an adequate contact between the surfaces needs to be adjusted. Tab. 4 presents the "Solid" contact properties.

Tab. 4. Solid contact properties

Designation	Value
Bounding buffer length	10^9
Plane tolerance factor	3
Contact spring coefficient	3,000
Contact damping coefficient	8,200
Rebound damping factor	0.25

4.3. Simulation and results

In this section, two scenarios will be presented. First, the NL2D-EWC will be treated as a quarter-car model by applying a step motion to the RT, the same as in Fig. 4(a). In 3 s of time simulation, the dynamical behaviour is approved by the 3D-EWC with a step that is 0.05 m high at 1.5 s and without considering

the user's weight ($m_s = 50$ kg), as illustrated in Fig. 6.

The figure shows the vertical displacement, velocity and acceleration of the Sprung mass in the first part where a good correlation between the modelled and simulated behaviour is noticed. In the second part of Fig. 6, the rotations of the Control arm and those of the RT are quite identical to the simulation.

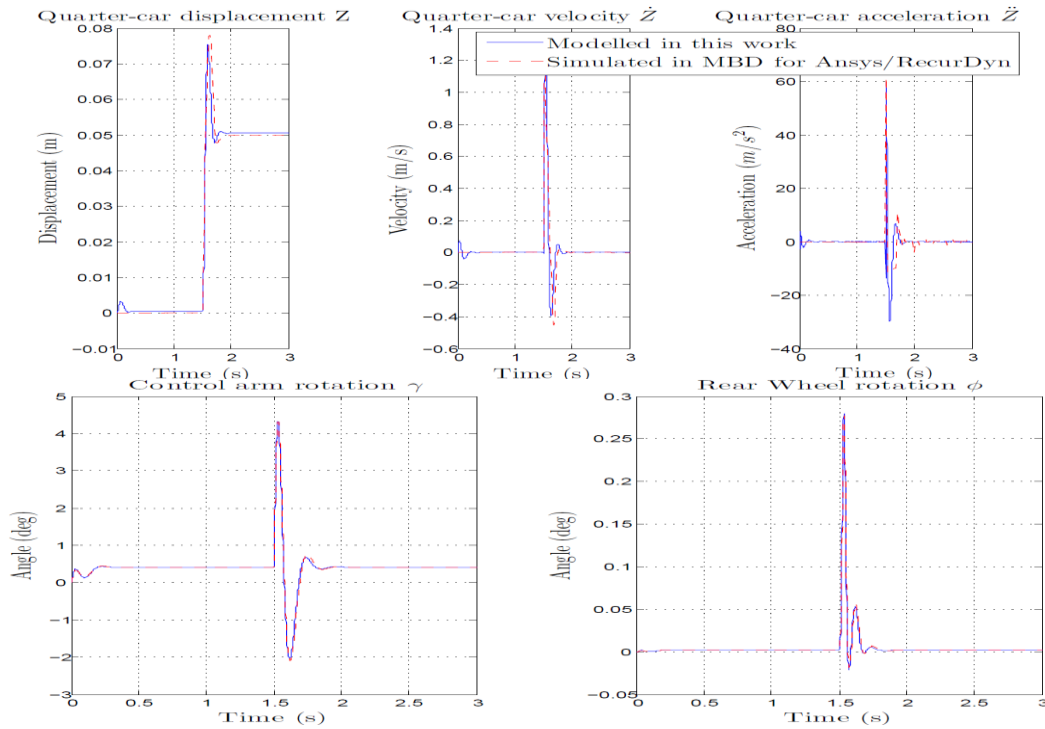


Fig. 6. NL2D-EWC quarter-car vs. MBD for Ansys model: The step case behaviour. NL2D-EWC, non-linear two-dimensional electric wheelchair

Second, the entire NL2D-EWC will be engaged by simulating a bump obstacle, as presented in Fig. 4(b), of 0.03 m length and $U_{1,2} = 0.02$ m high acting at two-time steps 0.25 s and 0.75 s on the FTs and RTs, respectively. The user's weight is considered and the total mass corresponding to the Sprung mass is $m_s = 130$ kg. The NL2D-EWC gives information about the position, velocity and acceleration of the four coordinates $y = (z \ \gamma \ \beta \ \varphi)^T$. From this point, we will be interested in the vertical motion of the Sprung mass shown in Fig. 7. The bump disturbance for the front wheel is given in MBD for Ansys/RecurDyn by the following composition of functions:

$$\text{STEP}(\text{time}, 1.0, 0.0, 1.1, 0.02) + \text{STEP}(\text{time}, 1.4, 0.02, 1.5, 0.0)$$

The highest peaks in Fig. 7 are related to the displacement and acceleration of the Sprung mass when the FT passes over the obstacle, while the lower peaks are associated with the RT passage; these observations assume relevance in light of the fact that a suspension exists that connects the tire to the Sprung mass. In those experiments, there is a good agreement between the results of the mathematical and the simulated models. The small differences may be due to the linearisation of the equations of motion as it was estimated in Hurel et al. [14] or merely to the complexity of the 3D model over the non-linear two-dimensional one.

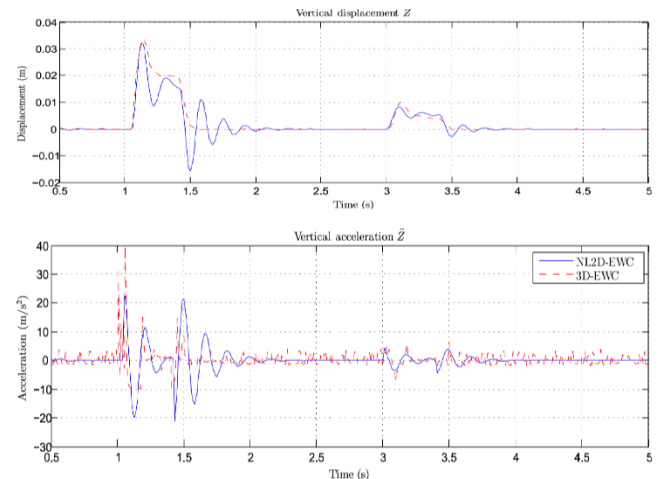


Fig.7. NL2D-EWC vs. 3D-EWC measurements: The bump case. 3D-EWC, three-dimensional electric wheelchair; NL2D-EWC, non-linear two-dimensional electric wheelchair

5. OPTIMISATION PROCESS FOR RIDE COMFORT, ROAD HOLDING AND SUSPENSION WORKSPACE

The optimal design of a multi-body system is started by defining an objective function, which contains the performance criteria. An objective function based on a process of multi-body dynamics

occurs in an interval of time. It is often considered as a time integral of a function that has a set of conditions within that span [9]. For that purpose, The NL2D-EWC model based on Jourdain's principle will be included in a global optimisation program.

5.1. Parameters of the dynamic optimisation

The weighted RMS of the Sprung mass' acceleration is frequently used to evaluate the riding quality of a vehicle [15]. The rider's comfort improves as the acceleration decreases. The MATLAB function rms returns the RMS level of the vector \ddot{Z}_S where the waveform is a continuous function of time [23]

$$f_1 = rms(\ddot{Z}) = \sqrt{\left(\frac{1}{t_{End}-t_0}\right) \cdot \int_{t_0}^{t_{End}} \ddot{Z}_S^2(t) \cdot dt} \quad (48)$$

The continual contact between the tires and the road surface is one of the essential factors underlying the designing of the suspension parameters. Therefore, the road holding will be a second objective. While applying the random processes theory for road holding evaluation, the RMS value of the dynamic vertical force F_{zi} ($i = front, rear$) between wheels and road, caused by the road irregularities, has been taken as the criterion for road holding. Sinha [32] concludes that for good road holding this value should have a minimum rate. The loads for FTs and RTs in Eq. (38) will be combined as

$$f_2 = \sqrt{\kappa_f^2 \cdot rms(F_{zf})^2 + \kappa_r^2 \cdot rms(F_{zr})^2} \quad (49)$$

$\kappa_f = 0.6$ and $\kappa_r = 0.4$ are coefficients imposed to regulate the combination. Due to the restriction of the structure and the vehicle's design, the space between the wheels and the suspended mass must be limited to one stroke, which is frequently referred to as the working space. To provide a better workspace, it is necessary to reduce this change in distance [29]. Consequently, the modulus of the vector between the attachment points D and E is chosen as the third cost function, which is given by

$$f_3 = \left\| \frac{r_{DE,0}}{|r_{DE,0}|} \cdot (|r_{DE,0}| - l_0) \right\| \quad (50)$$

Eq. (50) was presented previously as the deformed length of the non-linear spring-damper unit. The eight design variables are

$$V = (m_S \ m_C \ m_{FT} \ m_{RT} \ K_S \ N_S \ c_{zf} \ c_{zr})^T \quad (51)$$

Thus, the dynamic optimisation problem can be described as

$$\text{Minimise } \begin{cases} f_1(V) \\ f_2(V) \\ f_3(V) \end{cases}$$

While the initial state of the NL2D-EWC was presented previously, the bounds of the optimisation variables are resumed in Tab. 5.

If an objective function has sensitivity to varying parameters, it may have difficulty during the process. The problem arising from comparing one value of mass and another of stiffness is expected to be clearly apparent. The transformation of the initial representation, which contains information about the physical nature, into a scaled representation is numerically efficient [10]. Each variable V_i will be scaled to 1 by

$$\hat{V}_i = \frac{V_i - lb_i}{ub_i - lb_i} \quad (52)$$

where \hat{V}_i , lb_i and ub_i are the new scaled variable, the lower bound and the upper bound, respectively. It is necessary that the original design variables be used to calculate the objective function.

Tab. 5. Variables bonds of the dynamic optimisation

Variables	Bonds	
	lower	upper
m_S	46	80
m_C	0.9	3.5
m_{FT}	2.5	4.5
m_{RT}	5	14
K_S	10,000	20,000
N_S	1,000	2,500
c_{zf}	90,000	100,000
c_{zr}	90,000	100,000

5.2. Generation of an artificial-random road profile

The random road profile in Fig. 4(c) is chosen to be the form of excitation in the process. The literature is rich in characterisation of the road profile where most of it is made by the PSD. Doods and Robson [7] illustrate the profile classifications presented in ISO-8608 (International Organization for Standardization), from smooth irregularities (class A) to rough terrain (class E). Rill [26] and Balkwill [3] both describe an efficient generation of a random profile, which can have the form of

$$\Phi(\Omega) = \Phi(\Omega_0) \cdot \left(\frac{\Omega}{\Omega_0}\right)^{-\omega} \quad (53)$$

where the wave number expressed in (rad/m) is

$$\Omega = 2\pi/L \quad (54)$$

and the value of PSD at $\Omega_0 = 1$, ($m^2/(rad/m)$) is

$$\Phi_0 = \Phi(\Omega_0) \quad (55)$$

L represents the wavelength (m), Ω_0 is the reference wave number (rad/m) and ω is the waviness. A sinusoidal approximation of a random profile U_R by a superposition of N ($0 \leq N \leq \infty$) waves is

$$U_R(s) = \sum_{i=1}^N A_i \cdot \sin(\Omega_i \cdot s - \Psi_i) \quad (56)$$

The momentary position of the wheelchair with the associated longitudinal speed v_x and the phase angles Ψ_i is given by

$$s = v_x \cdot t \quad (57)$$

Eq. (56) can offer a PSD $\Phi(\Omega_0)$ if it has a set of amplitudes

$$A_i = \sqrt{2 \cdot \Phi(\Omega_i) \cdot \Delta\Omega} \ , \quad i = 1(1)N \quad (58)$$

The applied input of the random road profile shown in Fig. 8 is associated with a roughness of a class B, a good road that is modelled by the values in Tab. 6. The NL2D-EWC travels at a constant speed $v_x = 8 \text{ km/h}$ and it is supposed that the rear wheel has the same input as the front wheel but delayed by $\delta t = (d \cdot \cos\gamma + d_2)/v_x$. The phase angles are distributed

uniformly and randomly as $\Psi_i = 2\pi.\text{randn}(\text{size of } i = 1(1)N)$. The MATLAB function randn produces the same normally distributed pseudorandom numbers each time the program restarts, which is ideal for an optimisation process.

Tab. 6. PSD characteristics of a class B profile

Designation	Value	Unit
N	200	–
Ω_0	1	(rad/m)
$\Delta\Omega \equiv [\Omega_{min}, \Omega_{max}]$	[0.05, 32.83]	(rad/m)
Φ_0	5.10^{-6}	($m^2/(rad/m)$)
ω	2	–

PSD, power spectral density

The road profiles in Fig. 8 are the same, but the phase shift between the continuous black profile, related to the FT, and the dotted magenta profile, linked to the RT, represents the time between the passage of the tires over the same point. These two profiles will be the step inputs u_f and u_r of the road in the following section.

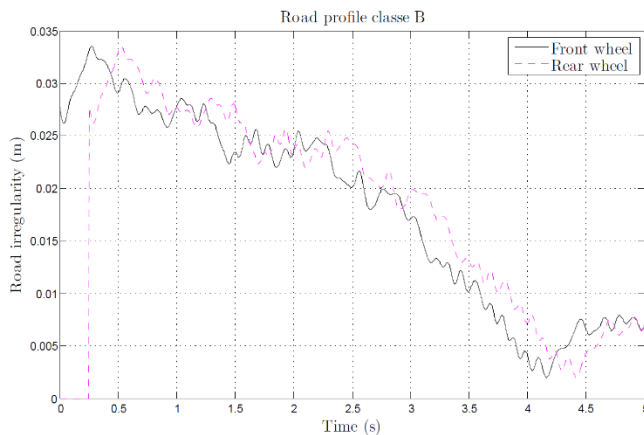


Fig. 8. Excitation for smooth road of Class B

5.3. Multi-objective optimisation with genetic algorithm

Considered as meta-heuristics, evolutionary algorithms based on populations of solutions can solve multi-objective problems and generate solutions in the form of fronts. Thus, Deb [6] published in 2001 a book on the use of evolutionary algorithms for multi-objective optimisation, in which his Non-dominated Sorting Genetic Algorithm (NSGA) was upgraded and improved to NSGA-II. During its execution, the genetic algorithm constantly alters a group of solutions to pick individuals from the actual population to be parents. Under some criteria, the chosen parents are served to create a new generation of children, or simply the next individuals. This consecutive creation of generations yields steadily to one or more optimal solutions, depending on the number of objectives ([19]). This work will benefit from the variety of options in the MATLAB Optimisation Toolbox. The genetic algorithm gamultiobj, a variant of NSGA-II (<https://www.mathworks.com>), will be used to evaluate the effectiveness of the NL2D-EWC model with the options provided in Tab. 7 and the remaining default parameters.

Tab. 7. Problem setting with gamultiobj options

Designation	Value
PopulationSize	250
CrossoverFraction	0.8
MaxGenerations	400
FunctionTolerance	10^{-4}

The solutions are shown in the decision-variables space in Fig. 9(a) and the objective space in Fig. 9(b) by using parallel-coords. The solution set is distributed rather irregularly in parallel coordinate plots, which is not a badly-distributed solution set, as uniformly-distributed solutions can have distinct values on different objectives.

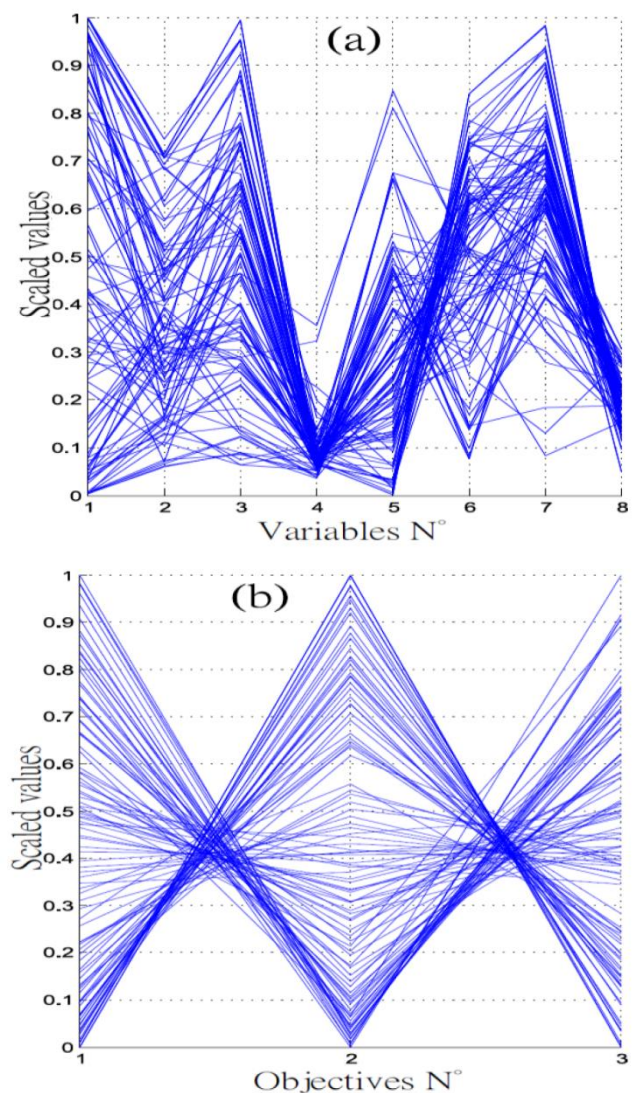


Fig. 9. Parallel Coordinates representation: (a) Sensitivity to the problem parameters, (b) Distribution of solutions

These solutions for the three objectives are illustrated in the 3D Pareto front of Fig. 10. From the variety of solutions, one can recognise those in extremities with the best score for each criterion. It is observed, in the non-dominant solutions of (a), (b) and (c), that the 2D Pareto front of the RMS of vertical acceleration and the Suspension workspace seem to be non-convex and the two

criteria have almost the same optimal solutions. Otherwise, there

is a clear diversity with the Combined tires' loads.

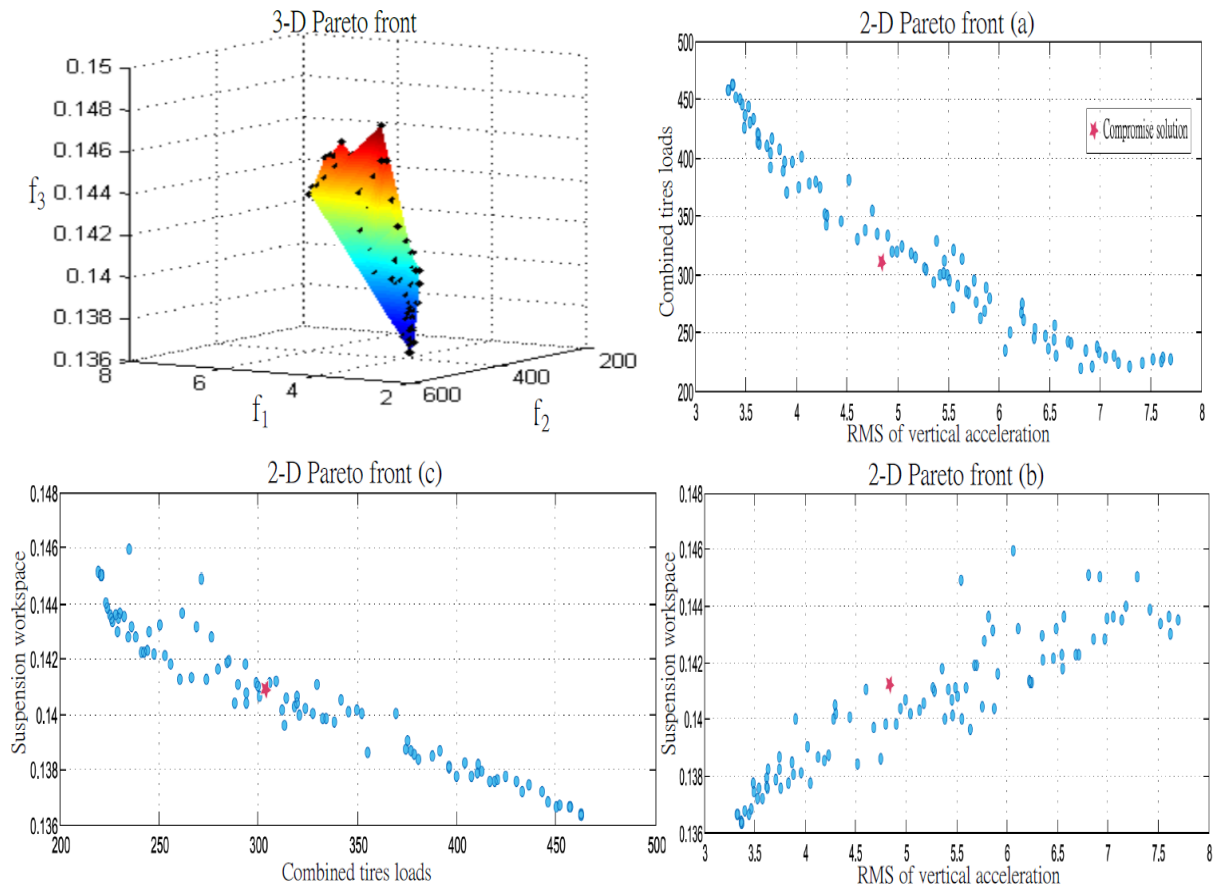


Fig. 10. Surface plot of 3D Pareto front and 2D-Pareto fronts for all combination (a, b, and c). RMS, root-mean-square

The compromised solution, marked by a red star in the figure, can be selected depending on the design preference, but this operation is sometimes difficult. In order to visualise the relation between criteria and facilitate the selection of the compromise point, the decision can be made easier by introducing Level Diagrams (LD) visualisation, which helps to understand the calculated Pareto front and gives correlation between objective and decision space. Reynoso-Meza et al. [25] proposed that each objective $f_p(V)$, ($p = 1, 2$ and 3), is scaled similarly to Eq. (52)

$$\hat{f}_p(V) = \frac{f_p - f_p^{min}}{f_p^{max} - f_p^{min}} \quad (59)$$

For every normalised objective vector $\hat{f}(V) = [\hat{f}_1(V), \dots, \hat{f}_m(V)]$ a p -norm $\|\hat{f}(V)\|_p$ is applied to assess the distance to an ideal and minimal solution at the same time, where

$$\begin{cases} \|\hat{f}(V)\|_1 = \sum_{p=1}^2 \hat{f}_p(V)^2 \\ \|\hat{f}(V)\|_2 = \sum_{p=2}^3 \hat{f}_p(V)^2 \\ \|\hat{f}(V)\|_3 = \hat{f}_1(V)^2 + \hat{f}_3(V)^2 \end{cases} \quad (60)$$

The LD representation shows a two-dimensional graph for each objective and variable. The arranged sets $(f_p(V), \|\hat{f}(V)\|_p)$ are plotted in each objective and variable sub-graph. Consequently, a prearranged solution will have a similar y-value in all displays. This correspondence makes it possible to compare solutions concurring to the chosen norm according to the general tendencies along the Pareto front. Fig. 11 demonstrates LD plots for each combination, the knee point of which is clearly manifested in all of them. It is noteworthy to observe that the figure is divided into three rows according to the colours. The graphs with red markers are LD for vertical acceleration and combined wheel load, where the minimum value (knee) on the y-axis represents the best score for each objective but in relation to the other. The same goes for the yellow and blue rows. The compromise solution shown in the previous figure was selected with help of the LD representations. The results of the optimisation process, with a CPU-time (central processing unit) of 64,679 s, are displayed in Tab. 8. The table compares the scores of the best trade off (corresponding to the compromised solution) with the best candidate in each criterion; considered individually, these scores demonstrate better values. The optimal variables are illustrated as well.

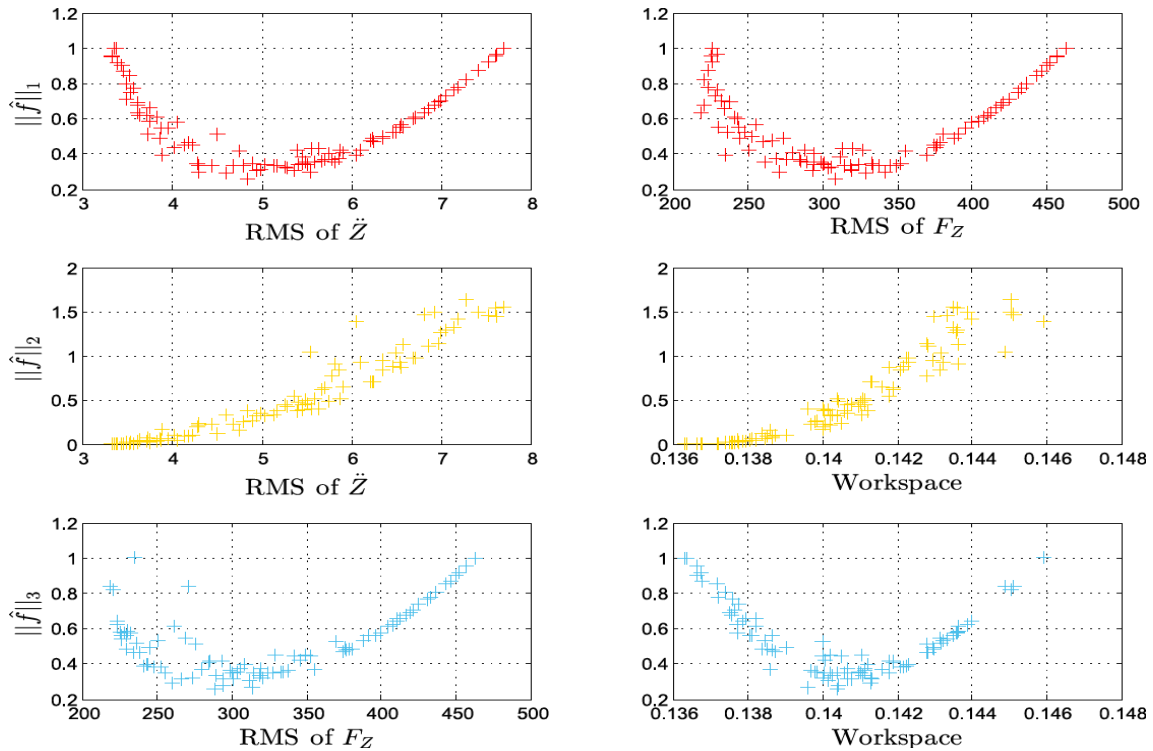


Fig.11. LD representation of Pareto fronts for each bi-objectives. LD, level diagrams; RMS, root-mean-squar

Tab. 8. Best trade off, best candidate in each criterion and optimal variables

Best trade off (compromised solution)		Best candidate in each criterion	
Designation	Value	Designation	Value
f_1	4.8400	f_1	3.3281
f_2	309.3130	f_2	219.2769
f_3	0.1412	f_3	0.1363
Optimal variables of the compromised solution			
Variable	Optimal value	Variable	Optimal value
m_s	64.8411 kg	K_s	14,477 N/m
m_c	1.3581 kg	N_s	1,932.6 N.s/m
m_{FT}	3.4178 kg	c_{zf}	96,210 N/m
m_{RT}	5.5654 kg	c_{zr}	91,481 N/m

The comparison between the original and the optimised vertical acceleration in Fig. 12 reveals an acceptable decrease in the maximum peak related to the first impact with the obstacle but a slight one for the rest of the time simulation.

Fig. 13 displays front and RTs optimised loads relative to their original curves. Both loads achieved a small improvement, especially the frontal. This superiority of the front load is due to the number of variables affecting the behaviour of the FT, which is lower than that of the RT linked to the Control arm and to the Sprung mass.

Similar to the other objectives, the suspension workspace in Fig. 14 gains a general reduction of the RMS although the simulation of the optimal values has no advantage over the origin curve after the FT-obstacle impact period.

The behaviour of the three criteria was identical with some

slight difference in the values of the best compromise and the best candidate in each criterion, especially for the combined tires' load. This is due to the non-dominant role of the mass m_s in the motion of the FT and the favouring of the coefficient κ_f ($\kappa_f = 0.6$ and $\kappa_r = 0.4$) in the formula for this objective (f_2) in Eq. (49). Optimisation with user's mass has shown that for high Sprung mass or high user's mass, the RMS of vertical acceleration and the suspension workspace will be lower. However, for the load of the tires it is the opposite.

The simulations presented previously in the optimisation process did not take into account the mass of the user. To increase the results, a new simulation was run by adding a fixed average additional mass (80 kg) to the variable mass of the Sprung mass. Tab. 9 contains a comparison between the values without and with the user's mass.

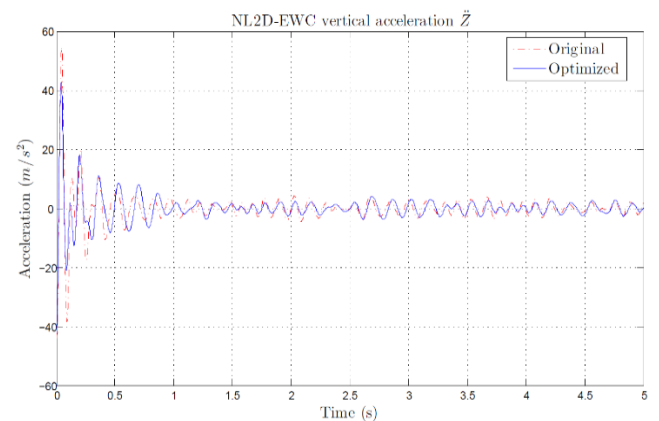


Fig.12. Vertical acceleration of the sprung mass: Optimised vs. origin. NL2D-EWC, non-linear two-dimensional electric wheelchair

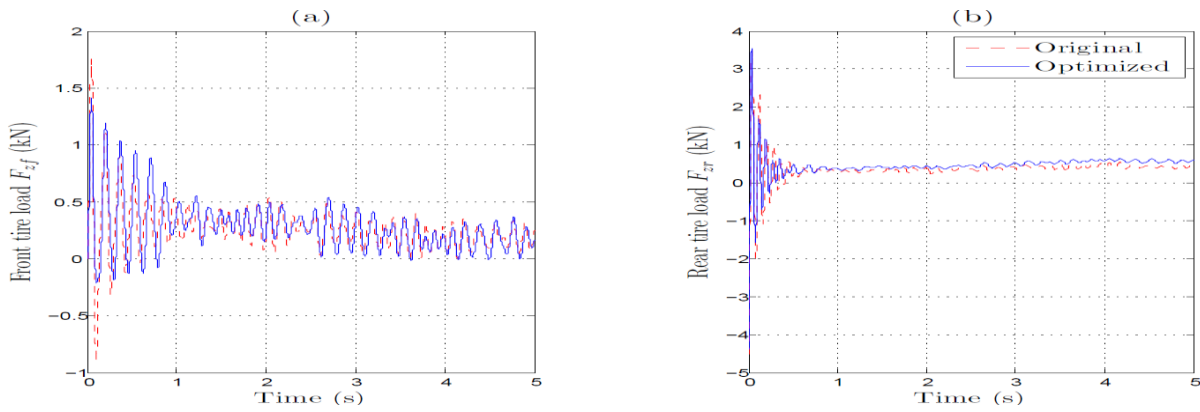


Fig.13. Wheel's load: (a) FT load: Optimised vs. origin, (b) RT load: Optimised vs. origin. FT, front tire; RT, rear tire

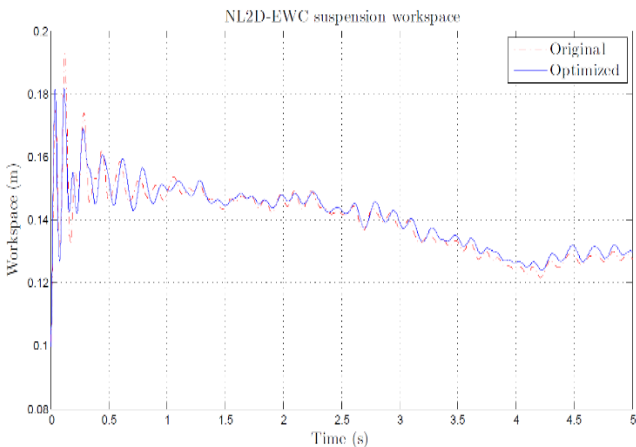


Fig.14. Suspension workspace: Optimised vs. origin. NL2D-EWC, non-linear two-dimensional electric wheelchair

Tab. 9. Best trade off, best candidate in each criterion of the optimisation without and with the user's mass

Objective	Optimisation without the user's mass		Optimisation with the user's mass	
	Best trade off	Best candidate	Best trade off	Best candidate
f_1	4.8400	3.3281	2.1924	1.9229
f_2	309.3130	219.2769	792.9069	569.6984
f_3	0.1412	0.1363	0.1312	0.1280

6. CONCLUSION

This paper presents a description of Jourdain's principle through its application in modelling an electric wheelchair. Therefore, the equations of motion were formulated on this interpretation to facilitate their comprehension. The approach provided advantages over other classical formulations. The concept of generalised coordinates and velocities was used to embed the constraints and derive first-order differential equations. An appropriate choice of velocities conducts to decoupled second derivatives. The method also suggested that the virtual power of constraint forces vanishes from the beginning, which was another advantage. The straightforward implementation of the principle

was noteworthy and the reduced number of symbolic equations characterised the efficiency of the calculations.

Despite the slight dissimilarities, the comparison between the responses of the two-dimensional non-linear model and the three-dimensional one built into the simulation software showed that a precise setting in the multi-body modelling of mechanical systems could offer great results in a short time with low processing capacity requirements.

The improved ride comfort, road holding and working space of the suspension made it possible to test the effectiveness of the model. The objective cost functions for these criteria have been defined and inserted into a MATLAB multi-objective genetic algorithm. The scaling of the variables allowed a balanced scanning in their intervals. Acceptable solutions were captured on the Pareto fronts, but the non-convexity between ride comfort and the suspension workspace was noticeable, making the latter unprofitable. While the FT load was initially preferred over the rear load, the final decision of the compromise solution between all criteria was estimated by using the LD visualisation. It has been noticed that the generation of a random road profile by the PSD considerably increased the processing time.

REFERENCES

- Ahmad S, Tokhi M, Toha S. Genetic Algorithm Optimisation for Fuzzy Control of Wheelchair Lifting and Balancing. Uksim European Symposium On Computer Modeling And Simulation. 2009.
- Anandan A, Kandavel A. Investigation and performance comparison of ride comfort on the created human vehicle road integrated model adopting genetic algorithm optimized proportional integral derivative control technique. Proceedings Of The Institution Of Mechanical Engineers Part K: Journal Of Multi-Body Dynamics. 2020; 234(2): 288-305.
- Balkwill J. Performance vehicle dynamics: Engineering and Applications. Elsevier. 2018.
- Chen S, Shi T, Wang D, Chen J. Multi-objective optimization of the vehicle ride comfort based on Kriging approximate model and NSGA-II. Journal Of Mechanical Science And Technology. 2015; 29(3):1007-1018.
- Dad K, Khan M, Jie W, Lee M. A low cost genetic algorithm based control scheme for wheelchair control in hospital environment. Proceedings Of International Conference On Artificial Life And Robotics. 2016; 21:212-216.
- Deb K. Multi-objective optimization using evolutionary algorithms. John Wiley & Sons, Ltd. 2001.
- Dodds C, Robson J. The description of road surface roughness. Journal Of Sound And Vibration. 1973; 31(2):175-183.

8. Fossati G, Miguel L, Casas W. Multi-objective optimization of the suspension system parameters of a full vehicle model. *Optimization And Engineering*. 2018; 20(1):151-177.
9. Garcia de Jalon J, Bayo E. *Kinematic and dynamic simulation of multibody systems*. Springer. 1984.
10. Gill P, Murray W, Wright M. *Practical optimization*. SIAM. 2019.
11. Hahn H. *Rigid body dynamics of mechanisms*. Springer. 2003.
12. <https://www.karmanhealthcare.com/product/xo-202/> [online cit.: 2020.06.16].
13. <https://www.mathworks.com/help/gads/gamultiobj-algorithm.html>. [online cit.: 2021.01.29].
14. Hurel J, Mandow A, Garcia-Cerezo A. Nonlinear two-dimensional modeling of a McPherson suspension for kinematics and dynamics simulation. *12th IEEE International Workshop On Advanced Motion Control (AMC)*. 2012.
15. Jazar R. *Vehicle dynamics – theory and application (3rd ed.)*. Springer. 2017.
16. Jourdain P. Note on an Analogue of Gauss Principle of Least Constraint. *The Quarterly Journal of Pure and Applied Mathematics*. 1909; 40:153-157.
17. Kane T. Dynamics of Nonholonomic Systems. *Journal Of Applied Mechanics*. 1961; 28(4):574-578.
18. Kane T, Levinson D. The Use of Kane's Dynamical Equations in Robotics. *The International Journal Of Robotics Research*. 1983; 2(3):3-21.
19. Messac A. *Optimization in practice with MATLAB for engineering students and professionals*. Cambridge University Press. 2015.
20. Nariman-Zadeh N, Salehpour M, Jamali A, Haghgoo E. Pareto optimization of a five-degree of freedom vehicle vibration model using a multi-objective uniform-diversity genetic algorithm (MUGA). *Engineering Applications Of Artificial Intelligence*. 2010; 23(4):543-551.
21. Pacejka H, Besselink I. *Tire and vehicle dynamics*. Elsevier/BH. 2012.
22. Papastavridis J. On Jourdain's principle. *International Journal Of Engineering Science*. 1992; 30(2):135-140.
23. Paulter N, Larson D, Blair J. The IEEE Standard on Transitions, Pulses, and Related Waveforms. Std-181-2003. *IEEE Transactions On Instrumentation And Measurement*. 2004; 53(4):1209-1217.
24. Piedboeuf J. Kane's equations or Jourdain's principle?. *Proceedings Of 36th Midwest Symposium On Circuits And Systems*. 1993.
25. Reynoso-Meza G, Blasco X, Sanchis J, Herrero J. Comparison of design concepts in multi-criteria decision-making using level diagrams. *Information Sciences*. 2003; 221:124-141.
26. Rill G. *Road vehicle dynamics*. CRC Press. 2012.
27. Roberson R, Schwertassek R. *Dynamics of Multibody Systems*. Springer Berlin Heidelberg. 1988.
28. Sankardoss V, Geethanjali P. Parameter estimation and speed control of a PMDC motor used in wheelchair. *Energy Procedia*. 2017; 117:345-352.
29. Seifi A, Hassannejad R, Hamed M. Use of nonlinear asymmetrical shock absorbers in multi-objective optimization of the suspension system in a variety of road excitations. *Proceedings Of The Institution Of Mechanical Engineers. Part K: Journal Of Multi-Body Dynamics*. 2016; 231(2):372-387.
30. Shabana A. *Computational dynamics*. John Wiley & Sons. 2010.
31. Shirahatti A, Prasad P, Panzade P, Kulkarni M. Optimal design of passenger car suspension for ride and road holding. *Journal Of The Brazilian Society Of Mechanical Sciences And Engineering*. 2008; 30(1):66-76.
32. Sinha B. *Influence of road unevenness on road holding and ride comfort*. Stockholm: Department of Machine element design. Royal Institute of Technology. 1973.
33. Van der Sande T, Besselink I, Nijmeijer H. Rule-based control of a semi-active suspension for minimal sprung mass acceleration: design and measurement. *Vehicle System Dynamics*. 2016; 54(3):281-300.
34. Vingback J, Jeppsson P, van Deventer J. Evaluating Ride Comfort for Wheelchair Passengers Utilizing a Motionbase Simulator. *16th International Conference On Advanced Vehicle Technologies; 11th International Conference On Design Education; 7th Frontiers In Biomedical Devices*. 2014; 3.
35. Wang S, Zhao L, Hu Y, Yang F. Vibration Characteristics Analysis of Convalescent-Wheelchair Robots Equipped with Dynamic Absorbers. *Shock And Vibration*. 2018; 1-16.

Mohamed Belhorma:  <https://orcid.org/0000-0001-7063-4170>

Aboubakar S. Bouchikhi:  <https://orcid.org/0000-0002-3389-9177>

MHD FORCED CONVECTION USING FERROFLUID OVER A BACKWARD FACING STEP CONTAINING A FINNED CYLINDER

Meriem TOUMI¹, Mohamed BOUZIT², Fayçal BOUZIT², Abderrahim MOKHEFI²

¹Laboratory of Maritime Sciences and Engineering LSIM Faculty of Mechanical Engineering,
University of Science and Technology of Oran, Mohamed Boudiaf, El Mnaouar, B.P.1505, 31000, Oran, Algeria.

²Mechanics, Modeling and Experimentation Laboratory L2ME, Faculty of Sciences and Technology,
Bechar University B.P.417, 08000, Bechar, Algeria,

meriem.toumi@univ-usto.dz, bouzit_mohamed@yahoo.fr, faycal.bouzit@yahoo.fr, abderrahim.mokhefi@univ-bechar.dz

received 21 September 2021, revised 15 November 2021, accepted 2 December 2021

Abstract: In this paper, a numerical study of forced convection on a backward facing step containing a single-finned fixed cylinder has been performed, using a ferrofluid and external magnetic field with different inclinations. The partial differential equations, which determine the conservation equations for mass, momentum and energy, were solved using the finite element scheme based on Galerkin's method. The analysis of heat transfer characteristics by forced convection was made by taking different values of the Reynolds number (Re between 10 and 100), Hartmann number (Ha between 0 and 100), nanoparticles concentration (ϕ between 0 and 0.1) and magnetic field inclination (γ between 0° and 90°); also, several fin positions α [0° – 180°] were taken in the counter clockwise direction by a step of 5. After analysing the results, we concluded that Hartmann number, nanoparticles concentration, Reynolds number and magnetic field angles have an influence on the heat transfer rate. However, the fin position on the cylinder has a big impact on the Nusselt number and therefore on heat transfer quality. The best position of the fin is at ($\alpha = 150^\circ$), which gives the best Nusselt number and therefore the best heat transfer, but the fin position at ($\alpha = 0^\circ$) remains an unfavourable case that gives the lowest Nusselt values.

Key words: fin positions, forced convection, nanoparticles, heat transfer, finned cylinder, magneto-hydrodynamic, backward facing step

1. INTRODUCTION

The presence of the singularities on the fluid flows in the duct causes changes in the characteristics of the flow and heat transfer, and this is the reason for the sudden expansions or backward facing step being of great interest in many industrial applications. It was performed a numerical analysis to study the effect of Reynolds number on the flow characteristics; the results obtained indicated that the sizes of recirculation zones are influenced by variation of Reynolds number [1-2]. A numerical investigation was carried out on a backward facing step to study the effect of Reynolds number and the aspect ratio on the separation and reattachment fluid flow and heat transfer characteristics. A significant influence on heat transfer was observed [3-4]. A mixed convection using different values of control parameters such as Reynolds number, Richardson number and Grashof number was numerically studied. Their results indicate that there exists an effect on structure of fluid flow and heat transfer and that a secondary recirculating flow always occurs inside the primary recirculation zone [5-6]. A numerical simulation of forced convection to study the effect of the Prandtl number on mean temperatures, heat transfer coefficients and heat fluxes was presented. Therefore, for low Prandtl numbers, the Nusselt number achieves the smaller value. The maximum heat transfer location moves upstream of the reattachment point for larger Prandtl numbers [7]. An oscillating fin had mounted on the top wall of backward facing step; the oscillating fin was identified as the most effective method since it involved the highest average Nusselt number and lowest pressure drop; also, there is negligible change in average Nusselt

number resultant to the increase in the oscillation amplitude [8]. A circular cylinder was added in a duct. The Nusselt number reaches a maximum value of 155% compared to the case of a geometry without a cylinder [9].

Convective heat transfer of fluid flows in presence of nanoparticles and magnetic field are intensively studied. The use of nanofluids under the influence of the magnetic field has become one of the most prominent researched topics in recent times. It was observed that when the Reynolds number and nanoparticles volume fraction increase, the rate of heat transfer increases. Increase in Hartmann number causes a degradation in the rate of heat transfer [10]. The effect of step height on flow and characteristics of heat transfer studied by [11], they observed that average Nusselt number and skin friction coefficient increase with the increase of the step height. Numerical investigations of convective flow to study the effect of nanoparticles' insertion in base fluid on heat transfer quality was performed by [12-17]. They observed that average Nusselt number increases with increasing nanoparticles' fraction volume relative to the pure fluid (without the presence of the nanoparticles). Nanoparticles cause changes in the characteristics of flow, increase vortices number and improve mass transfer. [18-19] investigated the effect of Baffle locations at the top wall and at the bottom wall of a duct; based on the analysis of their numerical results, they indicate that the effects of distance height baffle and their locations on fluid flow and characteristics of heat transfer are significant. When length baffle increases, the recirculation region behind the backward facing step shrinks and average Nusselt number increases by increasing the length baffle. The blockage shapes had used, and their effect on nanofluids' convective flow was studied [20-22]. Their results

indicate that average Nusselt number takes the highest value when triangular blockage shapes are added on backward facing step. For trapezoidal blockage shapes, average Nusselt number is lowest. In addition, they observed that heat transfer enhancement is obtained for angular velocities $\Omega = -4.5$ and 1.5 in the cylindrical blockage shapes' case. [23-28] set out to study thermal transfer control and quality; for this purpose, they used the presence of the external magnetic field with inclination. Magnetic dipole force and a rotate cylinder can control the length and size of the recycle zones. They observed that an inclined and vertical magnetic field causes the elimination of the recycle zone behind the step. Cylinder rotation affects distribution of Nusselt number. Heat transfer rate improves when Reynolds number is high. In other research, it was discussed that most degraded heat transfer rates achieved with partial magnetic field were centred on walking. Magneto-hydrodynamic study of natural convection involves an inclined T-shaped enclosure filled with different types of nanofluids using Rayleigh number and Hartmann number and the performance of magnetic field inclination. Average Nusselt number increases with increasing Rayleigh number, magnetic field inclination, heat source location and size of nanoparticle fraction, while it decreases with increasing Hartmann number.

Using the ferrofluid Fe3O4–H2O and the presence of the external magnetic to study forced convective flow inside a backward facing step comprising a rotating cylinder of fixed diameter [29]. They show that increasing Hartmann number implies a decrease in average Nusselt number, but when increasing Reynolds number, concentration of nanoparticles and magnetic field inclination, as well as the mean number of Nusselt, increase. In addition, when the cylinder rotates counter clockwise, the heat transfer rate improves.

Studies are always carried out to find the best method and the best tool to achieve a most significant improvement in the rate of heat transfer by the use of control parameter and especially the addition of nanoparticles in the base fluid, in presence of external magnetic field.

In the present work, adding a single fin on a fixed cylinder is the main parameter used. Forced convection flow of a ferrofluid on a backward facing step containing a single fin attached to a fixed cylinder in the presence of an external magnetic field with different inclinations is studied. The present study was made by taking different values of the Reynolds number (Re between 10 and 100), Hartmann number (Ha between 0 and 100), nanoparticles concentration (ϕ between 0 and 0.1) and magnetic field inclination (γ between 0° and 90°), along with considering several fin positions α [0° – 180°]. Certain positions of the fin prove their effectiveness in improving the heat transfer phenomenon, while other positions have shown an unfavorable effect on the heat transfer rate. This investigation does not currently find place in the literature, to our knowledge.

2. PHYSICAL PHENOMENON

2.1. Description of backward facing step configuration

In the present work, a 2D numerical study of the forced convection of a laminar and Newtonian ferrofluid flow, on a backward facing step containing a single fin fixed on a cylinder, is performed in the presence of a magnetic field with different inclinations; the physical configuration with boundary conditions are presented in Fig. 1. The one phase ferrofluid model is used. The height of the backward facing step is H and the height of the channel is $2H$. γ is the inclination angle of the external magnetic field, D is the diameter of the fixed cylinder where the position is at $(4H, H)$ and the length of the fin is $0.4H$. At the inlet ($T = T_c$) represents the cold flow and parabolic velocities are imposed. At the lower wall downstream ($T = T_h$) is the hot temperature. The other walls are adiabatic and have no slip velocity (Fig. 1). The viscous dissipation, thermal radiation and Joule heating are not considered while modelling the energy equation [29]. The thermo-physical properties of water and iron oxide are presented in Tab. 1.

2.2. The mathematical equations

The partial differential equations, which determine the conservation equations for mass, momentum and energy in dimensional form are expressed as the following:

$$\frac{\partial u}{\partial x} + \frac{\partial v}{\partial y} = 0 \tag{1}$$

$$\rho_{ff} \left[u \frac{\partial u}{\partial x} + v \frac{\partial u}{\partial y} \right] = \left[-\frac{\partial p}{\partial x} + \mu_{ff} \left(\frac{\partial^2 u}{\partial x^2} + \frac{\partial^2 u}{\partial y^2} \right) + \sigma_{ff} B_0^2 (v \sin \gamma \cos \gamma - u \sin^2 \gamma) \right] \tag{2}$$

$$\rho_{ff} \left[u \frac{\partial v}{\partial x} + v \frac{\partial v}{\partial y} \right] = \left[-\frac{\partial p}{\partial y} + \mu_{ff} \left(\frac{\partial^2 v}{\partial x^2} + \frac{\partial^2 v}{\partial y^2} \right) + \sigma_{ff} B_0^2 (u \sin \gamma \cos \gamma - v \cos^2 \gamma) \right] \tag{3}$$

$$\left[u \frac{\partial T}{\partial x} + v \frac{\partial T}{\partial y} \right] = a_{ff} \left(\frac{\partial^2 T}{\partial x^2} + \frac{\partial^2 T}{\partial y^2} \right) \tag{4}$$

The dimensional and dimensionless boundary conditions are presented in Tab. 2 and Tab. 3 respectively.

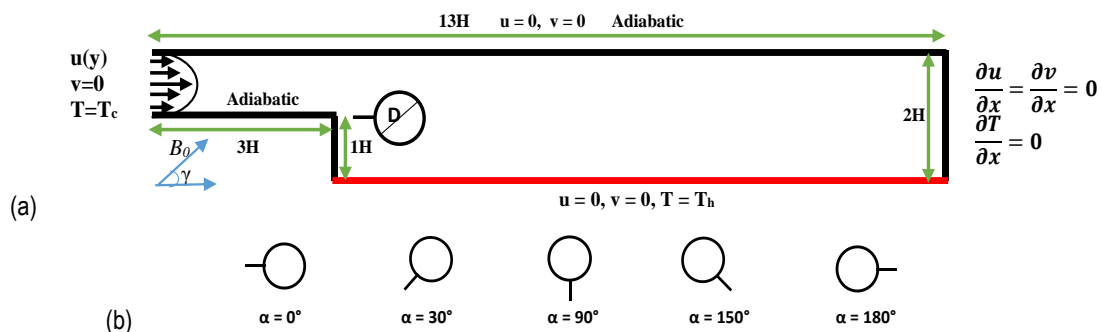


Fig. 1. Physical problem of backward facing step with boundary conditions (a), Fin position (b)

Tab. 1. Thermo-physical properties of Water and Iron Oxide

	ρ (Kg/m ³)	C_p (J/ Kg. K)	k (W/m.K)	β (1/K)	σ (1/ Ω .m)
Distilled Water	997.1	4,179	0.613	21×10^{-5}	0.05
Iron. Oxide Fe ₃ O ₄	5,200	670	6	1.18×10^{-5}	25,000

Tab. 2. Boundary conditions

The inlet	$u = u(y), v = 0, T = T_c$
The downstream bottom wall	$u = 0, v = 0, T = T_h$
The outlet. \mathbf{n} is the surface normal direction coinciding with the x axis at the outlet	$\frac{\partial u}{\partial \mathbf{n}} = \frac{\partial v}{\partial \mathbf{n}} = \frac{\partial T}{\partial \mathbf{n}} = 0$
Other walls are adiabatic and the velocity is no-slip.	$u = v = \frac{\partial T}{\partial \mathbf{n}} = 0$
Finned cylinder is adiabatic	$\frac{\partial T}{\partial \mathbf{n}} = 0$
Finned cylinder velocity components:	$u = 0, v = 0$

2.3. The dimensionless form equations

Scales, which are used to obtain the dimensionless equations (5)–(8), are presented below:

$$X = \frac{x}{H}, \quad U = \frac{u}{\bar{u}}, \quad \theta = \frac{T-T_c}{T_h-T_c}, \quad Pr = \frac{\nu_f}{\alpha_f}, \quad Ha = B_0 H \sqrt{\frac{\sigma_{ff}}{\mu_{ff}}}$$

$$Y = \frac{y}{H}, \quad V = \frac{v}{\bar{u}}, \quad P = \frac{p}{\rho_{ff} \bar{u}^2}, \quad Re = \frac{H \bar{u}}{\nu_f}$$

$$\frac{\partial V}{\partial X} + \frac{\partial V}{\partial Y} = 0 \quad (5)$$

$$U \frac{\partial U}{\partial X} + V \frac{\partial U}{\partial Y} = -\frac{\partial P}{\partial X} + \frac{1}{Re} \frac{\mu_{ff}}{\rho_{ff} \nu_f} \left(\frac{\partial^2 U}{\partial X^2} + \frac{\partial^2 U}{\partial Y^2} \right) + \frac{\rho_f \sigma_{ff} Ha^2}{\rho_{ff} \sigma_f Re} (V \sin \gamma \cos \gamma - U \sin^2 \gamma) \quad (6)$$

$$U \frac{\partial V}{\partial X} + V \frac{\partial V}{\partial Y} = -\frac{\partial P}{\partial Y} + \frac{1}{Re} \frac{\mu_{ff}}{\rho_{ff} \nu_f} \left(\frac{\partial^2 V}{\partial X^2} + \frac{\partial^2 V}{\partial Y^2} \right) + \frac{\rho_f \sigma_{ff} Ha^2}{\rho_{ff} \sigma_f Re} (U \sin \gamma \cos \gamma - V \cos^2 \gamma) \quad (7)$$

Tab. 4. Convergence test of mesh

Elements Number	4375	13548	41558	87325	172333
Time	9 s	19 s	89 s	240 s	467 s
Nu_{avg}	2.68620	2.66430	2.65797	2.65821	2.65813
θ_{avg}	0.15511	0.15777	0.15888	0.15898	0.15801
V_{avg}	0.38551	0.39098	0.39421	0.39482	0.39503

The mesh test was done for a configuration where $Re = 100$, $Pr = 6.2$, $Ha = 25$, $\phi = 0.05$, $\gamma = 0^\circ$ and $\alpha = 135^\circ$. After performing the calculations on five grids, we noticed the values of Nu_{avg} , θ_{avg} and V_{avg} having too small a difference in each of the last two grids and thus we chose the penultimate grid which has the number of elements 87,325.

2.5. Compute of the average and local Nusselt number

Convection is one of the methods of heat transfer. The term convection refers to the heat transfer processes that occur be-

$$U \frac{\partial \theta}{\partial X} + V \frac{\partial \theta}{\partial Y} = \frac{1}{Re Pr} \frac{\alpha_{ff}}{\alpha_f} \left(\frac{\partial^2 \theta}{\partial X^2} + \frac{\partial^2 \theta}{\partial Y^2} \right) \quad (8)$$

Tab. 3. The dimensionless boundary conditions

The inlet	$U = U(Y), V = 0, \theta = 0$
The downstream bottom wall	$U = 0, V = 0, \theta = 1$
The outlet. \mathbf{n} is the surface normal direction coinciding with the x axis at the outlet	$\frac{\partial U}{\partial X} = \frac{\partial V}{\partial X} = \frac{\partial \theta}{\partial X} = 0$
Other walls are adiabatic and the velocity is no-slip.	$U = V = \frac{\partial \theta}{\partial \mathbf{n}} = 0$
cylinder-fin is adiabatic	$\frac{\partial \theta}{\partial \mathbf{n}} = 0$
Finned cylinder velocity components	$U = 0, V = 0$

2.4. Thermo-physical properties of ferrofluid

- Density: $\rho_{ff} = (1 - \phi)\rho_f + \phi\rho_p$
- Thermal diffusivity: $\alpha_{ff} = \frac{k_{ff}}{(\rho C_p)_{ff}}$
- Electrical conductivity: $\delta_{ff} = \delta_f \left[1 + \frac{3(\delta-1)\phi}{(\delta+2)-(\delta-1)\phi} \right]$,
 $\delta = \frac{\delta_p}{\delta_f}$
- Specific heat: $(\rho C_p)_{ff} = (1 - \phi)(\rho C_p)_f + \phi(\rho C_p)_p$
- Thermal expansion coefficient: $(\rho \beta)_{ff} = (1 - \phi)(\rho \beta)_f + \phi(\rho \beta)_p$
- Thermal conductivity: $\frac{k_{ff}}{k_f} = \frac{k_p + 2k_f - 2\phi(k_f - k_p)}{k_p + 2k_f + \phi(k_f - k_p)}$
- Dynamic viscosity: $\mu_{ff} = \frac{\mu_f}{(1-\phi)^{2.5}}$

tween a surface and a moving fluid when they are at different temperatures. To measure the intensity of heat transfer in the fluid due to its movements and to characterise the heat exchange between the fluid and the wall, the Nusselt number is used.

The local Nusselt number on the hot wall is calculate as fol-

lows:

$$Nu = \frac{h_{ff}L}{k_f} \tag{9}$$

$$h_{ff} \text{ is the heat transfer coefficient of ferrofluid. } h_{ff} = \frac{q_w}{T_h - T_c} \tag{10}$$

q_w stands for heat flux on the heated wall:

$$q_w = -k_{ff} = \frac{T_h - T_c}{L} \frac{\partial \theta}{\partial y} \Big|_{y=0} \tag{11}$$

$$Nu = \frac{k_{ff}}{k_f} \left(\frac{\partial \theta}{\partial Y} \right) \tag{12}$$

The average Nusselt number on the hot wall is calculated as follows:

$$Nu_{avg} = \int_0^{L_s} Nu dx \tag{13}$$

L_s is the total length of the heated part.

3. NUMERICAL METHOD

The partial differential equations in the dimensionless form provided in Eqs (5)–(8), which determine the conservation equations for mass, momentum and energy, as well as the boundary conditions which are associated with them, were solved using the finite element scheme based on the Galerkin method.

The computational domain or geometry is divided into several elements that represent the approximate geometry; several meshes are tested until the optimal one is found and used to start the numerical calculation and find the approximate results.

Triangular elements are used to discretise the computational domain. Five grids of different sizes were used until the optimal

one could be chosen; the choices were among an enlarged mesh of 4,375 elements, a normal mesh of 13,548 elements, a fine mesh of 41,558 elements, and an extra fine mesh of 87,325 elements and an extremely fine mesh of 172,333 elements. To ensure mesh independence and to achieve optimal mesh distribution with accurate results and minimal computation time, the mesh containing 87,325 triangular elements were used to perform the computations. (Tab. 4)

4. RESULTS AND DISCUSSION

The main objective is to study the effect of fin position. Therefore, a numerical investigation is undertaken that concerns the forced convection of the flow of a ferrofluid on a backward facing step containing a single fin attached to a fixed cylinder in the presence of an external magnetic field with different inclinations.

In this study the control parameters such as Reynolds number (Re), Hartmann number (Ha), magnetic field tilt angle (γ) and nanoparticle concentration (ϕ) are considered, and the fin position on the cylinder (α) is the key parameter that enables us to study its effect on the quality of heat transfer.

To carry out our numerical study, it is necessary to validate the results. Therefore, we need to compare the results obtained by the present numerical study with the results of [29]. The validation is done with the effect of the Hartmann number (Ha = 0.0 and Ha = 100) on the isotherms and the average Nusselt number, for Pr = 6.2, Re = 100, $\gamma = 0^\circ$ and $\phi = 0.05$ (Fig. 2).

The validation plot (Fig. 2) shows that our results are closely similar those of [29] and we find excellent consistency and very acceptable agreements.

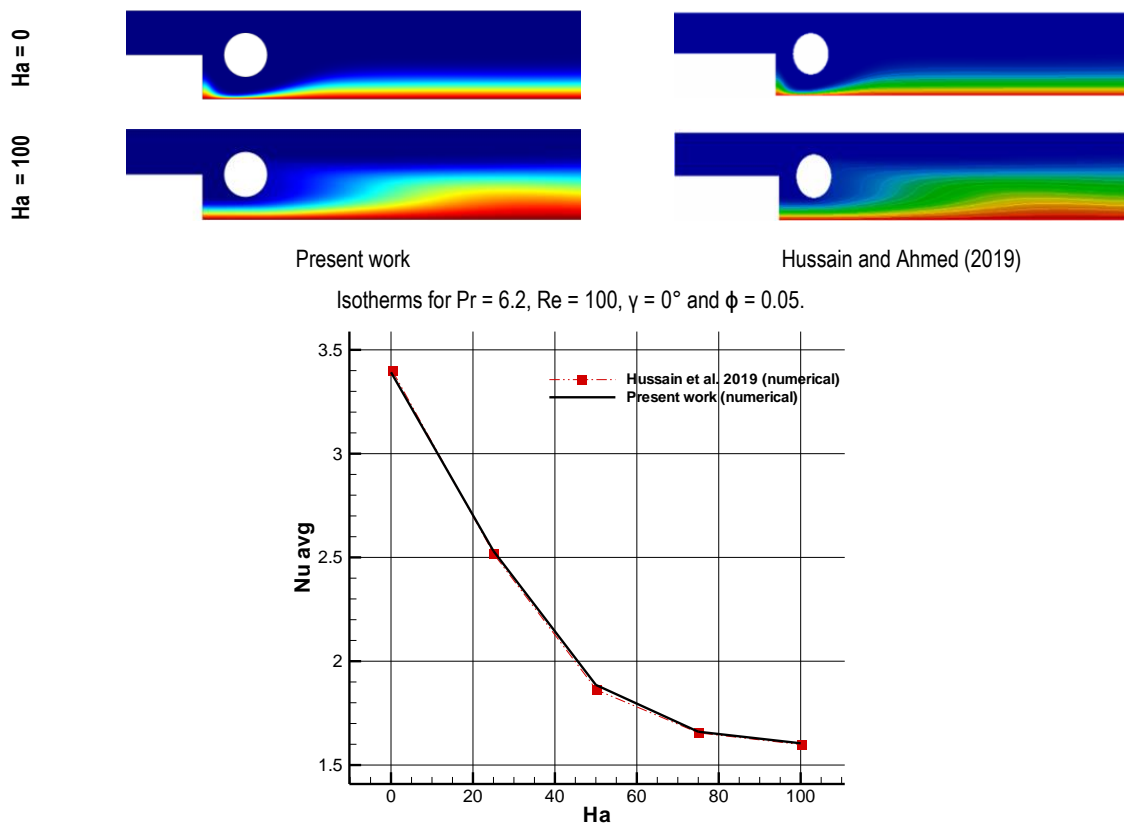


Fig. 2. Validation of results

Different values of control parameter are taken, encompassing the Reynolds number (Re between 10 and 100), Hartmann number (Ha between 0 and 100), nanoparticles concentration (ϕ between 0 and 0.1), magnetic field inclination (γ between 0° and 90°) and fin positions α [0° – 180°]. Grashof and Richardson numbers are equal to zero and Prandtl number = 6.2.

Simulations were carried out for several fin positions on the cylinder ranging from 0° to 180° in steps of 5.0 . The results are therefore voluminous and for this reason it was chosen to present

the streamline contours and isotherms for the most significant fin angle values ($\alpha = 0^\circ, 30^\circ, 90^\circ, 150^\circ$ and 180°).

Results obtained by numerical simulations for the study of forced convection of ferrofluid flow in a backward facing step geometry containing a single fin fixed on cylinder are analysed qualitatively through the contours of isotherms, and streamlines are presented in Figs 3–6; also, quantitative analysis is made by the calculation of the average Nusselt number, presented in Figs 7–10, and of the local Nusselt number, presented in Figs 11–14.

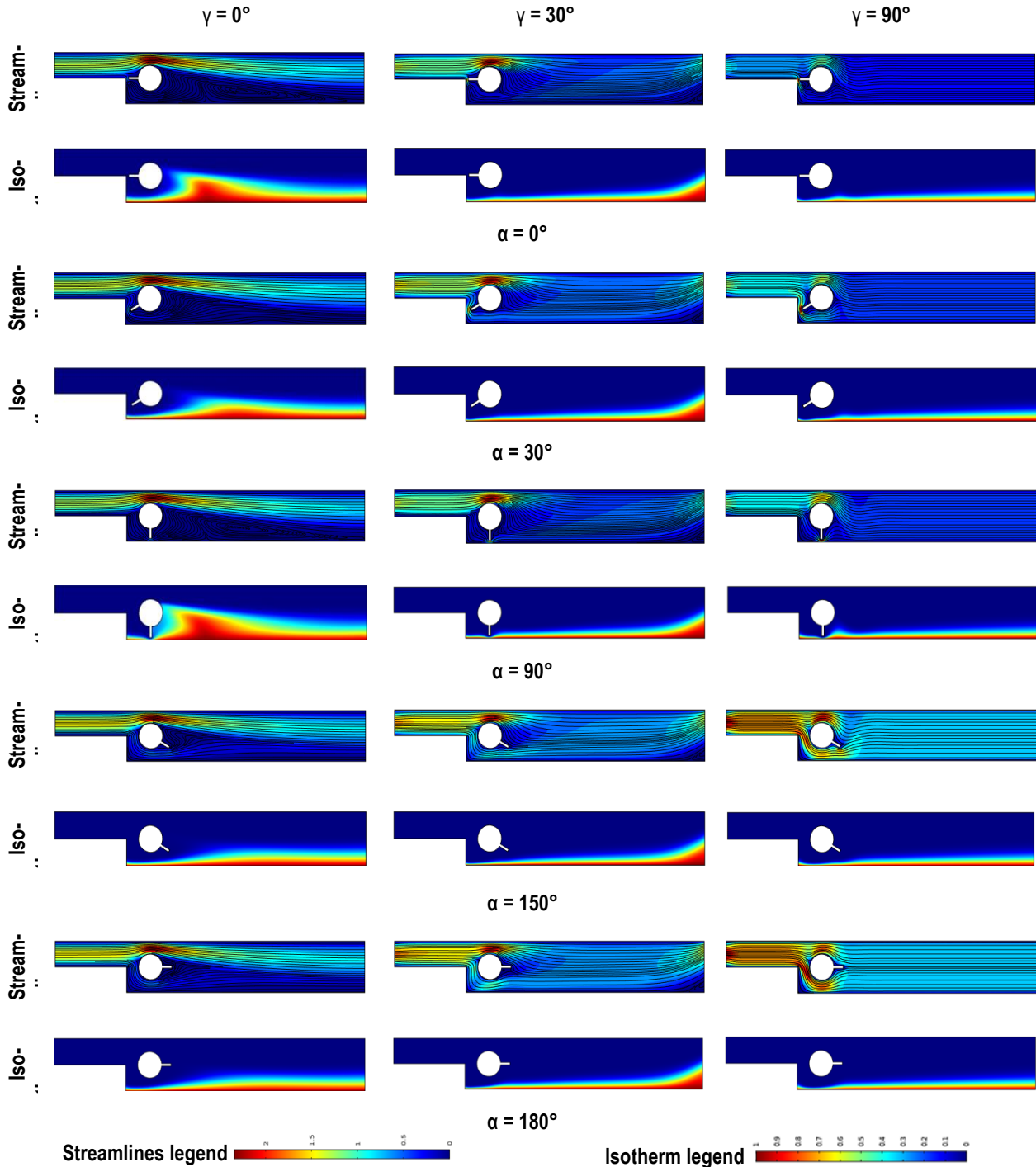


Fig. 3. Effect of Magnetic field inclination γ with different fin positions for $Pr = 6.2, Re = 100, Ha = 20$ and $\phi = 0.04$

Fig. 3 highlights magnetic field inclination effect on the current lines' structure and on isotherms for different positions of fin cylinder, with $Pr = 6.2, Re = 100, Ha = 20$ and $\phi = 0.04$. The contours

in Fig. 3 are shown for magnetic field inclination cases ($\gamma = 0^\circ, 30^\circ$ and 90°) and fin position ($\alpha = 0^\circ, 30^\circ, 90^\circ, 150^\circ$ and 180°). Weak forced convection exists when the magnetic field is horizon-

tal ($\gamma = 0^\circ$) with ($\alpha = 0^\circ, 30^\circ$ and 90°); we notice in streamlines' images the presence of a vortex that slows down ferrofluid flow circulation, and we observe from isotherm contours that the amount of heat transmitted is small. For $\alpha = 150^\circ$ and $\alpha = 180^\circ$ the vortex is absent and the thermal layer in duct is thick. This leads us to conclude that the thermal heat transfer has improved due to fin position. When the magnetic field undergoes an inclination ($\gamma = 30^\circ$ and $\gamma = 90^\circ$), a very significant improvement in heat transfer is manifested, especially for $\alpha = 150^\circ$ and $\alpha = 180^\circ$ where substantial thickness of the thermal layer is observed and the vortex is no longer present, which implies that the flow of ferrofluid starts to move towards the bottom wall. For $\gamma = 30^\circ$, the flow concentration is just above the cylinder and flow lines are almost straight; and for $\gamma = 90^\circ$, the ferrofluid concentration is around all

the obstacles (cylinder and fin); and at the top and bottom, the flow lines corresponding to the ferrofluid are parallel. For ($\alpha = 0^\circ, 30^\circ$ and 90°) the transfer remains less efficient due to the effect of

the presence of the external magnetic leads to a decrease in the heat transfer quality due to Lorentz force, which slows down the ferrofluid movement. When the magnetic field is inclined, forced convection is in enhancement. As a result, Lorentz force, in itself, depends on the angle between magnetic field and ferrofluid velocity.

The effect of magnetic field inclination ($\gamma = 30^\circ$ and 90°) and fin position ($\alpha = 150^\circ$ and 180°) on the heat transfer allows a gain in transfer rate compared to the case of the horizontal magnetic field.

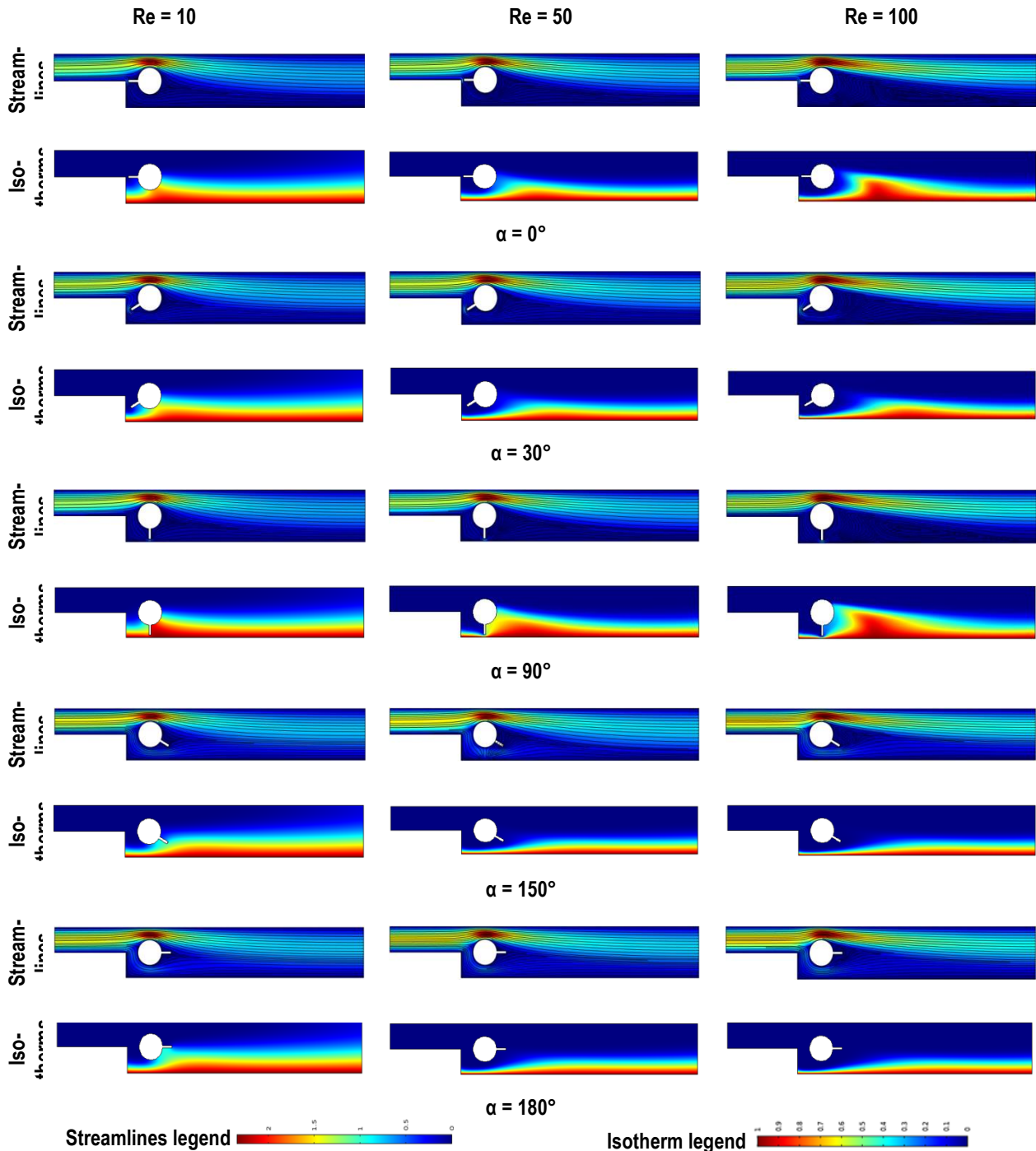


Fig. 4. Effect of Reynolds number Re with different fin positions for $Pr = 6.2$, $\gamma = 0^\circ$, $Ha = 20$ and $\phi = 0.04$

Concerning the influence of Reynolds number on the streamlines and isotherms, from Fig. 4 it is evident that for $Re = 10$ with all fin positions ($\alpha = 0^\circ, 30^\circ, 90^\circ, 150^\circ$ and 180°), the flow is slow and the thermal layer is thin, which results in poor heat transfer quality. This effect is attributable to the fact that for a low value of Reynolds number, inertial forces related to velocities are negligible and viscous forces are high, which explains a slow motion of ferrofluid. As the Reynolds number increases, the velocity inertia

forces also increase and therefore the motion of the ferrofluid starts to become faster. So, for $Re = 50$ and $Re = 100$ with ($\alpha = 0^\circ, 30^\circ$ and 90°), the heat transfer quality has improved slightly and it is more efficient when ($\alpha = 150^\circ$ and 180°) since the thermal layer has become thick.

It can be concluded that as Reynolds number increases, heat transfer improves and fin position still has its effect on the improvement.

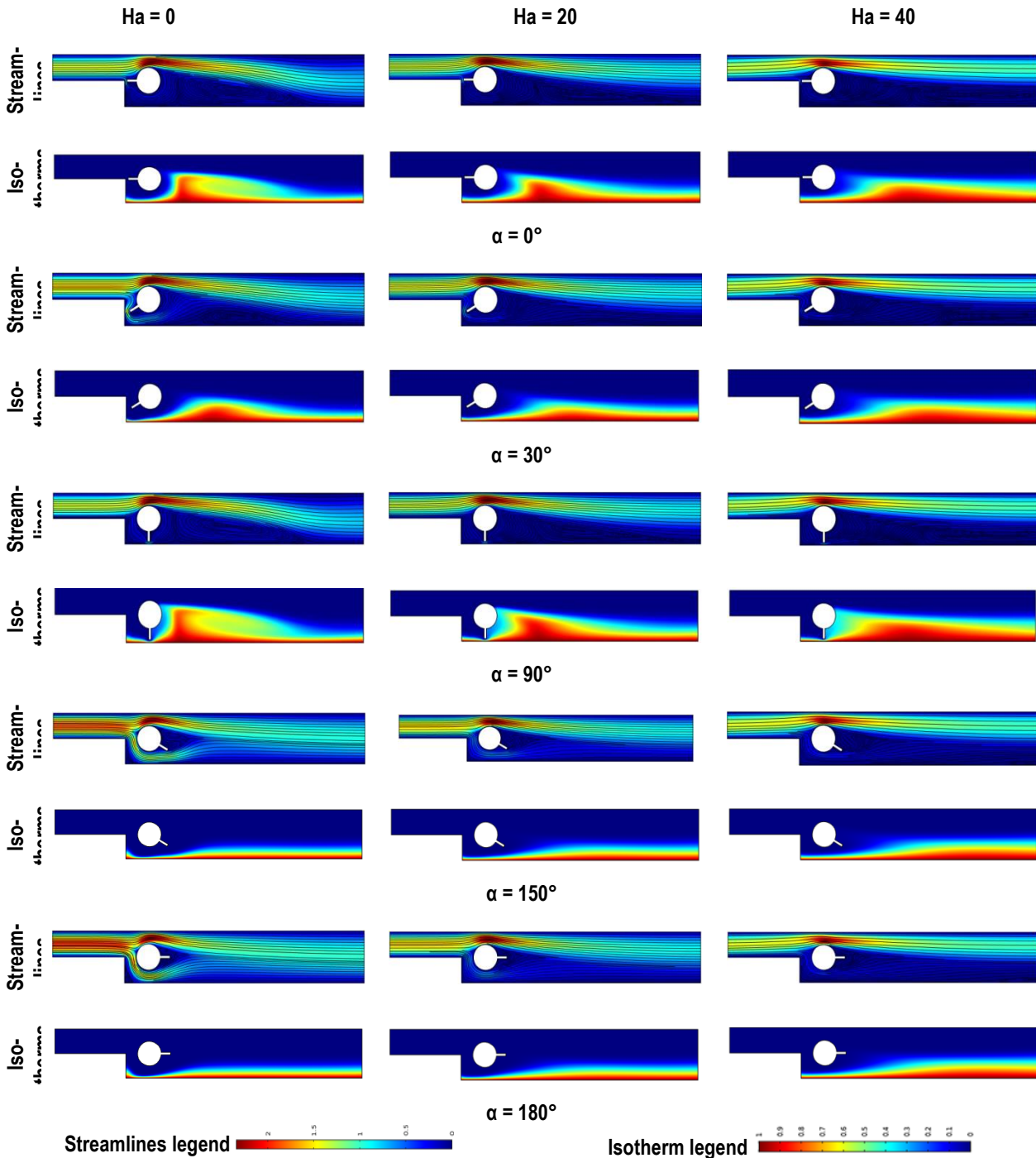


Fig. 5. Effect of Hartmann number Ha with different fin positions for $Pr = 6.2, \gamma = 0^\circ, Re = 100$ and $\phi = 0.04$

The dimensionless Hartmann number represents the external magnetic field strength. Hartmann number ($Ha = 0, 20$ and 100) and fin position ($\alpha = 0^\circ, 30^\circ, 90^\circ, 150^\circ$ and 180°) have an effect

on streamlines and temperature field for $Pr = 6.2, \gamma = 0^\circ, Re = 100$ and $\phi = 0.04$), as shown in Fig. 5.

Fig. 5 shows that in the absence of magnetic field $Ha = 0$ with fin positions ($\alpha = 0^\circ, 30^\circ$ and 90°), it is observed that in the streamline images a vortex that forms behind the obstacle causes a slowing down of fluid motion; so, on temperature field contours the thermal layer is reduced, reflecting poor forced convection. For ($\alpha = 150^\circ$ and 180°) streamlines are straight and parallel and the flow motion is therefore fast, and thermal layer is thin; hence, good forced convection is available for those fin positions with $Ha = 0.0$.

In presence of the magnetic field ($Ha = 20$ and 40) with ($\alpha = 0^\circ, 30^\circ$ and 90°), the thermal layer is thin, and ferrofluid movement has become slow and undergoes braking due to Lorentz force. Placing the fin on the cylinder at $\alpha = 150^\circ$ and $\alpha = 180^\circ$, forced convection is slightly improved compared to the other three positions.

As Hartmann number increases, the thickness of thermal layer decreases for all fin positions due to Lorentz force.

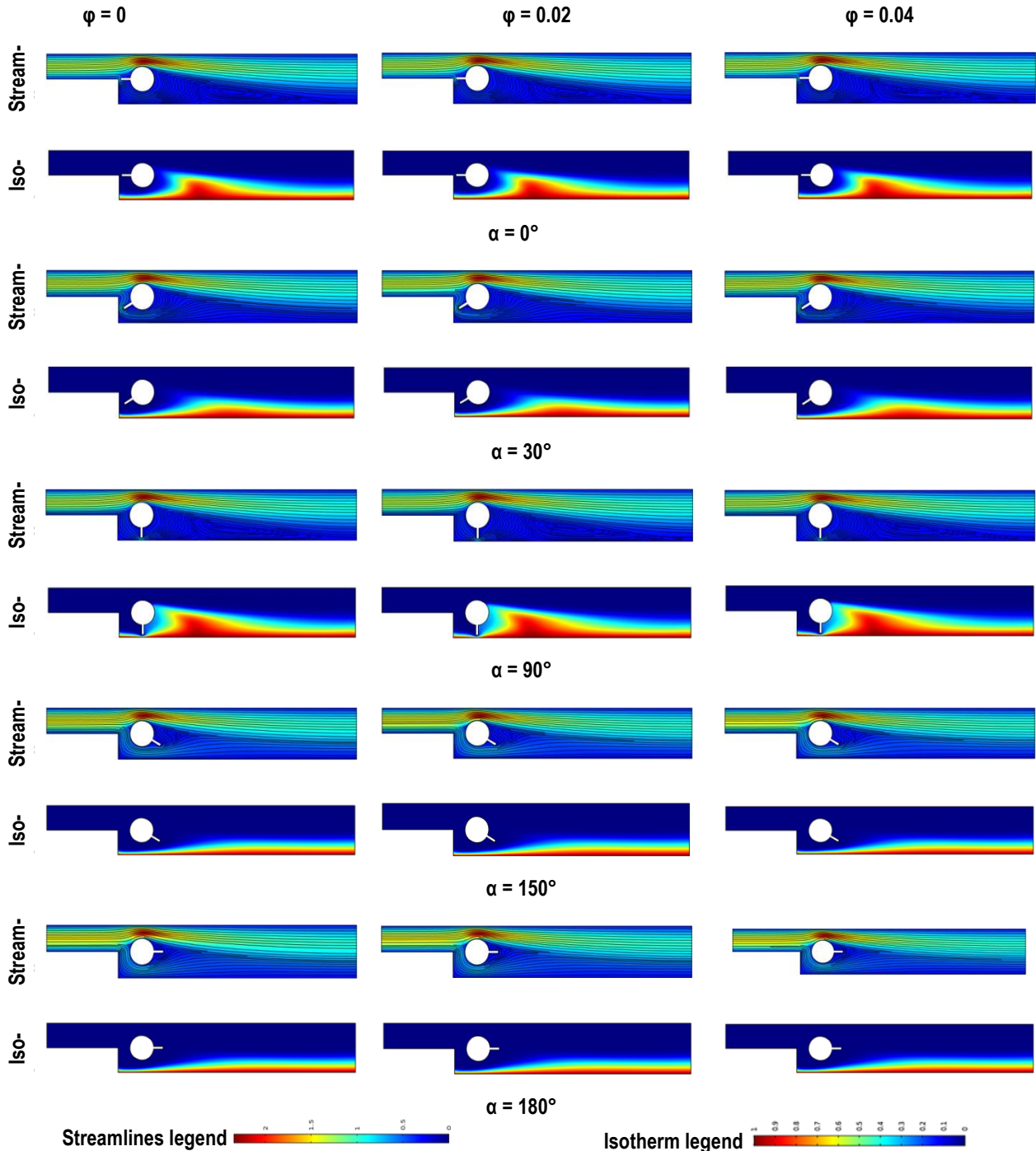


Fig. 6. Effect of nanoparticles concentration ϕ with different fin positions for $Pr = 6.2, \gamma = 0^\circ, Re = 100$ and $Ha = 20$

Fig. 6 shows the effect of nanoparticles' concentration and fin position on the structure of streamlines and isotherms, for $Pr = 6.2, \gamma = 0^\circ, Re = 100$ and $Ha = 20$. To illustrate the streamlines and isotherms and to present concentration of the magnetite

Fe_3O_4 effect, we have chosen ($\phi = 0.0, 0.02$ and 0.04) among the set of values used in numerical simulation.

It is observed that insertion of Fe_3O_4 nanoparticles in a base fluid in the presence of moderate magnetic field $Ha = 20$ contrib-

utes to improvement of heat transfer compared to cases of pure distilled and ionised water fluid. Heat transfer quality increases with increasing nanoparticles' concentration under the thermal conductivity effect of the ferrofluid. The position of the fin on the cylinder still has its effect on the quality of heat transfer. For

($\alpha = 0^\circ, 30^\circ$ and 90°), the thermal layer is thin, indicating a degraded heat transfer due to these positions. For ($\alpha = 150^\circ$ and 180°) forced convection is improved because the thermal layer has become thick and streamlines are parallel.

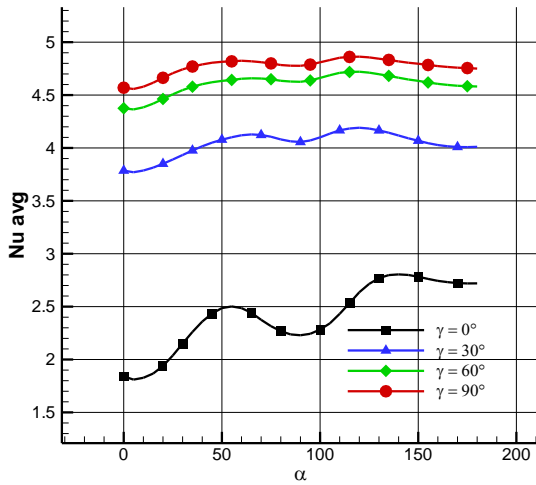


Fig. 7. Effect of magnetic field inclination with different fin positions on average Nusselt number for $Pr = 6.2, Re = 100, Ha = 20$ and $\phi = 0.04$

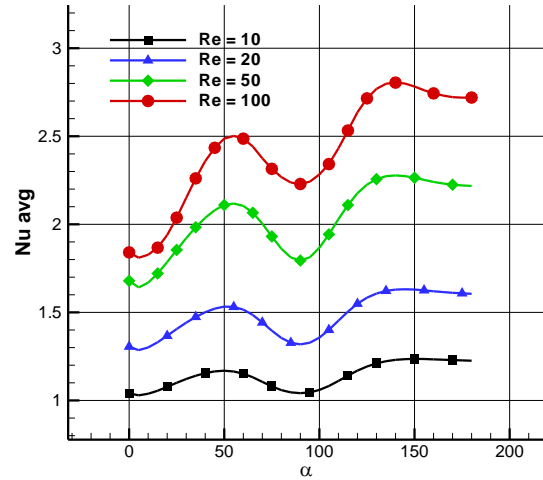


Fig. 8. Effect of Reynolds number with different fin positions on average Nusselt number for $Pr = 6.2, \gamma = 0^\circ, Ha = 20$ and $\phi = 0.04$

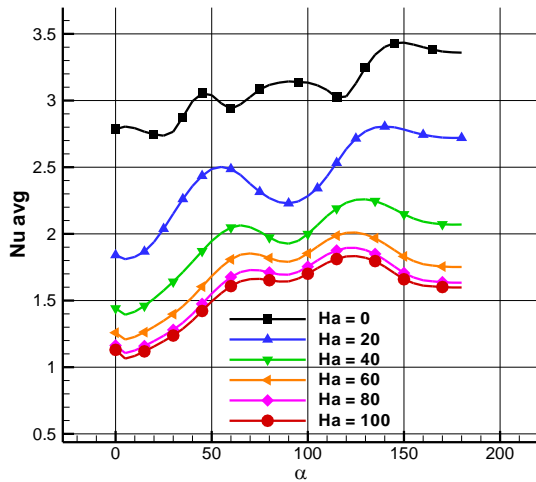


Fig. 9. Effect of Hartmann number with different fin positions on average Nusselt number for $Pr = 6.2, \gamma = 0^\circ, Re = 100$ and $\phi = 0.04$

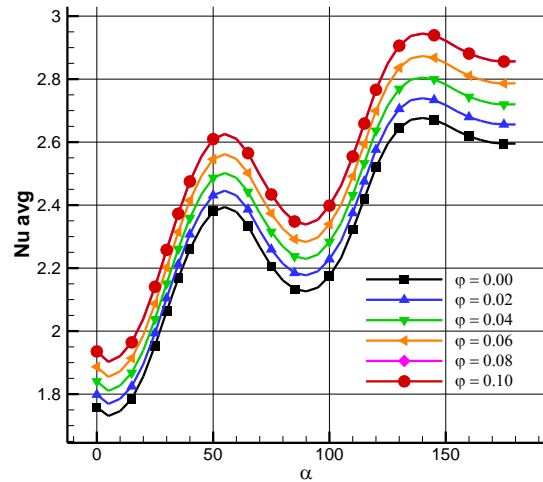


Fig. 10. Effect of nanoparticles concentration with different fin positions on average Nusselt number for $Pr = 6.2, \gamma = 0^\circ, Re = 100$ and $Ha = 20$

In this section, the analysis of the results of average Nusselt number variation as a function of different parameters (magnetic field inclination, Reynolds number, Hartmann number and nanoparticles' concentration) and fin position on cylinder is provided. Study of ferrofluid movement behaviour and the quality of heat transfer in duct is made for different values of these parameters.

The variation of the average Nusselt number as a function of the magnetic field inclination γ with variation of fin position for $Pr = 6.2, Re = 100, Ha = 20$ and $\phi = 0.04$ is presented in Fig. 7. Fig. 7 shows that the best heat transfer rate by forced convection is at $\gamma = 90^\circ$ with $\alpha = 150^\circ$ such that the average Nusselt reaches its maximum value of 4.7965, while it takes a smaller value when $\gamma = 0^\circ$ with $\alpha = 0^\circ$. So, to conclude, increasing γ increases the average Nusselt number due to the fact that Lorentz force, in itself, depends on the angle between magnetic field and ferrofluid flow velocity, with a better fin position $\alpha = 150^\circ$. The effect on fin

position and Reynolds number on the average Nusselt number is presented in Fig. 8 for $Pr = 6.2, \gamma = 0^\circ, Ha = 20$ and $\phi = 0.04$. The highest average Nusselt value achieved 2.7825 for $Re = 100$ with $\alpha = 150^\circ$, while for the lowest Reynolds value ($Re = 10$) with $\alpha = 0^\circ$, the average Nusselt takes the lowest value which attains 1.0404, resultant to which the heat transfer rate was reduced. Therefore, as the Reynolds number increases, average Nusselt number also increases, because inertial forces make the ferrofluid flow faster. Fig. 9 displays the results of the average Nusselt number variation as a function of Hartmann number and fin position on cylinder for $Pr = 6.2, \gamma = 0^\circ, Re = 100$ and $\phi = 0.04$. For $Ha = 0$ with $\alpha = 150^\circ$, the average Nusselt number reaches a high value which corresponds to 3.4340. On the other hand, $Ha = 100$ with $\alpha = 0^\circ$ shows the lowest mean Nusselt value which attains to 1.2585. So, increasing Hartmann number leads to decrease in the average Nusselt number because of Lorentz force, which slows

down the flow. To perceive the effect of nanoparticle concentration and fin position on heat transfer rate improvement for $Pr = 6.2$, $\gamma = 0^\circ$, $Re = 100$ and $Ha = 20$, we present Fig. 10. The results show that the increase in ϕ generates an improvement in heat transfer rate due to thermal conductivity of ferrofluid. The

highest value of average Nusselt number was obtained when ($\phi = 0.1$ with $\alpha = 150^\circ$) and the smallest value of average Nusselt number corresponds to the case ($\phi = 0.0$ with $\alpha = 0^\circ$).

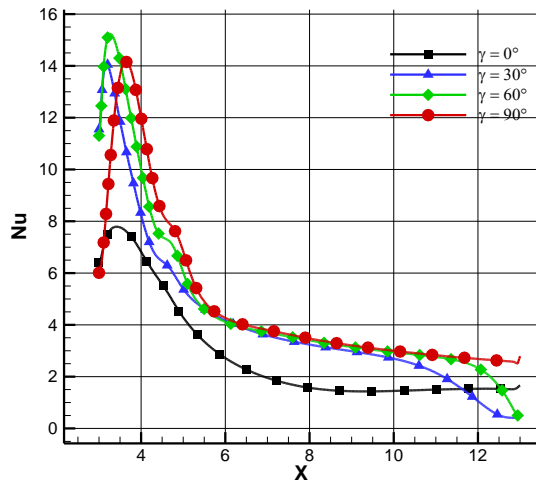


Fig. 11. Effect of magnetic field inclination on local Nusselt number along the heated wall for $Pr = 6.2$, $Re = 100$, $Ha = 20$, $\phi = 0.04$ and $\alpha = 150^\circ$

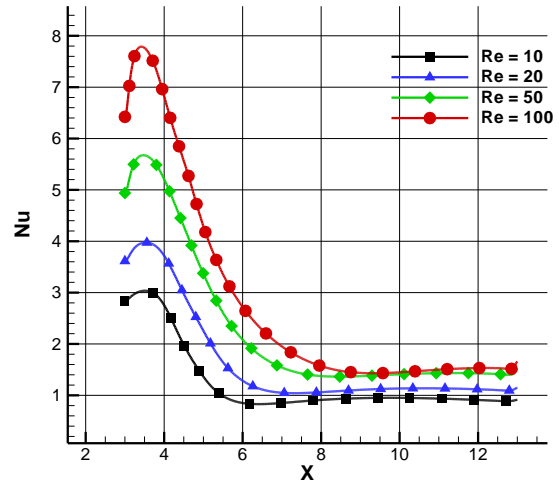


Fig. 12. Effect of Reynolds number on Local Nusselt number along the heated wall for $Pr = 6.2$, $\gamma = 0^\circ$, $Ha = 20$, $\phi = 0.04$ and $\alpha = 150^\circ$

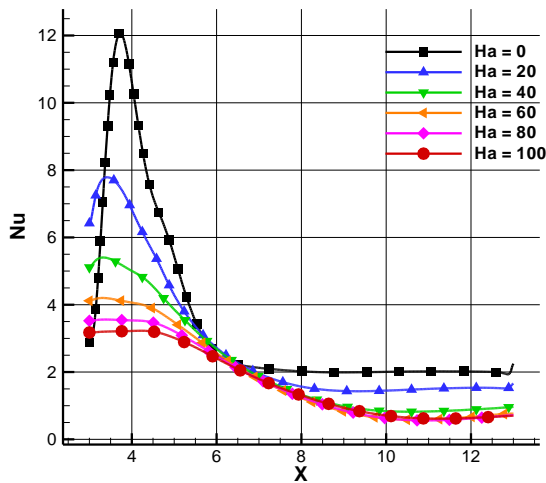


Fig. 13. Effect of Hartmann number on local Nusselt number along the heated wall for $Pr = 6.2$, $\gamma = 0^\circ$, $Re = 100$, $\phi = 0.04$ and $\alpha = 150^\circ$

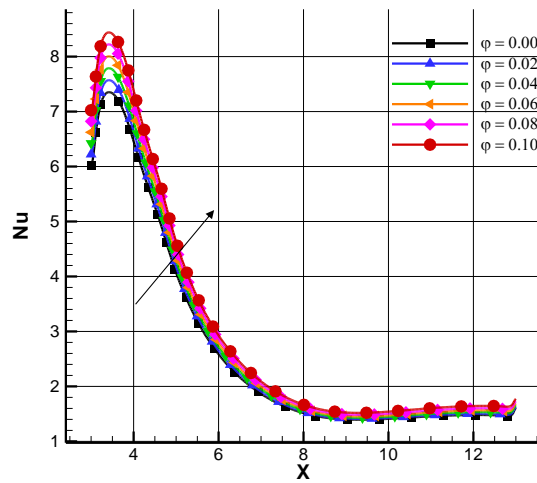


Fig. 14. Effect of nanoparticles concentration on local Nusselt number along the heated wall for $Pr = 6.2$, $Ha = 20$, $\gamma = 0^\circ$, $Re = 100$ and $\alpha = 150^\circ$

Figs 11–14 present the evaluation of the local Nusselt number as a function of all the control parameters used in the present study (magnetic field inclination, Reynolds number, Hartmann number and nanoparticle concentration) with the most favoured fin position $\alpha = 150^\circ$. The local Nusselt number is calculated along the hot bottom wall to show the development of heat transfer at this wall.

For all four graphs in Figs 11–14, it is observed that the local Nusselt number distribution is maximum in the vicinity of the obstacle (finned cylinder) and the backward facing step (from $X = 3$ up to $X = 6$); thus this part corresponds to a strong temperature gradient, causing cooling of the heated plate. After the obstacle ($X > 6$), the local Nusselt number starts to decrease and takes minimum values as the displacement towards the duct exits; so, the temperature gradient is low.

From Fig. 13, which illustrates the effect of the Hartmann number on the variations of the local Nusselt number along the hot wall, it is observed that as the Hartmann number increases, the peaks of the local Nusselt number decrease. In Figs 11, 12 and 14, it is observed that as the values of the parameters (magnetic field inclination, Reynolds number and nanoparticle concentration) increase, the local Nusselt number increases.

5. CONCLUSIONS

A numerical study of the forced convection of ferrofluid on a backward facing step containing a finned cylinder with different fin positions on cylinder was conducted by changing angles of inclination of the magnetic field. The partial differential equations,

which determine the conservation equations for mass, momentum and energy, were solved using finite element scheme based on Galerkin method. Analysis of heat transfer characteristics by forced convection was made by considering different values of Reynolds number, Hartmann number, nanoparticles' concentration and magnetic field inclinations, and by taking several fin position angles (between 0° and 180°).

Compared to previously published research results, we note excellent consistency and very acceptable agreements. We can summarise our findings as follows.

- Magnetic field inclination has an effect on heat transfer quality; Nusselt number is more important in the vertical direction than in the horizontal one.

NOMENCLATURE:

B_0	Magnetic field strength (Tesla)		
H	heat transfer coefficient (W/m^2K)	ϕ	nanoparticle concentration
Ha	Hartmann number, $B_0H\sqrt{\frac{\sigma_{ff}}{\mu_{ff}}}$	a	thermal diffusivity (m^2/s)
K	thermal conductivity ($W/m K$)	β	expansion coefficient ($1/K$)
H	inlet step height, (m)	γ	inclination angle of magnetic field
n	normal coordinate	θ	dimensionless temperature $\frac{T-T_c}{T_h-T_c}$
Nu	local Nusselt number	ν	kinematic viscosity (m^2/s)
Nu_{avg}	averaged Nusselt number	ρ	density of the fluid (kg/m^3)
p	pressure (Pa)	σ	electrical conductivity ($\mu S/cm$)
P	non-dimensional pressure	μ	dynamic viscosity, $N s/m^2$
Pr	Prandtl number ($\frac{\nu_f}{a_f}$)	α	fin position
Re	Reynolds number ($\frac{H\bar{u}}{\nu_f}$)		
T	temperature (K)	c	Cold
C_p	Thermal specific heat ($J/Kg K$)	h	Hot
u, v	x–y velocity components (m/s)	avg	average
U, V	dimensionless velocity components	ff	ferrofluid
x, y	Cartesian coordinates (m)		
X, Y	dimensionless coordinates		

- The results show that when magnetic particles' concentration of ferrofluid increases, the thermal diffusivity also increases.
- The heat transfer rate increases as the Reynolds number increases too.
- When the Hartmann number increases, the heat transfer rate is reduced.

However, fin position on fixed cylinder has the maximum influence on heat transfer quality. The best fin position is at ($\alpha = 150^\circ$), which gives the best Nusselt number; however, the fin position at ($\alpha = 0^\circ$) remains an unfavourable case that gives the lowest Nusselt values.

Greek symbols

ϕ	nanoparticle concentration
a	thermal diffusivity (m^2/s)
β	expansion coefficient ($1/K$)
γ	inclination angle of magnetic field
θ	dimensionless temperature $\frac{T-T_c}{T_h-T_c}$
ν	kinematic viscosity (m^2/s)
ρ	density of the fluid (kg/m^3)
σ	electrical conductivity ($\mu S/cm$)
μ	dynamic viscosity, $N s/m^2$
α	fin position

Subscripts

c	Cold
h	Hot
avg	average
ff	ferrofluid

REFERENCES

- Erturk E. Numerical solutions of 2-D steady incompressible flow over a backward-facing step, Part I: High Reynolds number solutions. *Computers & Fluids*. 2008; 37:633–655.
- Temik P. New contributions on laminar flow of inelastic non-Newtonian fluid in the two-dimensional symmetric expansion: Creeping and slowly moving flow conditions. *J Non-Newtonian Fluid Mech*. 2010; 165:1400–1411.
- Xie WA, Xi GN. Fluid flow and heat transfer characteristics of separation and reattachment flow over a backward-facing step. *Int J of refrigeration*. 2017; 74:177–189.
- Lan H, Armaly BF, Drallmeier JA. Three-dimensional simulation of turbulent forced convection in a duct with backward-facing step. *Int J of Heat and Mass Transfer*. 2009; 52:1690–1700.
- Khanafer K, Al-Azmi B, Al-Shammari A, Pop I. Mixed convection analysis of laminar pulsating flow and heat transfer over a backward-facing step. *Intl J of Heat and Mass Transfer*. 2008; 51:5785–5793.
- Barrios-Pina H, Viazzo S, Rey C. A numerical study of laminar and transitional mixed convection flow over a backward-facing step. *Computers & Fluids*. 2012; 56:77–91.
- Zhao P, Ge Z, Zhu J, Liu J, Ye M. Quasi-direct numerical simulation of forced convection over a backward facing step: Effect of Prandtl number. *Nuclear Engineering and Design*. 2018; 335:374–388.
- Kumar S, Vengadesan S. The effect of fin oscillation in heat transfer enhancement in separated flow over a backward facing step. *Int J of Heat and Mass Transfer*. 2019; 128:954–963.
- Kumar A, Dhiman AK. Effect of a circular cylinder on separated forced convection at a backward-facing step. *Int J of Thermal Sciences*. 2012; 52:176-185.
- Hussain S, Ahmed SE, Akbar T. Entropy generation analysis in MHD mixed convection of hybrid nanofluid in an open cavity with a horizontal channel containing an adiabatic obstacle. *Int J of Heat and Mass Transfer*. 2017; 114:1054–1066
- Kherbeet AS, Mohammed HA, Munisamy KM, Salman BH. The effect of step height of microscale backward-facing step on mixed convection nanofluid flow and heat transfer characteristics. *Int J of Heat and Mass Transfer*. 2014; 68:554–566.
- Abu-Nada E. Application of nanofluids for heat transfer enhancement of separated flows encountered in a backward facing step. *Int J of Heat and Fluid Flow*. 2008; 29:242–249.
- Kherbeet AS, Mohammed HA, Salman BH. The effect of nanofluids flow on mixed convection heat transfer over microscale backward-facing step. *Int J of Heat and Mass Transfer*. 2012; 55:5870–5881.
- Hussain S. Finite Element Solution for MHD Flow of Nanofluids with Heat and Mass Transfer through a Porous Media with Thermal Radiation, Viscous Dissipation and Chemical Reaction Effects. *Advances in Applied Mathematics and Mechanics Adv. Appl. Math. Mech*. 2017; 9(4):904-923.

15. Nath R, Krishnan M. Numerical study of double diffusive mixed convection in a backward facing step channel filled with Cu-water nanofluid. *Int J of Mechanical Sciences*. 2019; 153(154):48–63.
16. Lv J, Hu C, Bai M, Li L, Shi L, Gao D. Visualization of SiO₂-water nanofluid flow characteristics in backward facing step using PIV. *Experimental Thermal and Fluid Science*. 2019; 101:151–159.
17. Hilo AK, Abu Talib A, Iborra AA, Hameed Sultan MT, Abdul Hamid MF. Experimental study of nanofluids flow and heat transfer over a backward-facing step channel. *Powder Technology*. 2020; 372:497–505.
18. Mohammed H A, Alawi O A, Wahid M A. (2015), Mixed convective nanofluid flow in a channel having backward-facing step with a baffle, *Powder Technology*, 275, 329–343.
19. Ma Y, Mohebbi R, Rashidi MM, Yang Z, Fang Y. Baffle and geometry effects on nanofluid forced convection over forward and backward-facing steps channel by means of lattice Boltzmann method. *Physica A*. 2020; 554,124696.
20. Selimefendigil F, Öztöp HF. Identification of forced convection in pulsating flow at a backward facing step with a stationary cylinder subjected to nanofluid. *Int Communications in Heat and Mass Transfer*. 2013;45:111–121.
21. Selimefendigil F, Öztöp HF. Numerical investigation and reduced order model of mixed convection at a backward facing step with a rotating cylinder subjected to nanofluid. *Computers & Fluids*. 2015b; 109:27–37.
22. Mohammed HA, Fathinia F, Vuthaluru HB, Liu S. CFD based investigations on the effects of blockage shapes on transient mixed convective nanofluid flow over a backward facing step. *Powder Technology*. 2019;346:441–451.
23. Selimefendigil F, Öztöp HF. Effect of a rotating cylinder in forced convection of ferrofluid over a backward facing step. *Int J of Heat and Mass Transfer*. 2014;71:142–148.
24. Selimefendigil F, Öztöp HF. Influence of inclination angle of magnetic field on mixed convection of nanofluid flow over a backward facing step and entropy generation. *Advanced Powder Technology*. 2015a; 26:1663–1675.
25. Hussein AK, Bakier MA, Ben Hamida MB, Sivasankaran S. Magneto-hydrodynamic natural convection in an inclined T-shaped enclosure for different nanofluids and subjected to a uniform heat source. *Alexandria Engineering J*. 2016; 55:2157–2169.
26. Hussain S, Armaghani T, Jamal M. Magnetoconvection and Entropy Analysis in T-Shaped Porous Enclosure Using Finite Element Method. *J of thermophysics and heat transfer*. 2019. Available from: <https://doi.org/10.2514/1.T5821>
27. Geridönmez BP, Öztöp HF. Effects of inlet velocity profiles of hybrid nanofluid flow on mixed convection through a backward facing step channel under partial magnetic field. *Chemical Physics*. 2021; 540:111010.
28. Hussain S, Öztöp HF. Impact of inclined magnetic field and power law fluid on double diffusive mixed convection in lid-driven curvilinear cavity. *Int Communications in Heat and Mass Transfer*. 2021; 127:105549. <https://doi.org/10.1016/j.icheatmasstransfer.2021.105549>
29. Hussain S, Ahmed S E. Unsteady MHD forced convection over a backward facing step including a rotating cylinder utilizing Fe₃O₄-water ferrofluid. *J of Magnetism and Magnetic Materials*. 2019; 484:356–366.

Meriem Toumi:  <https://orcid.org/0000-0001-7840-0424>

Mohamed Bouzit:  <https://orcid.org/0000-0002-1417-7291>

Fayçal Bouzit:  <https://orcid.org/0000-0003-4718-0830>

Abderrahim Mokhefi:  <https://orcid.org/0000-0002-2036-2186>

MODELLING OF IRON ORE PROCESSING IN TECHNOLOGICAL UNITS BASED ON THE HYBRID APPROACH

Vladimir MORKUN* , Vitalii TRON* , Vadym ZYMOHLIAD* 

*Department of Automation, Computer Science and Technologies, Kryvyi Rih National University,
Vitalii Matusevich St., 11, Kryvyi Rih, Ukraine

morkunv@gmail.com, vtron@ukr.net, zimogladvadim@gmail.com

received 7 November 2020, revised 20 December 2021, accepted 22 December 2021

Abstract: The process line of concentrating iron ore materials is considered as a sequence of connected concentration units, some of which partially return ore materials to the previous unit. The output product of the final concentration unit in the process line is the end product of the whole line. Characteristics of ore, such as distribution of ore particles by size and distribution of iron content by size classes, are considered. Processing of iron ore materials by process units (a cycle, a scheme) is characterised by a separation characteristic – namely the function of extracting elementary fractions depending on physical properties of ore particles. The results of fraction analysis of ore samples in different points of the process line provide an experimental definition of separation characteristics and numerical values of the Rosin–Rammler equation factors. To identify dependencies that cannot be analytically described, the hybrid approach accompanied by the Takagi–Sugeno fuzzy models, in accompaniment with triangular membership functions determining fuzzy sets in preconditions, are used. To identify fuzzy sets in rule preconditions, triangular membership functions are used. Introduction of a-priori data on iron ore concentration as constraints for model parameters is a promising trend of further research, since it enables increased accuracy of identification despite limited availability of experimental data.

Key words: iron ore, Rosin–Rammler, fuzzy model, separation characteristics

1. INTRODUCTION

Iron ore processing is influenced by a variety of factors to varying extents. Among them, the following groups of factors are distinguished [23, 28–29, 34]: characteristics of mineralogical composition of ore; parameters of crushing machines determining the rate of size reduction of crushed ore; parameters determining grinding indices; parameters determining floatation processes. Based on this list, certain basic trends are distinguished in solving the problems of enhancing productivity of a concentration plant in terms of a marketable product [6, 7, 36, 37]: developing efficient regulations of the process conduction and upgrading technological equipment; designing automated control systems for concentration processes considering technological properties of processed ore; creating the system of automatic control over critical modes of technological processes and the expert decision support system.

The resulting separation characteristic of ore materials with a working point in the optimal cut-point is an essential indicator of improving the technological line of ore concentration [21, 22]. In technological flows of the ore concentration line at various stages, critically different types of ore materials in terms of their physical–mechanical and chemical–mineralogical characteristics are subjected to concentration; it is therefore expedient to investigate into the formation of a separation characteristic of technological concentration processes based on operating data on dynamics of their parameters [5, 20, 26].

Technological processes of ore-concentrating plants involve

multi-staged crushing and grinding to prepare ore for subsequent separation [17, 32]. The operations are aimed at releasing ore grains and extracting particles of various minerals by reducing grain sizes up to 0.1 mm and less. In some cases, the size of the impregnated useful component covers several size classes used to assess granulometric composition of concentration products at mining and concentration plants (Fig. 1): ‘+3’, ‘–3 + 1’, ‘–1 + 0.5’, ‘–0.5 + 0.25’, ‘–0.25 + 0.125’, ‘–0.125 + 0.071’, ‘–0.071 + 0.056’, ‘–0.056 + 0.044’, ‘–0.044 + 0’.

2. LITERATURE ANALYSIS

According to the research results [15–16, 32], to obtain quantitative evaluation of mineral products, except for the factor of mineral particles distribution $\gamma(\xi)$ by fractions with different physical properties ξ , the factor of useful components distribution $\beta(\xi)$ should also be used. The factors $\gamma(\xi)$ and $\beta(\xi)$ enable quantitative evaluation of ore materials. To facilitate quantitative evaluation of efficiency of process units, the authors suggest using separation characteristics $\varepsilon(\xi)$ determining the value of extracting ε of mineral fractions into concentration products. The useful component is extracted into concentrate from the initial ore materials due to different physical properties ξ of a given component and accompanying minerals. In working zones of concentration units, particles are separated under the influence of physical forces. Particles with some physical properties ($\xi > \xi_p$) move to one section of the working zone (concentrate), while particles with other properties ($\xi < \xi_p$) move to the other (tailings).

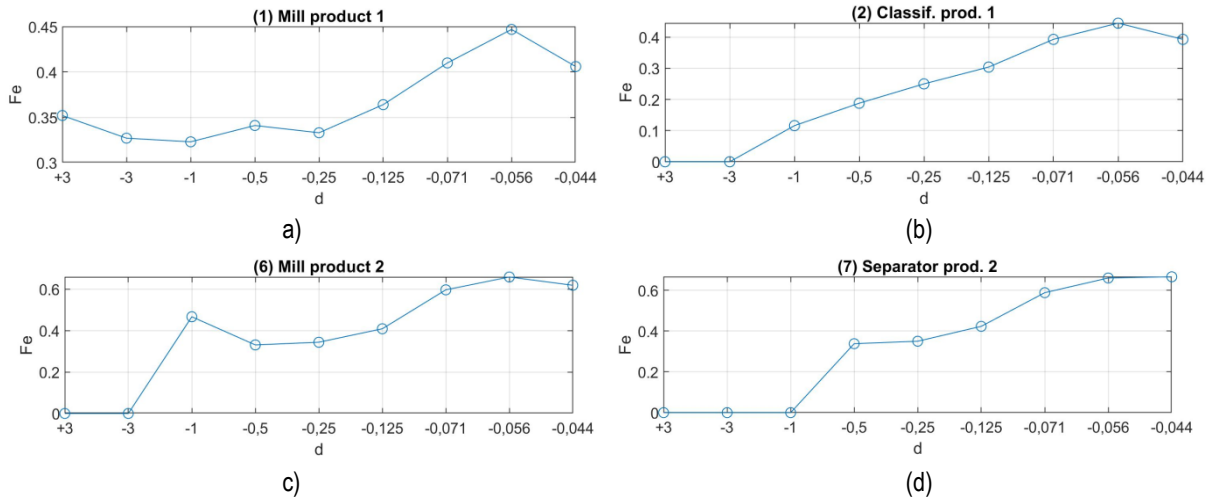


Fig. 1. Iron distribution by ore size classes at various points of the technological process

3. RESEARCH METHODS

In a general case, concentration units as control objects are operators transforming vectors of input variables into those of output variables. In compliance with this approach, the technological line of iron ore concentration is referred to as a set of n connected concentration units (Fig. 2). The first unit of the process line – usually a ball mill of wet grinding [19] – is fed with raw materials of $Q_0^{(P)}$ volume with certain qualitative characteristics ξ_0 . These characteristics include [23, 26]: distribution of raw materials by size; distribution of Fe_{tot} and Fe_{mag} content by size classes. Intermediate concentration product produced at the output of the first technological unit is a raw material for the next unit or it is partially returned to the previous unit for additional processing. A spiral classifier, a hydrocyclone and a deslimmer are examples of concentration units that return insufficiently ground ore particles. The final product of the last concentration unit in the process line, which is usually a magnetic separator, is concentrate, the end product of a given line.

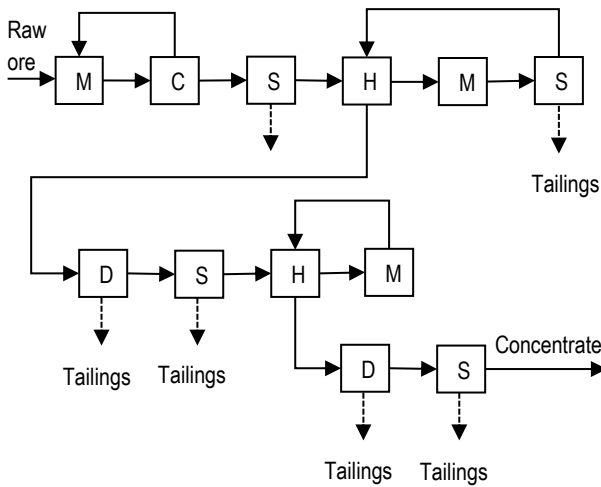


Fig. 2. Structural scheme of technological lines of iron ore concentration: M – mill, C – classifier; S – magnetic separator; H – hydrocyclone; D – deslimmer

Output parameters of each process unit $y_l = (y_{l-1}, y_l), l = 1 \dots n$ depend on the condition of a previous unit. In compliance with the method presented in [8], we denote a set of possible values of the condition vector of the i -th element by $Y_i, y_i \in Y_i$, the condition vector of the i -th subsystem composed of i successively connected elements – by y_{1i} , a set of possible values of the condition vector of the i -th subsystem:

$$Y_{1i} = \prod_{s=1}^i Y_s = \{y_s \in Y_s, s = \overline{1, i}\}, y_{1i} \in Y_{1i}, \tag{6}$$

the vector of the process complex composed of n successively connected elements:

$$y_{1n} = \prod_{i=1}^n Y_i = \{y_i \in Y_i, i = \overline{1, n}\}, \tag{7}$$

a set of possible values of the condition vector of a process complex at a mining and concentration plant – by $Y_{1n}, y_{1n} \in Y_{1n}$, the vector of parameters of the i -th element – by κ_i , and a set of its values – by $\kappa_i, \kappa_i \in K_i$. It should be noted that in this case, Y_i indicates technological constraints of a corresponding element of the technological complex.

where Θ is an operator of the grinding unit; $\{Q_1^{(Sturry)}, \{r_1[d], s_1[d]\}$ are vectors of output values; $\{Q_0^{(Ore)}, Q_0^{(Water)}\}$ is a vector of controlling actions; $\{r_0[d], s_0[d]\}$ is a vector of disturbance actions (the characteristic of the input flow of ore materials); t is a time variable.

The separating unit (a spiral classifier, a deslimmer, a hydrocyclone, a magnetic separator) as an operator assumes the following form:

$$\left\{ \left\{ Q_2^{(I)}, r_2^{(I)}[d], s_2^{(I)}[d] \right\}, \right\} = \Lambda_2 \left(\left\{ \left\{ Q_1^{(Sturry)} \right\}, \left\{ r_1[d], s_1[d] \right\}, t \right\} \right) \tag{9}$$

where Λ is an operator of the separating unit; $\{Q_2^{(I)}, r_2^{(I)}[d], s_2^{(I)}[d]\}$ are vectors of output values (discharge, middlings); $\{Q_2^{(II)}, r_2^{(II)}[d], s_2^{(II)}[d]\}$ are vectors of output values (sands, tailings); $\{Q_1^{(Sturry)}\}$ are vectors of controlling actions; and $\{r_1[d], s_1[d]\}$ is a vector of disturbance actions (characteristic of the input flow of ore materials).

The operator of the grinding unit is characterised by several inputs and outputs (MIMO).

$$\left\{ \left\{ Q_1^{(Slurry)} \right\}, \left\{ r_1[d], s_1[d] \right\} \right\} = \Theta_1 \left(\left\{ Q_0^{(Ore)}, Q_0^{(Water)} \right\}, \left\{ r_0[d], s_0[d], t \right\} \right) \quad (10)$$

Absolutely analytical representation of the operator of the grinding unit Θ_1 is impossible due to complexity of connections between output and input signals.

Among such signals in grinding, there are operator elements such as the following:

- redistribution (change of sizes) of particles in the output flow of ore materials:

$$\{r_1[d]\} = \Theta_1^r \left(\left\{ Q_0^{(P)}, Q_0^{(B)} \right\}, \{r_0[d], s_0[d]\}, t \right) \quad (11)$$

- redistribution (as a result of changed sizes) of Fe content in size classes of the output flow of ore materials:

$$\{s_1[d]\} = \Theta_1^s \left(\left\{ Q_0^{(P)}, Q_0^{(B)} \right\}, \{r_0[d], s_0[d]\}, t \right) \quad (12)$$

The operator of the separation unit in the same way as that of the grinding unit is characterised by multiple inputs multiple outputs (MIMO). At the same time, the separating unit has two output flows of ore materials; this doubling of the number of output values is comparable to the grinding unit.

$$\left\{ \left\{ Q_2^{(I)}, r_2^{(I)}[d], s_2^{(I)}[d] \right\}, \left\{ Q_2^{(II)}, r_2^{(II)}[d], s_2^{(II)}[d] \right\} \right\} = \Lambda_2 \left(\left\{ Q_1^{(II)} \right\}, \left\{ r_1[d], s_1[d] \right\}, t \right) \quad (13)$$

As in the case of designing a mathematical model of the grinding unit, absolutely analytical representation of the operator of the separating unit Λ_2 is impossible because of complex connections between output and input signals.

Among such signals in grinding, there are operator elements such as the following:

- redistribution (change of sizes) of particles in the output flow of ore materials:

$$\begin{aligned} \{r_2^{(I)}[d]\} &= \Lambda_2 \left(\left\{ Q_1^{(II)} \right\}, \{r_1[d], s_1[d]\}, t \right); \\ \{r_2^{(II)}[d]\} &= \Lambda_2 \left(\left\{ Q_1^{(II)} \right\}, \{r_1[d], s_1[d]\}, t \right), \end{aligned} \quad (14)$$

- redistribution (as a result of changed sizes) of Fe content in size classes of the output flow of ore materials:

$$\begin{aligned} \{s_2^{(I)}[d]\} &= \Lambda_2 \left(\left\{ Q_1^{(II)} \right\}, \{r_1[d], s_1[d]\}, t \right); \\ \{s_2^{(II)}[d]\} &= \Lambda_2 \left(\left\{ Q_1^{(II)} \right\}, \{r_1[d], s_1[d]\}, t \right), \end{aligned} \quad (15)$$

It should be noted that while using the material balance equation, one of the separating units can be calculated by values of another output. For example, the output parameter $\{r_2^{(II)}[d]\}$ can be calculated by the known output parameter $\{r_2^{(I)}[d]\}$ and the input one $\{r_1[d]\}$.

Iron ore processing by process units (a cycle, a scheme) is characterised by a separation characteristic $\varepsilon(\xi)$ – a function of extracting elementary fractions depending on physical properties of particles ξ of ore materials [32].

Dependency $\beta(\xi)$ of the useful component content on physical properties ξ of particles is one of the basic characteristics of ore

composition (32). Inside each fraction, separate particles can have different content of the component; a set $\bar{\beta}_1, \bar{\beta}_2, \dots, \bar{\beta}_n$ and the function $\beta(\xi)$ provide average values of the content inside a fraction. It is worth noting that in separating ore particles by the property ξ , the value of the useful component content β is secondary. Ore materials and concentration products are identified by the change of the physical property ξ of particles in a certain range $[\xi_{\min}, \xi_{\max}]$ due to available mineral aggregates. The output of the i -th fraction $[\xi_i, \xi_{i+1}]$ is determined as a ratio of mass of its particles to total mass of particles of all fractions in a range of $[\xi_{\min}, \xi_{\max}]$:

$$\bar{\gamma}_i = \gamma(\xi_i) \Delta \xi_i = P_i / \sum_{i=1}^n P_i \quad (16)$$

where $\gamma(\xi_i)$ is mass of the i -th fraction in the mixture, i.e. a discrete analogue of the differential function of distributing particles according to the physical property ξ ; $\Delta \xi_i$ is fraction size; P_i is productivity by the i -th fraction.

Final fractions are extracted by separating the total range $[\xi_{\min}, \xi_{\max}]$ of the changes of the physical property ξ of the particles' mixture by some number of final fractions $\Delta \xi_1, \Delta \xi_2, \dots, \Delta \xi_n$ [32]. Extraction of the solid final fraction $[\xi_i, \xi_i + \Delta \xi_i]$ into concentrate results in equality to the ratio of productivity of the solid of the given fraction in the concentrate $P_{i \text{ K}}$ and the input material $P_{i \text{ BX}}$.

$$\bar{\varepsilon}_{i \text{ K}} = \frac{P_{i \text{ K}}}{P_{i \text{ BX}}} = \frac{Q_{\text{K}} \bar{\gamma}_{i \text{ K}}}{Q_{\text{BX}} \bar{\gamma}_{i \text{ BX}}} = \frac{Q_{\text{K}} \gamma_{i \text{ K}}(\xi_i) \Delta \xi_i}{Q_{\text{BX}} \gamma_{i \text{ BX}}(\xi_i) \Delta \xi_i} \quad (17)$$

where $Q_{\text{K}}, Q_{\text{BX}}$ are productivities of the solid in the concentrate and the input material, respectively, t/h; $\bar{\gamma}_{i \text{ K}}, \bar{\gamma}_{i \text{ BX}}$ is output of a fraction in the concentrate and the input material, respectively; $\gamma_{i \text{ K}}(\xi), \gamma_{i \text{ BX}}(\xi)$ are distribution of the solid by fractions in the concentrate and the input material, respectively. Application of the given formula to each fraction enables a set of final extractions of fractions $\bar{\varepsilon}_{1 \text{ K}}, \bar{\varepsilon}_{2 \text{ K}}, \dots, \bar{\varepsilon}_{n \text{ K}}$. After fulfilling the condition $\Delta \xi_i \rightarrow 0, n \rightarrow \infty$, the mentioned set is transformed into a continuous function – a separation characteristic [32]

$$\varepsilon_{\text{K}}(\xi) = \frac{Q_{\text{K}} \gamma_{\text{K}}(\xi) d\xi}{Q_{\text{BX}} \gamma_{\text{BX}}(\xi) d\xi} = \bar{\gamma}_{\text{K}} \frac{\gamma_{\text{K}}(\xi)}{\gamma_{\text{BX}}(\xi)} \quad (18)$$

where $\bar{\gamma}_{\text{K}} = Q_{\text{K}} / Q_{\text{BX}}$ is the concentrate yield, unit fraction.

According to the method of experimentally determining the separation characteristic presented in [32], there is a need to measure productivity of the input material Q_{BX} and the concentrate Q_{K} . Next, fraction analysis of samples of the input material and the concentrate should be performed to define distribution functions $\gamma_{\text{BX}}(\xi), \gamma_{\text{K}}(\xi)$, followed by calculations using Eq. (18).

The density of distributing mass of fractions by sieve composition is described by Weibull distribution [30]

$$r[d] = A a d^{a-1} e^{-A d^a} \quad (19)$$

to which the equation of the distribution function $R[< d] = 1 - e^{-A d^a}$ corresponds. The Rosin–Rammler equation of granulometric composition by the total residue on the sieve with the cell d assumes the form of:

$$R[> d] = e^{-A d^a} \quad (20)$$

After changing the numerical value of the factor a , Eq. (20) enables describing a wide range of curves [30]. With $a > 1$, the density curve reaches its maximum and then decreases asymptot-

ically; with $a < 1$ the curve looks like a hyperbole. The larger the indicator A , the more concave the curve of granulometric composition. With $a = 1$ Eq. (19) changes into the one-parameter law of exponential distribution.

Eq. (20) is linearised with double logarithmation –

$$\ln(-\ln R[> d]) = \ln A + a \ln d \quad (21)$$

The size of the sieve cell $d_{\max} = D$, and the residue on which it equals v (i.e. $v = 0,05$), will correspond to the maximum statistic size of ore particles d_{\max} [30]

$$R[> d_{\max}] = v = e^{-Ad_{\max}^a} \quad (22)$$

After substituting A into Eq. (20), because of the maximum size of a particle, the expression assumes the form:

$$R[> d] = e^{\ln v (d/d_{\max})^a} \quad (23)$$

There are some technological products (i.e. classifier sands) with no fine fractions; this fact does not allow application of Eq. (20) to the product like that. Correction for d_{\min} can be considered if we shift the coordinate origin by a value of d_{\min} on the abscissa axis, i.e. transform the equation into the form suggested in [30]

$$R[> d] = e^{-A(d-d_{\min})^a} \quad (24)$$

In this form, the equation satisfies any lower boundary value. The distribution density expressed by Eq. (24) is similar to Eq. (19):

$$r[d_i] = Aa(d_i - d_{\min})^{a-1} e^{-A(d_i-d_{\min})^a} \quad (25)$$

The considered dependencies are also applied to the description of distributing the useful component mass (metal) of fractions [30].

$$S[> d] = e^{-B(d-d_{\min})^b} \quad (26)$$

An equation similar to that of the distribution density presented in Eq. (25) assumes the following form:

$$s[d] = Bb(d - d_{\min})^{b-1} e^{-B(d-d_{\min})^b} \quad (27)$$

$$S[> d] = \frac{e^{-B(d-d_{\min})^b} - e^{-B(d_{\max}-d_{\min})^b}}{1 - e^{-B(d_{\max}-d_{\min})^b}} \quad (28)$$

Eqs (26) and (25) are linearised with double logarithmisation in the coordinate system $Y = \ln(-\ln S[> d])$ and $X = \ln(d - d_{\min})$. The parameters of distributing the components, B and b , determine the character of the distribution curve of the granulometric composition and metal in the product.

Thus, the aggregate of both distributions enables full description of product composition in technological terms [30]. For example, based on distribution of mass of a product and that of metal in it, distribution of metal content by size fractions with $d_{\min} = 0$ can be described in the following way:

$$\alpha[d_i] = \frac{s[d_i]}{r[d_i]} \alpha_0 = \frac{\alpha_0 B b}{A a} d_i^{b-a} e^{A d_i^a - B d_i^b} \quad (29)$$

In a similar way, we write metal content in a fraction of larger (smaller) size by means of the ratios [30]

$$\alpha[> d] = \frac{S[> d]}{R[> d]} \alpha_0 = \frac{e^{-B d^b}}{e^{-A d^a}} \alpha_0 \quad (30)$$

$$\alpha[< d] = \frac{S[< d]}{R[< d]} \alpha_0 = \frac{1 - e^{-B d^b}}{1 - e^{-A d^a}} \alpha_0 \quad (31)$$

Thus, to form a mathematical model of iron ore processing in technological units, it is necessary to identify parameters of the dependencies presented above.

4. RESEARCH RESULTS

To calculate factors of the Rosin–Rammler equation based on experimental data gathered from the results of sieve analysis, the method suggested by L.P. Shupov [30] can be utilised. On the first stage, sieve analysis data determine total yield of fractions by the formulae: for the fraction $r[d_1] - R[> d_1] = r[d_1]$; for the fraction $r[d_i] - R[> d_i] = r[d_1] + r[d_2] + \dots + r[d_i]$; for the fraction $r[d_m] - R[> d_m] = 1$. While doing the research (Fig. 3), the authors consider the following size fractions of ore particles: $+3, -3 + 1, -1 + 0.5, -0.5 + 0.25, -0.25 + 0.125, -0.125 + 0.071, -0.071 + 0.056, -0.056 + 0.044, -0.044 + 0$. The testing results of the concentration line were obtained during the operations under the supervision of T.A. Oliinyk [12, 24].

To calculate factors of metal distribution B and b for each fraction (Fig. 4), metal content $\alpha[d_i]$ and metal share for this fraction are determined:

$$s[d_i] = r[d_i] \alpha[d_i] / \alpha_0 \quad (32)$$

where α_0 is total content of metal in the product. The metal share in the fraction is larger than d :

$$S[> d_i] = s[d_1] + s[d_2] + \dots + s[d_{i-1}] + s[d_i] \quad (33)$$

To determine the factors of the Rosin–Rammler equation in (30), the least square method is used. After linearising the expression in Eq. (20) by double logarithmation, we obtain:

$$\ln(-\ln R[> d]) = \ln A + a \ln d \quad (34)$$

we denote

$$Y_i^{(R)} = \ln(-\ln R[> d_i]); \quad Z_i^{(R)} = \ln d_i, \quad (35)$$

and for the useful component content

$$\begin{aligned} \ln(-\ln S[> d]) &= \ln B + b \ln d; \\ Y_i^{(S)} &= \ln(-\ln S[> d_i]); \quad Z_i^{(S)} = \ln d_i, \end{aligned} \quad (36)$$

Parameters of the Rosin–Rammler equation for different points of the technological line are presented in Tab. 1.

Parameters of the Rosin–Rammler equation for mathematical modelling of Fe content distribution by size classes of ore particles along the concentration line for different process line points are presented in Tab. 2.

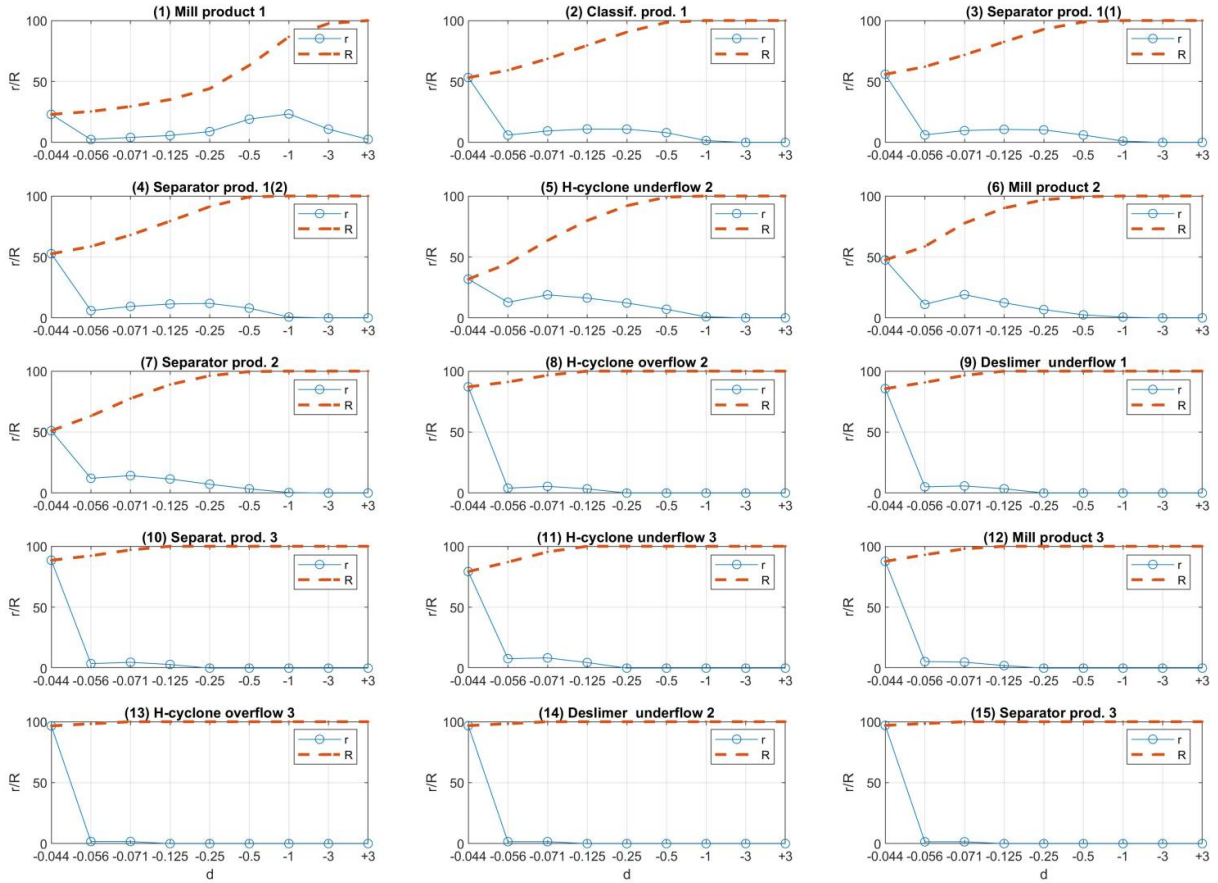


Fig. 3. Total yield of fractions in control points along the concentration line

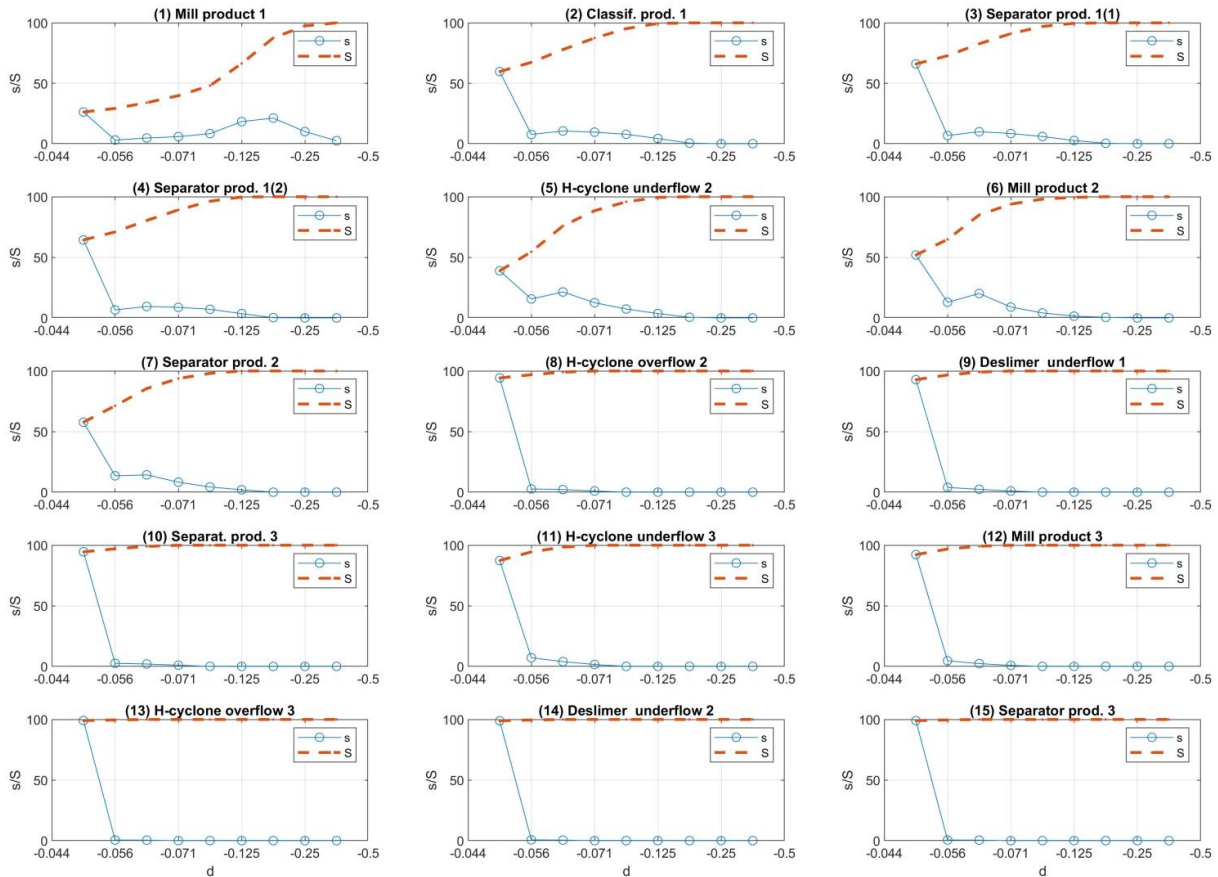


Fig. 4. Metal share in the fraction in control points along the concentration line

Tab. 1. Rosin–Rammler equation factors for distributing ore particles by size classes (R)

Unit	Factor A	Factor a	Determination factor	Mean square error
(1) Mill discharge 1st stage #1	0.0368	1.9400	0.8775	11.7944
(2) Classifier discharge #1	0.5924	0.8162	0.9004	6.3519
(3) Mag. separation 1st feed, 1st stage #1/#2	0.6612	0.7841	0.9054	5.7896
(4) Mag. separation 2nd feed, 1st stage #1/#2	0.5767	0.8354	0.8972	6.5903
(5) Hydrocyclone sands 2nd stage	0.2716	1.3088	0.9726	4.6582
(6) Mill discharge 2nd stage	0.5365	1.0084	0.9597	4.2967
(7) Mag. separation 2nd stage	0.6173	0.9121	0.9609	3.8813
(8) Hydrocyclone discharge 2nd stage	1.9728	0.5106	0.9201	1.4593
(9) Desliming sands 1st stage.	1.8733	0.5436	0.9363	1.4275
(10) Mag. product 3rd stage	2.0908	0.4914	0.9224	1.2758
(11) Hydrocyclone sands 3rd stage	1.5101	0.6462	0.9484	1.8387
(12) Mill discharge 3rd stage	2.0425	0.5471	0.9573	0.9749
(13) Hydrocyclone discharge 3rd stage	3.3499	0.4278	0.9423	0.3087
(14) Desliming sands 2nd stage	3.4106	0.4216	0.9420	0.2912
(15) Mag. product 4th stage	3.4752	0.4152	0.9418	0.2736

Tab. 2. Factors of Rosin–Rammler equation for distributing Fe content by size classes (S)

Unit	Factor B	Factor b	Determination factor	Mean square error
(1) Mill discharge 1st stage #1	0.0728	1.5968	0.9418	0.2736
(2) Classifier discharge #1	0.7806	0.7478	0.9418	0.2736
(3) Mag. separation 1st feed, 1st stage #1/#2	0.9579	0.6790	0.9418	0.2736
(4) Mag. separation 2nd feed, 1st stage #1/#2	0.9015	0.6884	0.9418	0.2736
(5) Hydrocyclone sands 2nd stage	0.4103	1.1733	0.9418	0.2736
(6) Mill discharge 2nd stage	0.6482	0.9729	0.9418	0.2736
(7) Mag. separation 2nd stage	0.7910	0.8580	0.9418	0.2736
(8) Hydrocyclone discharge 2nd stage	2.8185	0.4344	0.9418	0.2736
(9) Desliming sands 1st stage.	2.6107	0.4935	0.9418	0.2736
(10) Mag. product 3rd stage	2.8679	0.4243	0.9418	0.2736
(11) Hydrocyclone sands 3rd stage	2.0485	0.6049	0.9418	0.2736
(12) Mill discharge 3rd stage	2.5394	0.5340	0.9418	0.2736
(13) Hydrocyclone discharge 3rd stage	4.6735	0.3412	0.9418	0.2736
(14) Desliming sands 2nd stage	4.5014	0.3614	0.9418	0.2736
(15) Mag. product 4th stage	4.6428	0.3421	0.9418	0.2736

Abonyi et al. [1] considers identification of fuzzy models with the structure suggested in [31]. This fuzzy model is composed of a set of rules in the following form:

$$R_{i_1, \dots, i_n} : \text{if } z_1 \text{ is } A_{1, i_1} \text{ and } \dots \text{ and } z_n \text{ is } A_{n, i_n} \text{ then } y = f_{i_1, \dots, i_n}(z_1, \dots, z_n) \quad (37)$$

where n is the number of inputs, $\bar{z} = [z_1, \dots, z_n]$ is the vector containing all the inputs of the fuzzy model and $A_{j, i_j}(z_j)$ is the i_j -th fuzzy set of preconditions for the j -th input. The same symbol is applied to the fuzzy set and its membership function. M_j is the

number of fuzzy sets in the j -th input domain. $f_{i_1, \dots, i_n}(\bar{z})$ is a (crisp) output function. For the given input vector \bar{z} the output of the fuzzy model y is calculated as weighted:

$$y = \frac{\sum_{i_1=1}^{M_1} \dots \sum_{i_n=1}^{M_n} \beta_{i_1, \dots, i_n} f_{i_1, \dots, i_n}(z_1, \dots, z_n)}{\sum_{i_1=1}^{M_1} \dots \sum_{i_n=1}^{M_n} \beta_{i_1, \dots, i_n}} \quad (38)$$

where the weight $\beta_{i_1, \dots, i_n} > 0$ is the overall truth value of the $i_1 \dots i_n$ -th rule calculated by the formula:

$$\beta_{i_1, \dots, i_n} = \prod_{j=1}^n A_{j, i_j}(z_j) \quad (39)$$

To determine fuzzy sets in rule preconditions in Abonyi et al. [1], a triangular membership function is used:

$$a_{j,i_j} = \text{core} \left(A_{j,i_j}(z_j) \right) = \left\{ z_j | A_{j,i_j}(z_j) = 1 \right\} \quad (40)$$

where a_{j,i_j} are kernels of fuzzy sets.

The set carrier is determined by kernels of adjacent fuzzy sets:

$$\begin{aligned} A_{j,i_j}(z_j) &= \frac{z_j - a_{j,i_j-1}}{a_{j,i_j} - a_{j,i_j-1}}, \quad a_{j,i_j-1} \leq z_j \leq a_{j,i_j}; \\ A_{j,i_j}(z_j) &= \frac{a_{j,i_j+1} - z_j}{a_{j,i_j+1} - a_{j,i_j}}, \quad a_{j,i_j} \leq z_j \leq a_{j,i_j+1}. \end{aligned} \quad (41)$$

The above-mentioned method of determination guarantees that the total of membership functions is equal to one. These constraints enable obtainment of interpreted bases of rules. The output evaluation method presented in (1) can be applied without being bound to certain membership functions. As the product operator in Eq. (39) is applied to the connector 'AND', total values of truth satisfy the conditions:

$$\sum_{i_1=1}^{M_1} \dots \sum_{i_n=1}^{M_n} \beta_{i_1, \dots, i_n} = 1 \quad (42)$$

Thus, Eq. (2) can be simplified in the following way (1):

$$y = \sum_{i_1=1}^{M_1} \dots \sum_{i_n=1}^{M_n} \left[\left(\prod_{j=1}^n A_{j,i_j}(z_j) \right) f_{i_1, \dots, i_n}(z_1, \dots, z_n) \right] \quad (43)$$

In many fuzzy identification methods, a nonlinear autoregressive exogenous model (NARX), of both neural-network and fuzzy types, is used. This model determines nonlinear dependency between previous inputs–outputs and a forecast output (1):

$$y(k+1) = F \left(y(k), \dots, y(k - n_y + 1), u(k - n_d), \dots \right) \quad (44)$$

where n_y , n_u are maximum lags of input and output signals, respectively, n_d is discrete delay time and F is reflection of the fuzzy model.

Tagaki–Sugeno fuzzy NARX-like model interpolates between local linear invariant (LTI) ARX models in this way (1):

$$\begin{aligned} R_{i_1, \dots, i_n} : \text{if } z_1(k) \text{ is } A_{1,i_1} \text{ and } \dots \text{ and } z_n(k) \text{ is } A_{n,i_n} \text{ then} \\ y^{i_1, \dots, i_n}(k+1) &= \sum_{i=1}^{n_y} a_i^{i_1, \dots, i_n} y(k-i+1) + \\ &+ \sum_{i=1}^{n_u} b_i^{i_1, \dots, i_n} u(k-i-n_d+1) + c^{i_1, \dots, i_n} \end{aligned} \quad (45)$$

where $\bar{z}(k)$ is usually a subset $\{y(k), \dots, y(k - n_y + 1), u(k - n_d), \dots, u(k - n_u - n_d + 1)\}$. This fuzzy model can be considered as linear parameter-varying (LPV):

$$\sum_{i=1}^{n_y} a_i y(k-i+1) = \sum_{i=1}^{n_u} b_i u(k-i-n_d+1) + c \quad (46)$$

where

$$\begin{aligned} a_0 &= 1; \\ a_i &= - \sum_{i_1=1}^{M_1} \dots \sum_{i_n=1}^{M_n} \left(\prod_{j=1}^n A_{j,i_j}(z_j) \right) a_i^{i_1, \dots, i_n}, \quad i = 1, \dots, n_y; \\ b_i &= \sum_{i_1=1}^{M_1} \dots \sum_{i_n=1}^{M_n} \left(\prod_{j=1}^n A_{j,i_j}(z_j) \right) b_i^{i_1, \dots, i_n}, \quad i = 1, \dots, n_u; \\ c &= \sum_{i_1=1}^{M_1} \dots \sum_{i_n=1}^{M_n} \left(\prod_{j=1}^n A_{j,i_j}(z_j) \right) c^{i_1, \dots, i_n} \quad i = 1, \dots, n_y, \end{aligned} \quad (47)$$

Parameters a_i, b_i, c are usually constrained in boundaries of convex sets (polytopes) separated by parameters of some rules. This results from Eq. (47) and the fact that degrees of membership total one, as is shown in Eq. (6). It is indicated that some types of a-priori knowledge about the LTI model can be expressed as linear constraints of inequality [1, 33]:

$$\Lambda_{LTI} \theta_{LTI} \leq \omega_{LTI} \quad (48)$$

where $\theta_{LTI} = [a_1, a_2, \dots, a_{n_y}, b_1, \dots, b_{n_u}, c]$ denotes parameters of the LTI model. These constraints of the LTI model parameters determine a set of convex parameters Ω :

$$\Omega = \{ \theta_{LTI} | \Lambda_{LTI} \theta_{LTI} \leq \omega_{LTI} \} \quad (49)$$

Abonyi et al. (1) suggests the method of introducing a-priori data into fuzzy model. The set of parameters θ_{LTI} of the LTI model can be a subset Ω . Through the convexity Ω and the convexity of the applied method of fuzzy outputs, it is sufficient to check constraints for the rule outputs. This means that constraints can be adjusted to Takegi–Sugeno fuzzy model:

$$\Lambda^* \theta_{i_1, \dots, i_n} \leq \omega^* \quad (50)$$

where

$$\begin{aligned} \theta_{i_1, \dots, i_n} &= \\ &[a_1^{i_1, \dots, i_n}, a_2^{i_1, \dots, i_n}, \dots, a_{n_y}^{i_1, \dots, i_n}, b_1^{i_1, \dots, i_n}, \dots, b_{n_u}^{i_1, \dots, i_n}, c^{i_1, \dots, i_n}] \end{aligned}$$

denotes parameters of the i_1, \dots, i_n -th local model, Λ^*, ω^* are global constraints of the fuzzy model.

5. CONCLUSIONS

Technological concentration units as controlled objects are operators that transform vectors of input variables into those of output variables. Correspondingly, the process line of concentrating iron ore materials is considered as a sequence of connected concentration units, some of which partially return ore materials to the previous unit. The output product of the final concentration unit in the process line is the end product of the whole line. Characteristics of ore such as distribution of ore particles by size and distribution of Fe_{tot} and Fe_{mag} content by size classes are considered.

The operator of the separating unit, similar to that of the grinding one, is characterised by several inputs and outputs (MIMO). At the same time, the separating unit has two output flows of ore materials, thus doubling the number of output values in relation to the grinding unit.

As in the case of designing a mathematical model of the grinding unit, absolutely analytical representation of the operator of the separating unit is impossible due to complexity of connections between output and input signals. Among such signals in grinding, one should distinguish between operator elements such as redistribution (change of size) of particles in input flows of ore materials and redistribution of Fe content in size classes of output flows of ore materials.

Processing of iron ore materials by process units (a cycle, a scheme) is characterised by a separation characteristic – namely the function of extracting elementary fractions depending on physical properties of ore particles.

The results of fraction analysis of ore samples in different points of the process line provide experimental definition of the separation characteristics and numerical values of the Rosin–

Rammler equation factors.

To identify dependencies that cannot be analytically described, the hybrid approach, accompanied by the Takagi–Sugeno fuzzy models and triangular membership functions determining fuzzy sets in preconditions, is used. To identify fuzzy sets in rule preconditions, triangular membership functions are used.


Introduction of a-priori data on iron ore concentration as constraints for model parameters is a promising trend of further research, since it enables increased accuracy of identification with limited availability of experimental data.


REFERENCES

1. Abonyi J, Babuska JR, Verbruggen HB, Szeifert F. Incorporating prior knowledge in fuzzy model identification. *International Journal of Systems Science*. 2000; 31:657-667. doi.org/10.1080/002077200290966.
2. Bilenko LF. *Zakonomernosti izmelcheniya v barabannykh melnitsakh* [Regularities of grinding in drum mills]. Moscow: Nedra [in Russian]; 1984.
3. Bogatikov VN, Kulakov AG. Ispol'zovanie gibridnoy neyronnoy seti v raskrytii neopredelennosti funktsii razrusheniya materia-la pri izmelchenii [Application of the hybrid neural network in disclosing ambiguity of the material destruction function in grinding]. *Vestnik Kostromskogo gosudarstvennogo universiteta – Bulletin of Kostroma State University*. 2006; 11:29-31 [in Russian].
4. Bogatikov VN, Kulakov AG, Reev SN. Imitatsionnoe modelirovanie tehnologicheskogo protsessa sokrascheniya krupnosti materiala pri izmelchenii v agregate nepreryvnogo deystviya s zamknytim tsiklom. *Informatsionnyie tehnologii v regionalnom razviti* [Simulations of size reduction processes in grinding in the closed-loop continuous unit. Information technologies in regional development]. *Apatityi* [in Russian]. 2006.
5. Bublikov A, Tkachov V. Automation of the control process of the mining machines based on fuzzy logic. *Naukovyi Visnyk Natsionalnoho Hirnychoho Universytetu*. 2019; 3:112–118.
6. Golik V, Komashchenko V, Morkun V, Burdzieva O. Metal deposits combined development experience. *Metallurgical and Mining Industry*. 2015; 7(6):591-594.
7. Golik VI, Razorenov YI, Efremkov AB. Recycling of metal ore mill tailings. *Applied Mechanics and Materials*. 2014; 682:363-368.
8. Grechnikov AF, Grishanov DG, Pavlov OV, Pushkov AN. Soglasovannoe upravlenie tehnologicheskim kompleksom s posledovatelno soedinennymi elementami [Cohesive control over a technological complex with sequentially connected elements]. *Vestnik Samarskogo gosudarstvennogo aerokosmicheskogo universiteta – Bulletin of Samara State Aerospace University*. 2003; 2:29-33 [in Russian].
9. Gurevich LS. Modelirovanie strukturyi potokov v barabannoy melnitse [Modelling of flow structures in drum mills]. *Obogaschenie rud – Ore Concentration*. 1989; 2:34-37 [in Russian].
10. Kafarov VV, Verdiyana MA. Matematicheskie modeli strukturyi potoka materiala v melnitsakh [Mathematical models of the structure of material flows in mills]. Moscow: Tsement; 1977. [in Russian].
11. Kafarov VV, Glebov MB. Matematicheskoe modelirovanie osnovnykh protsessov himicheskikh proizvodstv: Uchebnoe posobie dlya vuzov [Mathematical modelling of basic processes of chemical enterprises: Teaching manual for universities]. Moscow: Vysshaya shkola; 1991 [in Russian].
12. Khmil IV. Osoblivosti tehnologiyi podrlbnennya magnetitovykh kvartstiv v umovakh ob'Emnogo nerlvnomirno-komponentnogo stisnennya. Dis. kandidata tehn. nauk: 05.15.08 [Peculiarities of grinding technology of magnetite quartzite under volumetric irregular-component compression: Candidate's thesis (Engineering) 05.15.08]; 2016. [in Ukrainian].
13. Kramer YB. O kinetike nepreryvnogo izmelcheniya [On kinetics of continuous grinding]. *Fiziko-mehanicheskie problemyi razrabotki poleznykh iskopaemykh – Physical and mechanical problems of mineral mining*. 1986; 130-131 [in Russian].
14. Kruglov VV. *Iskusstvennyie neyronnyie seti. Teoriya i praktika* [Artificial neural networks. Theory and practice]. Moscow: Goryachaya liniya–Telekom; 2001 [in Russian].
15. Linch AD. *Tsikly drobleniya i izmelcheniya* [Cycles of crushing and grinding]. Moscow: Nedra; 1981 [in Russian].
16. Maryuta AN, Kachan YG, Bunko VA. *Avtomaticheskoe upravlenie tehnologicheskimi protsessami obogatitelnykh fabrik* [Automated control over technological processes at concentrating plants]. Moscow: Nedra; 1981 [in Russian].
17. Morkun V, Morkun N, Tron V, Hryshchenko S. Synthesis of robust controllers of technological units control systems of ore-dressing factory. *Eastern-European Journal of Enterprise Technologies*. 2018; 1-2(91):37-47.
18. Morkun V, Morkun N, Pikilnyak A. The adaptive control for intensity of ultrasonic influence on iron ore pulp, *Metallurgical and Mining Industry*. 2014; 6:8-11.
19. Morkun V, Morkun N, Tron V. Distributed closed-loop control formation for technological line of iron ore raw materials beneficiation. *Metallurgical and Mining Industry*. 2015; 7:16-19.
20. Morkun V, Morkun N, Tron V. Distributed control of ore beneficiation interrelated processes under parametric uncertainty, *Metallurgical and Mining Industry*. 2015; 8:18-21.
21. Morkun V, Morkun N, Tron V. Identification of control systems for ore-processing industry aggregates based on nonparametric kernel estimators, *Metallurgical and Mining Industry*. 2015; 1:14-17.
22. Morkun V, Morkun N, Tron V. Model synthesis of nonlinear nonstationary dynamical systems in concentrating production using Volterra kernel transformation, *Metallurgical and Mining Industry*. 2015; 10:6-9.
23. Morkun V, Tron V. Automation of iron ore raw materials beneficiation with the operational recognition of its varieties in process streams, *Metallurgical and Mining Industry*. 2014; 6: 4-7.
24. Oliinyk TA. Doslidzhennia vplivu dinamichnykh efektiv visokoenergetichnogo ultrazvuku na gazovi bulbashky u pulpi dlya upravlinnya parametrami ziyi gazovoi fazy u protsesi flotatsii: zvlst pro NDR [Investigation into dynamic effects of high-energy ultrasound on gas bubbles in slurry to control parameters of its gas phase in floatation: research report]. DVNZ «Krivorizkiy natsionalniy univrsitet». Kryvyi Rih; 2016 [in Ukrainian].
25. Pevzner LD, Kostikov VG, Lettiev OA, Kostikov RV. Razrabotka i issledovanie matematicheskoy modeli protsessa rudoizmelcheniya [Development of and investigation into the mathematical model of ore grinding]. *Gornyy informatsionno-analiticheskiy byulleten (nauchno-tehnicheskii zhurnal) – Mining information-analytical bulletin (scientific and technical journal)*. 2012; 11:312-320 [in Russian].
26. Porkuian O, Morkun V, Morkun N, Serdyuk O. Predictive control of the iron ore beneficiation process based on the Hammerstein hybrid model, *Acta Mechanica et Automatica*. 2019; 13(4):262-270.

27. Porkuian O, Morkun V, Morkun N. Measurement of the ferromagnetic component content in the ore suspension solid phase, *Ultrasonics*. 2020; 105:106103.
28. Stupnik N, Kalinichenko V, Pismennij S, Kalinichenko E. Features of underlying levels opening at «ArcelorMittal Kriviy Rih» underground mine. In: *New Developments in Mining Engineering 2015: Theoretical and Practical Solutions of Mineral Resources Mining*. 2015; 39-44.
29. Stupnik M, Kolosov V, Pysmennyi S, Kovbyk K. Selective mining of complex structured ore deposits by open stope systems. *E3S Web of Conferences*. 2019; 123:01007.
30. Shupov LP. Modelirovanie i raschet na EVM shem obogascheniya [Simulation and computer calculation of concentration schemes]. Moscow: Nedra; 1980 [in Russian].
31. Takagi T, Sugeno M. Fuzzy identification of systems and its application to modeling and control. *IEEE Trans. Systems, Man and Cybernetics*. 1985; 15(1):116-132.
32. Tihonov ON. Zakonomernosti effektivnogo razdeleniya mineralov v protsessah obogascheniya poleznykh iskopaemykh [Regularities of effective separation of minerals in concentration processes]. Moscow: Nedra; 1984 [in Russian].
33. Tulleken HJAF. Gray-box modelling and identification using physical knowledge and Bayesian techniques. *Automatica*. 1993; 29:285-308.
34. Tuz AA, Sanaeva GN, Prorokov AE, Bogatikov VN. Nechiotko-logicheskiy podhod k modelirovaniyu protsessa izmelcheniya v agregate nepreryvnogo deystviya s zamknutym tsiklom Aktsionernogo Obschestva «Kovdorskiy gorno-obogatitelnyy kombinat» [Fuzzy logic approach to modelling grinding in the closed-loop continuous unit of the JSC „Kovdor Mining Concentrating Works“]. *Internet-zhurnal "NAUKOVEDENIYE" – Internet-journal "SCIENCE STUDIES"*. 2016; 8(1).
<https://cyberleninka.ru/article/n/nechiotko-logicheskiy-podhod-k-modelirovaniyu-protsessa-izmelcheniya-v-agregate-nepreryvnogo-deystviya-s-zamknutym-tsiklom> [in Russian].
35. Tuz AA, Sanayeva GN, Prorokov AY, Bogatikov VN. Upravlenie tehnologicheskimi protsessami izmelcheniya i osnovnyie napravleniya ih avtomatizatsii [Control over grinding processes and basic trends of their automation]. *Vestnik evraziyskoy nauki – Bulletin of Eurasian Science*. 2016; 8(2):130–131 [in Russian].
36. Zlatorunskaya GE. Otsenka izmelchaemosti droblenoy rudyi po ee granulometricheskoy karakteristike [Assessment of ground ore by its granulometric characteristic]. *Obogaschenie rud – Ore Concentration*. 1985; 2 [in Russian].
37. Zolotkov NF, Dyomin VT, Kontsevov AV, Smirnov SV. Modernizatsiya i razvitiie sistem avtomatizirovannogo kontrolya i upravleniya [Updating and development of automated control systems]. *Gornyi zhurnal – Mining Journal*. 2012; 10:91-96 [in Russian].

 Vladimir Morkun:  <https://orcid.org/0000-0003-1506-9759>

 Vitalii Tron:  <https://orcid.org/0000-0002-6149-5794>

 Vadym Zymohliad:  <https://orcid.org/0000-0002-6822-6140>